Structure and Tracer Dynamics in Polyacrylamide Hydrogels

Doctoral Thesis
(Dissertation)

to be awarded the degree of
Doctor rerum naturalium (Dr. rer. nat.)

submitted by
Sebastian Seiffert
from Göttingen

approved by the Faculty of Natural and Materials Sciences,
Clausthal University of Technology

Date of oral examination
Dec. 14, 2007

Chairperson of the Board of Examiners
Prof. Dr. W. Schade

Chief Reviewer
Prof. Dr. W. Oppermann

Reviewer
Prof. Dr. D. Johannsmann

This thesis was written at the Institute of Physical Chemistry at Clausthal University of Technology, Clausthal-Zellerfeld, Germany, in the time between Aug 2004 and Nov 2007. Parts of it have been previously published as indicated in the prefaces of the corresponding chapters (q.v., list of publications, p 203).

Acknowledgements

I thank all the people who contributed to the present work. First and foremost my thanks go to *Prof. W. Oppermann* for suggesting the challenging topic and unhesitatingly giving any kind of support, while nevertheless leaving absolute freedom for the realization of the project. I also thank *Prof. D. Johannsmann* for reviewing this thesis and, especially, for his constructive criticism in numerous stimulating discussions.

Further thanks go to all people at the Institute of Physical Chemistry at Clausthal University of Technology for the pleasant atmosphere at and besides scientific work. In particular, I'd like to thank *Dr. A. Langhoff* and *Dr. J. Adams* for their never-ending willingness to provide help, encouragement, and well-intentioned advices for my everyday life as a prospective scientist.

As natural for a project like the present one, several parts of the work behind this thesis were kindly supported by a number of co-workers. In detail, I thank

- *Dr. J. C. Namyslo* and the *NMR group* of the Institute of Organic Chemistry, Clausthal University of Technology, for performing all high-resolution NMR measurements treated here, as well as *Dr. F. Stiemke* for giving various helpful tips for the analysis of the spectra,
- *Dr. L. Schwegler* and *P. Kuschel* from Bosch AG, Gerlingen, Germany, for providing the possibility to perform rheological measurements under UV exposure,
- *Prof. K. Saalwächter* from the Institute of Physics at Martin Luther University Halle-Wittenberg for providing the possibility to work on his minispec and for the nice further cooperation on the characterization of my PAAm samples by multiple-quantum NMR (Chapter 4.1),
- *Dr. J. Adams* for his assistance with fluorescence spectroscopy,
- *U. Cronjäger* and the *fine mechanics workshop* of the Institute of Physical Chemistry, Clausthal University of Technology, for the fabrication of various self-made components for experimental setups,
- *S. Fröbe* and *Dr. I. Nikiforova* for performing the AFM and ultracentrifugal analyses in the scope of Chapter 3.1.3,
- and, last but not least, *J. Gansel*, *M. Susoff*, and *Dr. A. Langhoff* for critical proofreading of this manuscript.

Very special thanks go to *G. Hauser* for the long-lasting fruitful cooperation on the development of the analysis procedures and computational algorithms for the systematic evaluation of FRAP experiments (Chapter 3.2).

Parts of the present work were funded by the German Research Foundation (DFG), which is gratefully acknowledged.

Finally, I thank my family and all my long-time friends, fellows, crewmembers, and band mates who joined and supported me during the past years, thus making them an absolutely unforgettable time. I think there’s no need to mention you in detail here, you know who you are and always will be!

Summary

The formation of polyacrylamide hydrogels as well as the dynamics of enclosed fluorescently labeled linear macromolecules and spherical nanoparticles were studied by means of rheology and multiple-quantum NMR, as well as fluorescence recovery after photobleaching (FRAP). The experiments were designed such that the transition from a semidilute solution to a permanent network could be covered. This was achieved by employing a matrix polymer carrying pendant dimethylmaleimide (DMMI) groups. Stepwise UV irradiation of such samples in the presence of a thioxanthone sensitizer causes successive dimerization of the maleimides leading to progressive crosslinking. Thus, investigations on network structures could be performed at intermediate stages, and the diffusion of linear and spherical tracers being enclosed in the matrix material could be observed within the interesting transition regime between a physically entangled system and a covalently crosslinked matrix. The extent of the photoreaction was simultaneously monitored by UV–vis spectroscopy.

To allow for the aforementioned studies, preliminary work focusing on the synthesis and characterization of fluorescently labeled polyacrylamides over a wide range of molar masses was performed, and a novel procedure for the systematic evaluation of spatially resolved FRAP experiments was developed.

Considering network formation, results obtained on crosslinking systems with different concentrations (20–80 g·L^{-1}) indicate that the generation of elastically active network strands occurs in proportion with DMMI conversion. The crosslinking efficiency varies markedly with polymer concentration but is surprisingly high, while the length of the network chains seems to be independent of concentration. Even though a fundamental investigation of the photoreaction showed that the dimerization of DMMI in aqueous media essentially leads to asymmetric products instead of the expected cyclobutane derivatives, crosslinking occurs without perceptible side reactions.

Studies on tracer dynamics in the semidilute domain were performed with varying concentrations of the matrix polymer (20–80 g·L^{-1}) as well as different molar masses (200 000–1 300 000 g·mol^{-1}) and particle radii (17 and 36 nm) of the enclosed labeled probes. Results indicate notable differences between the dynamics of flexible linear tracers and hard spherical particles:

While the behavior of the system is only marginally affected by the transition from a semidilute polymer solution to a chemically crosslinked network when linear chains are enclosed, spherical probes get completely immobilized when the degree of matrix-crosslinking exceeds a certain threshold.

Zusammenfassung

Die Entstehung von Polyacrylamid Hydrogelen sowie die Dynamik darin eingelagerter fluoreszenzmarkierter linearer Makromoleküle und kugelförmiger Nanopartikel wurde mit Hilfe von Rheologie und Multiquanten NMR Spektroskopie sowie durch Fluorescence Recovery After Photobleaching (FRAP) untersucht. Die Experimente waren dabei so ausgelegt, dass der Übergang von einer halbverdünnten physikalischen Netzwerklösung in ein permanent vernetztes chemisches Gel erfasst werden konnte. Dies wurde durch Verwendung von Matrixpolymeren mit seitenständigen Dimethylmaleinimid (DMMI) Gruppen erreicht, welche in Gegenwart eines Photosensibilisators durch UV Bestrahlung dimerisieren. Somit war eine sukzessive kovalente Vernetzung der funktionalisierten Ketten möglich, so dass Charakterisierungen der Netzwerkstrukturen sowie Analysen zur Dynamik der eingelagerten Sonden an Zwischenzuständen des Sol–Gel Übergangs durchgeführt werden konnten. Der Fortschritt der Photoreaktion wurde dabei simultan durch UV–vis Spektroskopie verfolgt.

Um die vorstehend genannten Untersuchungen in konsistenter Art und Weise durchführen zu können, wurde zunächst in Vorprojekten die Synthese von fluoreszenzmarkierten linearen Polyacrylamidketten über einen weiten Molmassenbereich untersucht und eine neue Methode zur systematischen Analyse von ortsaufgelösten FRAP Experimenten entwickelt.

Bezüglich der Netzwerkbildung weisen die an verschieden konzentrierten Systemen (20–80 $g\cdot L^{-1}$) erhaltenen Resultate darauf hin, dass die Bildung elastisch aktiver Netzketten proportional zur Photodimerisierung der DMMI Gruppen erfolgt. Die Vernetzungseffizienz variiert dabei stark mit der Polymerkonzentration, ist aber in allen Fällen überraschend hoch, während die mittlere Länge der Netzketten unabhängig von der Konzentration ist.

Obwohl eine grundlegende mechanistische Untersuchung der photochemischen DMMI Dimerisierung in wässrigen Medien deutliche Hinweise auf die bevorzugte Bildung eines asymmetrischen, nichtcyclischen Dimeren zeigt, scheint die Photovernetzung DMMI-funktionalisierter Ketten ohne nennenswerte Nebenreaktionen abzulaufen.

Untersuchungen zur Dynamik eingelagerter linearer und kugelförmiger Sonden wurden als Funktion der Matrixkonzentration (20–80 $g\cdot L^{-1}$) sowie der Tracermolmasse (200 000–1 300 000 $g\cdot mol^{-1}$) bzw. des Partikelradius (17 und 36 nm) im halbverdünnten Bereich durchgeführt. Die Ergebnisse weisen auf deutliche Unterschiede zwischen der Dynamik flexibler linearer Ketten und harter kugelförmiger Nanopartikel hin: Während sich eine fortschreitende chemische Vernetzung der umgebenden Matrix auf die Mobilität der ersteren kaum auswirkt, werden letztere vollständig immobilisiert sobald der Vernetzungsgrad eine gewisse Grenze überschreitet.

Contents

4 Structure and tracer dynamics in polyacrylamide hydrogels 135

List of important symbols and abbreviations

Symbols

c	Concentration
c^*	Threshold for coil overlap in a polymer solution
c_e^*	Threshold for entanglement formation in a semidilute polymer solution
c^{**}	Threshold for the crossover from a semidilute to a concentrated polymer solution
D	Generally: translational diffusion coefficient; In Chapter 4.1: dipolar coupling constant
d	Dimensionality of diffusion
G	Shear modulus
G'	Elastic part of the shear modulus
G''	Viscous part of the shear modulus
k	Boltzmann constant ($1.3806504(24) \times 10^{-23}$ J·K^{-1})
M	Generally: molecular weight; In Chapter 3.2: total amount of a diffusing substance
M_N	Number average molecular weight
M_η	Viscosity average molecular weight
M_W	Weight average molecular weight
N_A	Avogadro number (6.0221418×10^{23} mol^{-1})
R	Gas constant (8.314472 J·K^{-1}·mol^{-1})
r	Generally: (radial) coordinate
R_G	Radius of gyration
r_H	Hydrodynamic radius
T	(thermodynamic) temperature
t	Time
w	e$^{-1/2}$-radius of the Gaussian function

Greeks

η	Viscosity
$[\eta]$	Intrinsic viscosity
λ	Wavelength
ν	Unsubscripted: Flory exponent; Subscripted: density of crosslinking in a chemical network
ξ	(static) correlation length in a (semidilute) polymer solution
ξ_X	Average distance between junctions in a permanent network

Abbreviations

CLSM	Confocal Laser Scanning Microscope/Microscopy
DQ	Double-Quantum
FRAP	Fluorescence Recovery After Photobleaching
MQ	Multiple-Quantum
NA	Numerical Aperture
NMR	Nuclear Magnetic Resonance
UV–vis	Ultraviolet and visible range of the electromagnetic spectrum

Chemical compounds

AAm	Acrylamide 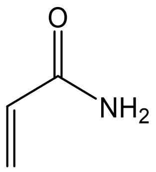
DMMI	Dimethylmaleimide (photodimerizable fragment) 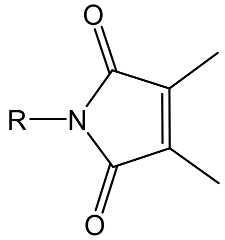
DMMIAAm	*N*-(*N*'-Acryloyl-2-aminoethyl)-dimethylmaleimide (Dimethylmaleimide-functionalized acrylamide) 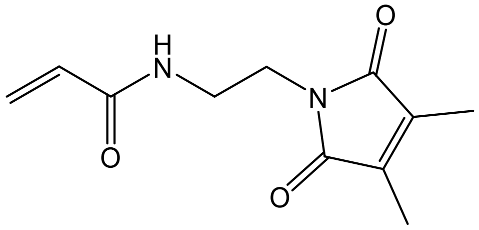
FITC	Fluorescein isothiocyanate 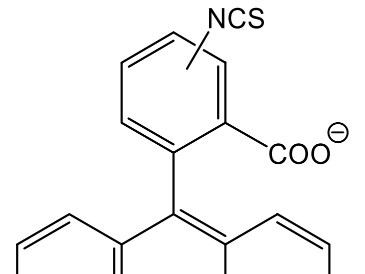
HE-DMMI	*N*-(2-Hydroxethyl)-dimethylmaleimide 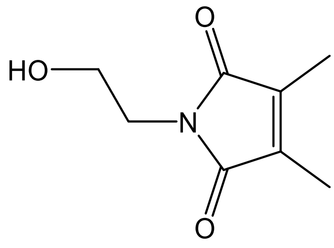

NAPMAAm	*N*-(3-Aminopropyl)-methacrylamide
	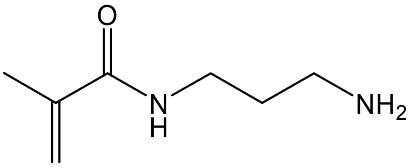
PAAm	Polyacrylamide
	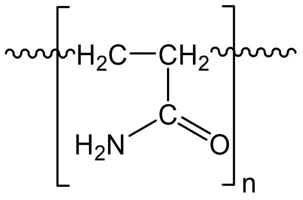
RITC	Rhodamine B isothiocyanate
	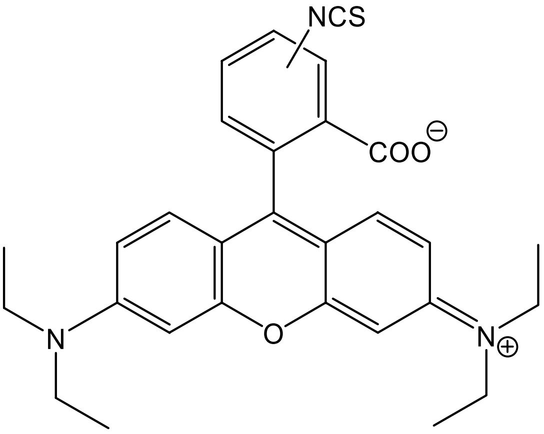
TXS	(Sodium) Thioxanthone-2,7-disulfonate
	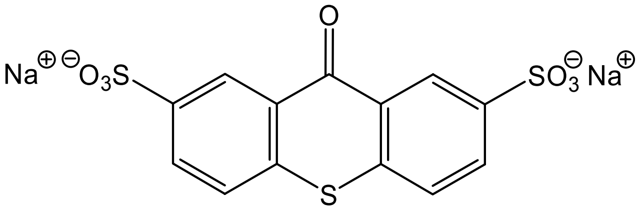

Unwissenheit die Basis von Philosophie
So viel geschieht ganz ohne das Wissen wie
—Torch

1 Introduction: scope, aims, and strategy of the present work

1.1 Hydrogels

Motivation and current state of research

Hydrogels formed by crosslinking of water-soluble polymers have gained increasing importance during the last decades, as they provide the basis for a variety of applications in fields like super-absorbent polymer technology, chromatography, or electrophoresis. Moreover, their potential in biophysics and nanotechnology, e.g., for controlled drug release or enzyme treatment, is still being explored. Much effort has thus been devoted to them, and the number of corresponding publications in any form—articles, books, patents, or contributions to conferences—is nearly no longer countable.

Currently, a main target in polymer sciences is to achieve a comprehensive knowledge about the relations between the *microstructural characteristics* and the *macroscopic properties* of polymer networks and gels, as these parameters ultimately trigger the behavior and, hence, the *functionality* of such materials. In many cases, one desires to obtain homogeneous and well-defined network architectures.

Objective I: Hydrogel formation by photocrosslinking of linear polyacrylamide chains

One of the most important nonionic, water-soluble synthetic polymers for the preparation of crosslinked structures in aqueous media is *polyacrylamide* (PAAm) [1–4], as it provides a multitude of outstanding properties and practical applications, e.g., in wastewater-treatment, flocculation, and enhanced oil recovery. Moreover, acrylamide polymers are often suited to serve as model systems for natural biopolymers.

The usual way to build up PAAm hydrogels is the free-radical crosslinking copolymerization of acrylamide with *N,N'*-methylenediacrylamide or another suitable crosslinker in aqueous solution [1, 5]. However, several previous investigations show that the network structures thus obtained often turn out to be relatively inhomogeneous [6–8]. Hence, it would be worthwhile to employ alternative approaches for PAAm network formation.

A favorable strategy for this could be to start from semidilute solutions of well-defined functionalized linear PAAm molecules which are subsequently crosslinked by selectively connecting their functional groups. It is an advantage of this method that the crosslinking thus achieved occurs in a random manner and, moreover, that the properties of the physically entangled system and the chemically crosslinked network structure can be consistently compared. Expediently, realizing the crosslinking of existent linear precursor chains through a *photochemical* reaction offers another convenient feature: the reaction is readily controlled by adjusting the irradiation conditions, and its progress can be stopped, if desired, by interrupting the light exposure. The system can thus be studied and characterized at any intermediate stage on its path from sol to gel before resuming the irradiation.

For the present work, use was made of the sensitized photochemical [2+2]-dimerization of dimethylmaleimide (DMMI) sidegroups. Although such types of photochemical crosslinking reactions have been utilized several times to prepare swollen hydrogels [9–13], there are no reports on a detailed and fundamental examination of the reaction mechanism when pendant DMMI moieties are employed to crosslink PAAm. Consequently, also the development of the network structure in such systems is largely unexplored. One major aim of the present project was thus to provide such fundamental knowledge. For this purpose, the DMMI dimerization reaction in aqueous solution was studied on low molecular weight model compounds, and the kinetics of the gelation process when PAAm hydrogels are formed via DMMI sidegroup dimerization was investigated, focusing in particular on the possibilities to monitor and control the progress of the reaction. Finally, rheological measurements and multiple-quantum NMR experiments were performed to provide information on the network structures on a macroscopic and microscopic scale, respectively.

1.2 Probe dynamics in polymer networks

Motivation and current state of research

Besides the last-mentioned types of analyses, a comprehensive characterization of crosslinked polymer systems also requires the investigation of *dynamic processes* within them. This has evolved as a central problem in polymer sciences, as benefits from such knowledge can be expected to be numerous: On the one hand, a consistent picture of the dynamic properties of semidilute macromolecular systems is of interest for the gain of insight into the fundamental mechanisms of polymer motion and to the derivation of structure–property relations. On the other hand, the need for a theoretical description of the diffusive behavior of active components that are enclosed in entangled or crosslinked polymer matrixes also plays an important role for concrete applications, e.g., in the fields of biophysics, separation techniques, and pharmaceutical research.

Large amount of experimental and theoretical work has thus been devoted to the problem, comprehending various studies on several systems like polymer solutions, melts, and gels, thereby employing numerous experimental techniques, e.g., scattering methods or spectroscopies. In order to avoid the risk of overestimating particular ones among them, no special work shall be cited here. Instead, the reader is referred to a set of comprehensive reviews [14–20] which finally show that by and large, previous investigations have led to some fundamentally different theoretical approaches to describe the dynamics in networks. The most famous ones among them are the reptation model derived by de Gennes [21–23] and Doi & Edwards [24–26] as well as the hydrodynamic scaling concept suggested by Phillies [27–35].

Objective II: Studies on tracer dynamics in semidilute solutions and hydrogels

Remarkably, one has to state that even though literally hundreds of references dealing with the topic of tracer-diffusion in macromolecular matrixes have been published, no comprehensive understanding could be achieved, and one has not been able to clearly confirm or reject one of the different theoretical approaches yet. Hence, the second central aim of the present work was to contribute another systematic study considering this problem. The outline for it reads as follows:

It is a matter of common knowledge that the preconditions for the application of the reptation and scaling theory are essentially realized in chemical networks. Nevertheless, only a rather limited number of reports deal with such systems. Moreover, there seems to be a complete lack of studies on the diffusion of probes in a surrounding matrix that is crosslinked in *successive* manner, which means: to study the *same* sample at *different degrees of crosslinking*, respectively. This, however, should allow to draw a consistent picture of the influence of chemical crosslinking on probe mobility in the interesting sol–gel transition regime.

For the present work, such a situation was thus realized by investigating the diffusive motion of tracers that are enclosed in matrixes which can be crosslinked via a photochemical reaction. As described above, a convenient way to achieve this was to employ precursor chains carrying DMMI moieties that are able to dimerize upon UV irradiation. The enclosure of probes could then be expected to be possible without interconnection of tracer and matrix, provided the probe material is unable to undergo related photoaddition reactions. This in turn allowed for the use of the same basis material for tracer and matrix simply by omitting the photoactive moieties in the first case.

Finally, *flexible linear polyacrylamide chains* and *rigid spherical polystyrene particles* having similar hydrodynamic radii in the dilute state were compared as two fundamentally different types of probes. Besides the gradual increase of the degree of matrix-crosslinking, parameters varied were the *concentration of the matrix* as well as the *molecular weights* and *particle sizes* of the linear and spherical tracers. A schematic representation of this central issue of the present work is illustrated in Figure 1.1.

1.3 Schedule for the present work

FRAP as the method of choice

To perform the above-discussed investigations on probe mobility in semidilute polymer matrixes, *fluorescence recovery after photobleaching* (FRAP) on a confocal laser scanning microscope (CLSM) was used to measure translational diffusion coefficients on a 10 μm scale. The main reasons for the choice of this particular technique were the following:

(i) Fluorescence methods are generally able to detect certain labeled fractions within an unlabeled background and thus to observe a kind of material in a surrounding which is similar or almost identical to the species of interest. Hence, it was possible to employ fluorescently labeled PAAm tracers being enclosed in unlabeled (but, instead, DMMI-functionalized) PAAm matrixes and thus to investigate *self-diffusion* processes in polymer networks without perceptible perturbations due to possible thermodynamic incompatibility between tracer and matrix.

(ii) From the variety of fluorescence-based methods to perform mobility measurements, FRAP was the most suitable approach for the present work, as the values of the translational diffusion coefficients of linear and spherical tracers in polymer networks typically lie below 10 $\mu m^2 \cdot s^{-1}$, which is a range being well-covered by this technique.

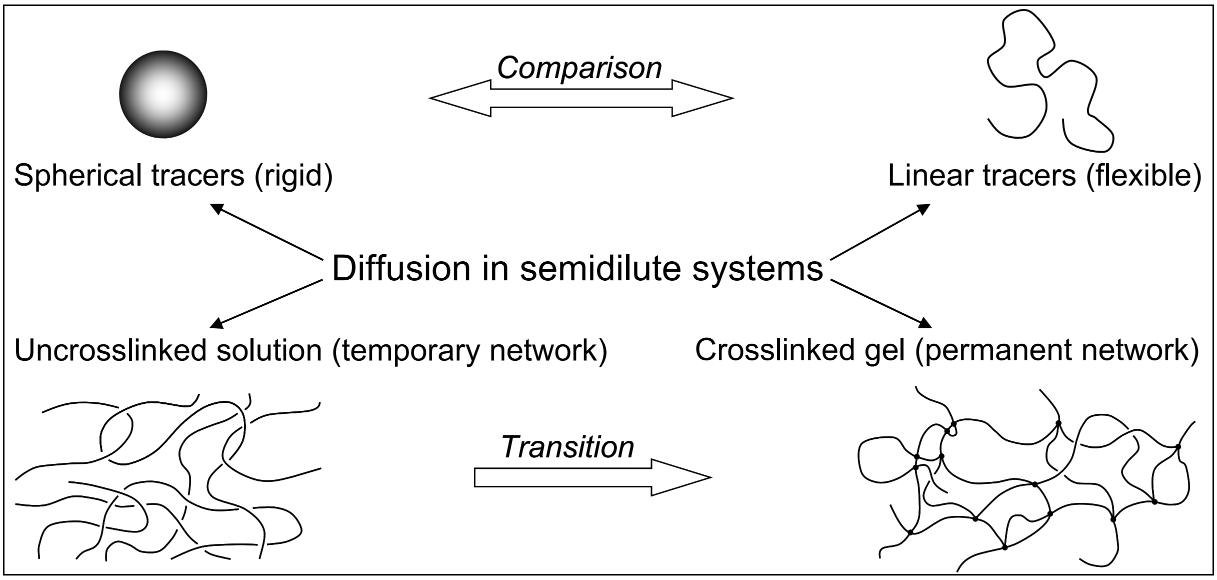

Figure 1.1 Schematic illustration of the basic intention of the present work.

Work plan

The use of FRAP naturally requires the use of fluorescently labeled tracer materials, which are commercially available in the case of spheres but need to be prepared synthetically in the case of linear chains. It was thus necessary to begin the project with the *synthesis and characterization of fluorescently labeled PAAm*.

Moreover, FRAP measurements require an *analysis procedure* which allows for a consistent and absolute quantification of the probes' diffusive mobilities. In this respect, the present work particularly required to account for polydispersity effects, i.e., to analyze multi-component diffusion processes. As unfortunately most of the classical procedures for the evaluation of FRAP data are *relative* methods and do only allow for the analysis of *single*-component diffusion, a novel technique for the systematic evaluation of spatially resolved FRAP data obtained by means of CLSM had to be derived first.

On the basis of these preliminary projects, it was then finally possible to focus the main objectives of the present work as discussed above, that is, to investigate the *gelation of photoactive PAAm* precursor chains as well as to study the *dynamics of enclosed linear and spherical tracers*.

Figure 1.2 displays a complete schedule for these four different subprojects which eventually all fall into place to the common target sketched in Figure 1.1.

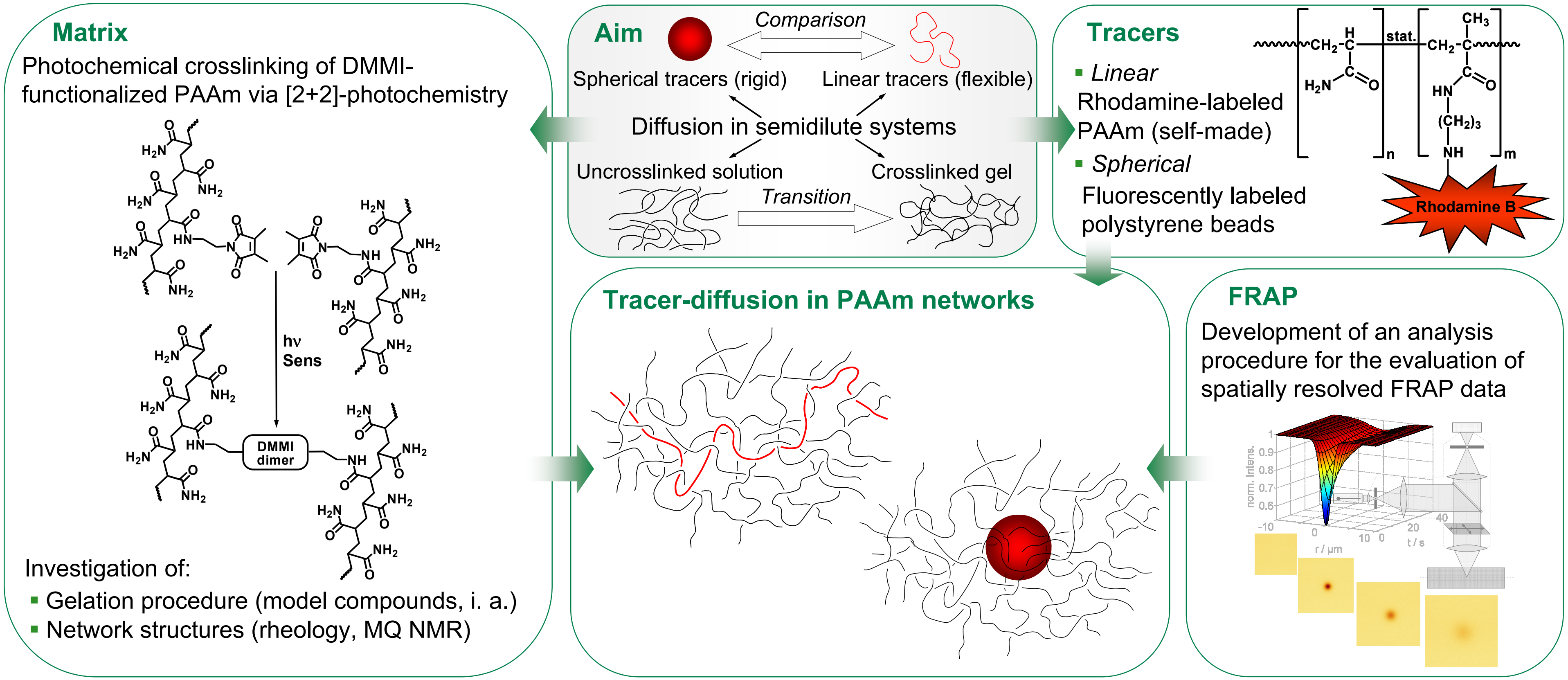

Figure 1.2 Comprehensive schedule for the present work. – In order to perform comparative studies on the diffusion of linear and spherical tracers in semidilute polymer systems with respect to realize a stepwise transition from an entangled solution to a permanently crosslinked gel, it was necessary to establish a synthesis procedure for the preparation of fluorescently labeled PAAm, to develop a convenient procedure for the analysis of spatially resolved FRAP data, as well as to study the photochemical gelation of DMMI-functionalized PAAm precursors.

2 Theoretical background

2.1 Polymer solutions and networks

2.1.1 Polymer solutions

2.1.1.1 Thermodynamic fundamentals and concentration regimes

Polymers are macromolecular chain molecules composed of a repeating sequence of several hundred or thousand monomer units. In solution, they typically shape in a coiled conformation which might be expanded or contracted, depending on the quality of the solvent: Dissolving a polymer in a good solvent leads to a situation where monomer–monomer interactions are readily replaced by monomer–solvent interactions. In consequence, the coils swell (large excluded volume). By contrast, poor solvents induce coil-shrinkage eventually leading to phase separation as solvent is expelled from the coils in order to enable monomer–monomer interactions. Certain pairs of solvents and polymers obey a special behavior at the so-called θ-temperature, where expanding and contracting tendencies are balanced (net-zero excluded volume). Coils at θ-conditions therefore exhibit their ideal unperturbed random conformation, and θ-solvents lie in the transition region between good and poor solvents. The θ-state is thus comparable to the behavior of real gases at the Boyle temperature with respect to the ideal equation of state.

Several characteristic values can be used to quantify the coil dimensions, e.g., the end-to-end distance, the radius of gyration, or the hydrodynamic radius in solution as illustrated in Figure 2.1 (see below). Moreover, numerous experimental and theoretical parameters serve as a measure of the effective interaction potentials between solvents and polymer segments. Popular examples are the Flory–Huggins interaction parameters [36–38] and the Hildebrand solubility parameters [39]. Besides these quantities, which originate from thermodynamic treatments of polymer solutions, the well-known semi-empiric Mark–Houwink–Sakurada equation describes the relation between the intrinsic viscosity $[\eta]$ of a polymer solution and the molecular weight M of the dissolved chains as

$$[\eta] = KM^{a} \qquad (2.1)$$

The parameters K and a can be estimated by suitable calibration and are tabulated for many pairs of polymers and solvents [40]. a is a measure of the quality of the solvent and has values predicted to be 0.5 for unperturbed coils in θ-solvents and 0.764 for perturbed coils in good solvents, assuming the coils to drag the solvent within their pervaded volume with them in both cases (Zimm behavior, cf. Chapter 2.2.5.1). By contrast, $a = 1$ applies to the other extreme where the solvent is assumed to be freely draining through the coils (Rouse behavior, cf. Chapter 2.2.5.1).

Solutions of linear polyacrylamides as treated in this work obey θ-behavior in methanol/water-mixtures with volume fractions around 2/3 near room temperature [41]. On the other hand, their pure aqueous solutions are often considered as being in good solvent, since the corresponding value of a has been reported to be about 0.75–0.8 in aqueous media at 25 °C [42], while the Flory–Huggins interaction parameters lie between 0.44 and 0.495 [43]. Thus, PAAm coils are notably expanded in water and begin to *overlap* at relatively low concentrations.

The *overlap concentration* c^* is reached when the volume fraction of polymer chains exceeds the volume fraction of monomers in each isolated coil. Above c^*, chains interpenetrate and eventually form temporary entanglements. The sample then more and more exhibits characteristics of an entangled *temporary network.*

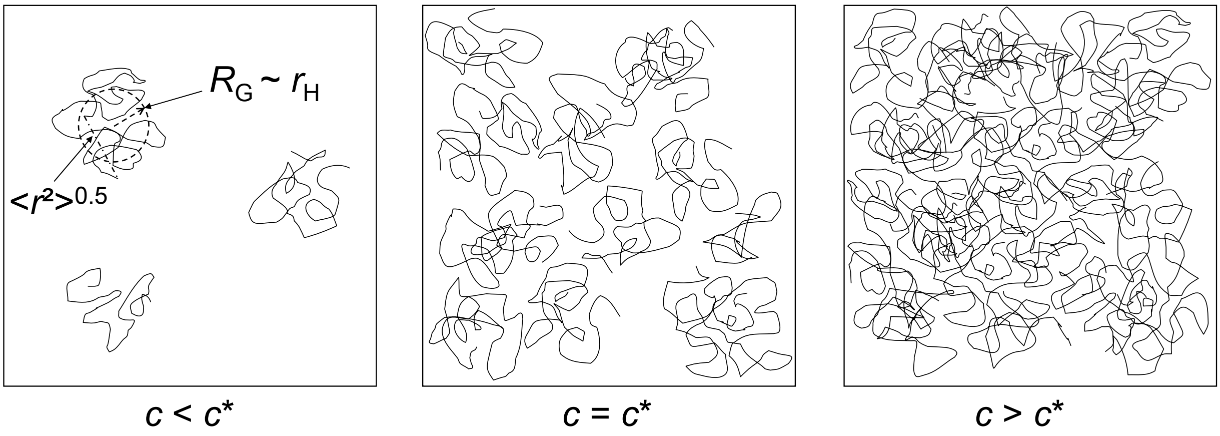

Figure 2.1 Transition from a dilute polymer solution ($c < c^*$) with isolated coils to a semidilute system with notable coil overlap ($c > c^*$). – Crossover between the two domains takes place at the overlap concentration c^*, where the coils have first peripheral contact. For characterization of the coil size, one employs parameters like the end-to-end distance $< r^2 >^{0.5}$, the radius of gyration R_G, or the hydrodynamic radius r_H.

Figure 2.1 depicts the three regimes of a dilute polymer solution with isolated coils, the critical overlap threshold c^*, and the situation well beyond this point where coils are entangled to a great extent. As in the last type of system the polymer concentrations are on the one hand still rather low in comparison with the large content of solvent, while on the other hand, micro- and macroscopic properties like the self-diffusion coefficient of the polymer-chains or the viscosity of the solution are notably affected by the entanglements, this situation is named the entangled *semidilute* region.

Several definitions of the overlap threshold c^* have been mentioned in literature [44–46], e.g.,

$$c^* = \frac{3M_\mathrm{W}}{4\pi R_\mathrm{G}^{\,3} N_\mathrm{A}} \tag{2.2}$$

and

$$c^* = \frac{1}{[\eta]} \tag{2.3}$$

with M_W the weight average molecular weight, R_G the radius of gyration, N_A the Avogadro number, and $[\eta]$ the intrinsic viscosity.

2.1.1.2 The semidilute regime

A characteristic parameter for the average mesh size in an entangled semidilute solution is the *correlation length* ξ as sketched in Figure 2.2a. It quantifies the particular scale below which each monomer on a chain is essentially surrounded by solvent and monomers belonging to the same chain. At the onset of overlap ($c \approx c^*$), coils have contact but are not yet strongly interpenetrating, so that ξ is comparable to the size of one coil as quantified by the radius of gyration. Above c^*, the correlation length decreases with increasing polymer concentration due to the increasing amount of coil overlap as expressed by eq (2.4) [23]:

$$\xi \propto \phi^{\frac{-\nu}{3\nu-1}} \qquad (2.4)$$

with ϕ the volume fraction of the polymer (note that $\phi \propto c$) and ν the Flory exponent [38]. Taking into account that ξ approximates R_G at c^*, one obtains

$$\xi \approx R_G \left(\frac{c^*}{c} \right)^{\gamma} \qquad (2.5)$$

with $\gamma = -0.75$ in good solvents ($\nu = 0.6$) and $\gamma = -1$ in θ-solvents ($\nu = 0.5$).

In a semidilute good solvent solution, the coils' excluded volume interactions are screened by overlapping chains on length scales larger than the correlation length. The system on these scales thus behaves like a melt of chains composed of a sequence of *correlation blobs* as illustrated in Figure 2.2b [23, 47]. These can be considered as Kuhn segments and the polymer conformation may thus be described as a random walk of them. Chain segments on mesoscopic scales inside the blobs underlie excluded volume interactions (i.e., swelling) and behave as in the dilute state. One can derive the following relation for the concentration dependence of the coil size R:

$$R \propto \phi^{-0.12} \qquad (2.6)$$

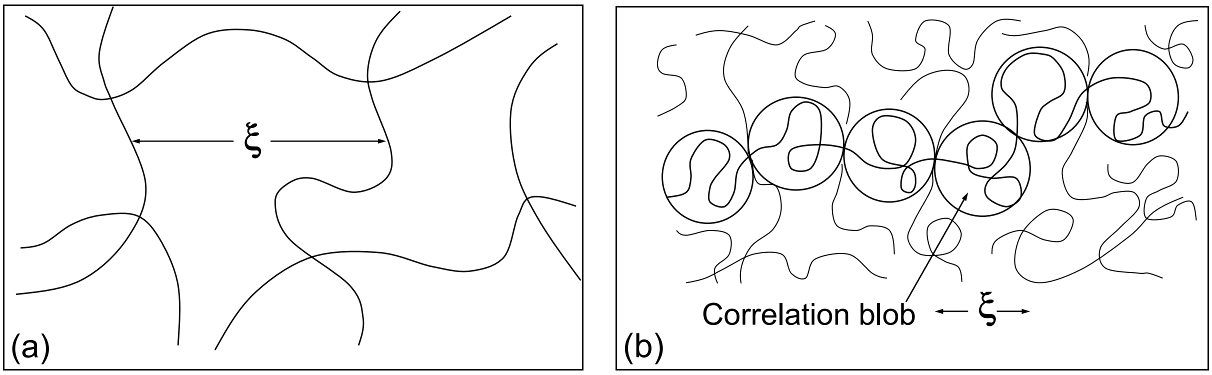

Figure 2.2 (a) The correlation length ξ as a measure of the average mesh size in a semidilute polymer solution (temporary network). – In the good solvent case, chain sections between entanglements behave as quasi-unperturbed subcoils with excluded volume interactions as in the dilute state. They can thus be modeled as so-called correlation blobs of size ξ (b). Adapted from [23].

On the other hand, excluded volume interactions become weaker than the thermal energy *kT* on scales below a second characteristic threshold which is termed the *thermal blob size* ξ_T. Chain segments shorter than ξ_T thus obey ideal behavior. In combination, this leads to the situation that coils in the semidilute regime in a good solvent show strong excluded volume interactions on intermediate (mesoscopic) scales between ξ_T and ξ, while they behave ideal on smaller and larger scales. Moreover, they shrink from their size in dilute solution with increasing concentration according to eq (2.6). The shrinkage finally ends when the *concentrated* (meltlike) domain is reached at the concentration c^{**} that often corresponds to polymer volume fractions close to unity. At this threshold, ξ has decreased down to ξ_T, and chains behave ideal on all length scales. The size of the coils then turns out to be independent of concentration, while the concentration dependence of the correlation length reads $\xi \propto \phi^{-1}$.

In θ-solvents, the latter scaling law also applies to the semidilute region (cf. eq (2.4) with $\nu = 0.5$). More generally, the concentrated regime for good solvents can be considered as a simple extension of the semidilute θ-situation to higher solvent quality, e.g., to higher temperature. In contrast to the above-discussed good solvent situation, θ-solutions show ideal chain statistics on all length scales at all concentrations, and no change of polymer conformation occurs at the correlation length ξ. Notice that ξ in the θ-state is still defined as the particular length below which most of the segments surrounding a particular monomer belong to the same chain. However, as opposed to the good solvent situation, ξ does not correspond to a particular threshold marking a change of chain conformation in the θ-state. θ-solutions thus only require the discrimination between the dilute and the semidilute region with non-overlapping and overlapping chains, respectively, having ideal coil size in both cases.

By contrast, good solvents comprise three regions: the non-overlapping *dilute* regime with swollen coils ($c < c^*$), the *semidilute* domain ($c^* < c < c^{**}$) with chain conformations similar to the dilute situation at intermediate length scales (between ξ_T and ξ) and conformations analogous to melts on large length scales (above ξ) where the coil-size weakly decreases with increasing concentration, and finally the *concentrated* (meltlike) region ($c^{**} < c < 1$) with ideal chain statistics on all length scales.

Note that both c^* and c^{**} are not precisely defined but more properly described as a region of crossover between the dilute and the semidilute as well as the semidilute and the concentrated regime, respectively. Regarding c^*, many authors actually prefer the use of two thresholds which describe the critical concentration of the first coil overlaps c^* on the one hand and the concentration of notable entanglement c_e^* on the other hand [46, 47].[1] The semidilute regime can thus be further subdivided into the *unentangled* ($c^* < c < c_e^*$) and the *entangled* ($c_e^* < c < c^{**}$) semidilute regime. In good solvents, c^* and c_e^* often differ by a factor of about 2–5 [18], whereas $c^* \approx c_e^*$ ($= c^{**}$) in θ-solvents.

2.1.2 Polymer networks

2.1.2.1 Fundamentals

If the system under consideration contains polymer chains that are crosslinked by covalent bonds or (strong) attractive interactions, one speaks about a chemical or physical *network*. In the presence of solvent, the resulting colloidal two-phased system is called *gel*. Figure 2.3 displays the difference between an entangled solution (temporary network, Figure 2.3a) as discussed in the preceding paragraph and a (chemically) crosslinked permanent network (Figure 2.3b). The architecture of the latter system can be described as a 3-dimensional porous structure which is a single macromolecule without end groups in the ideal case. Consequently, the number of crosslinks multiplied by their functionality should equal the twofold number of network chains. However, in the real case, junctions are built randomly, and network defects like loops and dangling chains as also illustrated in Figure 2.3b occur. The theoretical density of crosslinking

$$\nu_{\mathrm{th}} = \frac{n_{\mathrm{cl}} f}{2V} \tag{2.7}$$

with n_{cl} the molar amount of crosslinker and f as its functionality has therefore to be corrected by the fraction of network defects ζ to $\nu_{\mathrm{eff}} = \zeta\nu_{\mathrm{th}}$.

---

[1] More precisely, c^* corresponds to a situation where the correlation length ξ is in the order of the coil size, whereas c_e^* represents the scenario where the so-called tube diameter as introduced in Chapter 2.2.5.2 equals the coil size.

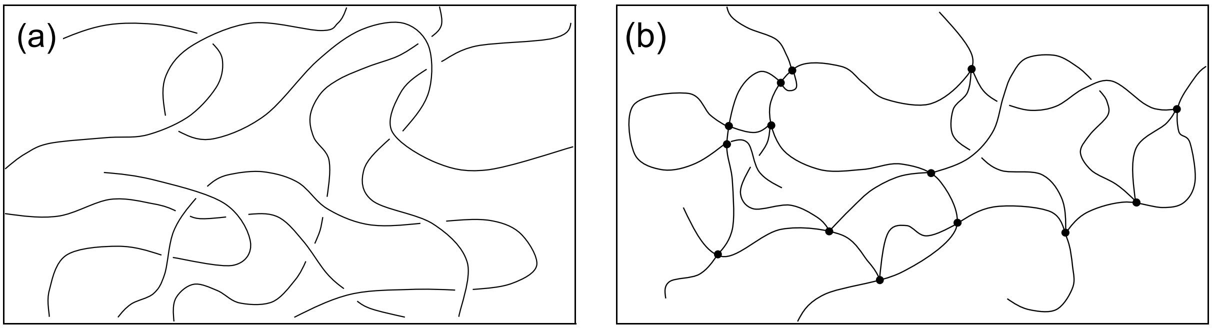

Figure 2.3 Schemes of network structures. – (a) Physically entangled temporary network. (b) Permanently crosslinked network. Also shown in (b) are typical network defects like loops or dangling chains.

In the unperturbed state, network chains are not elongated and thus posses a certain conformational entropy. This manifests itself in a special kind of elasticity of polymer networks: as the number of possible conformational arrangements of the network chains decreases upon deformation, a restoring force originates from the so-induced decrease of entropy. In similar regard, polymer networks are not able to dissolve but may solely swell upon addition of solvent due to the chemical connection of the network chains. The equilibrium of swelling is reached when the decrease of entropy of the network chains induced by the uptake of solvent is just about to be compensated by the decrease of the Gibbs free energy of mixing.

2.1.2.2 Gelation

Interlinkage of linear polymer chains leads to progressively larger branched macromolecules that initially are still soluble in a (good) solvent. Up to a certain extent of crosslinking one speaks about a sol, until a large macromolecule spanning the entire system appears at the *gel point*. Beyond this point, a certain fraction of the sample is no longer soluble but may solely swell upon uptake of solvent, and one speaks about a gel. The transition from a system containing solely finite (branched) polymers (exclusively sol) to a system containing also an "infinite" molecule (gel) is called the *sol–gel transition* or *gelation*. The gel point is the well-defined threshold for the first appearance of a gel fraction which subsequently increases with proceeding reaction.

Different types of gelation are compiled in Figure 2.4. In principle, chain linkage can either occur due to physical interactions or by the formation of covalent (chemical) bonds connecting the chains. While the first type is called *physical* gelation, one speaks about *chemical* gelation in the second case. Note that besides such processes where long (functionalized) precursor chains are interconnected, chemical gelation may also occur as a consequence of crosslinking (co)polymerizations involving suitable (co)monomers with functionalities $f > 2$. For the present work, however, the first approach was followed by linking polyacrylamide chains functionalized with dimethylmaleimide moieties which readily dimerize upon UV irradiation.

Generally, it is convenient to distinguish between strong and weak gelation. While chemical gelation is strong in almost all cases, physical gels may appear strong or weak depending on the case at hand and the experimental conditions, e.g., the observed time scale, temperature, and the forces applied to the network. Strong physical bonds that are effectively permanent can be formed by glassy or microcrystalline nodules as well as double or triple helices. By contrast, weak physical gelation is induced by the formation of hydrogen bonds, block copolymer micelles above their glass transition temperature, and ionic associations, which all have finite lifetimes and are able to break and reform continuously (bonding–nonbonding equilibrium). Gelation in these cases proceeds less sharply than in the first case, but is conceptually more comparable to a glass transition, that is, the progressive freezing of a certain number of degrees of freedom.

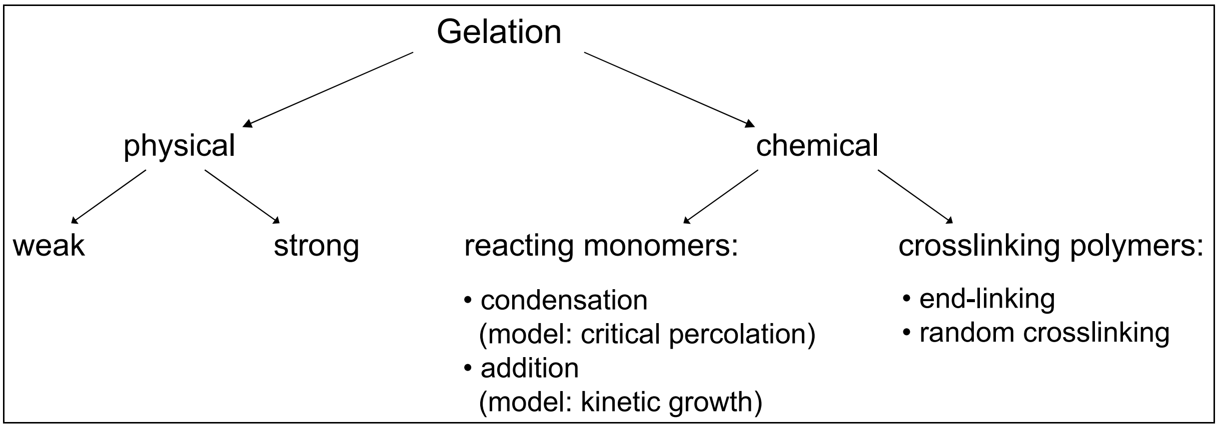

Figure 2.4 Classification of gelation transitions. – Adapted from [47].

To describe the sol–gel transition, several models applying to the different cases of network formation have been developed. They can be divided into equilibrium gelation models (such as the so-called mean-field gelation and critical percolation theory) and growth models (like the concepts of cluster–cluster aggregation and kinetic gelation). In the first case, gelation kinetics only affects the rate of network formation while in the second case, the rate of crosslinking also strongly influences the network structures formed. All theories mentioned above are well described in literature (e.g., [47]), and it is not the intention of this chapter to treat them in detail. However, it is important to state that all the gelation processes mentioned here have at least a small region close to the gel point which is called the critical region. Here, the reacting structures are just at overlap and can be described by the critical percolation model.

In any case, gelling systems at conversions p below the critical percolation threshold p_c (i.e., the gel point) have no gel fraction while their sol fraction equals unity. At $p = p_\mathrm{c}$, a gel fraction firstly occurs which subsequently grows with proceeding reaction. A rough estimate for the gel point is

$$p_\mathrm{c} \approx \frac{1}{f-1} \tag{2.8}$$

in case of interlinkage of precursor molecules (monomers or polymers) with functionality f. At conversions above p_c, the gel fraction increases steadily and can be quantified as

$$P_\mathrm{gel} \propto \left(\frac{p - p_\mathrm{c}}{p_\mathrm{c}} \right)^{\beta} \tag{2.9}$$

where β is one of the so-called critical exponents that characterize gelation as a second-order phase transition. The percolation model predicts $\beta = 0.4$, whereas the mean-field gelation theory gives $\beta = 1$ in cases where the crosslinking molecules have significant overlap [23, 47]. In both cases, however, eq (2.9) shows that when the extent of gelation reaches approximately twice the gel point, nearly all precursors are attached to the network and essentially no sol fraction remains. By contrast, the elastic modulus E of the forming network increases more slowly:

$$E \propto (p - p_\mathrm{c})^\kappa \tag{2.10}$$

with κ = 1.7–1.9 as derived from the percolation theory and confirmed by experiments [23, 48, 49]. This phenomenon can be addressed to network defects such as dangling chains as also depicted in Figure 2.3b, which are a part of the gel fraction P_gel but do not contribute to elastic storage.

Regarding phenomenology, several ways for the detection of the gel point and the occurrence of macroscopic gelation in a crosslinking polymer system are imaginable. Without treating all of them in detail, the following section intends to give an overview of the most popular phenomena:

The most apparent criterion for gelation in a sample is that its viscosity shows a singularity towards infinity at the gel point. The material subsequently gains elastic properties, and the storage modulus G' exceeds the loss modulus G'' in dynamic shear experiments (cf. next section for a definition of these quantities). Hence, many authors refer to $G' = G''$ as the gel point. However, as shown by Chambon and Winter [50], this is not quite correct because both G' and G'' depend on shear frequency. Thus, measurements at different frequencies would indicate different gel points. A more precise indication of the gel point in terms of rheology has therefore been proposed with the formulation

$$G' \propto G'' \propto \omega^n \tag{2.11}$$

which states that G' and G'' are not necessarily equal but show an equal dependence on the frequency ω at the gel point. An alternative formulation of this finding would be that the loss tangent (tan δ, cf. next subchapter) is independent of ω at the gel point.

During gelation, the complex shear modulus $G^*(\omega) = G'(\omega) + \mathrm{i}G''(\omega)$ shows a frequency dependence as illustrated in Figure 2.5 and obeys the power law $G \propto \omega^n$ at the gel point. Note that in this respect, a scenario with $G' = G''$ only applies to $n = 0.5$! Beyond the gel point, extrapolation to $\omega \to 0$ yields the *equilibrium modulus* G_eq which increases steeply with proceeding crosslinking and is thus a measure of the density of the network (cf. Chapter 2.1.2.4).

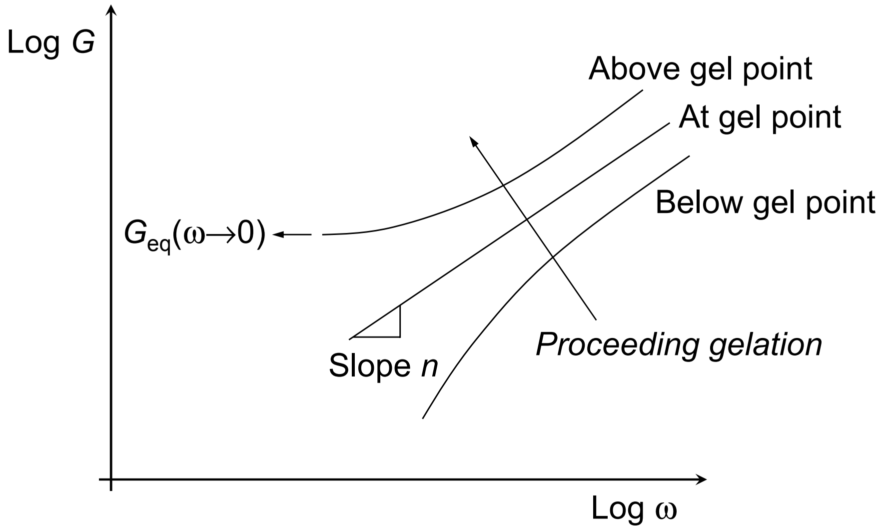

Figure 2.5 Scheme of the $G(\omega)$-course with proceeding gelation.

In addition to rheology, also static light scattering can serve as a tool for the detection of the gel point: when crosslinking has exceeded the critical percolation threshold, one observes nonergodic behavior on time scales comparable to the duration of a measurement. Thus, strong intensity fluctuations occur when different volumes are investigated within gels.

In their final crosslinked states, network structures obtained by different types of gelation are often studied with regard to their structure and properties. However, when experiments are about to be performed on gels, one has to take care about the experimental conditions. In contrast to most other materials, characterization of network structures and gel properties requires the precise discrimination between

(i) the experimental conditions during gel formation (e.g., concentration, solvent quality, and the extent of gelation at interrupt of the reaction)

and

(ii) the experimental conditions at the moment of study

Hence, gels have to be described in terms of two ensembles, the "preparative ensemble (i)" and the "analytic ensemble (ii)". For the present work, however, such type of separate treatment was not necessary as polyacrylamide networks were studied during and immediately after their preparation under equal experimental conditions.

2.1.2.3 Viscoelastic behavior of polymer gels

Many materials of interest in classical physics can be described by the theories of elastics and hydrodynamics. In this regard, mechanical properties of solids are in accordance with Hooke's law, where stress is always directly proportional to strain on small deformations (elastic behavior). By contrast, viscous liquids show proportionality between stress and the rate of strain according to Newton's law. In polymer physics, however, one often observes a type of intermediate behavior, and macromolecular materials exhibit viscous and elastic properties similarly. One therefore speaks about *viscoelastic* behavior — a phenomenon that often turns out to be truly spectacular.

In the scope of the present work, solely shear shall be considered as one example of mechanic deformation. The shear stress σ is defined as the ratio of the applied force and the cross-sectional area *A*, which is also the area of any plane perpendicular to the direction wherein the material is being sheared:

$$\sigma \equiv \frac{f}{A} \tag{2.12}$$

The shear strain γ is defined as the horizontal displacement Δx relative to the thickness of the sample *h* (cf. Figure 2.6):

$$\gamma \equiv \frac{\Delta x}{h} \tag{2.13}$$

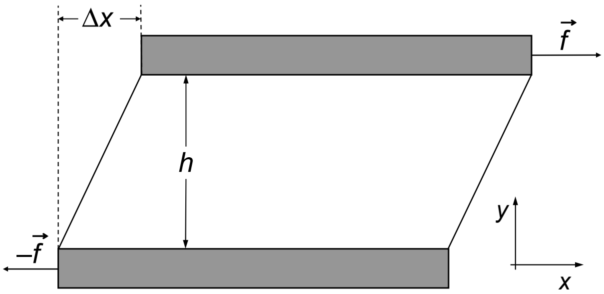

Figure 2.6 2-Dimensional representation of shear deformation by application of equal and opposite forces to two parallel plates. – Adapted from [47].

If the material under consideration is a perfectly elastic solid, the shear stress σ and shear strain γ are proportional, with the constant of proportionality defining the *shear modulus*

$$G \equiv \frac{\sigma}{\gamma} \tag{2.14}$$

On the other hand, if the material sheared is a simple liquid, the shear rate $\dot{\gamma} \equiv \frac{\mathrm{d}\gamma}{\mathrm{d}t}$ is linearly connected to the shear stress σ, with the constant of proportionality defining the *shear viscosity* $\eta \equiv \frac{\sigma}{\dot{\gamma}}$

A simple linear viscoelastic experiment easy to implement is *oscillatory* shear. This technique has become popular in polymer physics as it provides access to several orders of magnitude on the temporal scale simply by studying the viscoelastic properties of the material at varying frequencies. Applying a sinusoidal strain with angular frequency ω like

$$\gamma(t) = \gamma_0 \sin(\omega t) \tag{2.15}$$

yields a stress of

$$\sigma(t) = G\gamma(t) = G\gamma_0 \sin(\omega t) \tag{2.16}$$

in the case of elastic solids and

$$\sigma(t) = \eta \frac{\mathrm{d}\gamma(t)}{\mathrm{d}t} = \eta\gamma_0\omega \sin\left(\omega t + \frac{\pi}{2}\right) \tag{2.17}$$

in the case of viscous liquids, where the stress still oscillates with the same angular frequency ω but is out-of-phase with the strain by $\pi/2$. More generally, the linear response of a viscoelastic material always shows the stress leading the strain (2.15) by a *phase angle* δ:

$$\sigma(t) = \sigma_0 \sin(\omega t + \delta) \tag{2.18}$$

Solids which obey Hooke's law show $\delta = 0$ at all frequencies, whereas viscous liquids obeying Newton's law show $\delta = \pi/2$. Since stress is considered as a sinusoidal function with the same frequency as strain, it can be separated into two orthogonal functions which oscillate with the same frequency, one in-phase with the strain and the other out-of-phase with the strain by $\pi/2$:

$$\sigma(t) = \gamma_0 [G'(\omega)\sin(\omega t) + G''(\omega)\cos(\omega t)] \tag{2.19}$$

This equation defines $G'(\omega)$ as the *storage modulus* and $G''(\omega)$ as the *loss modulus*:

$$G' = \frac{\sigma_0}{\gamma_0} \cos\delta \tag{2.20}$$

$$G'' = \frac{\sigma_0}{\gamma_0} \sin\delta \tag{2.21}$$

The ratio of loss and storage modulus is the tangent of the phase angle, which is called the *loss tangent*:

$$\tan\delta = \frac{G''}{G'} \tag{2.22}$$

Storage and loss modulus are the real and the imaginary parts of the complex modulus

$$G^*(\omega) = G'(\omega) + \mathrm{i}G''(\omega) \tag{2.23}$$

Swollen polymer networks well above the gel point behave as viscoelastic solids with $G' >> G''$. In the low frequency limit, G' turns out to be independent of frequency and is thus termed the *equilibrium modulus* $G_{\mathrm{eq}} = \lim\limits_{\omega \to 0} G'(\omega)$ as shown in Figure 2.5. Measurements on polymer gels can thus be adequately treated utilizing the approximation $G \approx G'$ if the following requirements are met:

Besides the above-mentioned condition of $G' \gg G''$, the measurement has to be performed in the *linear viscoelastic domain* where both G' and G'' are independent of the deformation amplitude γ. Furthermore, the crosslinking density inside the gel has to be spatially homogeneous, and the temperature should be well above the glass transition temperature of the material under consideration. Note that all these conditions are met for the measurements of the elastic modulus in Chapter 4.1, so that the approximation $G \approx G'$ holds for these experiments.

Classification of rubbery systems and features of the viscoelastic behavior

Generally speaking, all types of (linear) polymers are able to exhibit a great variety of mechanic behavior, depending on chain flexibility, temperature, and the time scale under consideration. At low temperatures, polymers are typically present in glassy or crystalline states and therefore show elastic behavior. Elevated temperatures allow for rotations of single bonds, and polymer chains can shape in a large number of conformations with similar energy. In such states, polymer samples typically show the so-called *rubber elastic* behavior (cf. next chapter) provided that the molecular weight is sufficiently high to form entanglements or that the material is permanently crosslinked. One is thus able to observe a practically constant value for the so-called *plateau modulus*. At still higher temperatures or longer time scales, uncrosslinked chains on the other hand become able to undergo irreversible displacements finally leading to flow, so that viscoelastic and viscous properties are observed.

As indicated above, the variables “time” and “temperature” can be superimposed in all the regimes discussed. Since most of the processes underlying the different types of mechanical behavior are thermally activated, an increase of temperature simply acts as an acceleration of the relaxation and creep processes. Hence, a particular behavior observed at high temperature may similarly be observed at lower temperature on a longer time scale. Since moreover, the frequency in oscillatory experiments is inversely related to the time, all relations describing the dependency of mechanical properties (e.g., the shear modulus) on time, frequency, or temperature can be translated into each other. One thus speaks about the *principle of time–temperature superposition*.

Furthermore, the stress applied to a sample from a combination of small step strains can be simply described by the linear combination of the stresses resulting from each individual step dγ_i applied at time t_i. This finding states that, for linear response, the stress resulting from each step is independent of all other steps. The system "remembers" the deformations imposed on it earlier and continues to relax from each earlier deformation as new ones are applied. This phenomenon is called the *Boltzmann superposition principle*.

2.1.2.4 Rubber elasticity

Crosslinked polymer networks well-above their glass transition and melting temperature are named *rubbers*. They act as an important class of materials with practical use in various forms such as rubber bands, gaskets, adhesives, or tires due to their possibility of being enormously stretched without breakage or even loss of elasticity. These remarkable properties originate from the entropic nature of elasticity in rubbers as mentioned in brief in Chapter 2.1.2.1. It is thus convenient to perform a quantitative treatment of the phenomenon of rubber elasticity from the thermodynamic point of view. For simplification, one often starts from the *affine network model* [51–56], where the relative deformation of each network strand is assumed to be the same as the macroscopic relative deformation imposed on the whole network. Moreover, solely strong crosslinks are considered, whereas the influence of entanglements is neglected. In this case, a comparison of the sum-entropy of the network chains before and after deformation can be drawn utilizing the Boltzmann equation

$$S = k \ln W \tag{2.24}$$

with k being the Boltzmann constant and W the number of chain conformations that can be obtained from the distribution of end-to-end vectors. For convenience, this distribution is approximated to be the same as in the case of linear uncrosslinked chains (Gaussian statistics). Finally, one obtains

$$\Delta S = -\frac{nk}{2}\left(\lambda_x{}^2 + \lambda_y{}^2 + \lambda_z{}^2 - 3\right) \tag{2.25}$$

with λ_x, λ_y, and λ_z the relative deformations in x-, y-, and z-direction, respectively, and n the number of elastically effective network strands.

As the main contribution to the free energy of the network originates from the changes in entropy, enthalpic contributions can be neglected. This yields the following equation for the change in free energy upon network deformation:

$$\Delta F = -T\Delta S = \frac{nkT}{2}\left(\lambda_x{}^2 + \lambda_y{}^2 + \lambda_z{}^2 - 3\right) \tag{2.26}$$

For uniaxial deformations at constant volume, this equation simplifies to

$$\Delta F = \frac{nkT}{2}\left(\lambda^2 + \frac{2}{\lambda} - 3\right) \tag{2.27}$$

The force required to deform the network is the derivative of the free energy with respect to length along the axis of deformation. Division by the cross-sectional area then yields the stress as follows:

$$\sigma = \frac{nkT}{V}\left(\lambda^2 + \frac{1}{\lambda}\right) \tag{2.28}$$

The coefficient relating stress and deformation is the shear modulus G, which finally turns out to be

$$G = \frac{nkT}{V} = \nu kT = \frac{\rho RT}{M_\mathrm{s}} \tag{2.29}$$

in the affine network model, with ν the density of crosslinking (number of network strands per volume), M_s the average molecular weight of the network strands, and ρ the network density (mass per unit volume). The modulus G thus equals kT per network strand.

A more realistic treatment also takes spatial fluctuations of the crosslinks into account, as they lead to a net-lowering of the free energy by reducing the cumulative stretching of the network strands. The *phantom network model* [57] therefore introduces the structure factor $(f-2)/f$ correcting for the fluctuation of the f-functional crosslinks:

$$G = \nu kT\left(\frac{f-2}{f}\right) \tag{2.30}$$

In the case of swollen gels, the mobility of crosslinks and network strands is sufficiently high, so that the phantom network model applies. In the present work, crosslinks imposed by photochemical dimerization of maleimide sidegroups were tetrafunctional, thus yielding

$$G = \frac{1}{2}\nu kT \tag{2.31}$$

If *entanglements* are taken into account, the situation becomes more complicated. By and large, one can describe G as the sum of a contribution originating from the crosslinks and a contribution originating from entanglements:

$$G \cong G_{\text{x-links}} + G_{\text{ent}} = \rho RT\left(\frac{1}{M_{\text{x-linked}}} + \frac{1}{M_{\text{ent}}}\right) \tag{2.32}$$

G is thus controlled by the crosslinks in case of low molecular weight strands between them, whereas it is controlled by entanglements in case of high molecular weight strands between the crosslinks. For the present work, crosslinked systems were studied in the lower semidilute domain and had comparatively short strands, so that the influence of entanglements could be neglected.

If one also desires to account for *interactions* between the networks strands, enhanced mean-field models such as the constraint junction model, the diffused-constraint model, the nonaffine tube model, or the nonaffine tube-slip model have to be used [47]. Furthermore, non-Gaussian statistics has to be taken into account at large deformations, where the situation is better described by finite extensibility models such as the so-called inverse Langevin function for freely jointed chains [58].

2.1.2.5 Characterization of network structures by multiple-quantum NMR

In the last century, enhanced NMR methods have gained increasing importance in polymer research. One popular example of such an approach is called *multiple-quantum (MQ) NMR*. This technique can be used to render information on the local chain order and effective crosslinking density in polymer networks by focusing on residual proton–proton dipolar couplings and their distribution. Since a detailed description of the underlying quantum mechanical phenomena and the corresponding experimentation would be rather complex, these aspects lie beyond the scope of this work. The following chapter instead just intends to give a brief overview about the possibilities for the characterization of network structures by MQ NMR, whereas readers with further ambitions are referred to more specialized literature (e.g., [59, 60]).

In general, the proton line shape, or, equivalently, the transverse relaxation behavior of the proton NMR signal of polymers or networks far above their glass transition temperature or in the swollen state reflects the time scale of the chain dynamics and also the presence of restrictions to the dynamics, that is, the presence of crosslinks. Isotropically mobile, unconnected chains (i.e., sol), which fluctuate rapidly, contribute a slowly relaxing component (narrow line), while network chains fluctuate slightly anisotropically due to the constraints imposed by the crosslinks and thus exhibit a significantly faster relaxation (broader line). Therefore, the different components of a swollen network can be distinguished.

The reason for the broader lines of network chains is ultimately related to the fact that their NMR response is partially solidlike, i.e., dipolar interactions are only incompletely averaged out. Note that strong dipolar interactions lead to very broad lines in solids, while they are totally averaged out in the case of isotropically mobile liquids. The presence of crosslink-induced *residual dipolar couplings* (D_{res}) in a network (which is a “soft” solid) leads to the accelerated relaxation behavior as compared to a normal liquid. Theory shows that the magnitude of residual dipolar coupling is inversely proportional to the chain length between the crosslinks and thus directly proportional to the local crosslink density [59, 61]. Its precise measurement is therefore highly worthwhile. Technically speaking, the intensity decay process in a relaxation experiment is in this case due to coherent spin evolution (dipolar dephasing) rather than “real” fast-motion-induced relaxation. Since true relaxation processes always act simultaneously with the dipolar dephasing, making analyses of relaxation curves model-dependent, it is advantageous to *directly* measure the residual dipolar couplings in an experiment where their presence leads to a quantifiable intensity *build-up* rather than a decay. In this respect, MQ NMR has evolved as one of the most quantitative approaches, as not only absolute values of D_{res}, but also its distribution can be measured [59, 62–65].

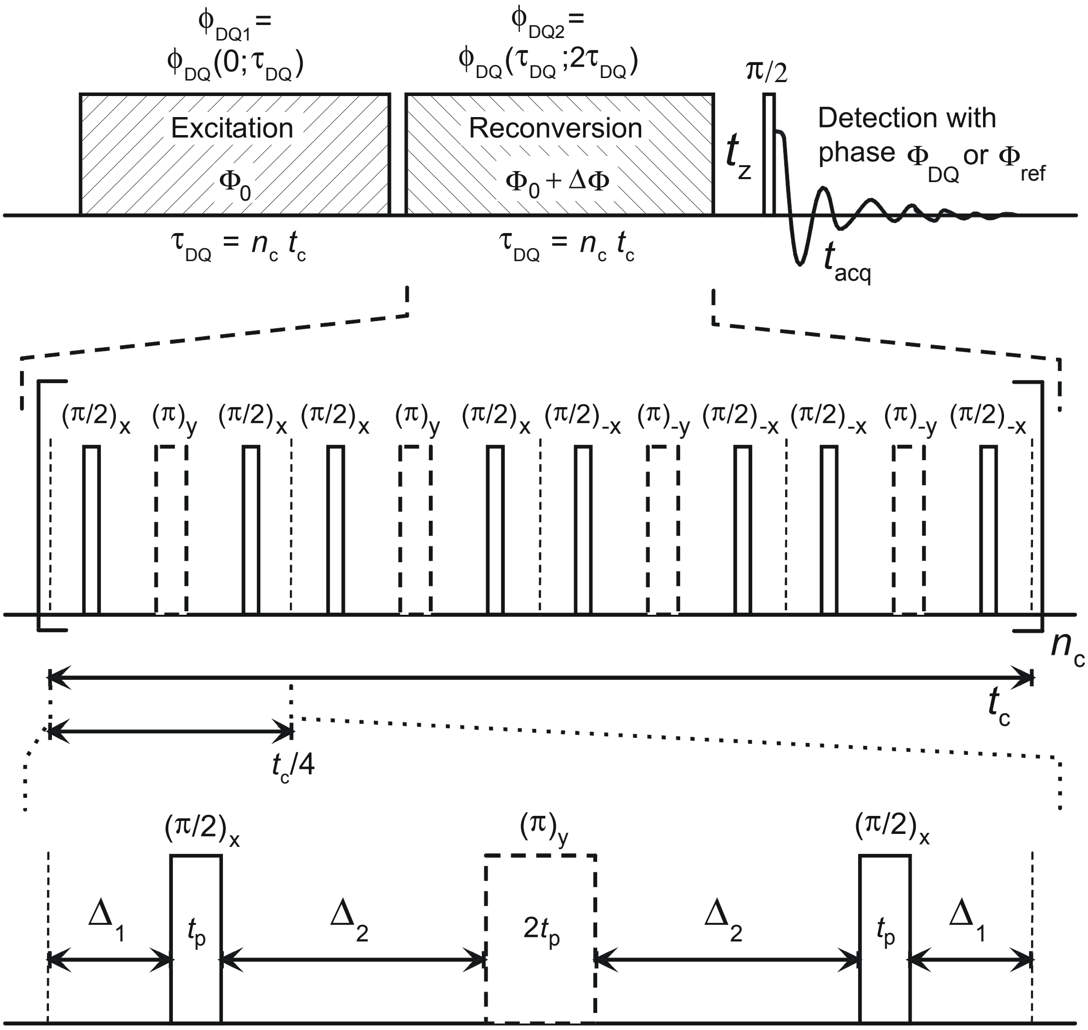

Figure 2.7 Scheme of a static MQ NMR experiment [66]. – The phase factors relevant for evolution under the pulse sequence blocks, ϕ_{DQ}, generally represent spin evolution under a dipolar double-quantum (DQ) Hamiltonian [59]. Coherence selection is realized by an incremented shift $\Delta\phi_{DQ}$ of the carrier phase ϕ_0 of the reconversion pulse sequence with appropriate receiver phase cycling to obtain the DQ-filtered (ϕ_{DQ}) or reference (ϕ_{ref}) intensities. Zooms illustrate the detailed pulse sequence of an improved DQ experiment of Baum and Pines [64, 66]. Details on the exact timing and the equivalence of cycle time (t_c) of number (n_c) incrementation to realize a specific τ_{DQ} can be taken from ref [64]. For the present work, $n_c = 2$ was employed. Courtesy of K. Saalwächter [59].

Realization of MQ NMR experiments

The principle of the technique is illustrated in Figure 2.7. By and large, a MQ NMR experiment yields the evolution of a time-dependent double-quantum (DQ) intensity built-up $I_{DQ}(\tau_{DQ})$ which reflects the magnitude of the homonuclear residual couplings arising as a consequence of the topological restrictions of the network chains. $I_{DQ}(\tau_{DQ})$ depends on the product of the residual dipolar coupling and the incremented evolution time τ_{DQ} under a specific pulse sequence (cf. Figure 2.7) [59, 64] which is applied to excite all even quantum orders in the sample (what is a multispin system). After excitation, the appliance of a second sequence block is necessary to reconvert the higher-order MQ coherences into observable magnetization. Finally, a read-out pulse generates detectable single-quantum coherence (transverse magnetization). To excite DQ coherence, a simple $\pi/2$–τ–$\pi/2$ pulse sequence can be used. Moreover, a π pulse centered between the $\pi/2$ pulses can serve as an effective suppressor of flip angle imperfections. For more details on pulse sequences and MQ coherences, cf. refs [64] and [66].

Subsequent selection of the DQ-filtered intensity is performed by a four-step phase cycling scheme. Additionally, a reference intensity $I_{ref}(\tau_{DQ})$ which belongs to that part of the free induction decay (FID) that has not yet evolved into DQ coherences is measured in a concurrent experiment differing only in the receiver phase of the selecting phase cycle. It contains a complementary contribution from dipolar coupling modulated magnetization of the network (a part of the dipolar spin evolution process), and also all contributions from more mobile non-network components. As measurements are conducted on a low-field instrument, both $I_{DQ}(\tau_{DQ})$ and $I_{ref}(\tau_{DQ})$ can be determined from an average over the initial part of the corresponding featureless FID after a 90° pulse that follows the actual MQ pulse sequence, during which the signal does not decay appreciably [59, 62–65, 67]. Note that $I_{DQ}(\tau_{DQ})$ and $I_{ref}(\tau_{DQ})$ contain contributions from all $4n + 2$ and $4n$ quantum orders, respectively, and that $I_{DQ}(\tau_{DQ})$ should equal $I_{ref}(\tau_{DQ})$ in the long-time limit. However, even though the experimental procedure comprises the excitation of multiple higher quantum orders, all arguments can be restricted to DQ coherences as only these reach significant intensities.

Evaluation of MQ NMR data

For the evaluation of data, the sum of DQ and reference intensities $I_{\Sigma MQ} = I_{DQ}(\tau_{DQ}) + I_{ref}(\tau_{DQ})$, which comprises the full magnetization of the sample subject to dipolar-induced relaxation, is firstly normalized to $I_{\Sigma MQ}(\tau_{DQ}=0) = 1$. In many cases, $I_{\Sigma MQ}$ initially turns out to be accompanied by a slowly decaying long-time tail that originates from signals of uncoupled, i.e., isotropically mobile components like sol fractions and nonelastic parts of the network (such as dangling chains, loops etc.) which are only detected in the reference experiment. A subsequent estimation and subtraction of these contributions can therefore be utilized to quantify the *composition of the sample* in terms of mobile fraction (sol), gel fraction, and magnitude of network defects, which consequently are determined as proton integral fractions.

After subtraction of the long-time tails, one finally obtains a DQ built-up curve with a 50% intensity plateau value. Fitting this to an adequate equation [59] yields an apparent dipolar coupling constant (D_{res}) as a characteristic parameter which is related to the network structure [63] and therefore provides a link to the theories of rubber elasticity, swelling, or stress-optical properties. As stated above, D_{res} describes the *local crosslinking density* and is consequently inversely related to the average length of the chains between crosslinks. Importantly, corresponding distributions are also accessible and carry information about heterogeneities [62–64].

A general procedure for this type of analysis has been described in the literature [59, 65] and will again be discussed in Chapter 4.1.4.4. However, in this work it was not possible to proceed in this manner, but an alternative path had to be taken that bases on the need that in networks $I_{DQ}(\tau_{DQ})$ equals $I_{ref}(\tau_{DQ})$ in the long-time limit.

2.2 Transport phenomena

2.2.1 Fundamentals

When a gradient of a physical quantity (e.g., temperature, charge density, velocity, pressure, or concentration) is present in a system in the absence of additional forces, a corresponding flux (i.e., a conduction of energy, charge, momentum, or matter itself) immediately arises to even it. The transport phenomena corresponding to the examples mentioned are named thermal or electric conductivity, viscosity (i.e., fluid dynamics or transfer of momentum), and diffusion. They all rest upon the second law of thermodynamics, i.e., the hunt for maximum entropy. In the following sections, the fundamentals of *diffusion* processes as phenomena where matter itself is transported as a consequence of concentration gradients, that is, gradients of the thermodynamic chemical potential, shall be focused.

As to be derived from equilibrium thermodynamics, the work required to shift a unit amount of material from a region with the chemical potential μ to a region with the chemical potential $\mu + \mathrm{d}\mu$ is $\mathrm{d}w = \mathrm{d}\mu$. In the 1-dimensional case, a gradient of μ is only present in one direction, and hence

$$\mathrm{d}w = \mathrm{d}\mu = \left(\frac{\partial \mu}{\partial x}\right)_{p,T} \mathrm{d}x \qquad (2.33)$$

In classical mechanics, the work required to shift an object through a distance $\mathrm{d}x$ against a force F is

$$\mathrm{d}w = -F\mathrm{d}x \qquad (2.34)$$

By comparing these equations, one can state that the gradient of the chemical potential acts like a (thermodynamic) force

$$F = -\left(\frac{\partial \mu}{\partial x}\right)_{p,T} \qquad (2.35)$$

Note that F is not necessarily a real force pushing molecules down the slope of the chemical potential, but rather reflects the spontaneous tendency of matter to spread into a medium until a uniform distribution is achieved—which is a direct consequence of the second law. Indeed, there is no physical need for an equilibration of concentration gradients as a consequence of diffusion, and a net-flux of matter is not compulsory forced to proceed from regions with high concentrations to such with low concentrations. By contrast, the only reason why diffusion always occurs in the direction predicted by the diffusion laws treated in this chapter is given by elementary laws of probability: one simply finds from the statistical consideration of diffusion processes as random phenomena that the likelihood to observe an equilibration of a concentration gradient is much greater than the opposed probability of its increase! However, thinking in terms of phantom (effective) thermodynamic forces as done in this section can nevertheless be useful and illustrative in many cases.

In a solution where the activity of the species considered is a, the chemical potential of the solute turns out to be

$$\mu = \mu^0 + RT \ln a \qquad (2.36)$$

Hence, the thermodynamic force acting is

$$F = -RT \left(\frac{\partial \ln a}{\partial x} \right)_{p,T} \qquad (2.37)$$

In ideal solutions, the activity $a = f\, c$ equals the concentration c (i.e., $f \approx 1$), thus yielding

$$F = -RT \left(\frac{\partial \ln c}{\partial x} \right)_{p,T} \qquad (2.38)$$

This form of eq (2.38) allows for a thermodynamic derivation of the fundamental principle that each diffusive flux of matter is proportional to the concentration gradient being responsible for its occurrence — as expressed by Fick’s first law of diffusion.

2.2.2 Fick’s first law of diffusion

As pointed out in the preceding section, the thermodynamic force which originates from a concentration gradient induces a flux of molecules. These reach constant velocity s when F equals the complementary frictional force F_R. Thus, $s \propto F$. Furthermore, the flux J is proportional to the drift velocity s, and F is proportional to the concentration gradient $\partial c/\partial x$. The combination of these proportionalities yields *Fick’s first law of diffusion* [68]

$$J = -D\left(\frac{\partial c}{\partial x}\right)_{p,T} \tag{2.39}$$

stating that the flux of matter through unit area is proportional to (and occurs as a direct consequence of) the concentration gradient normal to the section. The constant of proportionality is named the *translational diffusion coefficient* and has the dimension $(\text{length})^2 \cdot (\text{time})^{-1}$. The above-mentioned frictional force can be written as

$$F_\mathrm{R} = f_\mathrm{R} s \tag{2.40}$$

with f_R the friction coefficient. Assuming the diffusing particles to be spherical, one obtains

$$f_\mathrm{R} = 6\pi\eta r_\mathrm{H} \tag{2.41}$$

with r_H the hydrodynamic radius of the spheres and η the dynamic viscosity of the surrounding medium. Hence, the *Einstein relation* [69]

$$D = \frac{kT}{f_\mathrm{R}} \tag{2.42}$$

with k the Boltzmann constant and T the thermodynamic temperature reads

$$D = \frac{kT}{6\pi\eta r_\mathrm{H}} \tag{2.43}$$

in the case of spherical particles, where it is named *Stokes–Einstein relation*.

2.2.3 The diffusion equation (Fick's second law of diffusion)

When the preceding discussion is expanded to systems with nonstationary diffusion processes, a differential equation connecting the rate of change of concentration at a certain spatial coordinate with the curvature (i.e., the second derivative) of the concentration dependence on the distance can be derived. It is of fundamental importance for any quantitative treatment of diffusion processes and is named the *diffusion equation* or *Fick's second law*. For the 1-dimensional case, when diffusion proceeds in x-direction only, it reads

$$\frac{\partial c}{\partial t} = D\left(\frac{\partial^2 c}{\partial x^2}\right) \tag{2.44}$$

The corresponding differential equations for the 2- and 3-dimensional cases are

$$\frac{\partial c}{\partial t} = D\left(\frac{\partial^2 c}{\partial x^2} + \frac{\partial^2 c}{\partial y^2}\right) \tag{2.45}$$

and

$$\frac{\partial c}{\partial t} = D\left(\frac{\partial^2 c}{\partial x^2} + \frac{\partial^2 c}{\partial y^2} + \frac{\partial^2 c}{\partial z^2}\right) \tag{2.46}$$

respectively [70]. Therein, c represents the concentration of the substance under consideration, while D is again the translational diffusion coefficient. All these equations can be expressed in terms of vector analysis as

$$\frac{\partial c}{\partial t} = div(D\, grad\, c) \tag{2.47}$$

By and large, they describe the diffusion in an isotropic medium for the 1-, 2-, or 3-dimensional case, stating that the rate of accumulation of diffusing material depends on the difference between the rate of inflow and outflow into an element of infinitesimal thickness, which in turn depends upon the rate at which the concentration gradient changes. In principle, the diffusion equation can thus be regarded as a mathematical formulation of the intuitive notion that nature has a tendency to eliminate the wrinkles in a distribution.

However, when expressed in this way, the information supplied by eqs (2.44)–(2.47) may seem to be quite meager and general. It is therefore necessary to concretize the situation by deriving analytical solutions that describe different particular situations of interest. As Fick's second law is a second-order differential equation in space and a first-order differential equation in time, two boundary conditions for the spatial dependence and an additional initial condition for the time dependence have to be specified. Depending on them, various solutions can be obtained [70].

The following section concentrates on three simple cases which are relevant for the present work. In all of them, the initial condition is defined by a sharp delta pulse as origin of the diffusion process which subsequently proceeds into an infinite medium where the concentration must be everywhere finite and the total number of molecules is constant at all times.

1. When at time $t = 0$ the substance is totally localized in a plane somewhere in an infinitely extended medium, diffusion occurs in one dimension only (normal to the plane), and the solution to eq (2.44) is

$$c(r,t) = \frac{M}{2(\pi D t)^{1/2}} \cdot \exp\left(\frac{-r^2}{4Dt}\right) \tag{2.48}$$

2. When at $t = 0$ the substance forms a line source along the axis of a cylinder of infinite width, spreading occurs in two dimensions, and one obtains

$$c(r,t) = \frac{M}{4(\pi D t)} \cdot \exp\left(\frac{-r^2}{4Dt}\right) \tag{2.49}$$

3. When diffusion originates from a point source in an infinite 3-dimensional medium, the concentration profiles that develop will be spherically symmetrical according to

$$c(r,t) = \frac{M}{8(\pi D t)^{3/2}} \cdot \exp\left(\frac{-r^2}{4Dt}\right) \tag{2.50}$$

In eqs (2.48)–(2.50), r represents the generalized (radial) coordinate and M denotes the total amount of the diffusing species in the 3-dimensional case, while in the 2- or 1-dimensional case, it stands for the amount of substance per unit length or unit area, respectively. The three equations can be combined to one by introducing the parameter d for the diffusion dimension:

$$c(r,t) = \frac{M}{(4\pi Dt)^{d/2}} \cdot \exp\left(\frac{-r^2}{4Dt}\right) \tag{2.51}$$

Figure 2.8 shows some typical distributions of a diffusing species for these simple cases of 1-, 2-, or 3-dimensional diffusion at three successive instants. The curves broaden and become shallower with increasing time. In each case, the concentration profiles are *Gaussians* whose $e^{-1/2}$-radius is $\sqrt{2Dt}$. The decrease of the prefactor with time depends on the dimensionality: the higher the diffusion dimension, the faster occurs the drop of concentration at $r = 0$.

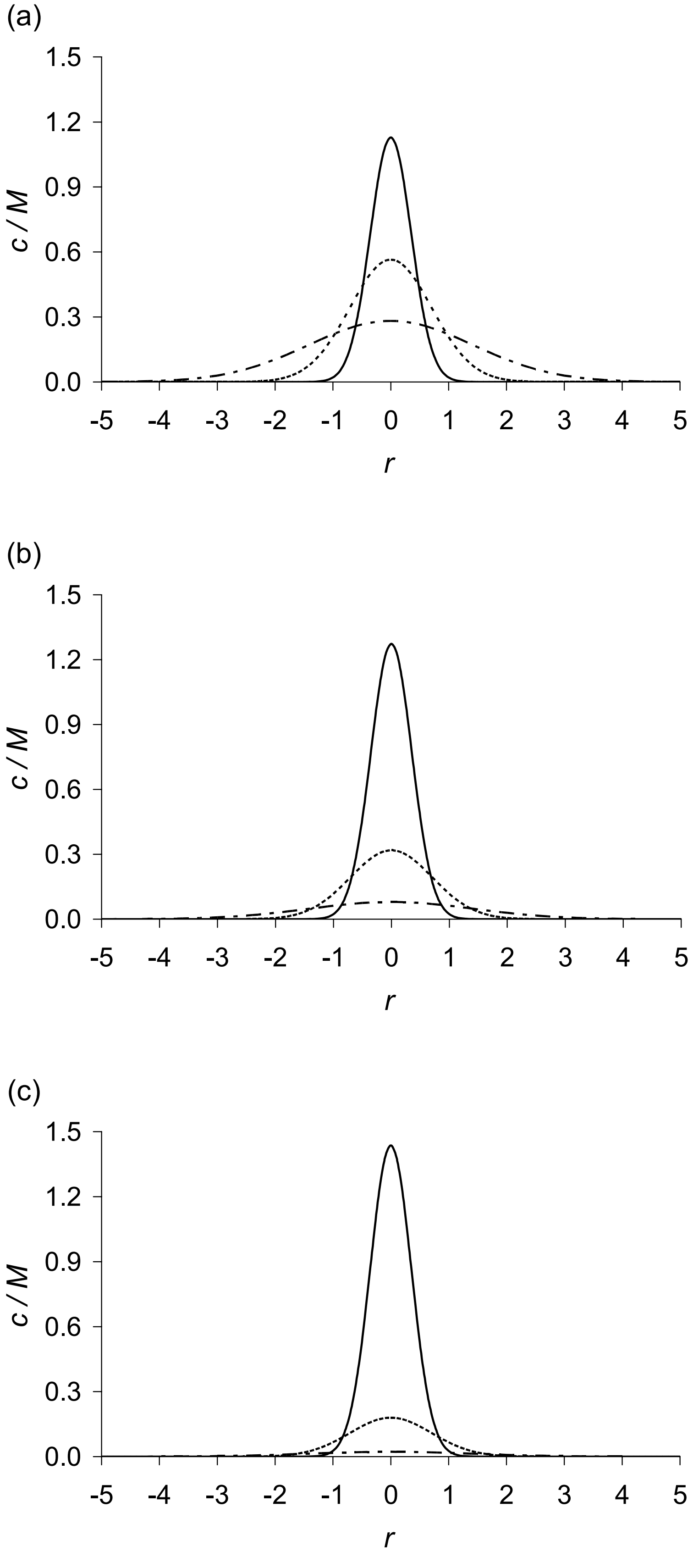

Figure 2.8 Concentration profiles for simple (a) 1-, (b) 2-, or (c) 3-dimensional diffusion at three distinct moments, *Dt* = 1/16 (solid line), *Dt* = 1/4 (dotted line), and *Dt* = 1 (chain-dotted line). – Adapted from [70].

2.2.4 Diffusion from a statistical perspective

An intuitive picture of the mechanism of diffusion is one in which particles move in a series of small steps and gradually migrate away from their original position. Diffusion processes can therefore be modeled on a lattice whereon the particles can jump randomly through a distance λ and do so in time τ. This means that the total distance covered by a diffusing molecule in a time t is $(t/\tau)\lambda$. However, this does *not* mean that each particle will be found at this particular distance from the origin after a period of t, as the direction of the steps is different on each occasion and, hence, an evaluation of the net-distance needs to take this into account (note that one generally assumes the probabilities to be equal for all possible directions on each jump). If one simplifies the discussion by solely considering the 1-dimensional case, that is, the so-called 1-dimensional *random walk*, one can estimate the *probability* to find a molecule at a distance x from the origin at time t to be

$$p = \left(\frac{2\tau}{\pi t}\right)^{1/2} \cdot \exp\left(\frac{-x^2\tau}{2t\lambda^2}\right) \tag{2.52}$$

One observes that eq (2.52) is of similar form as eq (2.48). For the diffusion coefficient, this type of model yields the *Einstein–Smoluchowski relation* [69, 71]

$$D = \frac{\lambda^2}{2\tau} \tag{2.53}$$

which in „macroscopic form“ corresponds to

$$D = \frac{< x^2(t) >}{2t} \tag{2.54}$$

with $< x^2(t) >$ being the mean square distance by which a diffusing molecule or particle with diffusion coefficient D is typically displaced from the origin after the time t.

2.2.5 Diffusion in polymer systems

In cases where the diffusing species are (dissolved) polymers, one has to account for their characteristic shape as macromolecular coils. In addition to the movement of the coils center of mass, segmental displacements are possible. Regarding the surrounding of the diffusing chain, a precise discrimination between unentangled (dilute) and entangled behavior is necessary.

As one aim of this work was to analyze diffusion processes of different types of macromolecular tracers in polymer systems, the following section presents the fundamental properties and quantitative relationships associated with the diffusion of macromolecules.

2.2.5.1 Dilute solutions

Basically, two classical theories are commonly known for the description of coil dynamics in dilute solution. Their fundamental difference arises from the fact that they account for the possibility of solvent to drain through the coil on its movement in contrary manner. One can imagine two extreme cases: on the one hand, solvent can be modeled to be freely draining through the coils, while on the other hand, coils can be assumed to drag the solvent within their pervaded volume with them. The first case is described by the *Rouse theory* [72] which disregards hydrodynamic interactions between the chain segments and models the coils as a coupled harmonic oscillator consisting of N beads connected by $N - 1$ mass-less elastic springs. Each pair of spring and bead can be considered as a Kuhn segment. The beads only interact with each other through the connecting springs, and each bead is characterized by its own independent friction with the coefficient f_{seg}. Hence, the total friction coefficient of the Rouse chain is the sum of the contributions of each of the N beads:

$$f_{\mathrm{R}} = N f_{\mathrm{seg}} \tag{2.55}$$

In this case the Einstein relation (2.42) yields a reciprocal dependence of the diffusion coefficient D on the molar mass M:

$$D_{\mathrm{Rouse}} = \frac{kT}{f_{\mathrm{R}}} = \frac{kT}{N f_{\mathrm{seg}}} \propto M^{-1} \tag{2.56}$$

By contrast, the second extreme is described by a model originating from *Zimm* [73] which assumes strong hydrodynamic interactions between the chain segments and therefore accounts for the viscous resistance imparted by the solvent wherein the segments move. As segments always drag solvent with them on their motion, a force acting on further solvent molecules at distance r and being roughly proportional to $1/r$ arises. It can thus be considered as long-range hydrodynamic interaction which finally also affects the movement of all other chain segments. Hence, moving coils can be modeled as solid objects of size $R \approx bN^{\nu}$ with b the root mean square size of the above-mentioned springs between N beads and ν the Flory exponent with values of $\nu = 0.5$ for ideal chains in θ-solvents and $\nu = 0.6$ for perturbed coils in good solvents. The Stokes–Einstein relation (2.43) then reads

$$D_{\text{Zimm}} \approx \frac{kT}{\eta R} \approx \frac{kT}{\eta b N^{\nu}} \propto M^{-\nu} \tag{2.57}$$

Indeed, there is evidence that hydrodynamic interactions between segments and solvent within the pervaded volume of the coils are strong in dilute solutions. For this reason, the Zimm model gives a better description of coil dynamics in the dilute state than the Rouse model (which actually only applies to low molecular weights). Several studies in dilute θ- as well as good solvent solution confirmed the predicted scaling laws [74, 75]. In 1956, Zimm published a full calculation where he averaged the hydrodynamic interactions to obtain the following result for an ideal chain [73]:

$$D_{\text{Zimm}} = \frac{8}{3\sqrt{6\pi^3}} \frac{kT}{\eta R} \tag{2.58}$$

Both theories can be considered as borderline cases of a more general one which is named the *Kirkwood–Riseman theory* [76]. In this model, variable hydrodynamic interactions between N_{seg} „effective“ segments of length L_{seg} are modeled with the segmental friction coefficient f_{seg}. The diffusion coefficient can thus be described as

$$D = \frac{kT}{N_{\text{seg}} f_{\text{seg}}} \left(1 + \frac{8\sqrt{2N_{\text{seg}}} f_{\text{seg}}}{3\sqrt{12\pi^3} \eta L_{\text{seg}}} \right) \tag{2.59}$$

For the first extreme of solvent being freely draining through the coils, f_{seg} turns out to be small and the second summand in eq (2.59) can be neglected. One thus obtains a relation according to the Rouse model. If on the other hand coils are totally dragging solvent with them, the first summand can be neglected, and eq (2.59) describes D to be inversely related to the end-to-end distance of unperturbed coils in θ-solvents $[r]_0 = N_{\mathrm{seg}}^{0.5} L_{\mathrm{seg}}$. In good solvents, coil expansions have to be taken into account, e.g., by including into eq (2.59) an expansion factor $\alpha = [R_{\mathrm{G}}]/[R_{\mathrm{G}}]_{\theta}$ that describes the relation of the radii of gyration in good and θ-solvent.

All of the models presented so far are based on the assumption of isolated coils and therefore only apply to the dilute regime. Hence, if the discussion is expanded to the semidilute situation, one observes deviations from the above-mentioned behavior that notably increase with increasing polymer concentration: Initially, first coil overlaps in the unentangled semidilute region lead to a situation where the applicability of the Rouse or Zimm model depends on the length scale considered. At still higher concentrations, entanglements come into play, and solutions can be considered as temporary networks. Beyond this point, chain dynamics and diffusion processes are notably influenced by the entanglements, and corresponding theories have to be applied to give a quantitative description. Two well-known approaches for this purpose are the reptation model that has been theoretically derived by De Gennes and Doi & Edwards, as well as the hydrodynamic scaling concept which was introduced by Phillies on the basis of experimental observations.

Since in this work, dynamic properties were essentially studied in the semidilute regime, the fundamentals of these theories are outlined in the subsequent section.

2.2.5.2 Semidilute systems

Unentangled semidilute solutions

As stated above, dynamic properties of dilute polymer solutions are in most cases well described by the Zimm model. By contrast, *unentangled* polymer melts are better characterized by the Rouse model, as in such systems hydrodynamic interactions are screened in similar manner as it has been outlined for the screening of excluding volume effects in Chapter 2.1.1.2. In this regard, it has also been mentioned that the situation in semidilute systems depends on the length scale considered: while excluded volume interactions of the coils are screened by the overlapping chains on length scales larger than the correlation length ξ (many-chain statistics, meltlike situation), they play a role inside the correlation blobs on length scales below ξ (single-chain confirmations, dilute-like behavior).

If one focuses the dynamic properties of semidilute solutions with interpenetrating but still unentangled coils, a similar behavior is observed, and a hydrodynamic screening length ξ_h separating two domains needs to be introduced. On length scales below ξ_h hydrodynamic interactions dominate and dynamics is described by the Zimm model. By contrast, length scales larger than ξ_h show Rouse-like behavior because hydrodynamic interactions are screened by surrounding chains. In this respect, Wang and Zimm suggested the description of the restricted hydrodynamic coupling of segments with the aid of a screening parameter [77].

One may not wonder that the hydrodynamic screening length ξ_h in semidilute solutions is expected to be proportional to the static correlation length ξ. In melts, both excluded volume and hydrodynamic interactions are fully screened to the level of individual monomers so that $\xi_h \approx \xi \approx b$ (with b the segmental length), while at the overlap concentration c^* both excluded volume and hydrodynamic interactions apply over length scales comparable to the size of the coils R with $\xi_h \approx \xi \approx R$.

The diffusion coefficient of a single chain in an unentangled semidilute solution decreases as a power law in concentration:

$$D \approx \frac{kT}{\eta b} \cdot \frac{\phi^{-(1-\nu)/(3\nu-1)}}{N} \tag{2.60}$$

with ϕ the volume fraction of polymer and the scaling exponent $-(1 - \nu)/(3\nu - 1) = -1$ in θ-solvents ($\nu = 0.5$) and $-(1 - \nu)/(3\nu - 1) = -0.5$ in good solvents ($\nu = 0.6$). Rewriting this equation by inclusion of the Zimm diffusion coefficient D_Zimm for dilute solutions according to eq (2.57) as well as the overlap threshold $\phi^* = N^{-(3\nu - 1)}$ [47] yields

$$D \approx D_\text{Zimm}\left(\frac{\phi}{\phi^*}\right)^{-(1-\nu)/(3\nu-1)} \tag{2.61}$$

Substituting ϕ and N by the more common values M for the molecular weight of the diffusing polymer and c as its concentration then leads to the following scaling law for the semidilute unentangled domain as derived by Hess [78, 79] for the good solvent situation:

$$D \propto M^{-1}c^{-0.5} \tag{2.62}$$

Entangled systems

In the preceding section, semidilute but still unentangled systems just slightly above c^* have been focused. If the polymer volume fraction is further increased, chains more and more interpenetrate and eventually form temporary entanglements. Many authors term the corresponding threshold as the *entanglement concentration* ϕ_e^* or c_e^*. Note that the latter one not necessarily equals the overlap threshold ϕ^* or c^*, but in contrary, one often observes c_e^* to be the (2–5)-fold of c^* in good solvents [18]. Beyond c_e^*, chain dynamics is strongly influenced by the entanglements that impose topological constraints with lifetimes comparable to the relaxation modes of the chains. Hence, one observes notable dependencies of macroscopic and microscopic sample properties such as the viscosity or the diffusion coefficient on the concentration and molecular weight of the chains involved. In similar regard, chemical crosslinks in polymer networks act as fixed obstacles and impose a permanent hindrance on the movement of enclosed materials.

Theoretical descriptions of these situations can be given on the basis of *tube models*, among which a simple one was proposed by de Gennes [21–23] and Doi & Edwards [24–26] which is named the *reptation model*. Basically, it draws a picture of densely entangled polymer systems where the surrounding of a particular chain is modeled as a tube composed of long-living topological constraints that are imposed by neighboring chains. The tube confines the motion of the enclosed chain which is thus only able to creep (i.e., to *reptate*) along its own contour (the *primitive path*) in a 1-dimensional way. On the other hand, segmental displacements in perpendicular manner are assumed to be restricted by surrounding chains to an average distance of a few nanometers (the *tube diameter*). Motion of the chain therefore conceptually consists of the diffusion of small loops along the primitive path (a principle similar to unraveling a knot) and the resulting chain migration proceeds as curvilinear diffusion around the obstacles. Figure 2.9 depicts this principle schematically.

The average time that is necessary for complete rearrangement of the chain conformation (i.e., for complete renewal of the tube) is called the *reptation time*. It is predicted to be proportional to the third power of the chains molar mass:

$$\tau_{\mathrm{rep}} \propto M^3 \tag{2.63}$$

In passable agreement, various experiments pointed to exponents of about 3.4. During the time τ_{rep}, a chain diffuses exactly out of its confining tube of length L_{tube}. This defines the 1-dimensional Rouse-like tube diffusion coefficient D_{tube}:

$$L_{\mathrm{tube}}{}^2 = 2D_{\mathrm{tube}}\tau_{\mathrm{rep}} \tag{2.64}$$

If one considers longer time scales, macroscopic 3-dimensional diffusion can be imagined as a consecutive chain movement from one tube into another. Note that this picture in principle corresponds to the statistical modeling of diffusion as a series of consecutive jumps on a lattice (cf. Chapter 2.2.4). The theoretical treatment of this situation leads to characteristic scaling relations for the dependence of the macroscopic translational diffusion coefficient D on molecular weight M and polymer concentration c, namely

$$D \propto M^{-2} c^{(2-\nu)/(1-3\nu)} \tag{2.65}$$

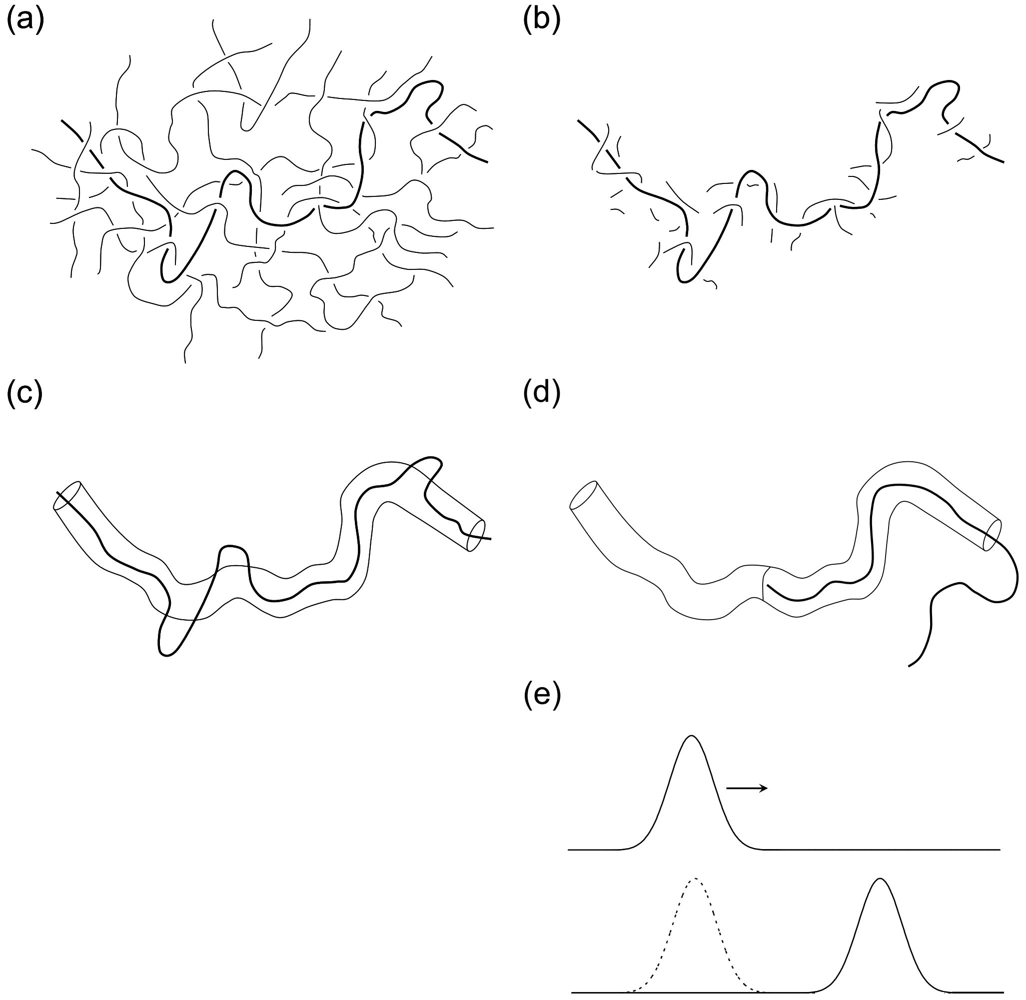

Figure 2.9 Principles of the reptation mechanism. – (a) Schematic representation of some entangled polymer chains and accentuation of one particular chain. (b) Relevant segments for the modeling of a confining tube. (c) Tracer chain trapped in its original tube ($t = 0$). (d) Possible confirmation at time $t > 0$. (e) Principle of chain movement in the reptation scenario: an accumulation of a stored length on one particular portion of the entangled chain is circulated to different loops up to the moment where a certain essential constraint has been relaxed.

In good solvents ($\nu = 0.6$), this corresponds to [22]

$$D \propto M^{-2} c^{-1.75} \tag{2.66}$$

whereas θ-solvents ($\nu = 0.5$) show [80]

$$D \propto M^{-2} c^{-3} \tag{2.67}$$

Later on, Schaefer et al. extended and revised the basic scaling and reptation theory by mean-field arguments for excluded volume interactions and derived the so-called marginal solvent model [81] which predicts

$$D \propto M^{-2} c^{-2.5} \tag{2.68}$$

Note that in principle, eqs (2.66) and (2.67) for the good and θ-solvent behavior can be considered as asymptotic limits of the latter model, which applies to *any* solvent situation.

The assumption of fixed obstacles in the tube concept, meaning that the walls of the tube have to be long-living on the time scale of chain motion, has been questioned. This approximation surely holds in the case of networks with strong (chemical) junctions or in entangled matrixes with chains that are markedly longer than a considered test-chain, but may fail in cases of weakly entangled systems where the chains surrounding a particular test-chain have comparable length to the latter and can therefore be regarded as moving test-chains too. In such situations, entanglements around a chain are permanently solved and reformed on a time scale comparable to the reptation time, which finally leads to a situation with a fluctuating tube termed as *constraint release* [82, 83]. In this picture, the tube is able to perform local jumps with a rate reciprocally proportional to the lifetime of the topological constraints τ_{tube}. Hence, the constraint release mechanism leads to a Rouse-like motion of the confining tube and its primitive path itself in addition to the chain reptation, and one observes

$$D_{\text{tube}} \propto \frac{1}{\tau_{\text{rep}}} + \frac{1}{\tau_{\text{tube}}} \tag{2.69}$$

Depending on the ratio of $\tau_{\text{rep}}/\tau_{\text{tube}}$, the overall-situation can thus be more or less dominated by pure reptation, reptation and constrained release, or mainly tube fluctuation alone.

In the last decades, the dynamic properties of semidilute and concentrated polymer systems have attracted a vast amount of experimental work,1) and the scaling laws mentioned in this section were supported in a limited concentration range: First and foremost, the predicted *M*-dependence of *D* could be confirmed in melts as well as semidilute solutions. However, the situation is less clear with respect to the *c*-dependence:

In principle, one expects *D* to be independent of *c* when dilute solutions are analyzed. In the good solvent limit, an increase the polymer concentration should then lead to a situation where one firstly passes the overlap concentration *c** and observes a behavior of $D \propto M^{-1}c^{-0.5}$ in the unentangled semidilute regime. At still higher concentrations, one eventually reaches the entanglement threshold c_e*, where $D \propto M^{-2}c^{-1.75}$ applies. Moreover, a second change of the *c*-dependence is expected at the border to the concentrated regime *c***, which finally should lead to the θ-like situation with $D \propto M^{-2}c^{-3}$.2)

In case of a θ-solvent, the borders of the different regions are more coincident, and one expects no or at least a quite limited semidilute unentangled range with $D \propto M^{-1}c^{-1}$ and an extended domain with $D \propto M^{-2}c^{-3}$ beyond c_e* (≈ *c** = *c*** in the θ-scenario).

Nevertheless, real experiments seldom show such type of "discrete" behavior, but instead, double-logarithmic plots of *D* vs. *c* are often smoothly curved. Even though one is able to find the predicted scaling exponents by fitting power laws within different intervals on the *c*-axis in many cases, this is ultimately based on the assumption of fundamentally different behaviors in certain concentrations ranges, thus requiring the definition of corresponding borders for the crossover from one region to another, i.e., from one scaling law to another. In direct consequence, different definition of these borders would lead to different scaling exponents.

---

[1] Note that for reasons mentioned below, no particular work shall be cited here.

[2] As denoted in Chapter 2.1.1.2, concentrated solutions generally behave θ-like, even when being in good solvent.

To overcome this deficiency, a basically different approach to describe dynamic processes in polymer systems has been introduced by Phillies, who suggested a *universal scaling equation* being able to describe diffusion phenomena of various types of probes such as globular particles, linear chains, or star-shaped polymers in macromolecular matrixes over the entire range of matrix concentration between the dilute and the concentrated (near meltlike) regime [27–35]:

$$D = D_0 \cdot \exp\left(-\alpha c^{\nu} M^{\gamma} R^{\delta}\right) \tag{2.70}$$

In eq (2.70), D_0 symbolizes the probe-diffusion coefficient in the absence of the polymer matrix of concentration c and molecular weight M, while R represents the probe radius. ν, γ, and δ are scaling exponents, among which ν is predicted to lie between 0.5 and 1. α has been theoretically treated in ref [30]. For polymer self-diffusion, eq (2.70) simplifies to

$$D = D_0 \cdot \exp\left(-\alpha c^{\nu}\right) \tag{2.71}$$

with D_0 the diffusion coefficient of an isolated macromolecule.

These relations were initially introduced empirically as Phillies considered them to be able to describe a surprisingly large amount of experimental data. Subsequently, he presented a heuristic derivation of his *hydrodynamic scaling model* which essentially bases on the assumption that interchain *hydrodynamic* interactions significantly overweight the effects of *topological* constraints [29, 30]. In consequence, Phillies stated that “there is evidence for reptation in polymer melts, but the opposite is true in solution” [28] and that “neither reptation nor hydrodynamic screening necessarily exists in polymer solutions” [29]. Consequently, no fundamental differences between the diffusive behavior of flexible chains and rigid tracer particles are expected in his model. This is a fundamental contrast to the reptation scenario where only flexible linear chains are able to reptate, whereas motions of solid particles or branched macromolecules in entangled matrixes should be notably more hindered.

In the subsequent years, many workgroups devoted much effort[1] to the investigation of polymer self-diffusion as well as probe-diffusion in polymer matrixes, and it has been concluded that eq (2.70) is able to describe the collected data over a large range of concentrations without any need for a subdivision of the c-range into different domains. Only at very high concentrations (meltlike regime), a power law needs to be applied [33, 34]. Moreover, besides polymer self-diffusion, even diffusion processes of nonlinear tracers such as spherical particles or starlike macromolecules can be described by the hydrodynamic scaling model. In 2004, Phillies published an extensive re-examination of literature data and showed all of them to fit to his equation [35].

However, despite this apparent success of the hydrodynamic scaling approach, it has also been criticized by several authors who argue that a stretched exponential as eq (2.70) is a highly flexible analytic form thus being able to fit almost all types of experimental data sets.

Recapitulatory, one has to state that up to now literally hundreds of references dealing with the diffusion phenomena of various types of tracers in numerous macromolecular matrixes have been published, and both the reptation and the hydrodynamic scaling model had been subject to extensive critic. In order to avoid possible overestimations of particular ones among them, no special work shall be cited here; instead, the reader is referred to a set of comprehensive reviews [14–20]. However, after all, no comprehensive picture illustrating the mechanisms of polymer motion could be drawn and one has not been able to clearly confirm or reject one of the mentioned fundamentally different theoretical approaches yet.

Quite contrariwise, all imaginable types of results can be found in literature: while many papers tend to confirm the reptation model, others reject it, even after implementation of additional relaxation modes like constrained release. For the hydrodynamic scaling approach, one encounters a similar situation: on the one hand, many authors find their data to be surprisingly well described by the universal scaling equation, whereas others do on the other hand point out notable differences between the diffusive behavior of hard tracer particles and flexible linear polymer chains.

---

[1] Again, no particular work shall be cited here, instead cf. refs [14–20].

In addition, one also finds any types of mixes: several workers perform proper fits of their data with both the scaling laws according to the reptation concept *and* the stretched exponential function derived by Phillies, whereas others are not able or do not intend to describe their findings with either of these two theories but apply alternative explanations instead.

As stated in Chapter 1, it was thus one aim of this work to perform another systematic study considering this problem. For this purpose, comparisons of flexible linear and rigid spherical tracers were intended. Furthermore, a successive transition from an entangled polymer solution into a chemically crosslinked gel was realized by stepwise crosslinking of the matrix chains (cf. Figure 1.1). Since in order to achieve this, network chains were interlinked by means of photochemistry and mobility measurements were performed by a fluorescence technique, the following chapter now focuses on the fundamentals of the corresponding photochemical and photophysical processes.

2.3 Interaction of light and matter, luminescence, and photochemistry

2.3.1 Absorption of light and electronic excitation

Atoms and molecules exist in different discrete states of rotation, vibration, and electronic configuration. Transitions between these states can occur upon interaction of matter with electromagnetic radiation. This may basically populate a state E_2 from a state E_1 under absorption or emission of a photon of energy $|E_1 - E_2|$ (corresponding to a frequency of $\nu = \Delta E/h$ with h the Planck constant). Regarding electronic excitation, typical energies required lie in the range of some electron volts, which corresponds to photons in the visible and UV range of the electromagnetic spectrum. Corresponding irradiation of matter is thus able to populate electronically excited states from the ground state, accompanied by the population of excited vibrational states within the excited electronic state. The underlying rule for this process is the *Franck–Condon principle* [84–86] as schematized in Figure 2.10:

Since nuclei are much heavier than electrons, electronic excitation (which proceeds to within about 10^{-15} s) is essentially instantaneous relative to the time scale of nuclear motions. Nuclei thus have not enough time to rearrange and stay at their initial separation, wherefore the excited electronic state has a distribution of electron density differing from the one in the ground state. Figure 2.10 illustrates this aspect by the shift of the upper potential curve towards higher nuclear separation in consequence of the antibonding character of the former unoccupied molecular orbital. Upon excitation, nuclei are thus exposed to a new force field inducing vibration of the molecule, and the former average positions of the nuclei are now turning points of the oscillation. All such processes where the nuclear backbone of the molecule is therefore most likely to retain its conformation on excitation are named *vertical transitions* according to the Frank–Condon principle. Besides this type of semiclassical interpretation, a more profound description can be given in the words of quantum mechanics:

Before absorbing radiation, virtually all molecules populate the ground vibrational state of the ground electronic state according to the Boltzmann distribution at room temperature. The vibrational wave function has a maximum at the average position R_{eq}, from which transitions originate with maximum likelihood. Upon excitation, the probability for a molecule to end up in any particular vibrational level is proportional to the square of the vertical overlap of the vibrational wave functions of the original and the final state. Hence, the vertical transition intersects many vibrational levels and ends at such a one with maximum likelihood at a similar arrangement as R_{eq}. This corresponds to a wave function of a higher excited vibrational state within the excited electronic state as displayed in Figure 2.10. Note that this, however, is not the only vibrational level at which the excitation may end, because several of its neighbors also exhibit a high probability of having nuclei at the separation R_{eq}. Hence, transitions take place to all the vibrational levels in this region, but most intensely to the level having a wave function that overlaps the initial one most favorably. Moreover, the process described may in principle populate not only the first excited but also higher excited electronic states initially.

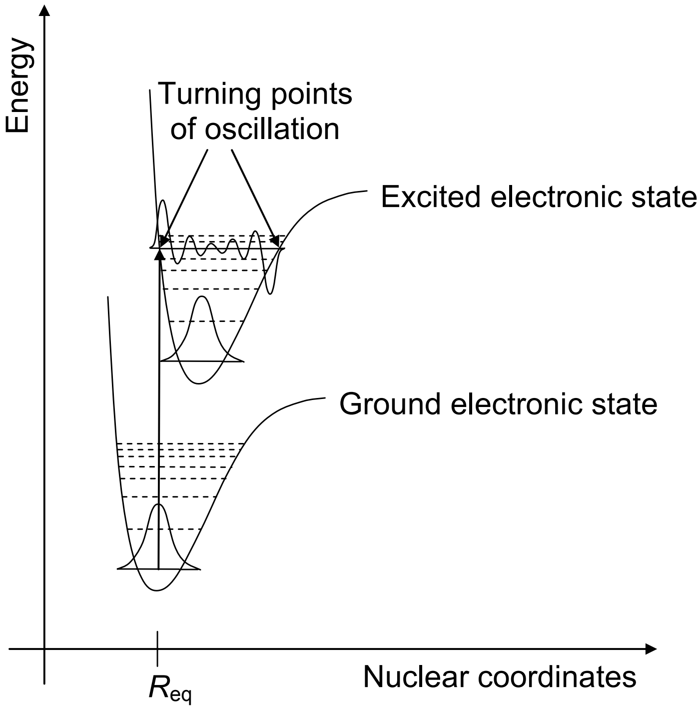

Figure 2.10 Schematic of the Frank–Condon principle for a diatomic molecule assuming Morse-like potential energy functions in both the ground and excited electronic state. – Since electronic transitions are notably faster than nuclear motions, vibrational levels are favored when they correspond to a minimal change of the nuclear coordinates, here labeled as the ground state equilibrium conformation R_{eq}. Adapted from [87].

After electronic excitation, several types of processes may follow subsequently. Figure 2.11 depicts an example of the *Jablonski diagram* [88], a scheme summarizing the most important ones among them. Directly after absorption of light (pathways "ex"), the excited molecule starts to dissipate energy by collisions with surrounding ground state molecules (e.g., the solvent), which leads to fast ($\sim 10^{-12}$ s) thermal relaxation to the ground vibrational state within the excited electronic state (dotted arrows). Additionally, molecules relaxed hereinto may be able to undergo spontaneous transitions to higher vibrational states of subjacent electronic levels—provided that the corresponding potential curves intersect—by a process named *internal conversion* (pathways "ic"). In combination, these two procedures lead to *Kasha's photochemical dogma* [89], stating that molecules which initially were excited to higher electronic states generally tend to perform a fast decay to the first excited state, where they finally arrive in the ground vibrational state.

In principle, this cascade may even proceed back down to the lowest vibrational level of the ground electronic state. However, for the dyes employed for the present work such a complete relaxation is prevented due to their large energy gaps to the ground state. Thus, the process described ends up in the ground vibrational state of the first excited electronic state in these cases. Here, the molecule remains for a period of typically some nanoseconds, which makes this state the first important origin for following photophysical and photochemical reactions. As the spin of the excited electron has not been affected by all previous processes, the molecule has retained its singlet character, wherefore the according state is called the *first excited singlet state* (S_1).

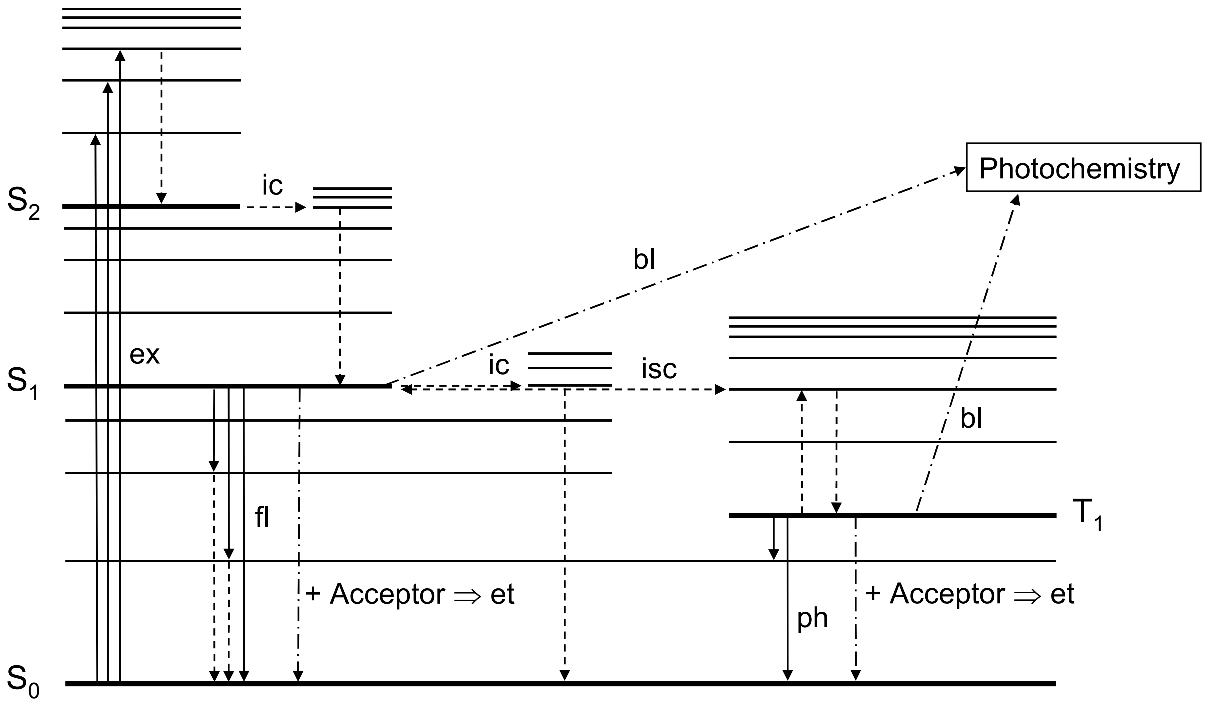

Figure 2.11 Jablonski diagram illustrating subsequent processes following upon electronic excitation (ex). – Full arrows: radiative processes, dotted arrows: thermal processes, chain-dotted arrows: mono- or multimolecular photochemical pathways. Abbreviations: S_0: ground electronic state, S_1: first excited singlet state, S_2: second excited singlet state, T_1: first excited triplet state, ic: internal conversion, isc: intersystem crossing, fl: fluorescence, ph: phosphorescence, bl: photobleaching, et: nonradiative energy transfer to an acceptor.

2.3.2 Subsequent processes I: Luminescence

After undergoing the sequence of thermal relaxation and internal conversion processes down to the ground vibrational level of the S_1 state, particular kinds of molecules are able to return to the ground electronic state by spontaneous emission of radiation, which is named *fluorescence* (pathway “fl” in Figure 2.11). Since this process again occurs according to the Frank–Condon principle, molecules emitting fluorescence light most likely find themselves in excited vibrational states of the ground electronic state (S_0) subsequently, wherefrom they finally descent back to the lowest vibrational level by thermal relaxation. In combination with Kasha’s photochemical dogma, this leads to the phenomenon that wavelengths emitted from excited molecules are always longer, i.e., red-shifted, as compared to the ones absorbed. As this effect has firstly been observed by Stokes in 1852 on solutions of quinine, it is named *Stokes shift* [90]. Note that vibrational levels of the ground and the first excited electronic state are often similar, wherefore absorbance and emission spectra appear according to the mirror image rule [91].

Directly after the emission of fluorescence light the molecule rapidly returns to its ground vibrational and electronic state. Hence, another excitation–emission cycle as introduced above may follow subsequently. Due to the ability to show this behavior several thousandfold before being destroyed (cf. Chapter 2.3.5.1), fluorescent dyes are able to produce high signal (i.e., light) intensities even at rather low concentrations. This makes analysis techniques based upon fluorescence phenomena very sensitive and popular.

The vast majority of fluorophores consists of a large delocalized system of π-electrons as such bonding systems allow for an effective excitation by moderate light energies and, moreover, ensure adequate stability to prevent dissociation of the molecule in its excited state. For the present work, the dyes utilized were the xanthene derivatives rhodamine B and thioxanthone disulfonate (TXS) as depicted in Figure 2.12.

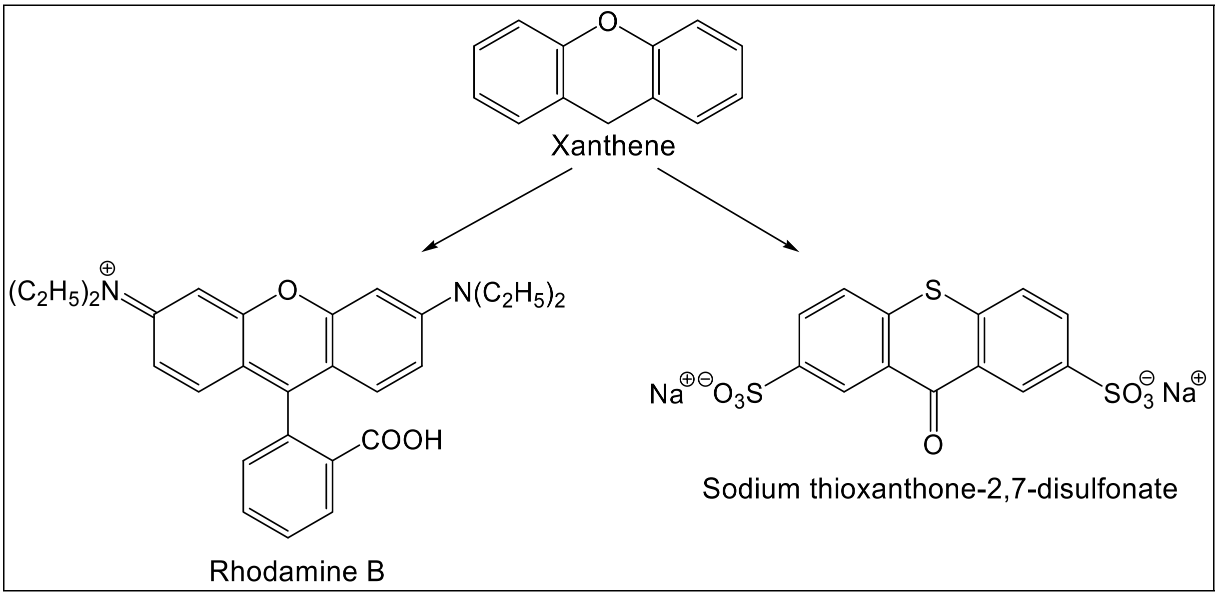

Figure 2.12 Structure of the xanthene dye and its derivatives employed for the present work.

Besides the emission of fluorescence light, another important pathway to depopulate the S_1 state is the *intersystem crossing* (isc) process as illustrated in Figure 2.13. Decoupling of the spins of the excited electron and the remaining ground state electron at a point where the potential curve of S_1 intersects the analogous curve of the *first excited triplet state* (T_1) leads to a population of the latter. Since therein a pair of two parallel electron spins is involved, T_1 turns out to be a long-living excited state which may in turn be the origin of several following processes. Similar to the phenomenon of fluorescence, the emission of a photon is one possible way to depopulate T_1 and to return to the singlet ground state. As this is accompanied by the need for a second spin inversion, typical decay times of this process named *phosphorescence* (pathway “ph” in Figure 2.11) are in the range of milliseconds. Since furthermore, the lowest vibrational level of T_1 lies below the corresponding level in S_1 in most cases, phosphorescence light appears red-shifted in comparison with fluorescence light. In some special cases where T_1 lies only slightly below S_1, a thermal re-excitation is possible, which then can lead to delayed fluorescence.

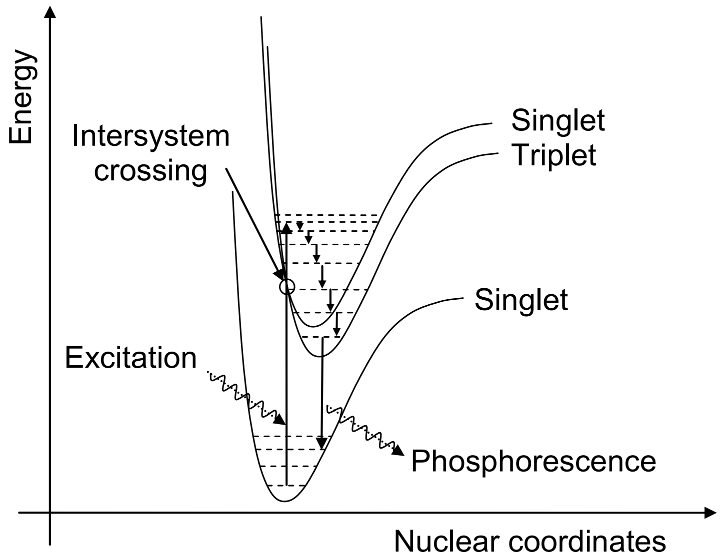

Figure 2.13 Schematic of intersystem crossing and emission of phosphorescence light for a simple molecule assuming Morse-like potential energy functions in the ground and excited electronic states. – Adapted from [87].

2.3.3 Subsequent processes II: Photochemistry and energy transfer

Besides the above-mentioned radiative ways for electronic deactivation, further important possibilities comprise *nonradiative* pathways like photochemical reactions. These include mono- or bimolecular processes originating from excited singlet or triplet states. Note that the latter are more favorable with regard to bimolecular reactions that require a collision of two reaction partners during the lifetime of the excited state. By contrast, monomolecular reactions often originate from the high energy singlet state. In both cases, however, the excess of energy provided by electronic excitation of the molecule(s) offers various possibilities to undergo chemical transformations either involving the excited state alone (adiabatic processes) or both the excited and the ground state (diabatic processes). In principle, subsequent reactions can lead to all kinds of mechanisms known from "classical" chemistry, e.g., rearrangements, fragmentations, additions, substitutions, cyclizations and ring-openings, as well as oxidation and reduction processes. In many cases, photochemical reactions thereby offer the possibility to perform commonly known reactions at rather low temperatures or to take alternative reaction pathways which can not be followed thermally (e.g., photoreactions of ketones, which undergo an umpolung upon excitation to their nπ* triplet states).

For the present work, one principally has to consider two types of photochemical deactivation processes which were employed to realize selective crosslinking of a functionalized PAAm matrix and to perform FRAP measurements on fluorescently labeled tracers. These are the sensitized photodimerization of olefins and the photobleaching pathways for fluorescent dyes. A more profound discussion focusing on these particular processes will be given within the following subchapters.

However, before considering this, one should pay attention to another important pathway for the deactivation of electronically excited molecules which is called *energy transfer*. Hereby, an excited molecule is deactivated to its ground state by transferring its excitation energy to an appropriate acceptor which in turn is excited in the following manner (pathway “et” in Figure 2.11):

$$D^* + A \rightarrow D + A^*$$

If this procedure requires a collision of the two partners, one speaks about the Dexter mechanism, whereas an alternative way is the nonradiative energy transfer over larger distances by the Förster mechanism [92]. Note that with respect to the former, one may even observe energy transfer between states of different multiplicity within the framework of Wigner’s spin conservation rule:

$$^1D^* + {^1A} \rightarrow {^1D} + {^1A^*}$$
$$^3D^* + {^1A} \rightarrow {^1D} + {^3A^*}$$

The latter reaction equation is of importance in the field of *photosensitization* as treated in more detail in Chapter 2.3.5.2. Generally, this term describes such processes where the excited triplet state of a molecule is populated not by direct excitation and subsequent intersystem crossing but by means of energy transfer from an excited triplet-donor. This allows for an effective as well as mild and selective excitation of a substrate to its T_1 state that otherwise may often not be accessible directly. Besides the aspect of photosensitization, the latter two reaction schemes are also relevant in cases where (undesired) singlet or triplet states are about to be quenched.

Further important mechanisms of energy transfer comprise the so-called triplet–triplet-annihilations as well as photo-induced electron transfer reactions. In the first case, two triplet states deactivate to produce at least one singlet state

$$^{3}D^{*} + {}^{3}A^{*} \rightarrow {}^{1}D + {}^{1/3/5}A^{*}$$

whereas in the second case, photoexcited donor or acceptor molecules induce redox-processes in the manner of

$$D^{*} + A \rightarrow D^{\cdot +} + A^{\cdot -}$$
$$D + A^{*} \rightarrow D^{\cdot +} + A^{\cdot -}$$

These will play a role when photobleaching reactions of xanthene dyes are discussed in Chapter 2.3.5.1.

2.3.4 Quantitative treatment of activation and deactivation processes

To allow for a quantitative treatment of the different mechanisms for excitation and deactivation discussed in the preceding section, one has to introduce values characterizing the dose of light that is necessary for excitation and the efficiency of the different pathways for electronic deactivation. In general, all excitation processes leading to the S_1 and T_1 states are the consequence of the initial absorption of a photon. For an ensemble of molecules, this process can be quantified by the *Lambert–Beer law*:

$$\log\left(\frac{I_0}{I}\right)_{\lambda} = \varepsilon(\lambda) c d \tag{2.72}$$

where I_0 represents the initial intensity of light at wavelength λ, while I denotes its residual intensity after passing a layer of thickness d that contains a dilute solution of the absorbing substance with the (molar) concentration c. ε is the molar absorption coefficient for the wavelength considered. A plot of ε as function of λ is called the *absorption spectrum* of the substance. It compiles the different efficiencies for the absorption of radiation within different ranges of light energy resulting as a consequence of several selection rules for electronic excitation [93].

Due to the proportionality between the absorbance $A = \log(I_0/I)$ and the concentration c of the absorbing substance at given λ, measurements of $A(\lambda)$ by means of UV–vis spectroscopy allow for a quantification of the amount of absorbing substance in a medium. This can be used, for instance, to quantify the conversion of (photo)chemical reactions by quantitative observation of the appearance of reaction products or the corresponding disappearance of educts.

After the absorption of a photon, the magnitude of participation of the different possibilities for deactivation of an excited state are quantified by *quantum yields* which count the relative contribution of each single deactivation pathway related to the entirety of all processes. For radiative deactivation processes, they can also be interpreted as the number of photons emitted relative to the number of photons absorbed. However, they generally quantify the efficiency of the different processes originating from excited states of a molecule. Depending on what kind of process a particular molecular species is favoring, it is titled as fluorescent or phosphorescent dye, quencher, or photosensitizer, for instance.

2.3.5 Important photochemical processes for the present work

2.3.5.1 Photobleaching

As stated above, fluorophores are in principle able to undergo the excitation–emission cycle over and over again — a fact that makes techniques based on fluorescence phenomena sensitive even at low concentrations of fluorescent substance. However, because there is a finite probability to take alternative pathways in the Jablonski diagram, sooner or later each fluorescent species may be converted into a nonfluorescent product by photochemical reactions. Since this leads to a continuous loss of fluorescence intensity, the entirety of all these processes is called *photobleaching*. In principle both the excited singlet as well as the triplet state can be the origin of such reactions as illustrated in Figure 2.11, where bleaching reactions are symbolized by the pathways “bl”. However, due to its significantly longer lifetime, the triplet state is often assumed to be the main origin of bimolecular photobleaching reactions, whereas monomolecular reactions often originate from the high energy singlet state.

As different fluorescent dyes posses different values of their quantum yields for photochemical reactions, they also show different photostability: dyes with lower probabilities for photochemical conversion are able to undergo more fluorescence emission–excitation cycles and appear more stable than such ones that are converted to nonfluorescent forms more easily. However, increasing the intensity and duration of irradiation induces notable photobleaching in almost all cases since in principle more molecules of the ensemble are excited while additionally, every single fluorophore is excited more often.

Basically, numerous types of reactions are able to convert fluorescent molecules into nonfluorescent species. However, as the fluorophores utilized in this work were xanthene derivatives as sketched in Figure 2.12, only those processes involved in the photobleaching of these species shall be introduced here.

Bleaching of xanthene dyes

Regarding a xanthene fluorophore like fluorescein, studies performed by Lindquist and Kasche [94, 95] as well as Usui et al. [96] showed evidence for mainly two types of bimolecular reactions of the excited dye. These are the homoreaction of a dye molecule with another one (D–D mechanism) as well as the heteroreaction of a dye molecule with oxygen (D–O mechanism). Both of them can lead to the production of a semireduced and a semioxidized form of the dye [97, 98] by electron transfer processes as illustrated in Figure 2.14. The origin of all these bleaching reactions has been pointed out to be the excited triplet state [98], whereas the short-living singlet state is not affected even in oxygen saturated solutions [99].

The semioxidized and semireduced radical forms of the dye produced in this manner may then undergo further reactions [100, 101] either reverting to the ground state dye or leading to nonfluorescent photoproducts.

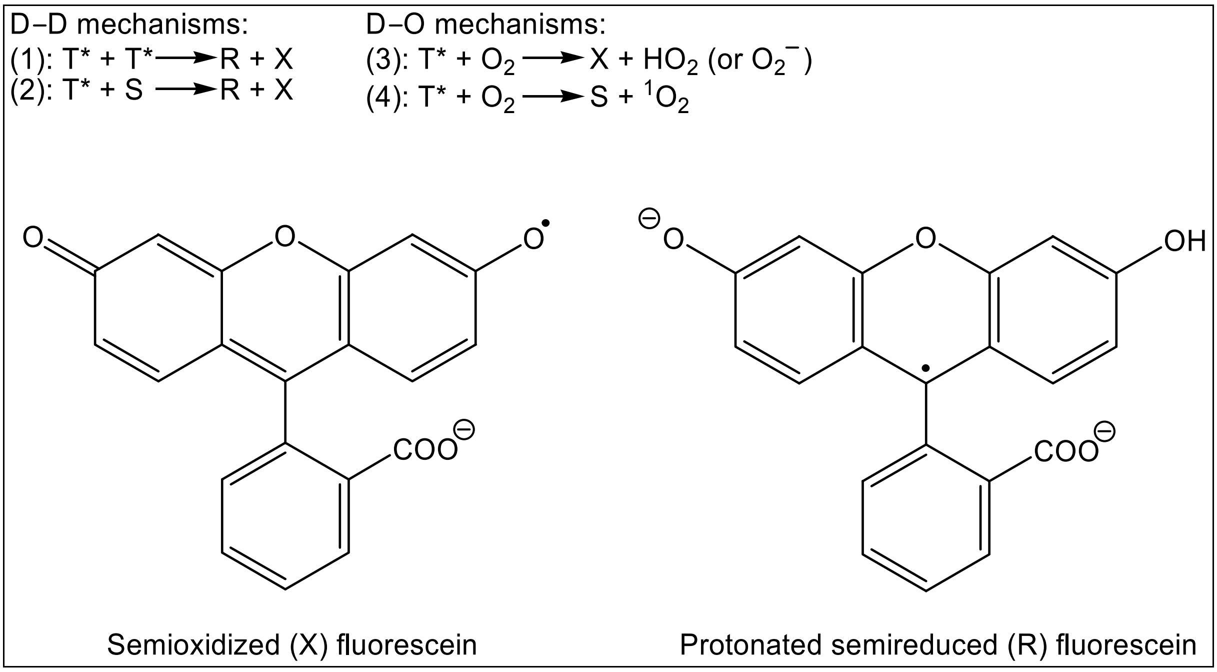

Figure 2.14 Main types of photobleaching reactions [97] for xanthene dyes and structures of the semioxidized (X) and protonated semireduced (R) radical forms of fluorescein [98].

Special attention has to be paid to Reaction (4) in Figure 2.14, which initially does not lead to bleaching of the dye, but produces highly reactive singlet oxygen by a physical triplet–triplet quenching process.[1] In subsequent steps, this reactive species may then attack other dye molecules and convert them into nonfluorescent forms. Since the ground state of the dye molecule involved in Reaction (4) is finally regenerated, this process may reoccur severalfold and, hence, produce singlet oxygen in catalytic manner. It has been estimated for fluorescein that between 10 (pH 12) and 100 (pH 2) singlet oxygen molecules are formed on average before the dye molecule is bleached for itself [95].

---

[1] Note that this type of formation of singlet oxygen has been observed and quantified for a great variety of dye molecules as summarized in ref [102].

D–D mechanisms only play an important role in cases where the mobility of the dye molecules is sufficiently high, whereas in cases of immobilized dyes only D–O mechanisms may occur. However, removal of oxygen may not necessarily solve bleaching problems, because oxygen acts as a triplet quencher, so that its removal could possibly reduce the fluorescence intensity due to significant population of the T_1 state.

Indeed, an effective way to avoid bleaching often is the addition of triplet quenchers and radical scavengers like mercaptoethylamine (MEA), which does not only suppress bleaching reactions via the dyes triplet state but is also able to regenerate semioxidized and semireduced xanthene fluorophores [98].

Newer studies on photobleaching phenomena of more stable dyes like rhodamines have shown evidence for the involvement of two-photon processes [103, 104]. In this respect, it has been argued that the strong dependence of the quantum yield of photobleaching on the intensity of irradiation can only be explained by the assumption of bleaching reactions originating from higher excited states.

2.3.5.2 Photochemical [2+2]-cycloadditions

Under exposure to UV light, olefins are able to undergo various types of photochemical transformations from their excited singlet or triplet states. One important example of such a process is the so-called *[2+2]-cycloaddition*, a reaction yielding cyclobutane derivatives as illustrated in Figure 2.15.

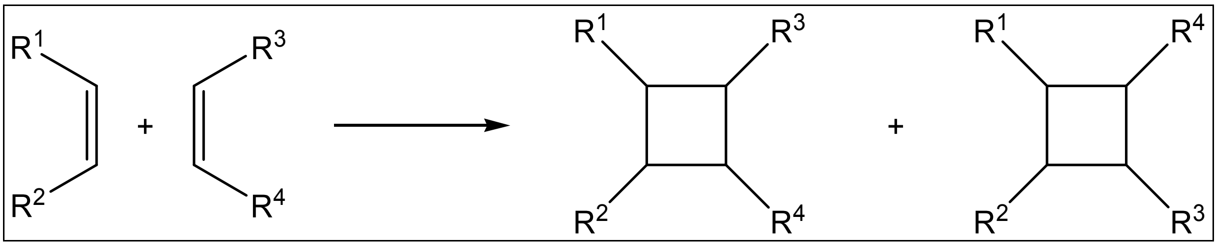

Figure 2.15 Scheme of the [2+2]-cycloaddition of olefins leading to cyclobutane derivatives.

Hereby, two new σ bonds are formed at the expense of two π bonds, which is in principle possible between differently as well as identically substituted olefins. In the latter case, one speaks about *cyclodimerization*. This particular reaction may be underwent by olefins with vicinal conjugated carbonyl groups like α,β-unsaturated ketones, carboxylic acids as well as their esters, amides, and anhydrides. In the last decades, much attention has been paid to the photochemical dimerization of cinnamates [105–108], coumarins [109–112], as well as the derivatives of fumaric and maleic acid [113–118].

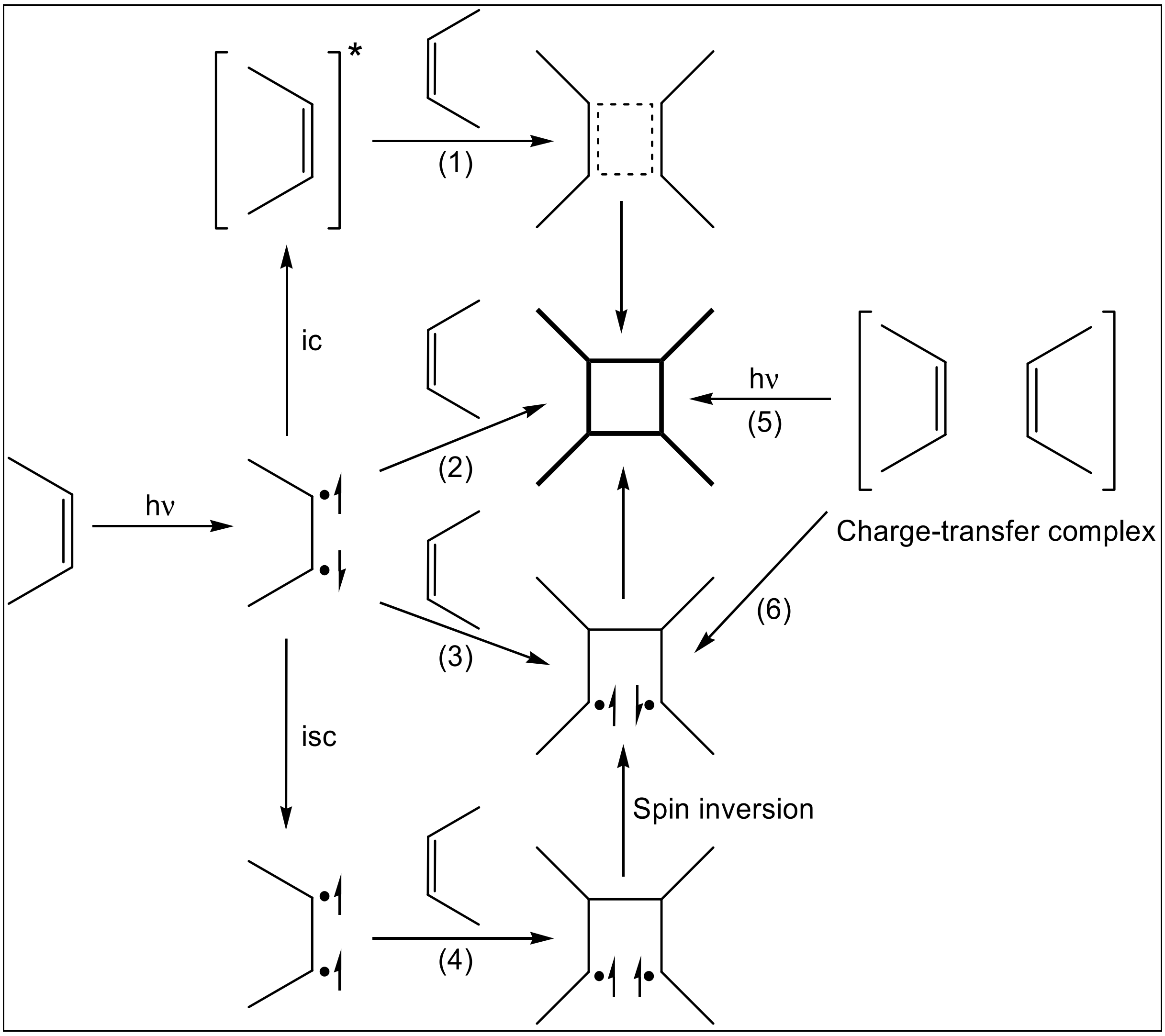

Figure 2.16 Mechanistic schemes of the unsensitized [2+2]-cyclodimerization of olefins. – Adapted from [118].

Photochemical [2+2]-additions can be carried out in unsensitized or in sensitized manner. Figure 2.16 depicts several pathways for the first case, i.e., the *unsensitized* [2+2]-reaction following on direct irradiation of olefins:

After the absorption of a photon, an excited C=C-functionalized molecule populates the vibrational ground state of the electronically excited S_1 state according to Kasha's rule. From there, a reaction along Path (1) results in cyclobutane formation after internal conversion to an excited vibrational state of the S_0 ground state and subsequent collision with a second ground state olefin. By contrast, a one-step process as illustrated by Path (2) leads to cyclodimerization in a concerted action according to the Woodward–Hoffmann rules. As this reaction originates from a *syn* exciplex that is stabilized by secondary orbital-interactions, the resulting cyclodimers are obtained in the stereospecific *cis* form [119–121].

Alternatively, dimerization can also be achieved in a multi-step procedure via the singlet (Path 3) or the triplet state (Path 4). In the latter case, the subsequent reaction occurs in a nonconcerted manner initiated by a long-living triplet exciplex, wherefrom the addition proceeds via an intermediate 1,4-diradical with wide geometry that finally relaxes to the ground state (S_0), where the second bond is formed [93]. Dimers are thus obtained as a mixture of *cis* and (favored) *trans* isomers when originating from a triplet intermediate.

In similar manner, the reaction may also occur from an excited charge-transfer complex in direct (Path 5) or indirect (Path 6) way.

While all of these pathways for [2+2]-cycloaddition actually follow on direct excitation of the olefin, an alternative route to [2+2]-chemistry is opened by *sensitized* mechanisms. This type of reaction is accompanied by some important advantages as compared to the direct irradiation of the olefin — especially in such cases where [2+2]-chemistry is about to be performed in polymer systems:

As in general the energy of the excited singlet state is considerably higher than that of the triplet state, direct excitation of (pendant) [2+2]-reactive groups requires short-wave UV light which, when radiated into a macromolecular system, might cause unwanted degradation of the polymer chains. In such cases, it is therefore advantageous to proceed from the T_1 state, which can be reached by nonradiative energy transfer from an excited, suitably chosen *sensitizer* (cf. Chapter 2.3.3).

The S_1 and T_1 states of the sensitizer molecule have to be closer together with their energies between those of the S_1 and T_1 states of the substrate. Figure 2.17a shows a scheme of such a sensitized process:

After excitation of the sensitizer to its S_1 state by comparatively long-wave UV light, it can undergo intersystem crossing to its slightly lower T_1 state and subsequently transfer the triplet energy to the substrate, from which the dimerization reaction proceeds. This way of effectively achieving a high population of the T_1 state as a starting point for photochemical reactions was described by Hammond et al. [118, 122–125]. Suitable sensitizer molecules for this purpose are aromatic ketones since they generally show a combination of strong spin–orbit coupling, leading to high quantum yield of intersystem crossing, and small energy gaps between the S_1 and T_1 states [119]. In addition, their $n\pi^*$ or $\pi\pi^*$ triplet states provide sufficiently high energy levels and lifetimes [126] to enable effective energy transfer to a substrate.

A slightly different mechanism of sensitized photoreactions was suggested by Schenck et al. [118, 127], who assumed the formation of an intermediate adduct between sensitizer and substrate as depicted in Figure 2.17b. This finally yields a stable diradical being able to undergo further reaction steps subsequently. In the end, the cycloadduct is formed under regeneration of the sensitizer in the manner of homogeneous catalysis.

Besides allowing for mild irradiation conditions by shifting the excitation towards longer wavelengths, the use of a sensitizer has the second advantage that the concentrations of the light-absorbing species and of the reacting species can be adjusted independently. This is necessary in order to keep the absorbance in the utilized wavelength-range small enough to ensure constant irradiation conditions over the whole reaction vessel, particularly when big, yet spatially homogeneous samples are to be prepared. Thus, a fundamental condition for the formation of a homogeneous crosslinking density is fulfilled in cases where [2+2]-additions are employed to generate polymer networks as done in this work.

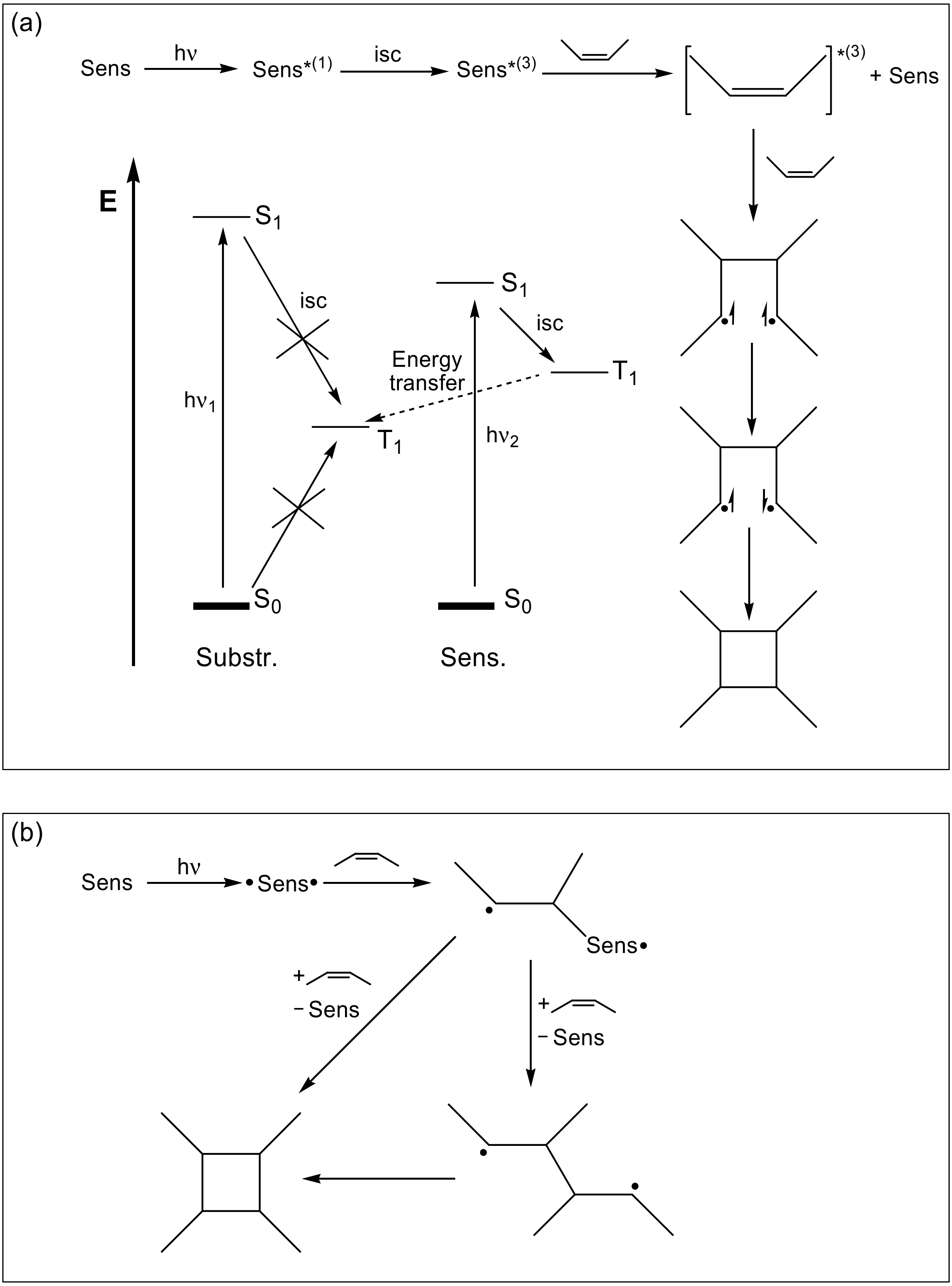

Figure 2.17 Mechanism of the sensitized [2+2]-cyclodimerization according to (a) Hammond et al. [118, 122–125] and (b) Schenck et al. [118, 127].

2.3.5.3 Crosslinking of polymer chains via [2+2]-photochemistry

As indicated in the preceding paragraph, the photodimerization of pendant olefinic sidegroups can serve to crosslink accordingly functionalized polymers. This type of achieving chemical gelation offers some decisive advantages in comparison with corresponding “classical” procedures:

First of all, a photochemical reaction is readily controlled by adjusting the irradiation conditions, and its progress can be stopped, if desired, by interrupting the light exposure. The system can thus be studied and characterized at any intermediate stage on its path from sol to gel, before resuming the irradiation. Furthermore, photochemical crosslinking procedures essentially employ the “clean reagent light”. This aspect can be useful to avoid problems that may be caused by impurities within the networks formed, e.g., due to residual amounts of unreacted chemical crosslinkers.

On these accounts, remarkable attention has been paid to photochemical crosslinking pathways during the last decades, and a variety of suitable moieties has been employed so far. Classical examples for popular sidegroups comprise cinnamates [128–135], coumarins [136, 137], maleic acid derivatives [138–148], and several other functionalities (e.g., see [149, 150]). A detailed discussion about the properties of these groups and the choice of an adequate one to be used for the present work will be given in Chapter 4.1.2.

Applications of photochemical crosslinking procedures may be found in various fields like photolithography, dentistry, printing technology, and the manufacturing of microelectronic devices and surface coatings. Note that also the formation of hydrogels has been performed utilizing [2+2]-photocrosslinking in the scope of several previous works (e.g., [9–13, 132, 136, 144–147]).

2.3.6 Confocal laser scanning microscopy

Microscopic methods belong to the most important experimental techniques in fields like cell and microbiology, as they use the principles of optical imaging to visualize physiological processes in a noninvasive manner within their natural environments. However, since transmitted and reflected light always mirror the entirety of all components of a (biological) sample, it is desirable to blank a certain fraction and to explicitly look at the remaining components in some cases.

As mentioned above, fluorescence light always exhibits the Stokes shift. This, in turn, allows for its effective separation from a primary excitation beam — a principle that is exploited in *fluorescence microscopes*. Such instruments thus allow for the selective detection of fluorescence emitted from microscopic areas of an appropriately labeled specimen, while unlabeled areas are blanked. Hence, a fluorescently labeled fraction or kind of material can be observed in a surrounding which is similar or almost identical to the species of interest, and experimental situations requiring a less important background to be ignored are readily realized. Naturally, labeling always affects the basic properties of the considered material, wherefore it is desirable to keep the amount of label as small as possible. In this respect, fluorescent labels offer the advantage that analytical methods based on fluorescence phenomena are among the most sensitive methods available. Consequently, fluorescence microscopes turned out to be analytical instruments providing a great variety of potential applications. Nowadays, they are routinely used in many branches of biology, chemical engineering, physics, and materials science. Besides the particular advantages that are offered by the use of fluorescence light, a further remarkable enhancement of the optical imaging facilities of microscopes has been introduced by the *confocal principle* [151]:

As commonly known, each optical path of rays has a finite depth of focus. When transparent objects of a certain thickness are observed in a conventional light microscope, the information of interest originating from the focal plane is superimposed by information from planes below and above the focal plane. Confocal microscopes thus intend to cut off all those information and, hence, to solely detect such light that originates directly from the focus. Therewith, the 3-dimensional object under observation is resolved into several confocal section planes which subsequently can be recomposed by a computer. This allows for the collection of highly resolved planar information and the construction of 3-dimensional stacks of images.

Figure 2.18 illustrates the principle of this technique. Basically, a laser serves as light source (1) whose primary beam may additionally be narrowed by a pinhole. The wavelength desired for irradiation of the sample (and for excitation of fluorescence if the setup is operating as fluorescence microscope) can be selected by a blocking filter (not shown). Thereafter, the beam is reflected by a dichroic mirror (2) and focused on the (labeled) specimen (4) by the objective (3).

Fluorescence light is emitted into all directions and recollected by the objective (3). Due to the Stokes shift, it is able to pass the dichroic mirror (2), which separates it from reflected and scattered parts of the excitation beam. After passing another blocking filter for wavelength selection, the light hits the confocal pinhole (5). At this point, almost only such light which originates directly from the focused spot in the focal plane is able to pass, as only this point is imaged directly into the pinhole. Therefore, all information from other areas of the sample (e.g., out of upper and lower planes) is virtually completely cut off. Behind the pinhole, each photon hits a detector (6) which quantifies the intensity of arriving light and passes this information to a computer system. By scanning many points along a line in x-direction and many of such lines in y-direction within the confocal plane, an optical $(x;y)$-section of the sample is constructed. The technical realization of the scanning ability is realized by two oscillating mirrors (7), one for the x- and one for the y-direction. Besides planar scanning, a repetition of the procedure within different planes in z-direction can be used to construct a 3-dimensional stack of images, thus allowing for a view of the object from any user-defined perspective. The realization of the latter feature is simply achieved by variable adjustment of the sample position in z-direction (8).

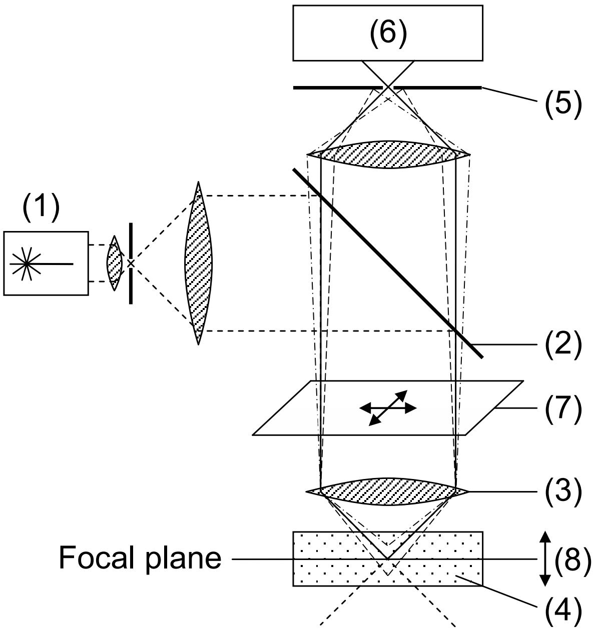

Figure 2.18 Schematic of a confocal laser scanning microscope. – Components:

(1) laser (light source)
(2) dichroic mirror
(3) objective
(4) specimen
(5) pinhole
(6) photomultiplier tube
(7) scanner
(8) z-translation stage

Due to their expedient facilities, confocal laser scanning microscopes are nowadays intensely used for advanced imaging techniques in life sciences and materials science. Moreover, the continuous development of computer-based data engineering led to an increasing use of such instruments as digital systems for measurement and control, coping with tasks of the entire range from imaging of complex 3-dimensional structures to the analysis and quantification of dynamic processes, e.g., by techniques like fluorescence recovery after photobleaching as introduced in the next subchapter.

2.3.7 Fluorescence recovery after photobleaching

With the aid of a confocal laser scanning microscope, one is able to excite fluorescent dyes within a certain region of a sample by irradiation with laser light of appropriate wavelength. If the intensity of irradiation is strongly increased, photobleaching effects as described in Chapter 2.3.5.1 are prone to occur to a notable extent. As therewith especially those fluorophores located in the focal spot are photobleached in selective manner, the generation of special user-defined bleaching geometries is possible. This aspect forms the basis for an experimental technique to quantify the diffusive mobility of fluorescent species in a sample named *fluorescence recovery after photobleaching* (FRAP). It has been introduced by Peters et al. in 1974 [152] and was firstly employed quantitatively to measure diffusion coefficients by Axelrod et al. in 1976 [153].

As stated above, the principle of FRAP is to irreversibly photobleach a certain region within a fluorescently labeled sample by irradiation with a short intense light pulse. Immediately after bleaching, a highly attenuated beam is used to measure the recovery of fluorescence inside the bleached area, which occurs due to the diffusion of unbleached fluorophores from the surroundings. The quantitative analysis of this process yields information about the diffusion coefficient and the fraction of mobile species as illustrated in Figure 2.19.

In the last 30 years, FRAP has evolved as an important and versatile technique to study the dynamics in various systems, such as living cells, membranes, and other biological environments. In polymer physics, photobleaching methods are employed to investigate diffusive processes in macromolecular systems, particularly in networks. The fundamentals of FRAP and some of its applications have been reviewed by Meyvis et al. [154].

Classical ways to analyze FRAP data mainly quantify the *rate of recovery* of fluorescence intensity within a preselected *region of interest* of certain (user defined) geometry (e.g., a circular disc form). Typically, one derives corresponding rate constants by fitting the curve illustrated in Figure 2.19 to a proper theoretical form. Several equations for this purpose have been derived and are to be found in literature (cf. Chapter 3.2.1.1 for further information).

Another important way to realize FRAP experiments is to bleach a *periodic pattern* followed by a subsequent quantification of the recovery process by means of Fourier analysis. However, both methods mentioned are accompanied by some drawbacks: On the one hand, the first type of analysis solely yields a certain time constant of the recovery process, whereas the spatial information needed to calculate a diffusion coefficient has to be added, thus requiring the knowledge of some calibration parameters. On the other hand, the approach of bleaching periodic patterns is only realizable on an above-µm scale of length. To overcome these limitations, a novel approach for the systematic evaluation of spatially resolved FRAP experiments performed on a confocal laser scanning microscope has been developed in the present work and will be introduced and described in detail in Chapter 3.2.

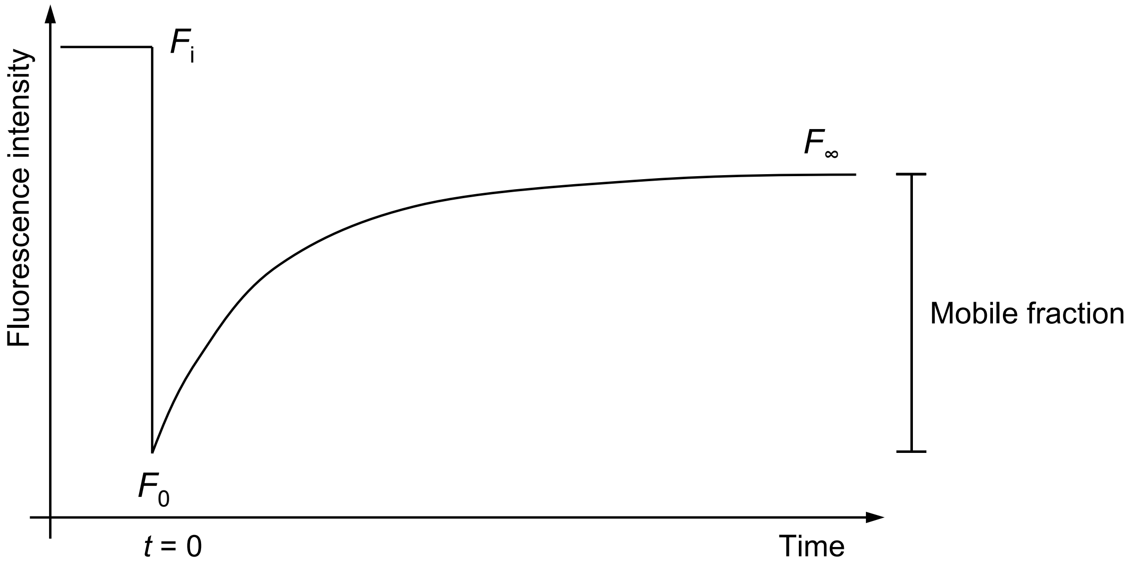

Figure 2.19 Recovery of fluorescence intensity after photobleaching. F_i denotes the initial intensity, whereas F_0 corresponds to the intensity immediately after bleaching. In the long-time limit, fluorescence recovery regains the intensity F_∞. Thus, F_∞/F_i is a measure of the mobile fraction, while the rate of recovery is associated with the translational diffusion coefficient.

3 Preliminary work

As pointed out in Chapter 1, the central aim of the present work was to investigate the structure and dynamics in hydrogel systems formed by photocrosslinking of functionalized polyacrylamide (PAAm). Besides the analysis of the crosslinking procedure and the network architectures themselves, a comprehensive exploration of the diffusive behavior of enclosed linear and spherical tracers was scheduled. For this purpose, it was partially desired to employ such tracer materials which are similar or almost identical to the matrix polymer. This generally requires the usage of suitably labeled probes. It was thus necessary to start with some preliminary work focusing on the synthesis and characterization of such materials, as well as the development of a proper way to analyze corresponding experiments (i.e., FRAP). The following sections present the central issues of these initial investigations, before the main parts of the work are discussed in Chapter 4.

3.1 Labeled tracers

3.1.1 Introduction

The use of fluorescently labeled species is one way of enabling detection or observation of a certain fraction or kind of material in a surrounding which is essentially indistinguishable from the species of interest [155–157]. The study of self-diffusion in semidilute PAAm systems in the scope of the present work thus requires such labeling. Since labeling naturally affects the basic properties of the considered material, it is desirable to keep the amount of labels as small as possible. In that respect, fluorescence labels have the advantage that analytical techniques based on fluorescence are among the most sensitive methods available.

In the context of the present work, it was intended to compare two different types of probes: *flexible polymer chains* and *hard nanoparticles*. Fluorescent forms of the latter are commercially available over a broad range of sizes and spectral characteristics [158]. By contrast, the first type of matter requires a proper synthetic preparation. A suitable route for this as well as an intense characterization of the so-obtained materials will now be discussed.

Moreover, a corresponding set of spherical tracers will be comprehensively characterized. This chapter thus covers the upper-right part of the schedule presented in Figure 1.2, as highlighted in Figure 3.1.

Note that parts of the following investigations have been previously performed in the scope of a former work [159], but shall nevertheless be included into the discussion in order to give a comprehensive view on the possibilities for the preparation of fluorescently labeled PAAm.

3.1.2 Flexible linear tracers

Fluorescence labeling is well established in biochemical research, and a large variety of suitably functionalized fluorescent dyes is available, in particular such which can bind to amine functions [158]. It has been pointed out in a previous work [159] that one can make use of these dyes and adopt the established labeling procedures to generate a broad spectrum of labeled polymers by providing linear PAAm functionalized with *amine moieties*. This offers the special advantage that particular spectroscopic or optical properties can be combined with desired macromolecular characteristics in an independent manner.

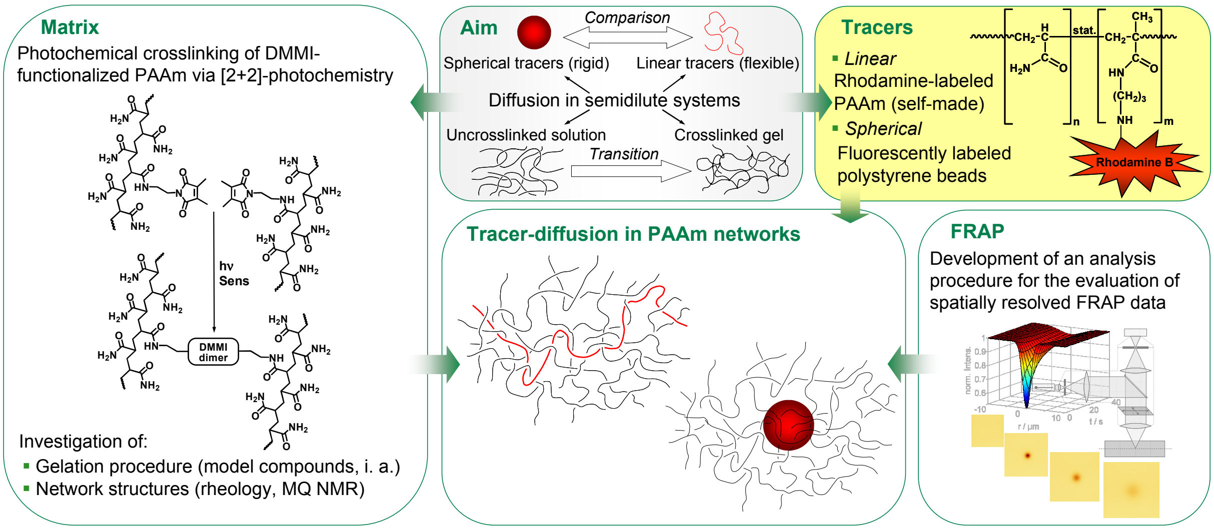

Figure 3.1 Classification of Chapter 3.1 in the context of the present work.

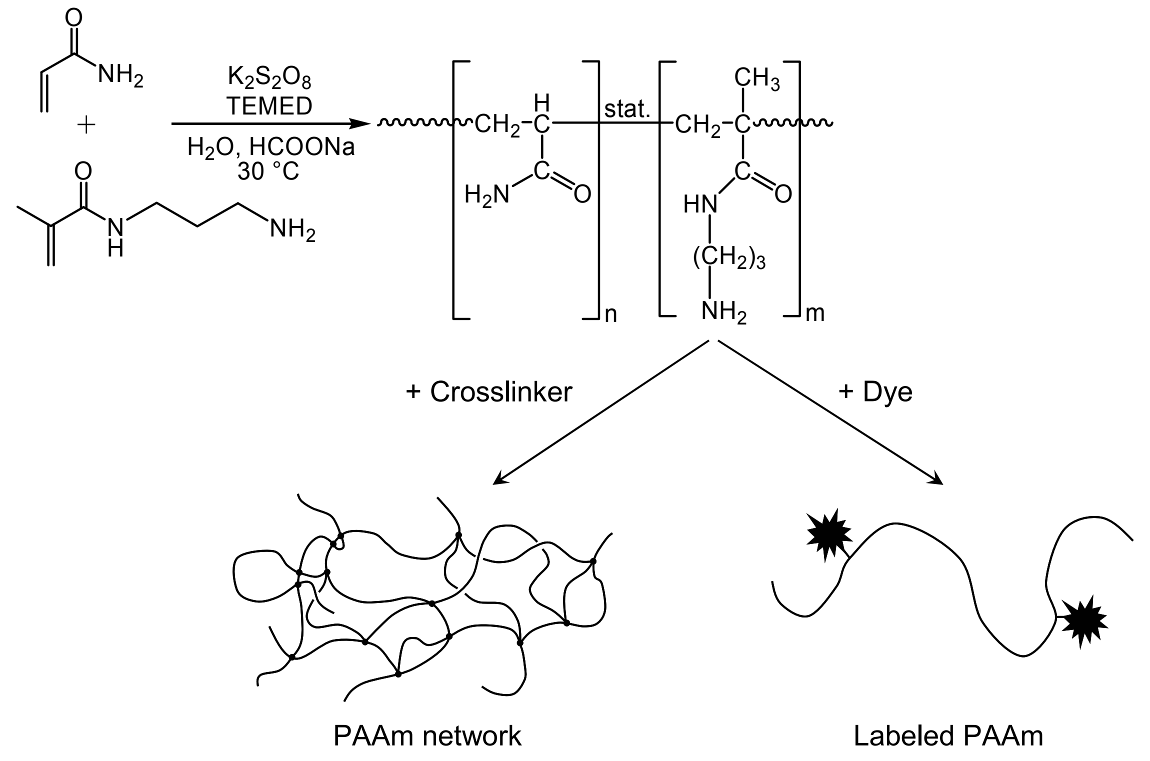

Figure 3.2 Scheme of the copolymerization of AAm with NAPMAAm and illustration of subsequent crosslinking or labeling.

Besides this specific aspect, the preparation of amine-functionalized PAAm as a versatile nucleophilic water-soluble basis material can serve for several other purposes too, e.g., for the facile formation of crosslinked hydrogels. In the scope of the present work, the above-mentioned previous investigation [159] on the preparation of well-defined amine-functionalized PAAm over a wide range of molar masses and the possibilities for a subsequent exhaustive saturation of the pendant amine functionalities with fluorescent dyes was thus pursued and refined correspondingly. A publication of these aspects can be found in ref [160].

Basically, there are two different pathways for the preparation of amine-functionalized PAAm: The functionalization can either be performed in a *polymer analogous reaction* starting from unfunctional PAAm, or a *copolymerization* of acrylamide (AAm) with a suitably chosen comonomer which carries the amine groups can be conducted. As PAAm itself is rather inert, the first method was dismissed.

To carry out the copolymerization, *N*-(3-aminopropyl)-methacrylamide (NAPMAAm) was employed as comonomer. It is readily available, and its α-methyl group is useful to obtain information about the structure and composition of the resulting copolymers by NMR spectroscopy. In the following sections, the copolymerization is discussed in terms of an estimation of the *reactivity ratios* of the monomers, an investigation of the resulting *copolymer structure*, and a study on the influence of sodium formate as a chain transfer agent to control the obtained *molecular weight* and *polydispersity* [161, 162]. Finally, *fluorescence labeling* and—as an example of another interesting application of this versatile basis material—*crosslinking* of the so-prepared amine-functionalized polymers as illustrated in Figure 3.2 is presented.

3.1.2.1 Experimental

Copolymerization

A scheme of the copolymerization of AAm with NAPMAAm utilized in this study is shown in Figure 3.2. The basic recipe for it adopted from Fevola et al. [162] reads as follows:

An aqueous solution of the monomers AAm (Merck) and NAPMAAm hydrochloride (Polysciences) as well as a certain amount of sodium formate (Fluka) was flushed with nitrogen for about 10 min at 30 °C. The total monomer concentration was 0.46 $\mathrm{mol \cdot L^{-1}}$ corresponding to 3–6 wt.-% depending on the composition, and the sodium formate concentration was varied as described below. Exact compositions are specified in Tables 3.1–3.3. The polymerization was initiated by addition of 0.1 mol-% (relating to the total amount of monomers) of potassium peroxodisulfate (Aldrich) and 0.25 mol-% of *N,N,N',N'*-tetramethylethylenediamine (TEMED, Fluka) in the form of small amounts of appropriately concentrated aqueous solutions. Several mechanisms of decomposition of the initiator–accelerator system are discussed in literature [163, 164]. While the reaction was running at 30 °C under nitrogen atmosphere, aliquots were withdrawn from the mixture and dropped into an excess of methanol in order to check for precipitation. This was done every minute in the beginning and at longer intervals if the reaction proceeded slowly.

When a perceptible precipitation was noticed, the reaction was interrupted by precipitation into a tenfold excess of methanol containing about 2 wt.-% of concentrated hydrochloric acid. Conversions achieved by this procedure were about 5% in all cases treated in this work. The corresponding reaction times are listed in Tables 3.1–3.3. The crude product was isolated by filtration, washed with methanol, redissolved in water and dialyzed against water for about ten days. Finally, the purified copolymer was isolated by freeze drying.

Characterization of the obtained material was performed by NMR spectroscopy, size exclusion chromatography (SEC), and solution-viscometry. ^{1}H NMR spectra were recorded on a Bruker Avance 400 digital FT spectrometer at 400 MHz in D_2O (to which all chemical shifts reported in ppm were referenced using $\delta(H_2O) = 4.79$ ppm [165]). SEC measurements were performed by Polymer Standards Service GmbH (PSS Mainz, Germany) utilizing PSS Suprema columns with an eluent composed of 0.1 mol·L^{-1} NaCl + 0.1 vol.-% TFAc. The system was calibrated with pullulan standards, wherefore the achieved molecular weights and polydispersities are quantified as apparent pullulan equivalent values. Measurements of the intrinsic viscosity were made on polymer solutions with concentrations of 0.5, 1, 1.5, and 2 g·L^{-1} at 25 °C with the aid of an Ubbelohde-viscometer with a capillary diameter of 0.36 mm. The solvent employed was an aqueous solution of 0.5 mol·L^{-1} NaCl in each case. Intrinsic viscosities were estimated from Huggins plots. For calculation of the viscosity average molecular weight, Mark–Houwink–Sakurada parameters reported by McCarthy et al. [42c] were used.

Fluorescence labeling

Labeling of the amine-functionalized PAAm with various fluorescent dyes was performed in the following manner:

To a solution of amine-functionalized PAAm with a concentration of 1 g·L^{-1} in 0.01 mol·L^{-1} aqueous Na_2CO_3, a fivefold molar excess, according to the total number of amine moieties in the reaction mixture, of fluorescein isothiocyanate (FITC, isomeric mixture, Fluka), rhodamine B isothiocyanate (RITC, isomeric mixture, Aldrich), or a corresponding succinimidyl ester was added either in crystalline form or as a small amount of a stock solution in an adequate solvent (e.g., water, 0.01 mol·L^{-1} Na_2CO_3, or water-free organic solvents like DMSO or methanol in case of moisture-sensitive dyes like succinimidyl esters). The mixture was stirred for 24 h at room temperature, and afterwards excess dye and other low molecular weight components were removed by extensive dialysis, initially against 0.01 mol·L^{-1} Na_2CO_3 solution and subsequently against distilled water, for about two weeks. Finally, the labeled PAAm was isolated by freeze-drying. All steps mentioned above were performed in the dark.

To quantify the amount of dye attached to the polymer and to check whether its spectroscopic properties were affected by the connection, the labeled product was characterized by UV–vis spectroscopy as well as static and time-resolved fluorescence spectroscopy. UV–vis spectra were recorded on a Jasco V-550 spectrometer, while static fluorescence measurements were performed on a Spex Fluorolog II photon counting spectrometer. Time-resolved fluorescence measurements were carried out by time correlated single photon detection, utilizing a pulsed laser LED at 376 nm (PicoQuant GmbH, Berlin) for fluorescence excitation. All spectroscopic analyses were performed in 1 cm quartz cuvettes (Hellma) utilizing adequately concentrated solutions as specified in the next chapters.

Crosslinking

A second significant application of the amine-functionalized material is its crosslinking to generate tailor-made hydrogels by addition of difunctional reagents which attach easily to the amine moieties. Dicarbonyl compounds like glutaraldehyde work well in this respect. The crosslinking reaction was performed within an oscillating rheometer in order to study the kinetics of gelation as well as the mechanical properties of the final gel.

In a typical procedure for such a crosslinking experiment, a PAAm sample carrying 0.8 mol-% of amine sidegroups and having a molar mass $M_\eta = 230\,000\ \text{g}\cdot\text{mol}^{-1}$ as determined by viscometry was employed. A semidilute solution ($50\ \text{g}\cdot\text{L}^{-1}$) in $0.01\ \text{mol}\cdot\text{L}^{-1}$ aqueous Na_2CO_3 was prepared and homogenized for several days. An amount of glutaraldehyde to achieve an equimolar ratio of carbonyl groups and amine sidegroups in the solution was added, and after short and intense mixing of the components, part of the crosslinking solution was placed on the plate of a Bohlin Gemini rheometer equipped with a cone and plate setup (diameter 40 mm, cone angle 4°). Oscillatory measurements at a frequency of 4 Hz and a stress amplitude of 1 Pa were immediately started. Another part of the crosslinking solution was transferred into a 2 mm quartz cuvette in order to visualize and quantify by fluorescence spectroscopy the chartreuse coloration which occurs upon addition of glutaraldehyde to amines.

3.1.2.2 Results and discussion

Estimate of reactivity ratios and copolymer architecture

To estimate the reactivity ratios r_1 and r_2 of the two monomers utilized here (1 = AAm, 2 = NAPMAAm), a set of low-conversion copolymers with varying monomer compositions was prepared according to the procedure outlined in the experimental part (3.1.2.1). The exact reaction conditions employed are listed in Table 3.1. The range of low fractions of NAPMAAm was studied in great detail because this is of particular interest for the applications of the functionalized material in the scope of the present work. The reaction times were adjusted to limit conversions to about 5% in each case.

The obtained copolymers were analyzed with regard to their monomer ratios by ^{1}H NMR spectroscopy. Figure 3.3 shows the NMR signals together with their allocation to different protons. It is obvious that the signal intensities of protons belonging to NAPMAAm moieties are increasing with rising amount of NAPMAAm in the feed, while the signals addressed to AAm become weaker.

According to common usage, f_2 denotes the mole fraction of NAPMAAm in the monomer mixture, while F_2 is its mole fraction in the resulting polymer. For a quantitative determination of F_2, the NMR spectra were normalized to NAPMAAm by simultaneously setting the integrals of Signals **3**, **5**, and **7** to values of 3, 2, and 2, respectively. The integral of Signal **1** (methine protons) then represents the amount of AAm per mole of NAPMAAm (= $1/F_2 - 1$). It was either estimated directly or deduced from the integral of the group (**1**,**4**,**6**,**2**) in the following manner: *Integral*(**1**) = (*Integral*(**1**,**4**,**6**,**2**) − 4)/3. Performing this procedure for each of the prepared samples yields the results compiled in Table 3.1. Figure 3.4 shows the copolymerization diagram, F_2 vs. f_2, indicating that azeotropic copolymerization occurs at about 80% of NAPMAAm.

To determine the reactivity ratios, the method of Kélen and Tüdös was applied; see ref [166] for details. The inset in Figure 3.4 demonstrates that the corresponding linearization of the data works quite well. From the linear fit, the reactivity ratios were determined to be

$$r_1 = 0.49 \qquad \text{and} \qquad r_2 = 0.85$$

The solid line in Figure 3.4 was calculated with these values.

In order to synthesize copolymers having a predetermined composition with fairly low fractions of NAPMAAm and to verify the values of r_1 and r_2 in this interesting region, four copolymerizations were performed where the concentration of NAPMAAm in the reaction mixture was calculated and adjusted to yield mole fractions of 4, 1, 0.5, and 0.1% in the resulting polymers. The corresponding quantities and experimental parameters are summarized in Table 3.2. Characterization of the obtained copolymers by ^{1}H NMR spectroscopy in the manner described above proved the consistency of the obtained values by showing close agreement between anticipated and actually obtained compositions.

Table 3.1 (a) Reaction mixtures for low-conversion copolymerizations of AAm with NAPMAAm hydrochloride in 100 mL distilled water under addition of 1.44 mmol of sodium formate and (b) ^{1}H NMR estimations of NAPMAAm-fractions in the resulting products in order to estimate the reactivity ratios.

(a)

Sample name	**mol-%$_{\text{AAm}}$**	n_{AAm} mmol	**mol-%$_{\text{NAPMAAm}}$**	n_{NAPMAAm} mmol	**Reaction time**[a)] min
AAm98C02	98	45.08	2	0.92	6
AAm95C05	95	43.70	5	2.30	8
AAm92C08	92	42.32	8	3.68	6
AAm90C10	90	41.40	10	4.60	10
AAm88C12	88	40.48	12	5.52	8
AAm85C15	85	39.10	15	6.90	8
AAm82C18	82	37.72	18	8.28	10
AAm80C20	80	36.80	20	9.20	10
AAm75C25	75	34.50	25	11.50	15
AAm70C30	70	32.20	30	13.80	20
AAm60C40	60	27.60	40	18.40	25
AAm50C50	50	23.00	50	23.00	40
AAm30C70	30	13.80	70	32.20	120
AAm10C90	10	4.60	90	41.40	120

[a] Reaction times were adjusted to give conversions around (5 ± 1)% in each case.

(b)

Sample name	**Integral of the methine signal in ^{1}H NMR spectrum** rel. number of protons	**Fraction of NAPMAAm in the copolymer** mol-%
AAm98C02	23.922	4.01
AAm95C05	9.728	9.32
AAm92C08	6.066	14.15
AAm90C10	4.802	17.23
AAm88C12	4.187	19.28
AAm85C15	3.329	23.10
AAm82C18	2.733	26.78
AAm80C20	2.492	28.64
AAm75C25	1.937	34.04
AAm70C30	1.514	39.78
AAm60C40	1.089	47.85
AAm50C50	0.770	56.50
AAm30C70	0.413	70.79
AAm10C90	0.123	89.02

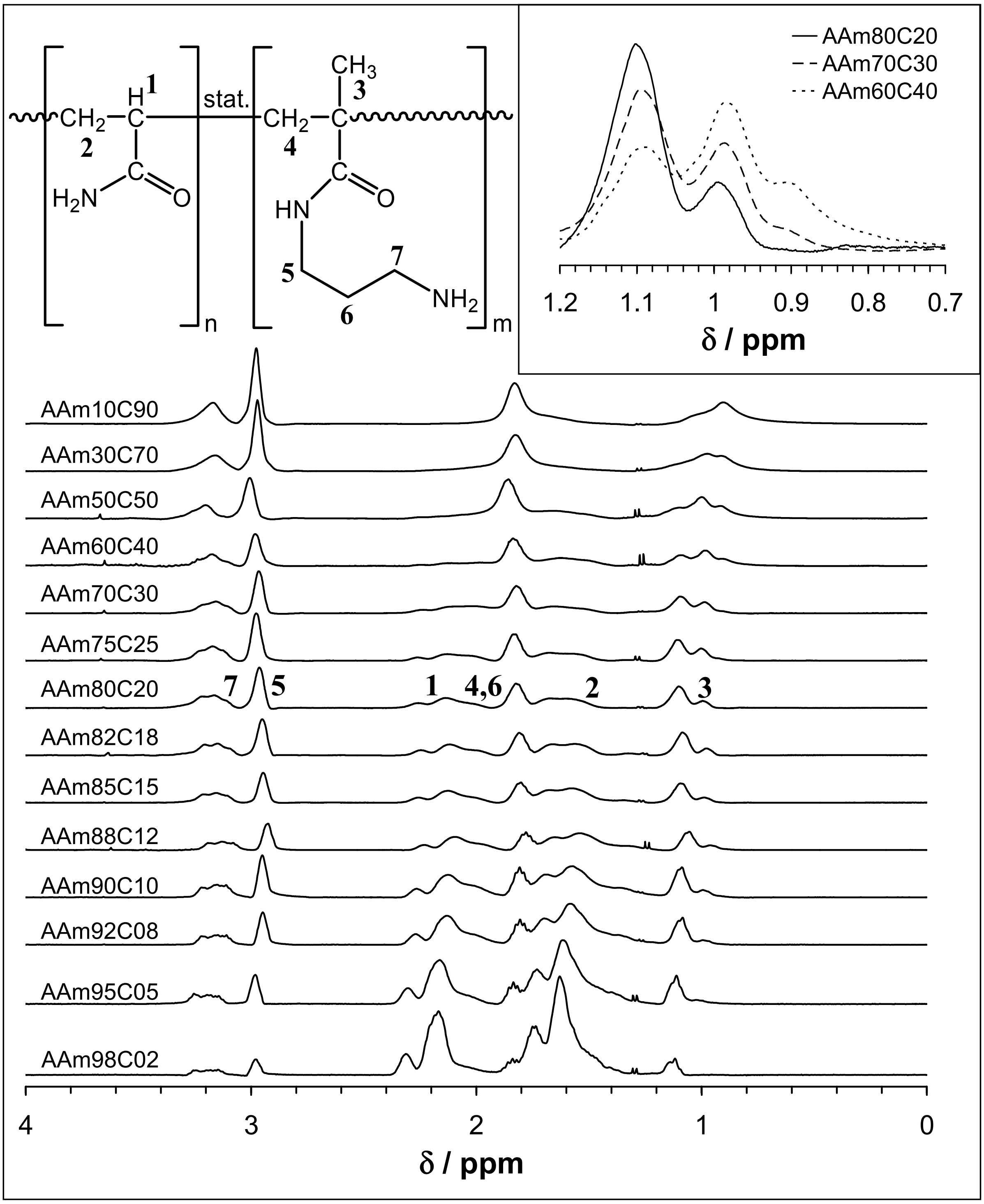

Figure 3.3 400 MHz ^{1}H NMR spectra (D_2O) of low-conversion AAm–NAPMAAm copolymers. – Numbers **1**–**7** marking particular protons in the copolymer structure are indicated for the corresponding NMR signals of sample AAm80C20. The inset shows the signal of the methyl group for three particular copolymer compositions. All spectra are normalized to the same total integral intensity.

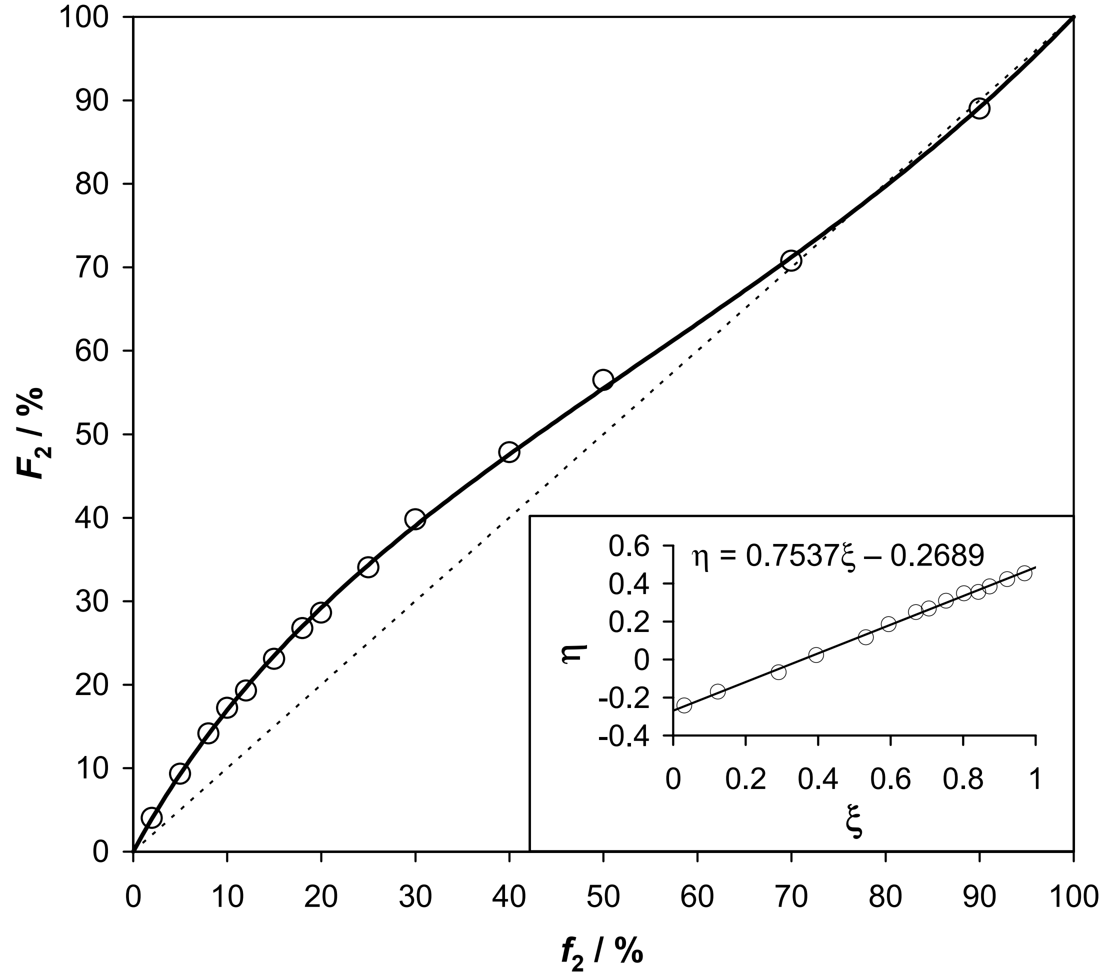

Figure 3.4 Copolymerization diagram for the system AAm/NAPMAAm. f_2 denotes the fraction of NAPMAAm in the reaction mixture, whereas F_2 represents its fraction in the low-conversion product. Circles are analytical results, the full line is calculated with $r_1 = 0.49$ and $r_2 = 0.85$. The inset shows the linearization of the data according to Kélen and Tüdös [166].

Table 3.2 (a) Reaction mixtures and (b) product characterizations for low-conversion copolymerizations of AAm with NAPMAAm hydrochloride in 100 mL distilled water under addition of 1.44 mmol of sodium formate in order to test the obtained reactivity ratios of $r_1 = 0.49$ and $r_2 = 0.85$. Conversions achieved were about 5% in each case.

(a)

Sample name	**Desired fraction of NAPMAAm in the copolymer**	**Composition of the reaction mixture**				
		mol-%$_{AAm}$	n_{AAm}	**mol-%$_{NAPMAAm}$**	$n_{NAPMAAm}$	**Reaction time**
	mol-%		mmol		mmol	min
PAAm-C04	4.0	97.97	45.07	2.03	0.93	6
PAAm-C01	1.0	99.51	45.78	0.49	0.22	6
PAAm-C0.5	0.5	99.76	45.89	0.24	0.11	6
PAAm-C0.1	0.1	99.95	45.98	0.05	0.02	6

(b)

Sample name	**Desired fraction of NAPMAAm in the copolymer**	**Characterization of the resulting low-conversion products**	
		Integral of the methine signal in ^{1}H NMR spectrum	**Fraction of NAPMAAm in the copolymer**
	mol-%	rel. number of protons	mol-%
PAAm-C04	4.0	23.922	4.0125
PAAm-C01	1.0	98.620	1.0038
PAAm-C0.5	0.5	198.970	0.5001
PAAm-C0.1	0.1	990.830	0.1008

A comment is appropriate on the shape of the signal of the methyl protons (Signal **3**) in the NMR spectrum. Figure 3.3 shows that at higher comonomer fractions, a second peak firstly appears at 1.0 ppm besides the original one at 1.1 ppm. At still higher amounts of NAPMAAm, a third signal shows up at 0.9 ppm, and the high-field peaks become stronger at the expense of the original one as the concentration of NAPMAAm is rising (cf. inset in Figure 3.3). These signals can be addressed to isolated comonomer units (1.1 ppm) and sequences of two (1.0 ppm) or more (0.9 ppm). The observation that the high-field peaks only occur at high fractions of NAPMAAm proves that there is *no tendency for block formation*. The appearance of pairs or longer sequences of NAPMAAm merely follows simple statistics. This is in agreement with the determined r-values, which are both below 1.

Many possible applications for the amine-functionalized PAAm (like the two examples mentioned in this chapter) require functionalization degrees below 3 mol-% and a *random distribution* of the amine functionalities along the polymer chain. The determination of the copolymerization parameters and the (qualitative) analysis of the methyl peak in the NMR spectra independently prove that this is achieved by the copolymerization of AAm with low amounts of NAPMAAm.

Molecular weight control

Sodium formate is well-known to be a suitable chain transfer agent for AAm polymerization [161, 162]. To prepare a certain range of molar masses, the concentration of HCOONa was systematically varied from 0.03 to 1 mole per mole of monomers.[1] The ratio of NAPMAAm to AAm in the reaction mixture was kept at 0.049 mol-% in order to obtain low-conversion copolymers with 0.1% of amine moieties, according to the reactivity ratios estimated above. In Table 3.3, the exact compositions and reaction times for these experiments are listed together with relevant analytical results.

Characterization of the obtained products by ^{1}H NMR spectroscopy revealed that all obtained products show the desired comonomer fraction of about 0.1% within experimental error. Size exclusion chromatography yielded the resulting molecular weight distributions whose characteristic moments are also listed in Table 3.3. The data show that a low amount of sodium formate produces high molecular weights with M_W above 2 000 000 g·mol^{-1} accompanied by relatively high polydispersities. However, upon increase of the amount of chain transfer agent up to an equimolar ratio, M_W drops to about 200 000 g·mol^{-1} and the polydispersity comes close to the theoretical limit of 2. These results show that sodium formate can be used to control the molecular weight of the amine-functionalized PAAm in a certain range by the method described here, although quite high amounts are required when low molar mass polymers are sought.

---

[1] In the complete absence of sodium formate, a tendency to microgel formation was observed, and such syntheses were not included.

Table 3.3 (a) Reaction mixtures and (b) product characterizations for low-conversion copolymerizations of AAm with NAPMAAm hydrochloride in 800 mL distilled water utilizing different amounts of sodium formate.

(a)

Sample name	n_{AAm} mmol	n_{NAPMAAm} mmol	n_{HCOONa} mmol	$n_{\mathrm{HCOONa}}/n_{(\mathrm{AAm + NAPMAAm})}$	**Reaction time**[a)] min
PAAm-C0.1-1	367.82	0.18	11.5	0.031	8
PAAm-C0.1-2	367.82	0.18	57.5	0.156	30
PAAm-C0.1-3	367.82	0.18	115	0.313	50
PAAm-C0.1-4	367.82	0.18	230	0.625	50
PAAm-C0.1-5	367.82	0.18	368	1.000	70

[a] Reaction times were adjusted to give conversions around (5 ± 1)% in each case.

(b)

Sample name	**Fraction of NAPMAAm in the copolymer** mol-%	M_{N}[b)] g·mol^{-1}	M_{W}[b)] g·mol^{-1}	$M_{\mathrm{W}}/M_{\mathrm{N}}$	[η] mL·g^{-1}	M_{η}[b)] g·mol^{-1}
PAAm-C0.1-1	0.11	557 500	2 550 000	4.6	415.65	1 300 000
PAAm-C0.1-2	0.09	423 000	1 280 000	3.0	253.38	670 000
PAAm-C0.1-3	0.13	232 000	590 000	2.5	170.72	400 000
PAAm-C0.1-4	0.09	134 000	348 500	2.6	115.74	240 000
PAAm-C0.1-5	0.12	88 350	201 000	2.3	75.03	130 000

[b] Number and weight average molecular weights (M_{N} and M_{W}) were obtained as apparent pullulan equivalent values by SEC. Viscosity average molecular weights (M_{η}) were calculated from the intrinsic viscosities [η] in polymer solutions in 0.5 mol·L^{-1} aqueous NaCl at 25 °C with the aid of Mark–Houwink–Sakurada parameters as reported by McCarthy et al. [42c].

Fluorescence labeling

Polymers labeled with fluorescent dyes were required for the present work as measurements of tracer dynamics in networks were intended to be performed by FRAP; cf. Chapter 4.2. In biochemistry, the targeted labeling of, e.g., proteins via their amine functionalities is quite common, and various fluorescent dyes carrying appropriate reactive groups such as isothiocyanates or succinimidyl esters are commercially available [158]. The procedures for labeling amine moieties are well documented, e.g., for proteins [167] or synthetic polymers [155]. For the present work, such a procedure was adopted to achieve fluorescence labeling of the AAm copolymers. Figure 3.5 shows the corresponding reaction scheme. In the following section, the spectroscopic properties of some polymers labeled with FITC and RITC are presented.

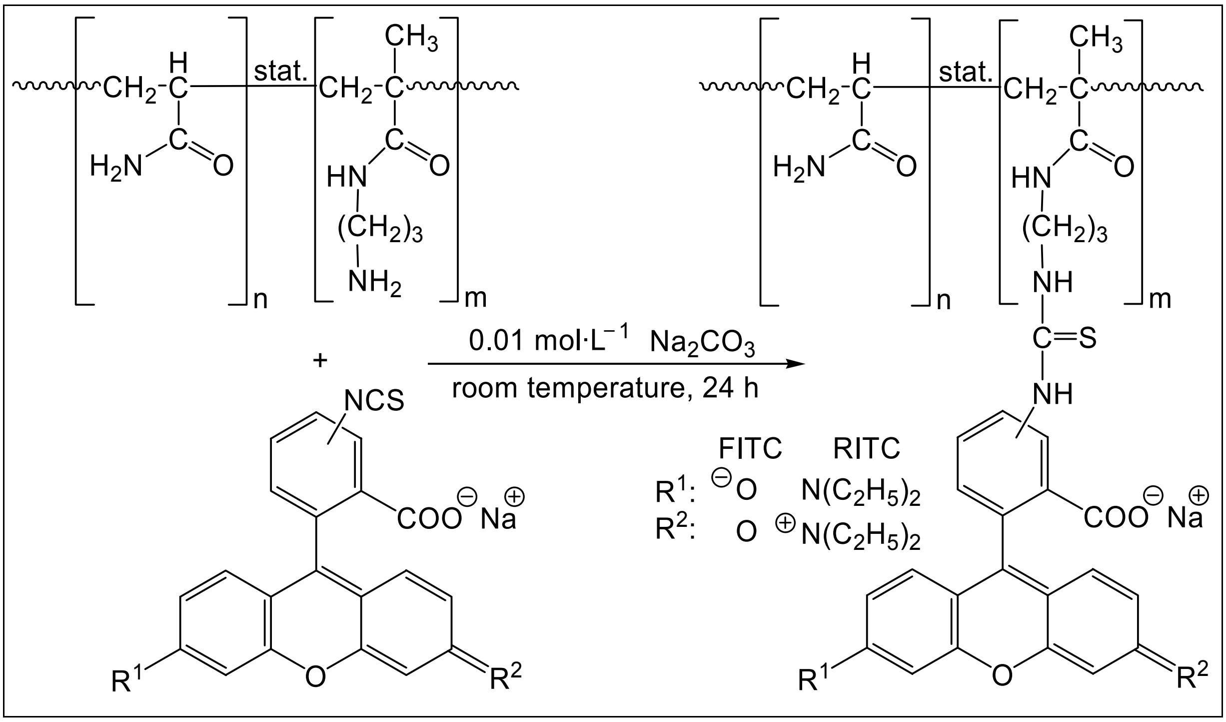

Figure 3.5 Reaction scheme for the attachment of FITC or RITC to AAm–NAPMAAm copolymers.

Figure 3.6 shows normalized fluorescence spectra of the FITC- and RITC-labeled sample PAAm-C0.1. This is a PAAm carrying 0.1 mol-% of amine groups and having a viscosity-average molar mass M_η of 1.4 million g·mol^{-1}. The spectra of the pure dyes are depicted for comparison. Spectra were recorded on solutions with concentrations of 1 g·L^{-1} of labeled PAAm-C0.1 or 5 µmol·L^{-1} of pure dye, respectively, and the solvent was 0.01 mol·L^{-1} aqueous Na_2CO_3 when the chromophore was fluorescein and deionized water when the chromophore was rhodamine B. In both cases there is no evidence for any perceptible effect on the dyes' spectral properties upon their linkage to the polymer. The spectra show the *same excitation and emission behavior* with maxima at λ_{ex} = 494 nm and λ_{em} = 519 nm for the case of FITC and the labeled FITC–PAAm, as well as λ_{ex} = 558 nm and λ_{em} = 583 nm for RITC and the labeled RITC–PAAm. *Fluorescence lifetimes* were also determined and remained constant at 3.8 ns (fluorescein) and 1.6 ns (rhodamine B), respectively. UV–vis *absorbance* measurements gave identical spectra for the free and attached dyes in each case. These findings demonstrate that standard optical parameters and setups can be employed when working with the obtained fluorescently labeled PAAm.

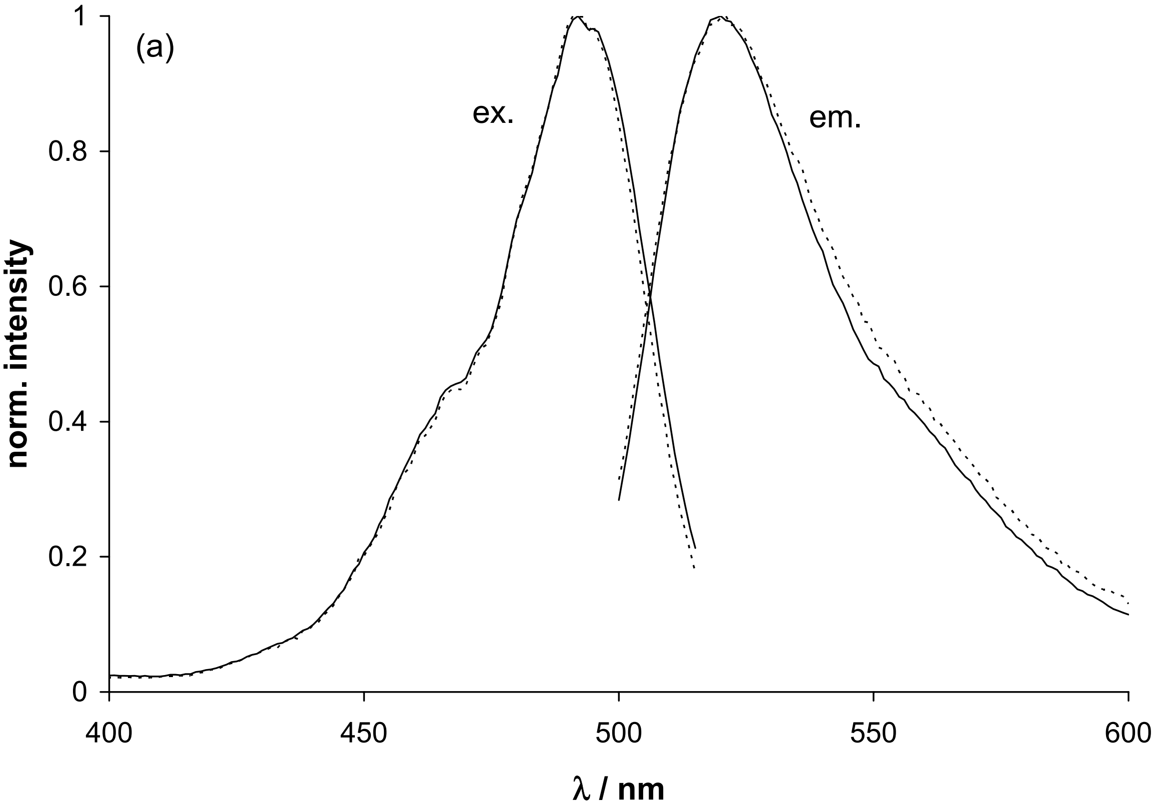

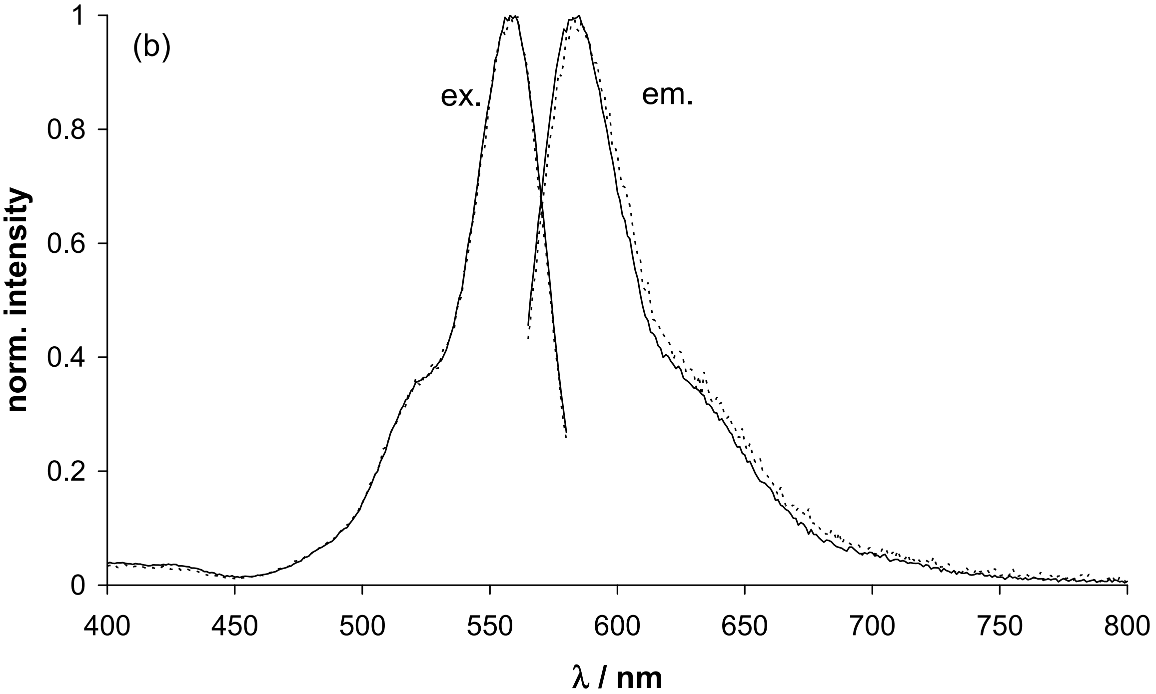

Figure 3.6 Fluorescence spectra of FITC (a) and RITC (b) (dotted lines) and of the corresponding labeled polymers (full lines). – Concentrations are 5 µmol·L^{-1} of free dye and 1 g·L^{-1} of labeled PAAm-C0.1 in 0.01 mol·L^{-1} Na_2CO_3 (a) or in aqueous solution (b).

To estimate the achieved degree of labeling, UV–vis absorbance values were used to calculate the amount of fluorophores within a dilute polymer solution. The molar absorption coefficients of the dyes were previously determined:

$\varepsilon_{\mathrm{FITC}}$ = 77500 L·mol^{-1}·cm^{-1} (λ = 494 nm, 0.01 mol·L^{-1} Na_2CO_3)
$\varepsilon_{\mathrm{RITC}}$ = 71100 L·mol^{-1}·cm^{-1} (λ = 558 nm, water)

in good agreement with literature data [155, 158]. Comparison of the amount of fluorophores determined by UV–vis absorbance with the amount of amine functionalities deduced from the NMR results allows a calculation of the relative degree of labeling. For an extensive number of labeled polymers, Table 3.4 shows such data. The results evidence almost quantitative conversion (93–100%) of the amine functionalities with the fluorescent dyes. This indicates the *high efficiency* of the described labeling procedure as well as the *stability of the linkage* between polymer and dye, which was not hydrolyzed during extensive dialysis over several weeks.

Similar results were achieved when dyes with other anchor groups (e.g., succinimidyl esters) were utilized for labeling (results not shown here). This reveals that a broad diversity of chromophores can be attached to the functionalized PAAm in a facile and effective manner (provided they are sufficiently water-soluble), yielding the possibility to prepare fluorescent PAAm in any spectral range desired.

Table 3.4 Characteristic data of labeled polyacrylamides. A_{max} denotes the absorbance at λ_{max}, which yields c_{Dye} according to the Lambert–Beer law; eq (2.72). $c_{\mathrm{amine\ moieties}}$ was calculated from the copolymer compositions estimated by NMR spectroscopy.

Sample name	**c_{sample} in test-solution** g·L^{-1}	**A_{max}**	**c_{Dye} in test-solution** µmol·L^{-1}	**Fraction of NAPMAAm in the copolymer** mol-%	**$c_{\mathrm{amine\ moieties}}$ in test solution** µmol·L^{-1}	**Relative degree of labeling** %
FITC-labeled samples:						
PAAm-C0.5	0.5	2.9011	37.44	0.50	38.37	98
PAAm-C0.1	1.0	1.0763	13.89	0.10	14.05	99
RITC-labeled samples:						
PAAm-C0.1	1.0	0.9296	13.08	0.10	14.05	93
PAAm-C0.1-1	1.0	1.1003	15.48	0.11	15.48	100
PAAm-C0.1-2	1.0	0.8412	11.83	0.09	12.65	94
PAAm-C0.1-3	1.0	1.2381	17.42	0.13	18.25	95
PAAm-C0.1-4	1.0	0.8579	12.07	0.09	12.65	96
PAAm-C0.1-5	1.0	1.1729	16.50	0.12	16.85	98

Crosslinking

Crosslinking of the functionalized PAAm by glutaraldehyde as another example of the great versatility of this material was performed in semidilute solution and monitored by rheology as described in the experimental part. The principle of the underlying reaction is depicted in Figure 3.7, whereas Figure 3.8 displays the rise of both components of the complex shear modulus, *G*' and *G*", with reaction time in a typical experiment. The concentration of the solution was 50 $g \cdot L^{-1}$, which is about five times the overlap concentration, and the copolymer contained 0.8 mol-% of amine groups. An equimolar amount (with regard to aldehyde groups) of glutaraldehyde was used and the reaction was carried out at 25 °C in 0.01 $mol \cdot L^{-1}$ Na_2CO_3.

Figure 3.8 shows that the storage modulus *G*' rises steeply in the beginning of the experiment. After three minutes, the *G*'-curve intersects the *G*"-curve, a fact often (not quite correctly [50]) taken as an indication of macroscopic gelation. *G*' and *G*" amount to only 7.6 Pa at this point. Hence, a very weak macroscopic network is initially formed. The storage modulus *G*' rises for more than two decades in the first 1000 s but does not level off, so that even after 10 000 s, where a value of the order of 300 Pa is attained, *G*' keeps increasing very slowly. By contrast, *G*" remains at about 10 Pa. This shows that the system behaves predominantly elastic.

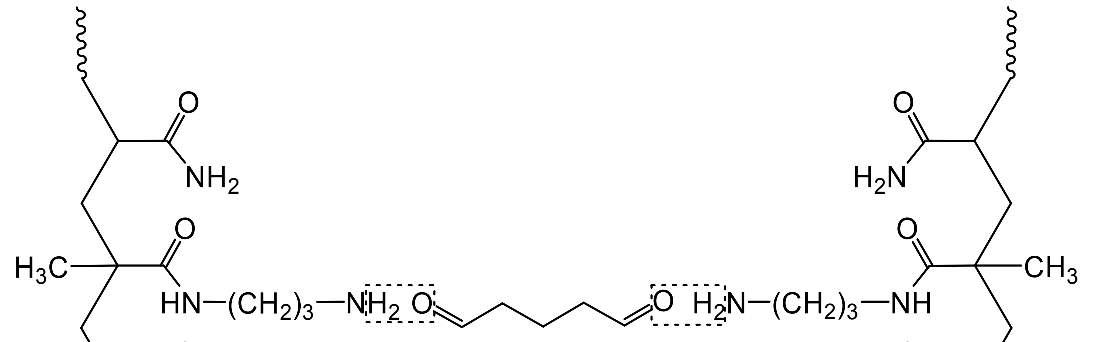

Figure 3.7 Schematic of the crosslinking reaction between amine-functionalized PAAm and glutaraldehyde.

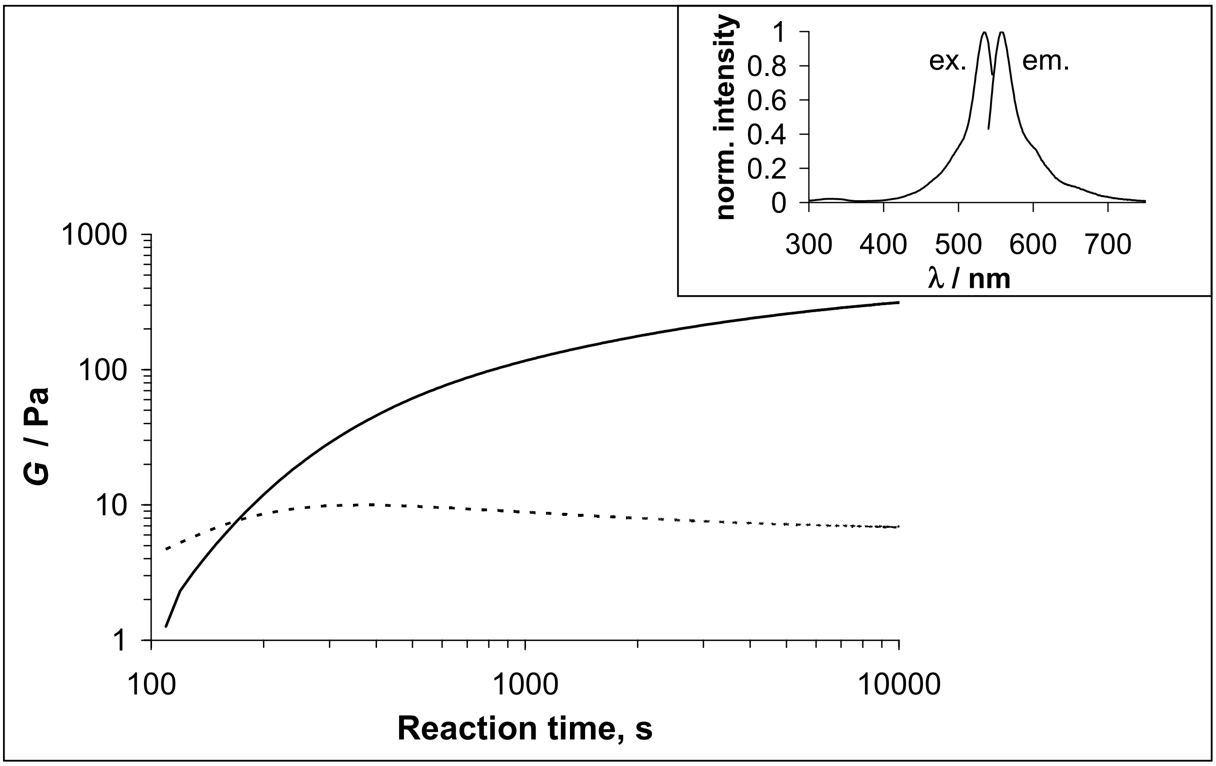

Figure 3.8 Course of the moduli *G*' (full line) and *G*'' (dotted line) during crosslinking of a semidilute solution containing 50 g·L^{-1} of functionalized PAAm in 0.01 mol·L^{-1} Na_2CO_3 and an equimolar amount of glutaraldehyde relative to the number of amine moieties. $T = 25$ °C. The inset shows the fluorescence spectra appearing immediately after mixing.

The theoretical modulus calculated from eq (2.31) under assumption that all amine moieties were linked via glutaraldehyde in a way leading to elastically effective network chains would be around 15 kPa. The fact that the actual modulus is far lower means that most of such linkages are intramolecular linkages (leading to elastically ineffective loops etc.) as opposed to intermolecular linkages. This is a common feature in rather dilute systems, and the low degrees of crosslinking efficiency are typical under such conditions [168]. However, they are still higher than those obtained by crosslinking copolymerization processes.

The reaction between amine and aldehyde groups depends decisively on the pH of the solution. The pH established by a 0.01 mol·L^{-1} Na_2CO_3 solution seems to be an optimum; changing the Na_2CO_3 concentration to either 0.1 mol·L^{-1} or 0.001 mol·L^{-1} leads to markedly slower gelation kinetics.

As soon as glutaraldehyde is added to the amine-functionalized PAAm solution an intense chartreuse color appears and persists, which is known to be due to fluorescence resulting from the linkage of just one of the aldehyde groups to an amine [169]. The corresponding fluorescence spectra are depicted in the inset of Figure 3.8.

3.1.3 Rigid spherical tracers

Fluorescently labeled *microspheres* are commercially available over a broad range of sizes from ~20 nm up to several microns with a variety of spectral properties [158]. For the present work, red-labeled (i.e., rhodamine-analogous-colored) spheres with diameters of about 20–100 nm were utilized in the scope of Chapter 3.2 and 4.2. These particular probes were chosen because their sizes and spectral features correspond closely to those of the linear tracers in aqueous medium. The following sections present the results of a comprehensive characterization of the spheres performed with the aid of various experimental techniques.

3.1.3.1 Experimental

Samples

Red-fluorescent carboxylate-modified polystyrene microspheres of type "580/605" with nominal diameters of 24, 40, and 100 nm were purchased as aqueous suspensions with concentrations of 2 or 5 wt.-% solids from Molecular Probes (Eugene). Characterizations of the particle sizes were performed by dynamic light scattering, ultracentrifugation, and atomic force microscopy. (Corresponding results obtained by FRAP will be added in Chapter 3.2 and 4.2.) Furthermore, UV–vis and fluorescence spectroscopy were employed to characterize the spectral properties of the spheres and to check whether equal masses of them show equal fluorescence intensities.

Spectral characterization

UV–vis spectra of the labeled microspheres were measured on a Jasco V-550 spectrometer. For this purpose, aqueous microsphere-suspensions were diluted to concentrations of 0.05 wt.-% solids and displaced in 1 cm quartz-cuvettes, respectively. Fluorescence spectra of the same solutions were recorded on a Spex Fluorolog II photon counting spectrometer.

Analyses of the particle sizes

Ultracentrifugal analyses

Ultracentrifugal analyses (UA) were performed on a commercial analytical ultracentrifuge of type OPTIMA XL-A 70 from Beckmann–Coulter detecting the UV–vis absorbance of the fluorescent microsphere-suspensions. Estimations of the sedimentation coefficients S were conducted by several measurements at three different rotational velocities (8 000–12 000 rpm) at 25 °C. From these values, the radii of the particles can be calculated [170, 171] via

$$r = \frac{1}{2}\sqrt{\frac{18\eta_{\mathrm{D}} S}{\rho_{\mathrm{P}} - \rho_{\mathrm{D}}}} \tag{3.1}$$

where η_{D} denotes the dynamic viscosity of the dispersing medium (0.89 mPa·s), ρ_{D} its density (0.997 $\mathrm{g{\cdot}mL^{-1}}$), and ρ_{P} the density of the particles (1.054 $\mathrm{g{\cdot}mL^{-1}}$).

Dynamic light scattering

Dynamic light scattering (DLS) was measured at 25 °C on an ALV/CGS-3-compact goniometer system S/N: CGS3-A0-028 from ALV-GmbH using a HeNe laser at $\lambda = 632.8$ nm for irradiation as well as an ALV/LSE 5003 correlator. After filtering and diluting the microsphere stock solutions to concentrations of 0.002 wt.-%, respectively, several measurements were performed at detection-angles of 60°, 90°, and 120°. Intensity-weighted distributions of the hydrodynamic radii were deduced from the correlation curves by simple fitting procedures as provided by the ALV-software. Results were averaged to determine the mean hydrodynamic particle radii.

Atomic force microscopy

To quantify the static (i.e., the non-hydrodynamic) particle diameters of the spheres, surface imaging via TappingMode atomic force microscopy (AFM) was performed with a Nanoscope III (Digital Instruments). Ultrasharp, noncontact silicon cantilevers (Pointprobes type NCH-W nanosensors, Sunnyvale, CA, USA) with resonance frequencies varying between 260 and 330 kHz were applied. Cantilever and tip were cleaned by immersion in and rinsing with ethanol.

Prior to use, mica plates were freshly cleaved by applying sticky tape yielding clean surfaces. Samples of the 24 and 40 nm microspheres were prepared by placing the appropriate mica plates for 5 min upright into a dilute microsphere-suspension with a concentration of about 0.5 wt.-%. Placing them upright and not horizontal avoids potential artifacts due to settled aggregates and therefore, it is ensured that only diffusion contributes to the resulting adsorption process. Afterwards, samples were gently dipped into deionized water and finally dried under vacuum for 12 h. In the end, this procedure yielded monolayers of isolated or merely slightly grouped spheres on the mica plates.

As this type of sample preparation did not give satisfying results when the 100 nm spheres were about to be analyzed, samples in that case were prepared by placing a small droplet of the required microsphere parent solution with a concentration of 2 wt.-% onto a prepared mica plate and eventually, the sample was air-dried for three days which yielded a multilayered but highly ordered microsphere-coating. Note that this type of sample preparation will hereinafter be referred to as the "droplet-method".

Diameters of the 24 and 40 nm microspheres were accessible by using the depth analysis command of the AFM software. As this provided merely reasonable results for isolated spheres, denser adsorbed areas were further investigated by determination of the height distance between peak and valley through the section analysis procedure. Given non-deforming particles as well as a densely packed film, the 100 nm samples were quantified by valley to valley distance measurements in the height image through the section analysis procedure.

3.1.3.2 Results

Spectral characterization

Results from spectroscopic analyses of the fluorescent microspheres reveal that the label employed provides characteristics rather *comparable to that of rhodamine B*. Irrespective of the particle size, UV–vis spectra taken from dilute microsphere-suspensions show similar absorbances over the entire visible wavelength-range with λ_{max} = 580 nm besides strong absorbances in the UV range that are addressable to the polystyrene basis material. Moreover, fluorescence spectra show no significant differences in both the excitation (λ_{max}^{ex} = 580 nm) as well as the emission (λ_{max}^{em} = 605 nm) behavior of the different spheres over the entire visible wavelength-range.

In combination, these findings ensure that *equal wt.-portions* of all types of spheres show *same fluorescence intensities*—which is the value to be quantified in FRAP analyses. Fluorescence spectra also assure that even though the excitation maxima lie in the yellow region for all types of microspheres, a sufficient excitation of the fluorophores is possible with the laser-wavelengths utilized in the confocal microscope that was employed in Chapter 3.2 and 4.2 due to the existence of relatively broad hypsochromic bands as illustrated exemplarily for the 24 nm spheres in Figure 3.9.

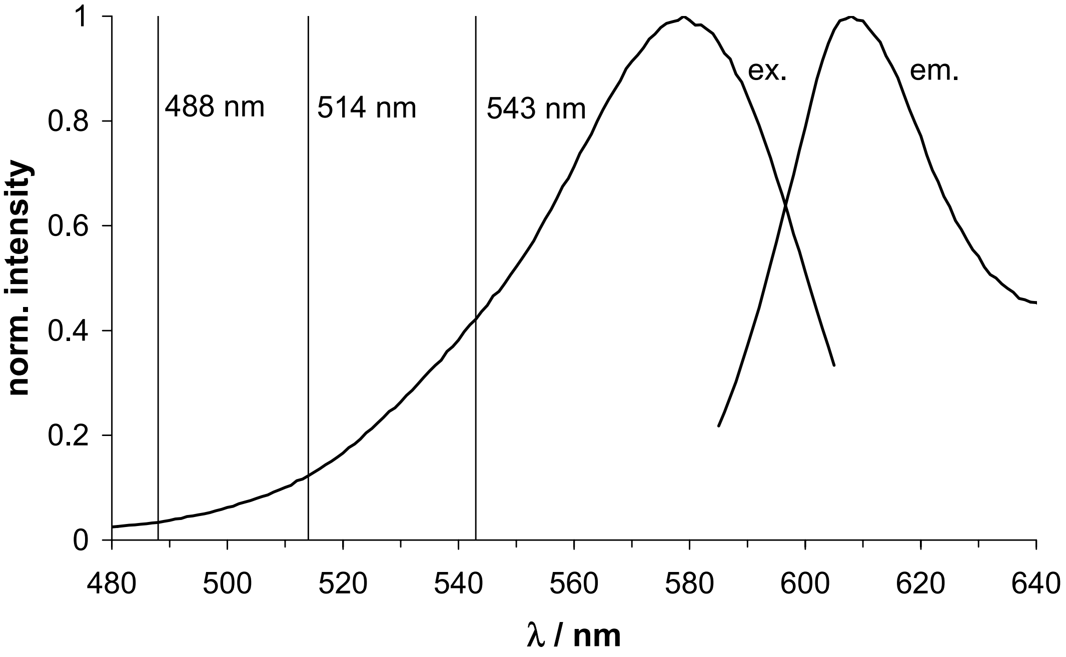

Figure 3.9 Fluorescence spectra of the red-labeled PS microspheres in aqueous suspension, exemplarily shown for the 24 nm size. – Also illustrated are the wavelengths employed for FRAP experiments in Chapter 3.2 and 4.2.

Particle sizes

Particle sizes of the microspheres estimated by various methods are compiled in Table 3.5. They are in good agreement with the manufacturer information in case of the 100 nm spheres but show slightly higher values for the sizes of the 24 and the 40 nm spheres when methods based on hydrodynamics are applied. With the aid of AFM, it was possible to determine particle size distributions from ensembles of about 100 single spheres, respectively, that could be quantified in each image. To illustrate the probes' heterogeneities, AFM-images obtained by the droplet-method are presented in Figure 3.10 together with the distributions. Results indicate the relative standard deviations to decrease with increasing particle radius from about 30% in case of the 24 nm spheres to ~4% in case of the 100 nm spheres, which are thus able to form a highly structured layer exhibiting long-range order, as to be seen in Figure 3.10c.

Table 3.5 (Hydrodynamic) radii of the microspheres employed for the present work as estimated by dynamic light scattering (DLS), ultracentrifugal analyses (UA), and atomic force microscopy (AFM). – Margins of error denoted for the AFM data reflect the standard deviations of the particle size distributions observed by this technique.

Method	*r*(24 nm microspheres) nm	*r*(40 nm microspheres) nm	*r*(100 nm microspheres) nm
DLS	16.7	51.5	49.5
UA	14.0	21.0	51.7
AFM	12.2 ± 3.8	21.5 ± 2.5	49.1 ± 2.0

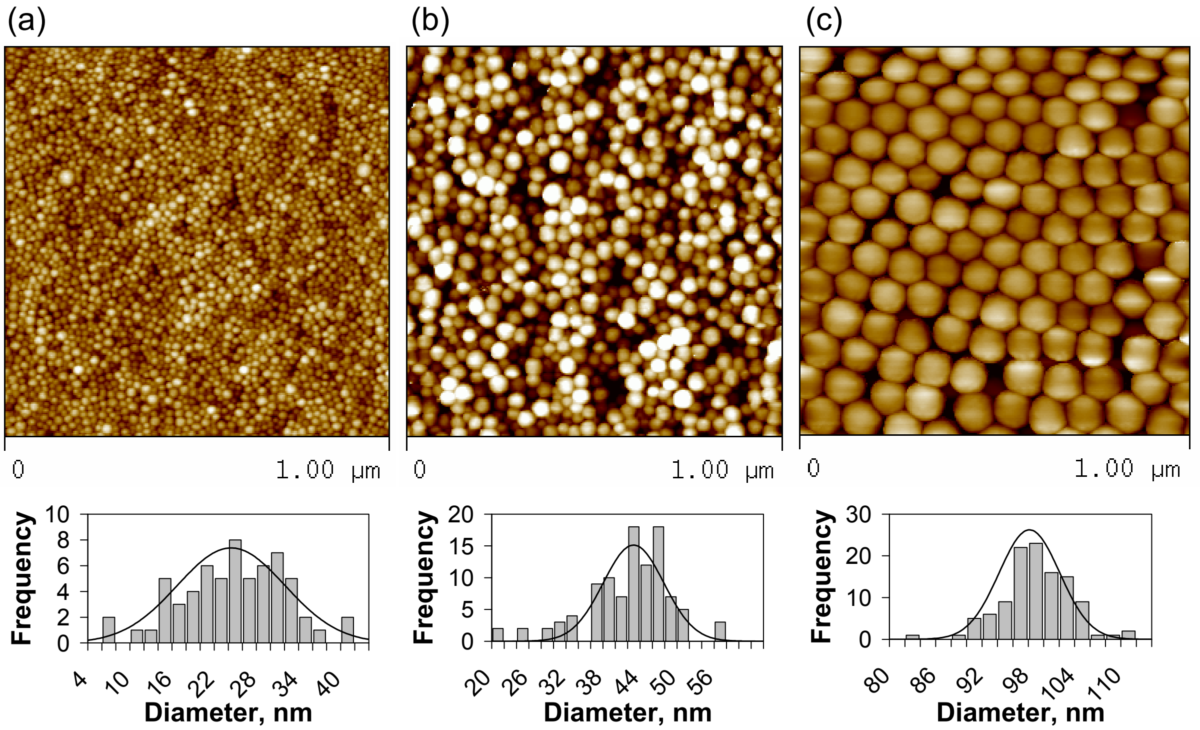

Figure 3.10 AFM images and particle size distributions of the (a) 24 nm, (b) 40 nm, and (c) 100 nm microspheres.

3.1.4 Conclusions and summary

It was shown in this chapter how amine-functionalized PAAm can be synthesized by free-radical copolymerization and how the degree of functionalization and the molar mass can be adequately controlled. The reactivity ratios for the copolymerization of AAm with NAPMAAm were determined to be $r_1 = 0.49$ and $r_2 = 0.85$. Sodium formate can be used for easy adjustment of the molar mass in the range M_w = 200 000 to several million g·mol^{-1}.

Application of the described procedures offers the possibility for the preparation of well-defined water-soluble polymers carrying *pendant nucleophilic amine moieties in random sequence*. Particular emphasis was placed on low degrees of functionalization, as such products are required when fluorescence labeling is intended. Expediently, this can be accomplished in a quantitative way. Hence, the degree of labeling can be readily adjusted by preparing samples with well-defined composition and subsequent exhaustive saturation of the amine moieties with fluorophores. Since a variety of dyes spanning the entire spectral range between the UV and IR region and being equipped with isothiocyanate functions, succinimidyl groups, etc., are commercially available and can be easily attached to the amine-functionalized PAAm, particular *spectroscopic* or optical properties can be combined with desired *macromolecular* characteristics. This is of interest for the application of a variety of analytical techniques, e.g., FRAP. For the intended work on the diffusive behavior of labeled polymers in matrixes (Chapter 4.2), the RITC-labeled samples listed in Table 3.4 were employed. By keeping their degrees of labeling small, it can be assumed that the properties of the PAAm basis material remain essentially unaffected by the pendant rhodamine B moieties. Note that a detailed discussion on the choice of this particular chromophore will be given in Chapter 4.2.2.

Besides labeling, another interesting field of application of amine-functionalized PAAm is its crosslinking by dialdehydes or other difunctional molecules. In contrast to the widespread crosslinking copolymerization [1, 5], one starts from a semidilute solution of predefined polymers with known properties and subsequently performs the random crosslinking reaction. The hydrogels thus obtained can be expected to be less inhomogeneous than such prepared by crosslinking copolymerization (q.v., [168]).

In addition to the preparation of labeled PAAm, spherical tracers were characterized with respect to their sizes and spectral properties. Results reveal that the latter correspond closely to the characteristics of rhodamine B. The particle sizes could be consistently determined by different methods. Among these, AFM allowed for the estimation of the size distributions, which show standard deviations between ±4% for the 100 nm spheres and ±30% in case of the 24 nm spheres. As to be pointed out in Chapter 4.2, the 24 and 40 nm spheres exhibit sizes that are closely comparable to the hydrodynamic radii of two of the linear PAAm tracers in aqueous solution. This allows for a consistent comparison of these different materials when probing their diffusion in polymer matrixes.

3.2 Systematic evaluation of FRAP experiments performed on a confocal laser scanning microscope

With the aid of the fluorescent tracer materials treated in the Chapter 3.1 one is able to perform investigations on the dynamic processes in polymer matrixes by methods like fluorescence recovery after photobleaching (FRAP). As stated in Chapter 2.3.7, most of the common approaches for the evaluation of FRAP experiments essentially focus on the *temporal* course of fluorescence intensity within a certain region of the sample. However, when FRAP is measured on a confocal laser scanning microscope (CLSM), the recovery process can be followed with high *spatial* resolution of a µm scale besides temporal resolution. This allows for a straightforward and facile analysis of the data yielding the translational diffusion coefficient as well as the dimensionality of the diffusion process without any need for calibration. Moreover, experiments representing multi-component diffusion can be readily analyzed as well, thus yielding the *distribution* of diffusion coefficients. The following chapter presents a corresponding procedure for the systematic evaluation of FRAP experiments that was developed as another preliminary part of the present work as sketched in Figure 3.11. While Chapter 3.2.1 focuses on the fundamentals of the method and presents a way to analyze simple one-component experiments, Chapter 3.2.2 deals with complex situations and multi-component diffusion. Publications of these contents can be found in refs [172–174].

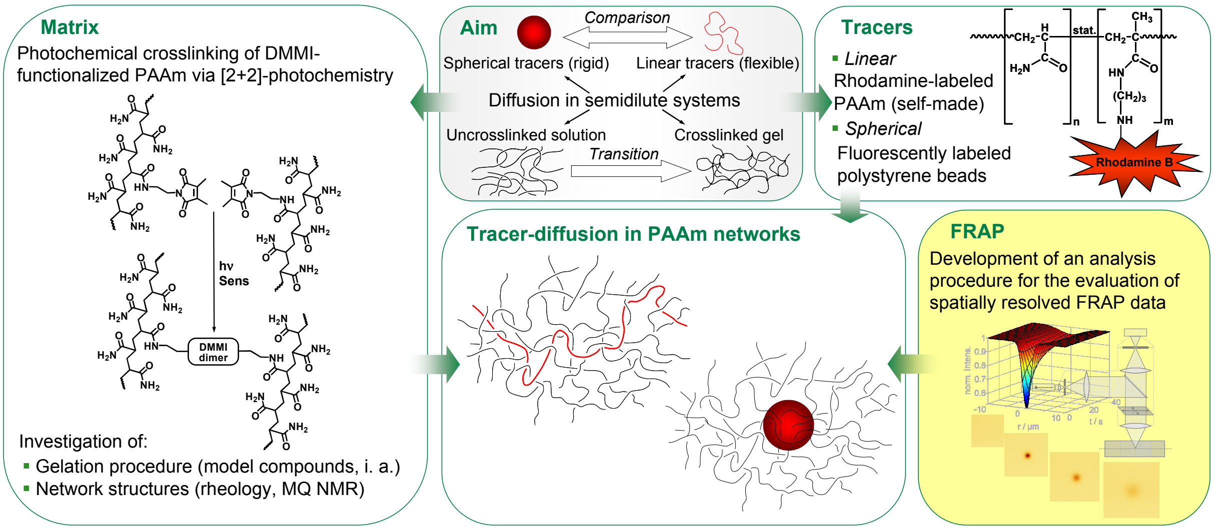

Figure 3.11 Classification of Chapter 3.2 in the context of the present work.

3.2.1 Simple cases and one-component diffusion

3.2.1.1 Introduction

As described in Chapter 2.3.7, the principle of each FRAP experiment is to photobleach a certain region within a fluorescently labeled sample by irradiation with a short intense light pulse. Immediately after bleaching, a highly attenuated light beam is used to measure the recovery of fluorescence inside the bleached area due to the diffusive exchange of bleached fluorophores by unbleached molecules from the surroundings. The analysis of this process yields information about the diffusion coefficient and the fraction of mobile species.

In a common FRAP experiment, only the *rate* of recovery of the fluorescence intensity within some preselected area is measured. On the other hand, performing the experiment on a CLSM reveals such information with high spatial resolution. Although this fact was referred to in some papers [175–178], it has not been pointed out that major advantages with regard to data evaluation can be drawn from this.

This chapter shows that the diffusion coefficient can be readily obtained without any calibration measurement. Furthermore, the dimensionality of the diffusion process can be extracted in an independent manner, and the comparison of different ways to analyze the data provides a sensitive check for consistency and margins of error. In the following sections, the fundamentals of the approach are discussed, the procedure is described in detail, and some experimental results of FRAP measurements on solutions of rhodamine B in glycerol and on aqueous suspensions of the microspheres characterized in Chapter 3.1.3 are presented to demonstrate that reliable results are obtained.

3.2.1.2 Theoretical outline

Any FRAP experiment makes use of the diffusion equation, which is described in detail in Chapter 2.2.3. Figure 2.8 (p 37) shows some typical distributions of a diffusing species for the simple cases of 1-, 2-, or 3-dimensional diffusion at three successive instants. The curves broaden and become shallower with increasing time. In each case, the concentration profiles are *Gaussians* whose $e^{-1/2}$-radius is $\sqrt{2Dt}$. The decrease of the prefactor in eq (2.51) with time depends on the dimensionality: the higher the diffusion dimension, the faster the drop of concentration at $r = 0$.

If one considers FRAP processes, the situation is in essence just inversed, as bleaching takes away a certain amount of the fluorescent molecules, while the considerations above dealt with a local excess of a substance. This means no more than a change of sign combined with a baseline shift.

By utilizing a CLSM and an objective of low numerical aperture (NA), it is readily possible to bleach geometries into the sample that correspond closely to the cases of diffusion from a *plane* or a *line source*. Hence, the solutions to Fick's second law that were mentioned in Chapter 2.2.3 are also applicable to FRAP processes.

In a real experiment, however, the initial conditions used so far to obtain exact solutions to the diffusion equation are never met perfectly. Instead of starting from a *Dirac function* (in one, two, or three dimensions) for the concentration profile at $t = 0$, that is, an infinitely sharp plane, line, or point source, the initial state will be characterized by some finite spatial width. Furthermore, some time is required to achieve bleaching. This means that it is *not* possible to exactly define the *zero point* of the time scale. Because in an experiment the initial conditions are only approximated, one should be aware that deviations from eq (2.51) are expected when such approximations cannot be neglected. That is the case when diffusion occurs fast in comparison with the duration of the bleach pulse, or when concentration profiles are analyzed on a length scale comparable to the spatial width of the bleaching beam.

The following discussion firstly takes up the case with ideal initial conditions. It will be shown that an analysis of both the temporal and the spatial course of the concentration yields information on the translational diffusion coefficient and the dimensionality of diffusion without any calibration. The deviations from the ideal conditions will be treated subsequently, and the problems related therewith will be solved. It will be shown that even under extremely unfavorable conditions it is possible to obtain a correct diffusion coefficient. Before doing that, classical FRAP experiments shall be briefly considered.

Classical FRAP experiments and recent developments

FRAP experiments carried out in standard fluorescence microscopes or similar setups generally proceed according to the following routine: A light pulse of high intensity is used to destroy fluorescent molecules in a small region of interest (e.g., a spot). Immediately thereafter, the recovery of fluorescence inside the bleached area due to diffusion of unbleached molecules from the surroundings is measured by means of a highly attenuated light beam. The process is quantified by the *integral fluorescence intensity* in the spot area. The analysis of the rate of recovery yields information about the diffusion coefficient.

The first suggestion for a quantitative treatment of FRAP experiments was given by Axelrod et al. [153]. They derived equations that can be used to fit an experimental recovery curve to a theoretical one. These equations are based on the assumptions that (i) fluorescence recovery (in the absence of any flow) is the result of pure 2-dimensional diffusion, (ii) a laser beam having a Gaussian or circular intensity profile is used for bleaching and detection, (iii) photobleaching occurs as an irreversible first-order reaction, and (iv) the duration of the bleaching pulse is short compared to the characteristic time for recovery. A calculation of the absolute value of D requires knowledge of the beam size and profile; hence, a calibration is necessary.

In the last 25 years, several authors have developed similar approaches for 2-dimensional diffusion [179–181]. By and large, they added some improvement to the data evaluation or the mathematical modeling. Recently, Braeckmans et al. [182] pointed out that the use of a CLSM enabled a much better control of the bleaching geometry. They also expanded the model to the 3-dimensional case. Kubitscheck et al. [183] derived an alternative way to determine the diffusion coefficient for the case of 3-dimensional diffusion based on numerical simulations of the postbleach process. In all of these approaches, however, the main emphasis was put on having well-defined initial conditions and solving the diffusion equation for that particular case. On the other hand, the detection of fluorescence recovery was always based on the *average* intensity measured inside the spot area. By doing that, all spatial information is averaged out and lost. If one employed both the *temporal* and the *spatial* information for the data analysis, this could not only serve as a check of consistency but, furthermore, permit the unambiguous determination of the dimensionality of diffusion.

Only a few reports in literature consider spatially resolved recovery data at all [175–178], but only in the papers of Kubitscheck et al. [176] and Cheng et al. [177] is the diffusion coefficient determined from fluorescence intensity profiles. However, these approaches do not suggest the possibility to estimate the diffusion dimension.

Evaluation of spatially resolved recovery data: The ideal case

The approach to the evaluation of FRAP data presented here is opposite to most of the classical methods. The experimental conditions for bleaching are chosen such as to ensure that the actual bleaching profile comes as close as possible to a line or plane source. The course of fluorescence recovery is followed on a length scale much greater than the width of the source. That way there is no need to consider the profile of the bleaching beam, a fact which leads to considerable simplification of the mathematical treatment.

The following consideration is fully based on eq (2.51). Rewriting it for the case of a FRAP experiment yields

$$I(r,t) = I_0 - \frac{M}{(4\pi Dt)^{d/2}} \cdot \exp\left(\frac{-r^2}{4Dt}\right) = I_0 - A(t) \cdot \exp\left(\frac{-r^2}{2w^2}\right) \qquad (3.2)$$

where I represents the fluorescence intensity at the position r and the time t after bleaching. M now is formally a fluorescence intensity (per length or area for $d = 2$ or 1) corresponding to the amount of fluorophore destroyed by bleaching, and w is the $e^{-1/2}$-radius of the Gaussian function.

The quantity D appears in the prefactor and the exponent of the Gaussian, hence, both terms can be used to determine it. Comparison of the exponential terms of eq (3.2) yields

$$w^2 = 2Dt \qquad (3.3)$$

and therewith the possibility to determine the diffusion coefficient by plotting w^2 vs. t for a series of intensity profiles obtained from images taken during the recovery process. A straight line with slope $2D$ passing through the origin should be expected.

On the other hand, an algebraic decay for the time dependence of *A*(*t*) is obtained:

$$A(t) = \frac{M}{(4\pi D)^{d/2}} \cdot t^{-d/2} \tag{3.4}$$

Eq (3.4) could also be used to calculate *D*, provided the quantity *M* is known by suitable calibration. As an alternative, eq (3.4) can be written in logarithmic form:

$$\log A = -\frac{d}{2}\log t + \log\frac{M}{(4\pi D)^{d/2}} = -\frac{d}{2}\log t + K \tag{3.5}$$

This means that a plot of log *A* vs. log *t* should give a straight line having a slope of –*d*/2, thus forming the basis for the experimental determination of the dimensionality of the diffusion process.

The real case

When the results of actual experiments are analyzed, one realizes major deviations from the ideal predictions according to eqs (3.3) and (3.5): First, a plot of w^2 vs. *t* shows an appreciable *intercept* instead of passing through the origin. This was also reported by Cheng et al. [177] without comment. Secondly, a plot of log *A* vs. log *t* is *curved* and approaches a straight line with a slope according to the anticipated dimensionality only at long times. Figure 3.12 shows a schematic comparison of the curves expected for the ideal case and the really measured curves.

The reason for these deviations is quite clear and has already been mentioned: The beginning of the experiment is theoretically characterized by a *sharp delta pulse* for bleaching. In real experiments, however, bleaching takes a certain period of time. Also, the bleaching beam has a finite width. Both deviations from the ideal case result in a *shift of the experimental time scale* (which starts at the scanning of the first image) compared to the ideal time scale.

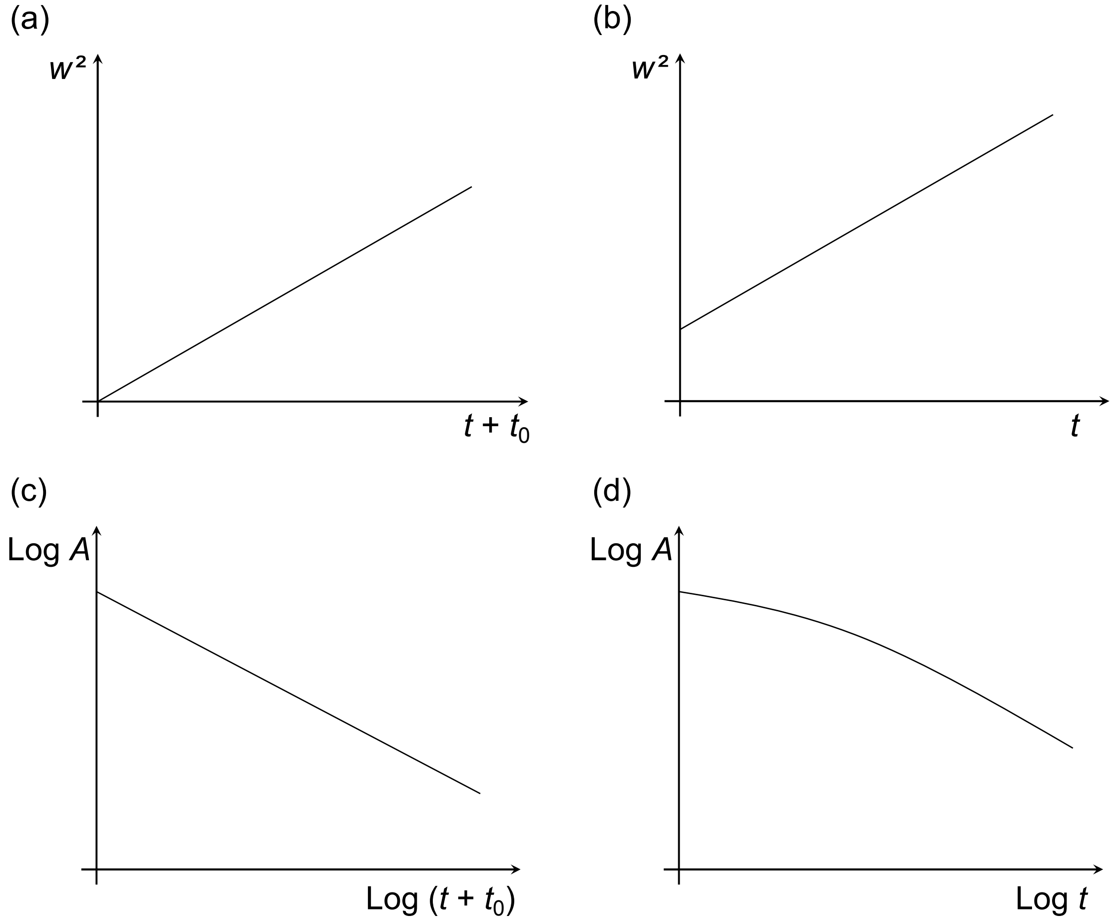

Figure 3.12 Comparison of the ideal (a & c) and real (b & d) course of w^2 vs. t and of log A vs. log t (schematic). – The time lag t_0 corrects for the deviations from ideality. The slope of the lines in (a) and (b) is $2D$, while it is $-d/2$ in (c).

If the duration of the bleaching pulse were infinitely short, the spatial width of the bleaching beam would account for a broadening of the bleached pattern, which in turn could be interpreted as the result of a bleaching pulse that was infinitely narrow on the spatial scale but whose bleach pattern was observed only after a certain period of time. By contrast, if the bleaching pulse were infinitely narrow on the spatial scale, it takes a certain period of time to get an adequate amount of bleaching. During that time, a diffusive broadening of the bleached pattern occurs, which again causes a temporal shift in the experimental time scale. It is thus possible to correct for these deviations either on the time scale or on the length scale:

$$w^2 = 2Dt + w_0{}^2 = 2D(t + t_0) \tag{3.6}$$

where $w_0{}^2$ denotes the intercept in Figure 3.12b, which may be transformed into a shift of the time scale t_0. It is important to note that this shift does not have any influence on the determination of the diffusion coefficient, since D is derived from the slope of the line. However, it greatly affects the course of log A vs. log t.

For a correct estimate of the diffusion dimension, it is thus absolutely necessary to apply the correct time shift t_0. Fortunately, there are two criteria which may be used to find it and which have to be met simultaneously: t_0 has to be chosen such that the *intercept* of the plot of w^2 vs. $(t + t_0)$ is *minimized* and that the *curvature* of the plot of log A vs. log $(t + t_0)$ is *minimized* as well. For convenience, one may proceed in two steps. The *extrapolation* of the observed line in the w^2 vs. t plot to $w^2 = 0$ gives a first estimate for t_0. In the second step, a quadratic function is fitted to the log A vs. log $(t + t_0)$ plot. *Iterative variation* of t_0 until the quadratic term vanishes is used for fine-tuning. The fact that both criteria are fulfilled with the same time shift t_0 is a sensitive check for consistency of the whole procedure. If the simultaneous minimization fails, deviations from purely diffusive transport must be suspected. Determination of the dimensionality of diffusion may serve as a check of the experimental conditions (cf. Chapter 3.2.2) or as a hint to an anisotropic sample.

3.2.1.3 Realization of the concept

In this section, the evaluation procedure is comprehensively described and illustrated using FRAP experiments performed on rhodamine B in glycerol. As said above, a CLSM allows bleaching of simple geometrical patterns like a line or a point into the confocal plane. By using an objective of low NA, this yields 3-dimensional bleaching geometries that correspond to the simple cases of 1-dimensional diffusion from a plane source or 2-dimensional diffusion from a line source. Then, eq (3.2) forms the basis for the determination of the diffusion coefficient D and the dimensionality d, respectively.

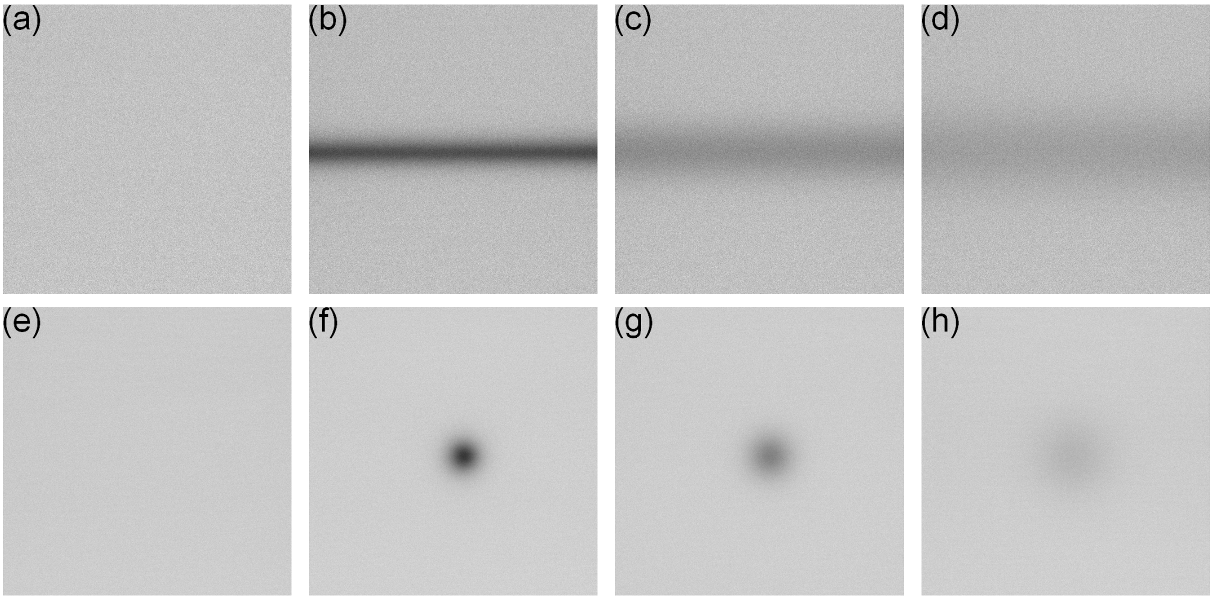

Figure 3.13 Images from a series taken during FRAP experiments on rhodamine B dissolved in glycerol (c = 0.4 g·L^{-1}) for 1-dimensional diffusion after bleaching a line (top) and for 2-dimensional diffusion after bleaching a point (bottom) into the focal plane. – Images (a) & (e) show the sample before bleaching, while images (b) & (f), (c) & (g), and (d) & (h) were taken at 1, 30, and 90 s after bleaching, respectively. The image sizes are about 80 × 80 µm^2 in all cases.

Figure 3.13 presents some typical images taken before and during FRAP experiments for the two cases mentioned above. They are for rhodamine B in glycerol at a concentration of 0.4 g·L^{-1} and show sections through the 3-dimensional sample along the confocal (x;y)-plane. Because an objective of comparatively low NA was used for bleaching, the displayed bleach patterns also exist along the z-axis above and below the confocal plane.

To analyze these data, the intensity profiles within the bleached areas have to be determined for each image (which represents a certain point in time during the fluorescence recovery process) and fitted to eq (3.2). The intensity data are averaged over different equivalent positions to reduce the statistical noise. The free fitting parameters are the baseline intensity I_0, the depth of bleaching (amplitude) A, and the e$^{-1/2}$-radius w. This yields the possibility to estimate the diffusion coefficient by plotting w^2 vs. t according to eq (3.3), while a plot of log A vs. log t should give the dimensionality d according to eq (3.5). As discussed in the preceding section, an appropriate shift of the time scale t_0 has to be applied. In detail, the data processing is highly automated and proceeds in the following steps:

1. **Normalization.** Performing a FRAP experiment on a CLSM yields a series of images of typically 512 × 512 pixels and 256 (color-coded) intensity values. For automation of the data analysis, a MATLAB software was written which firstly imports all these images and stores them as 512 × 512 matrices, where each entry quantifies the fluorescence intensity at that particular point by a number between 0 and 255. Then, the image-matrices corresponding to the FRAP process are normalized to the prebleach situation by dividing each FRAP image by a mean matrix over several prebleach-images. All further steps of the analysis are based on the resulting normalized FRAP matrices.

2. **Averaging.** Secondly, several profiles of fluorescence intensity have to be determined through the bleached region. If a point has been bleached into the confocal plane (which corresponds to 2-dimensional diffusion), it is required that the center of the bleached spot is exactly localized. This is done by a search algorithm as described in refs [159] and [172]. Next, a mean profile of fluorescence intensity through the center point is calculated by averaging all intensity data within small radial intervals. In the case of bleaching a line into the confocal plane (which corresponds to 1-dimensional diffusion), intensity data of sections running perpendicular to the bleached line are averaged. There is the option to omit some sections at the periphery of the images to avoid edge effects. As a result, an averaged (radial or linear, depending on the bleach pattern) profile of fluorescence intensity is obtained for each image and thus for each instant of the recovery process.

3. **Fitting of a Gaussian function.** The averaged intensity profiles for all FRAP images obtained during a recovery process are then fitted to eq (3.2) by the least-squares method. This yields a set of fit parameters for each image, e.g., w^2 and A, as a function of time. To demonstrate the quality of such fits, Figure 3.14 shows some examples of averaged intensity profiles and the corresponding fit functions. The data belong to the images depicted in Figure 3.13. The agreement is excellent, thus providing a sound basis for the determination of D and d.

4. **Estimate of the diffusion coefficient and the dimensionality.** In the end of the analysis-procedure, the fitting parameter w^2 is plotted versus t, which yields a straight line of slope $2D$. Extrapolation of this line to $w^2(t_0) = 0$ gives a first approximation for the time lag t_0. Afterwards, this value is fine-tuned by plotting log A vs. log $(t + t_0)$ and fitting the following quadratic function to the resulting curve:

   $$\log A = a \cdot \left[\log(t + t_0)\right]^2 + b \cdot \log(t + t_0) + c \qquad (3.7)$$

   By slight variation of t_0 until the coefficient a approaches zero, the correct value for the time lag t_0 can be deduced. Then, the plot of log A vs. log $(t + t_0)$ yields a straight line with slope $-d/2$.

As a result of the last step, the *real* FRAP experiment is transformed into the hypothetical *ideal* case characterized by an initial intensity profile having the form of a Dirac-function. This step is discussed in detail below.

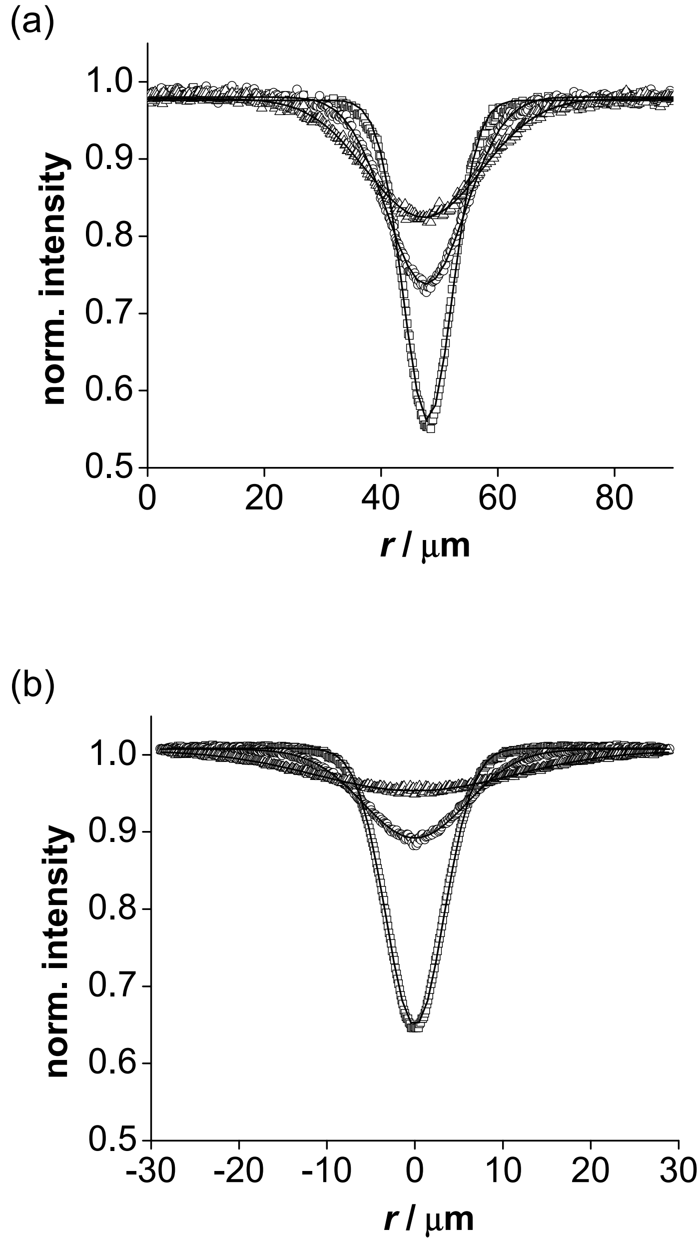

Figure 3.14 Averaged intensity profiles obtained from the FRAP images shown in Figure 3.13. – (a) 1-Dimensional diffusion, (b) 2-dimensional diffusion at 1 s (□), 30 s (○), and 90 s (△) after bleaching, respectively. The full lines represent the fitted Gaussian functions.

3.2.1.4 Materials and methods

Test solutions

Rhodamine B was obtained from Sigma and dissolved in glycerol at c = 0.4 g·L^{-1}. (The glycerol was not purified and may contain some water.) Fluorescently labeled polystyrene microspheres with nominal diameters of 24 and 100 nm as intensely characterized in Chapter 3.1.3 were purchased as aqueous suspensions from Molecular Probes (Eugene).

FRAP equipment

A Leica TCS SP2 confocal laser scanning microscope was used to perform FRAP measurements. Under a 10× DRY objective of NA = 0.3, the fluorophore was excited in the scanning mode with the 543 nm line of a HeNe laser at 50% of its maximum power (which was measured to be 0.22 mW at the object level). Bleaching was accomplished by irradiation of the fluorophore with the 543 nm line of the HeNe laser and the 514 and 488 nm lines of an Ar laser, each at full power (measured values at the object level were 0.22, 7.0, and 6.2 mW, respectively).

The further settings were: beam expander = 3, zoom = 20 (which led to an image size of about 80 × 80 μm^2), and line scanning speed = 800 Hz (in the scanning mode, images were taken at 1 fps) at a resolution of 512 × 512 pixels. For measuring the faster diffusion of the fluorescent microspheres in water, resolution was reduced to 256 × 256 pixels, while the scanning speed was accelerated to 1000 Hz in the bidirectional scanning mode. This led to a scanning rate of 5 fps.

Experimental FRAP protocol

Samples for FRAP experiments were prepared by placing a droplet of each solution on a microscopy slide and putting a coverglass on top. The system was sealed with nail polish. This yields samples with a thickness of about 60 µm. The confocal plane was set to be approximately in the middle of the sample. Before bleaching, a stack of ten images was scanned to record the prebleach situation. For bleaching a point into the confocal plane (which should lead to 2-dimensional diffusion), a chosen spot in this plane was irradiated for 3 s with the laser settings mentioned above. For bleaching a line (which should yield 1-dimensional diffusion), the mode was switched into *xt*-scanning and zoom was halved to ensure that the bleached line extends over the chosen image dimensions in order to prevent side effects. Subsequently, six images were scanned with the laser settings mentioned above. To record the postbleach series, the mode was switched back to *xyt*-scanning and zoom was doubled again. After bleaching, a series of images was recorded to document the recovery process with a temporal spacing of 1 s between each image for the measurements on rhodamine B in glycerol and 0.2 s for the measurements on fluorescent microspheres at T = (25 ± 0.1) °C, respectively. The time information was recorded automatically by the Leica confocal software into an information file that was accessed by the MATLAB software for analysis of the data.

Data extraction and fitting

The analysis of the recorded images was automatically performed by the MATLAB software mentioned above. All fitting results and interesting intermediate data (such as the averaged intensity profiles) were written to hard disk.

3.2.1.5 Results and discussion

To validate the concept, several FRAP experiments were performed on solutions of rhodamine B in glycerol and on suspensions of polystyrene microspheres in water.

Rhodamine B

Examples for some of the occurring FRAP images and the corresponding intensity profiles taken from measurements on rhodamine B in glycerol are shown in Figure 3.13 and 3.14. In Figure 3.15, the fit parameter w^2 is plotted versus (uncorrected) time for these two experiments, with one data set belonging to the line-bleaching experiment and the other one to the point-bleaching experiment. The full lines are linear least-squares fits to the data. The diffusion coefficient was estimated from the slope of these lines as $D_1 = 0.56\ \mu\text{m}^2\cdot\text{s}^{-1}$ for the 1-dimensional line-bleaching experiment and $D_2 = 0.51\ \mu\text{m}^2\cdot\text{s}^{-1}$ for the 2-dimensional point-bleaching experiment. The results show good agreement. Furthermore, extrapolation of the straight lines yields a first approximation for the time lag t_0, which was 10.8 s for line-bleaching and 6.4 s for point-bleaching.

To estimate or check the diffusion dimension, log A is plotted versus log $(t + t_0)$, while t_0 is fine-tuned by iteration in the manner described in the preceding chapters. This procedure is visualized in Figure 3.16 for the two experiments mentioned above. For comparison, plots of log A are shown versus the logarithm of the uncorrected time, the time corrected according to Figure 3.15, and the time corrected further by iteration so that the log–log plot turns out to be linear. It can be seen that the shift of the time axis is absolutely necessary to obtain the required linear course of the curve. For the point-bleaching experiment (Figure 3.16b), the two lines obtained after the first and second step of approximation do not differ appreciably. The time lag t_0 is moved from 6.4 to 5.4 s. The slopes of the corresponding lines give dimensionalities 2.05 or 1.99, respectively (theory: 2). For the line-bleaching experiment (Figure 3.16a), the iteration has a more visible effect. While t_0 is moved from 10.8 to 9.9 s, the dimensionality is estimated to be 1.15 or 0.95, respectively (theory: 1).

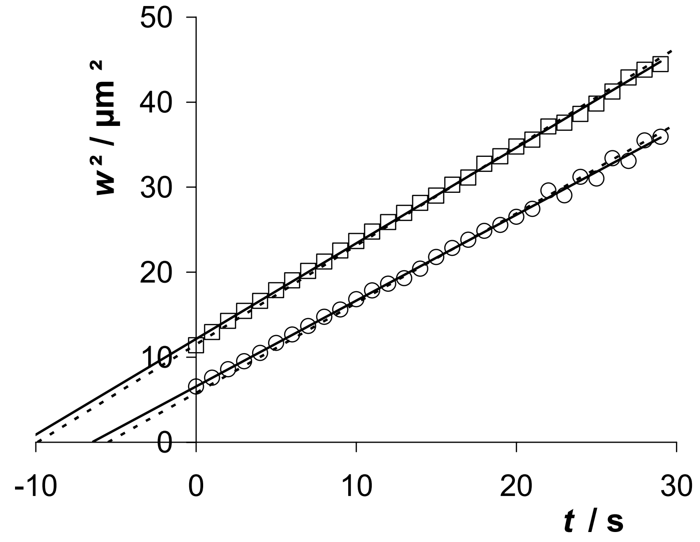

Figure 3.15 w^2 vs. t plots for two examples of FRAP experiments on rhodamine B in glycerol (c = 0.4 g·L^{-1}). – □: Line-bleaching, ○: point-bleaching experiment. The slopes of the full lines give the diffusion coefficient (0.56 and 0.51 µm^2·s^{-1}, respectively), while the extrapolation of the fitted lines to w^2 = 0 yields a first approximation for the time lag t_0 (10.8 and 6.4 s, respectively). The dotted lines are linear fits forced to intersect the abscissa at the t_0-values from iterative refinement.

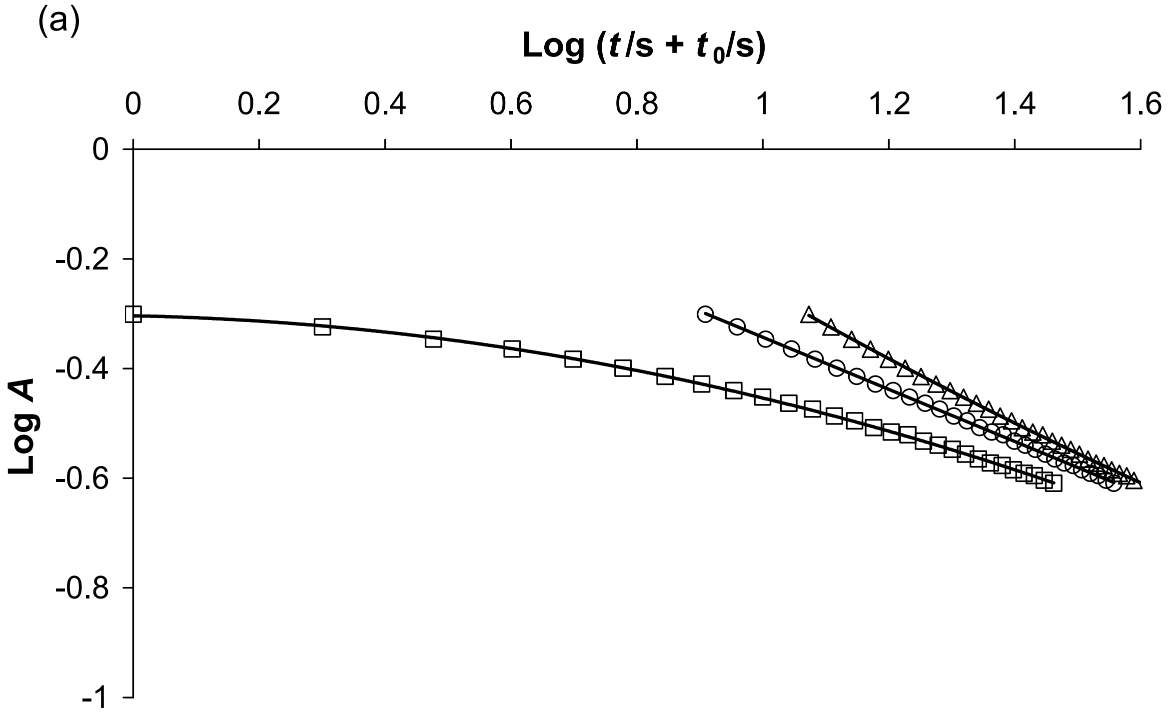

Figure 3.16 Plots of log A vs. log (t + t_0) for two examples of (a) line-bleaching and (b) point-bleaching experiments on rhodamine B in glycerol. □: Uncorrected (t_0 = 0), △: after extrapolation, ○: after iteration to optimize linearity.

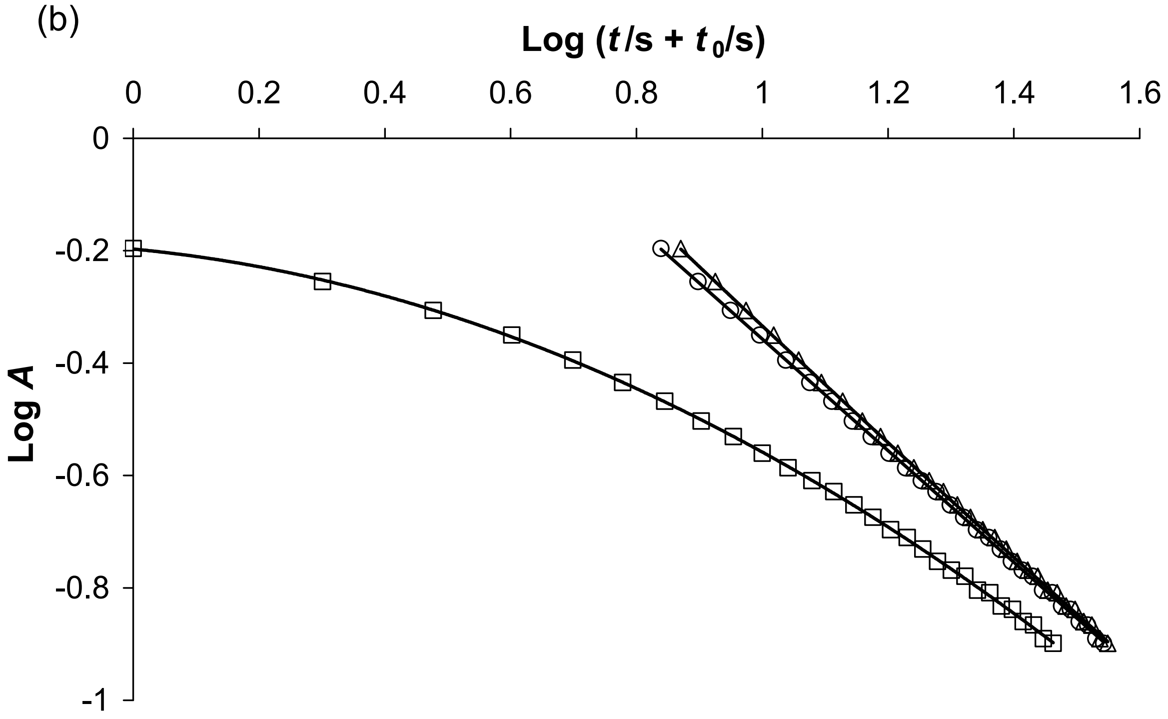

Figure 3.16 *Continued.*

When the linear fits in Figure 3.15 are forced to intersect the abscissa at the refined t_0-values, the dashed lines are obtained. These differ barely from the original lines, a fact emphasizing that the refinement gives rise to just minor changes. The values for the diffusion coefficient in this case change from D_l = 0.56 μm^2·s^{-1} to D_l = 0.58 μm^2·s^{-1} for the (1-dimensional) line-bleaching experiment and from D_2 = 0.51 μm^2·s^{-1} to D_2 = 0.53 μm^2·s^{-1} for the (2-dimensional) point-bleaching experiment. The agreement between the results achieved by the different ways of evaluation and by the different bleaching geometries is excellent. This is a strong argument in support of the concept.

So far, two simple experiments where compared. As a check for reproducibility, each bleaching experiment was repeated fivefold to obtain averages of D and d as well as the corresponding standard deviations. The data compiled in Table 3.6 show that the diffusion coefficient and the diffusion dimension can be estimated to within ±10%, with point-bleaching experiments showing a tendency to a larger scatter.

Table 3.6 Experimental results of several FRAP measurements on solutions of rhodamine B in glycerol.

Experiment	Data from extrapolation of w^2 vs. t plot		Data after iterative refinement		
	D $\mu m^2 \cdot s^{-1}$	d	D $\mu m^2 \cdot s^{-1}$	d	$d_{\text{theoretical}}$
Line-bleaching	0.56 ± 0.04	1.03 ± 0.11	0.58 ± 0.04	1.02 ± 0.03	1
Point-bleaching	0.56 ± 0.10	1.99 ± 0.09	0.57 ± 0.11	2.00 ± 0.09	2

Microspheres

Aqueous suspensions of microspheres with nominal diameters of 24 and 100 nm were investigated because they pose a particular challenge to FRAP measurements due to the fact that the diffusion is much faster than that of rhodamine B in glycerol. Moreover, the sizes of the microspheres could be determined by several independent methods (cf. Chapter 3.1.3) and thus, the absolute value of the diffusion coefficient could be checked. FRAP experiments were performed using the point-bleaching method (2-dimensional diffusion). Repeat measurements, which were analyzed according to the procedure described above in detail, gave

$$D_{24\text{ nm}} = (14.76 \pm 1.88)\ \mu m^2 \cdot s^{-1} \qquad \text{and} \qquad D_{100\text{ nm}} = (4.83 \pm 0.37)\ \mu m^2 \cdot s^{-1}$$

corresponding to hydrodynamic radii of

$$r_{24\text{ nm}} = (16.6 \pm 2.1)\text{ nm} \qquad \text{and} \qquad r_{100\text{ nm}} = (50.8 \pm 3.9)\text{ nm}$$

as calculated with the Stokes–Einstein relation (2.43) with $\eta = 0.89$ mPa·s and $T = 25$ °C. Both values show good agreement with the corresponding data listed in Table 3.5 (p 95).

The diffusion dimension was estimated to be around $d = 1.9$–2.0 in each case. These results are noteworthy not only because there is good agreement between the different experimental methods with regard to D, but also because they show that the method works well even for rapidly diffusing systems. In fact, in the experiments on the smaller spheres, the duration of the bleaching pulse was 3 s while scanning was performed for only 2 s (ten images were taken in intervals of 0.2 s). It is thus corroborated that the FRAP method described here is fairly robust and suitable for handling extreme experimental conditions.

3.2.1.6 Conclusions and summary

Performing FRAP experiments on a CLSM offers some advantages over the use of classical procedures because of two reasons: The generation of simple bleaching patterns coming close to a *line* or a *plane source* is readily possible, and the recovery process can be followed on the *time scale* and on the *spatial scale* as well. This makes the data evaluation particularly facile and straightforward. Analyzing the obtained fluorescence *intensity profiles* according to the method presented here provides not only the *diffusion coefficient* without any need for calibration, but also the *dimensionality* of diffusion. Since two independent criteria are used to correct the experimental time scale for the actual initial conditions, an internal check of consistency is automatically included, which would indicate systematic errors. The experiments performed to demonstrate the reliability of the method clearly show that the diffusion coefficient can be determined with high accuracy even under unfavorable conditions. The estimate of the dimensionality of the diffusion process agrees well with expectations. This proves that the evaluation method has a sound experimental basis.

Note that only slight modifications are needed to apply this method to analyze and quantify diffusion processes in anisotropic media. The principal axes of the medium would be obtained from the direction-dependent width of the Gaussian profiles when point-bleaching experiments were performed. Utilizing a CLSM with the ability to rotate the scanning field could provide a possibility to quantify the mobility along these directions also by line-bleaching experiments. Moreover, the method can be consistently expanded to cover the important field of multi-component diffusion processes, as described in detail in the next chapter.

3.2.2 Complex cases and multi-component diffusion

3.2.2.1 Introduction

All procedures for the evaluation of FRAP data mentioned so far—including the one presented in the preceding chapter—work reliably only on simple, single-component diffusion processes. They fail when there is *multi-component* diffusion or when the diffusion coefficients exhibit a *distribution*. (The methods based on Axelrod's original work can at least treat diffusion phenomena with an immobile fraction.) On the other hand, in a variety of interesting diffusion phenomena occurring in nature, polydisperse substances are involved.

Only a few papers address the subject of multiple discrete or continuously distributed components in FRAP experiments: Yguerabide et al. [184] pointed out that deviations from the linear form of a reciprocal recovery curve could serve as a hint for multi-component diffusion, and Van Zoelen et al. [185] introduced a corresponding second-order correction term to account for these deviations. However, the different diffusion coefficients cannot be measured by such methods. To overcome this deficiency, Greenberg and Axelrod [186] expanded the original Axelrod model to estimate recovery parameters of two diffusing species. Gordon et al. [181] improved the latter method by utilizing the whole series expansion for fitting. Moreover, Periasamy and Verkman [187] presented a method for analyzing FRAP experiments on multi-component systems and time-dependent diffusion coefficients by fitting the recovery curve to a particular theoretical form.

A common drawback of all the latter approaches is that they only consider the time dependence of the integral fluorescence intensity in a certain region of interest, whereas spatial information is omitted. Thus, all these methods share the limitations of the original Axelrod approach pointed out in 3.2.1.2. To overcome these limitations, the following section presents an upgrading of the analysis outlined in Chapter 3.2.1. It is shown that it is possible to estimate the distribution of diffusion coefficients in a calibration-free manner when the spatial and temporal information obtained by CLSM is appropriately taken into account.

After highlighting the problems encountered when the evaluation procedure based on a single D is applied to multi-component diffusion processes, the following section discusses the fundamental theoretical framework to deal with such situations. An improved evaluation method is described in detail, and experimental results of FRAP measurements on suspensions of differently sized microspheres are presented, showing that the individual D of the constituent components as well as their fractions are correctly obtained.

3.2.2.2 Theoretical outline

Fundamentals of the analysis of spatially resolved FRAP data

As stated in Chapter 3.2.1, the fundamental equation for the analysis of FRAP experiments is the solution to Fick's second law, which describes the temporal and spatial course of the concentration of a diffusing species. For the ideal case of a *simple one-component* diffusion process in an infinite medium starting at time $t = 0$ from a concentration profile having the form of a delta function in d dimensions, it reads as eq (2.51).

However, in the case of real FRAP experiments, ideal initial conditions are never met exactly since bleaching takes a certain time and does not produce a delta pulse on the spatial scale. Assuming the beam profile to be Gaussian, the non-ideal starting conditions on the spatial and temporal scale can be treated either as a pure spatial or a pure temporal deviation by introducing a time shift t_0 or an initial half-width w_0,[1] respectively, as worked out in Chapter 3.2.1:

$$\begin{aligned} c(r,t) &= \frac{M}{\left(4\pi D(t+t_0)\right)^{d/2}} \cdot \exp\left(\frac{-r^2}{4D(t+t_0)}\right) \\ &= \frac{M}{\left(4\pi Dt + 2\pi w_0{}^2\right)^{d/2}} \cdot \exp\left(\frac{-r^2}{4Dt + 2w_0{}^2}\right) \end{aligned} \tag{3.8}$$

---

[1] For a Gaussian profile, w is the distance from the center where the intensity has dropped to $e^{-1/2}$ ($\approx$ 0.6) times that of the maximum, or where the inflection point is located. In statistics, w is commonly termed standard deviation, while w^2 is the variance. In the following, the terms "width" or "diameter" are used for $2w$ when referring to concentration profiles or beam profiles. The index zero is meant to indicate initial conditions, i.e., $t = 0$.

A FRAP experiment on a CLSM could be realized by instantaneously bleaching a certain amount of a fluorescent substance with a Gaussian bleaching beam of diameter $2w_0$. The alternative interpretation in terms of eq (3.8) would assume a Dirac-shaped bleaching beam applied at $t = -t_0$. Under an objective lens of low NA, a linear bleaching pattern in the confocal plane would result in 1-dimensional diffusion, while bleaching a point in the confocal plane would initiate the 2-dimensional case; cf. Chapter 3.2.1. Since the measured quantity in a FRAP experiment on a CLSM is the spatial and temporal distribution of fluorescence intensity, which is in turn proportional to the concentration of the fluorophore, the following form of eq (3.8) can be used:

$$\begin{aligned} I(r,t) &= I_0 - \frac{M}{\left(4\pi D(t+t_0)\right)^{d/2}} \cdot \exp\left(\frac{-r^2}{4D(t+t_0)}\right) \\ &= I_0 - \frac{M}{\left(4\pi Dt + 2\pi {w_0}^2\right)^{d/2}} \cdot \exp\left(\frac{-r^2}{4Dt + 2{w_0}^2}\right) \end{aligned} \tag{3.9}$$

Herein, I stands for the (relative) fluorescence intensity at position r and time t after bleaching with a Gaussian bleaching beam of diameter $2w_0$ at $t = 0$, whereas I_0 denotes the constant background intensity at $r \to \infty$. The typical shape of such a spatially resolved FRAP curve according to eq (3.9) is depicted in Figure 3.17 (simulated for a process with $d = 2$, $D = 0.1$ µm^2·s^{-1}, and $w_0 = 1$ µm or $t_0 = 5$ s, respectively; I_0 is set to 1 and $M = 3$ µm^{-1}). One observes a *broadening* of the Gaussian-shaped *valley* with increasing time, while the *amplitude drops* in the form of a *hyperbolic decay*.

In some cases, the profile of the bleaching beam in the confocal plane may deviate from the ideal Gaussian form due to reflection, scattering, and other effects. However, in most of these cases, the resulting profile can be approximated as a *superposition* of several Gaussian components j with diameters $2w_{0,j}$ and corresponding fractions a_j, so that the following form of eq (3.9) is obtained:

$$\begin{aligned} I(r,t) &= I_0 - M \cdot \sum_j \frac{a_j}{\left(4\pi D(t+t_{0,j})\right)^{d/2}} \cdot \exp\left(\frac{-r^2}{4D(t+t_{0,j})}\right) \\ &= I_0 - M \cdot \sum_j \frac{a_j}{\left(4\pi Dt + 2\pi {w_{0,j}}^2\right)^{d/2}} \cdot \exp\left(\frac{-r^2}{4Dt + 2{w_{0,j}}^2}\right) \end{aligned} \tag{3.9a}$$

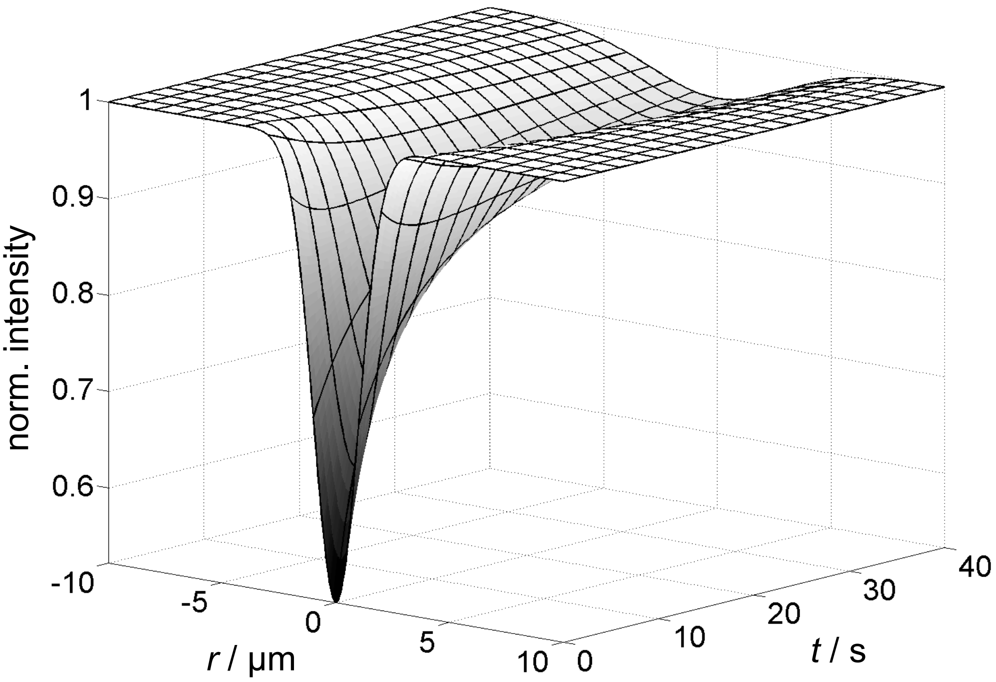

Figure 3.17 Typical shape of a spatially resolved FRAP curve according to eq (3.9) for a simulated simple single-Gaussian case with $d = 2$, $D = 0.1\ \mu\mathrm{m}^2\cdot\mathrm{s}^{-1}$, and $w_0 = 1\ \mu\mathrm{m}$ or $t_0 = 5$ s (as well as $M = 3\ \mu\mathrm{m}^{-1}$ and $I_0 = 1$).

Multi-component diffusion in a FRAP experiment

Considering a system where *several components* undergo diffusion in an independent manner, one simply has to *superimpose the individual profiles* according to eq (3.9) or (3.9a) of each diffusing (fluorescent) substance *i*. This leads to

$$\begin{aligned} I(r,t) &= \sum_i I_i(r,t) \\ &= I_0 - \sum_i \frac{M_i}{\left(4\pi D_i\left(t+t_{0,i}\right)\right)^{d_i/2}} \cdot \exp\left(\frac{-r^2}{4D_i\left(t+t_{0,i}\right)}\right) \\ &= I_0 - \sum_i \frac{M_i}{\left(4\pi D_i t + 2\pi w_0^{\,2}\right)^{d_i/2}} \cdot \exp\left(\frac{-r^2}{4D_i t + 2w_0^{\,2}}\right) \end{aligned} \tag{3.10}$$

for the case of a single-Gaussian bleaching profile and

$$\begin{aligned} I(r,t) &= \sum_i I_i(r,t) \\ &= I_0 - \sum_i M_i \cdot \sum_j \frac{a_j}{\left(4\pi D_i\left(t + t_{0,ij}\right)\right)^{d_i/2}} \cdot \exp\left(\frac{-r^2}{4D_i\left(t + t_{0,ij}\right)}\right) \qquad (3.10a) \\ &= I_0 - \sum_i M_i \cdot \sum_j \frac{a_j}{\left(4\pi D_i t + 2\pi w_{0,j}^{\ 2}\right)^{d_i/2}} \cdot \exp\left(\frac{-r^2}{4D_i t + 2w_{0,j}^{\ 2}}\right) \end{aligned}$$

for the case of a multi-Gaussian bleaching profile.

In all of the last-mentioned superposition steps, the principle of superposition of linear differential equations is employed: since eq (3.9) is an elementary solution to Fick's second law, each linear combination of such expressions is also a solution [70].

Assuming isotropic diffusion, one may fix *d* to a value of 1 in case of 1-dimensional line-bleaching or 2 in case of 2-dimensional point-bleaching. This yields forms of eqs (3.10) and (3.10a) with a reduced number of variables and a *coupled appearance* of the D_i in the pre-exponential (amplitude) as well as in the exponential terms (width), whereas the *amounts* of the diffusing substances M_i *only appear in the prefactors*. Hence, a consistent estimation of the D_i from both the time-dependent course of the amplitudes as well as the course of the widths of the superposed Gaussians is possible, while the fractions M_i associated to the particular D_i can be estimated independently from the prefactors.

Note that one can in principle also include the dimensionalities d_i as free fitting parameters. This is because *d* affects the particular hyperbolic shape of the course of the pre-exponential factor, whereas *M* solely acts as an overall scaling factor. However, such a simultaneous estimate of the distribution of dimensionalities besides the distribution of diffusion coefficients requires data sets with very high s/n ratio and a proper temporal and spatial resolution. A comparison between evaluations of the same data sets with fixed and with variable d_i will be drawn in Section 3.2.2.4.

Indication of multiple diffusion processes

Often, the compound whose diffusion is studied is a well-characterized substance with definite molecular or supramolecular size. This is a common situation in biological systems, and then the treatment based on one single diffusion coefficient as developed in Chapter 3.2.1 works perfectly. In other cases, one is aware of the fact that the species studied is likely to posses a size *distribution*. This is particularly relevant with synthetic macromolecules that have a molar mass distribution, and with synthetic nano- or microparticles exhibiting a size distribution. For simplicity, one may be tempted to treat such systems as having one average diffusion coefficient. In the following, it is shown that this simplistic approach can lead to serious problems and even failure of the evaluation of FRAP experiments. The observations indicating the necessity to include several diffusion coefficients or a continuous distribution are discussed in detail, and it is shown how to overcome these problems.

According to eq (3.10), the amplitudes at position $r = 0$ (center of the bleached pattern) are *larger* for components with *small* D-values than for ones with large D-values at all times $t > 0$, (even) when the substances are present in comparable amounts. If a single Gaussian is fitted to a multi-component concentration or fluorescence intensity profile, the fit thus turns out to be markedly dominated by slow compounds. In extreme cases, even at rather early times in the FRAP process, very fast components yield comparatively shallow and broad Gaussian contributions to the superposition, so that fitting the resulting overall-profile to a single Gaussian could possibly lead the fitting routine to interpret the fast components as a part of the baseline I_0. Hence, the single-Gaussian fitting results always show an overestimation of the contributions of the slow compounds which lead to profiles with comparatively narrow widths and deep amplitudes. Figure 3.18 illustrates this aspect for an example of a simulated intensity profile occurring in a FRAP experiment on a mixture of two diffusing components with different mobilities (D_1:D_2 = 1:100). At the particular time, the spreading of the faster component has already proceeded notably, so that its contribution to the superposition turns out to be a more or less shallow background curve. The slower component is responsible for the sharp peak appearing at the center of the bleached pattern. When this data set is fitted to a single-Gaussian, the influence of the fast component is largely ignored, and the shape of the fit curve is almost completely dominated by the less mobile compound.

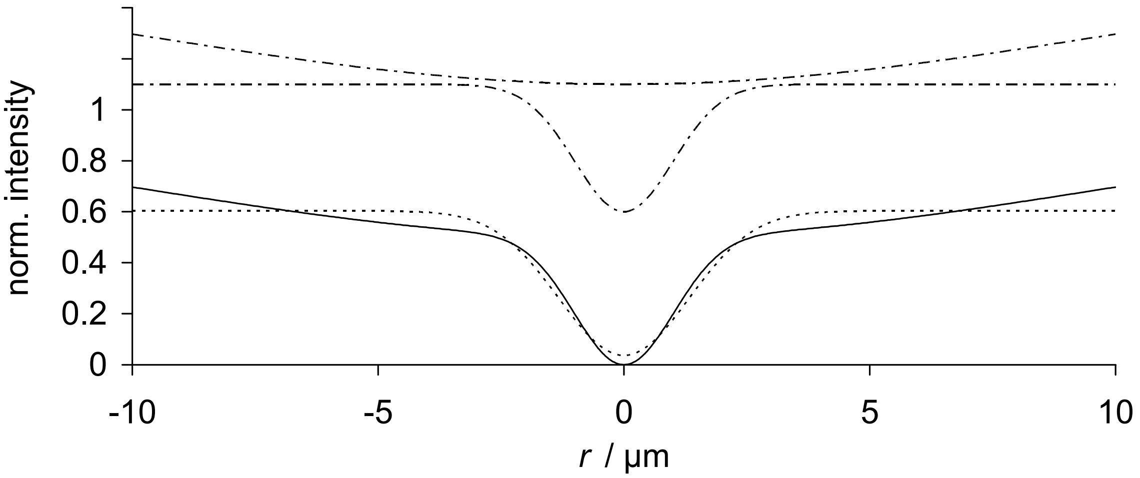

Figure 3.18 Superposition of two Gaussians (full line) with $e^{-1/2}$-radii of $w_1 = 1$ µm and $w_2 = 10$ µm, as well as amplitudes of $A_1 = A_2 = 0.5$, illustrating a typical concentration profile occurring at a certain point in time during a FRAP process involving two components of different mobilities (D_1:D_2 = 1:100). – The corresponding single-Gaussian fit (dotted line) shows the problems accompanied with it: On the one hand, the intensity due to the faster compound tends to merge with the baseline of the fit curve. On the other hand, the fitted width (1.3 µm) and amplitude (0.57) are dominated by the less mobile fraction. Chain-dotted lines illustrate the two single Gaussians in separate form. They are shifted vertically for greater clarity.

How much each component is taken into account also depends on the point in time considered. In Figure 3.19, the temporal development of the concentration profiles is illustrated for the more extreme case of two components whose diffusion coefficients differ by a factor of 1000, the faster one being present in 20-fold excess. Initially, this component dominates the behavior and the concentration profile broadens while the amplitude is rapidly decreasing. Later on, this contribution more and more merges with the background and the less mobile fraction is uncovered. The decrease of the amplitude then slows down markedly. Figure 3.19b shows data at three different points in time for greater clarity. When the widths of the curves are determined at 60% ($e^{-1/2}$) of the amplitudes, it is seen that after an initial increase an *apparent decrease* is observed. This is due to the fact that at the beginning of the experiment it is essentially the diffusion of the fast component which is monitored, while at a later stage a *backsliding* occurs onto the inner Gaussian pattern corresponding to the diffusion of the slow component.

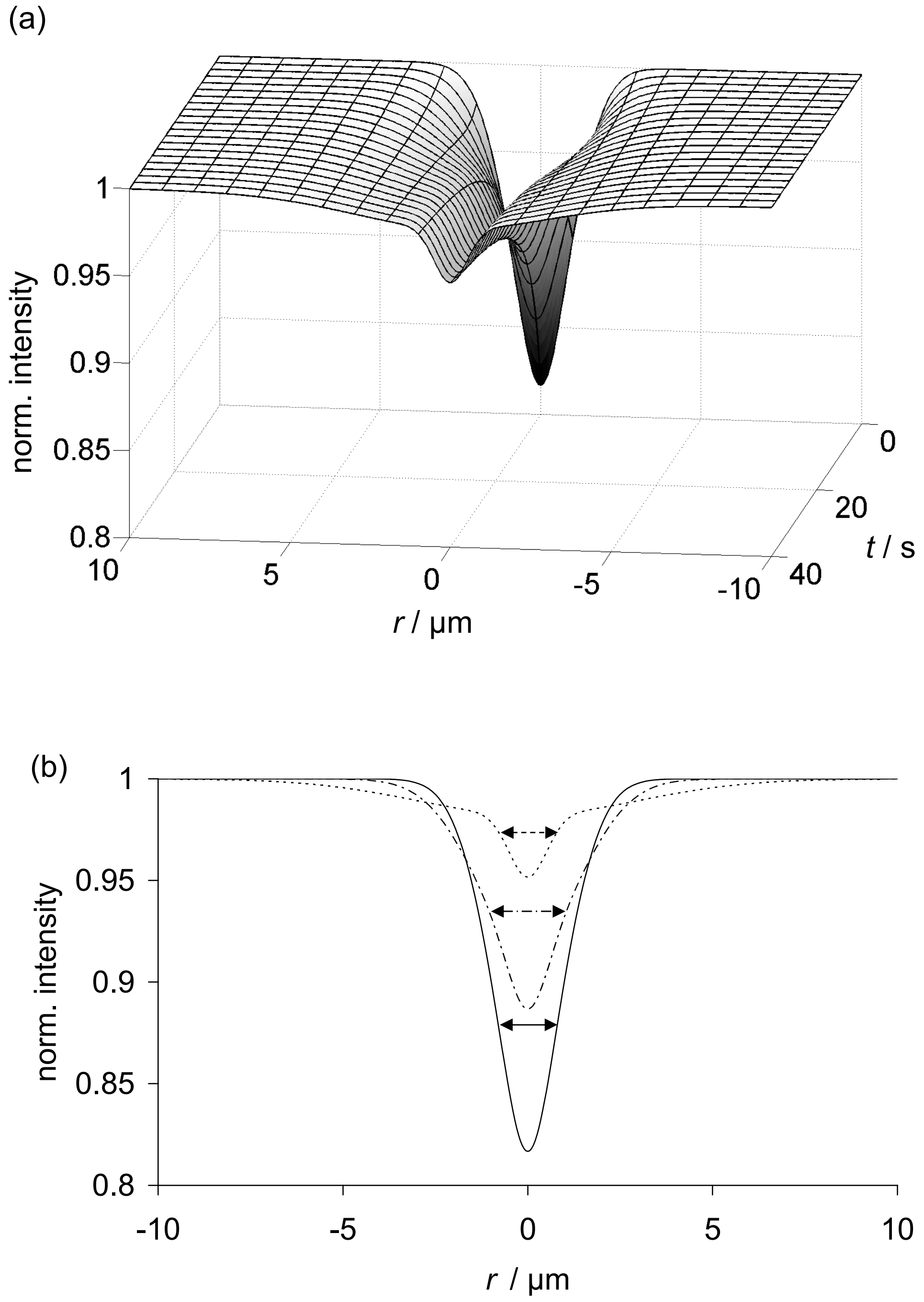

Figure 3.19 (a) Simulated shape of a typically occurring multi-Gaussian FRAP curve (normalized to $I_0 = 1$) for the case of a 2-dimensional two-component FRAP process with $D_1 = 0.1\ \mu\text{m}^2\cdot\text{s}^{-1}$ and $D_2 = 0.0001\ \mu\text{m}^2\cdot\text{s}^{-1}$ in a ratio of 20:1 (initiated by a bleaching beam with $w_0 = 0.5\ \mu\text{m}$ and a delay of 4 s between bleaching and scanning of the first image). (b) Sections through (a) corresponding to $t = 0$ s (full line), $t = 10$ s (chain-dotted line), and $t = 40$ s (dotted line) and illustration of their $\text{e}^{-1/2}$-diameters.

The two notable consequences resulting from these phenomena, which indicate that the treatment based on one single diffusion coefficient will fail, are as follows: First, when w^2 is plotted versus time for multi-component diffusion processes, one does *not* find a *linear* relationship (as in case of a single diffusion coefficient; cf. eqs (3.3) and (3.6) in Chapter 3.2.1.2), but *curves* like the ones sketched in Figure 3.20. In this respect, Figure 3.20a is characteristic of several mobile components having moderately different mobilities, whereas Figure 3.20b shows a typical result for systems where some components are markedly slower than others or even totally immobile. Secondly, the slope of a log–log plot of amplitude versus time does not reveal the correct dimension of the diffusion process, but a *smaller* number.

When such phenomena are observed, the resulting values for d and D derived from single-Gaussian fitting have no physical meaning and it is essential to apply an evaluation procedure taking into account multiple diffusion processes. In the following, an approach for data analysis is described by which the distribution of D-values can be obtained together with a simultaneous estimate of the corresponding dimensionalities in a calibration-free manner.

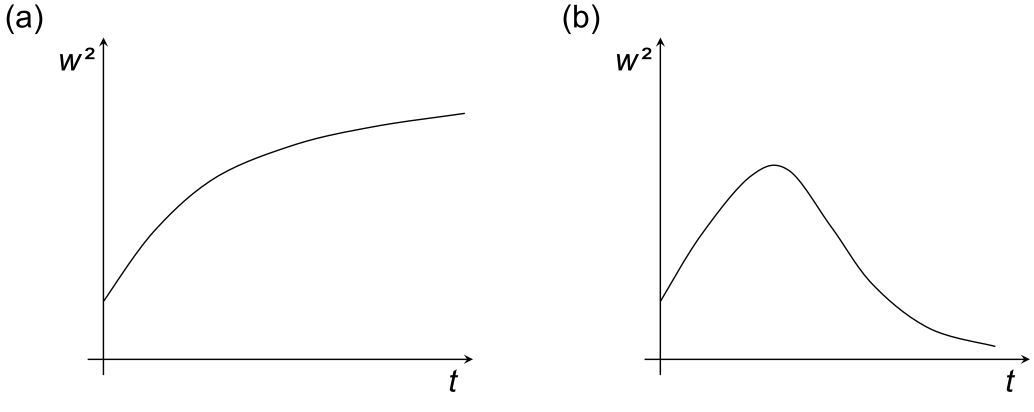

Figure 3.20 Typical shapes of apparent w^2 vs. t curves resulting from single-Gaussian fits to FRAP processes involving multi-component diffusion. – (a) depicts a w^2 vs. t plot for mixtures of several mobile components, whereas (b) shows a corresponding case involving components of markedly reduced mobility. Note that in cases where a subsequent long-time sampling is performed, one may observe a final re-increase of w^2 vs. t in (b) if the mobility of the slow fraction is sufficiently high (not shown here).

Evaluation of multi-component FRAP data

When the experimental data indicate that multi-component diffusion needs to be considered, fitting of the data set to eq (3.10) or (3.10a) is required. This yields the distribution of diffusion coefficients in terms of several discrete D-values and their respective weightings.

The analysis starts from a data set $I(r,t)$ like the one depicted in Figure 3.19a. This is obtained from the original intensity distribution in the confocal $(x;y)$-plane, $I(x,y,t)$, by appropriate averaging and normalization, as described in detail in Chapter 3.2.1 and ref [172]. Real data will contain some noise that needs to be adequately considered in the fitting routine (cf. appendix of ref [173]). The fitting procedure makes use of the whole spatial and temporal information. In this respect, the approach described goes further than suggested by Blonk et al. [188], who proceeded from a similar kind of data set but used only the temporal course of the amplitude to extract D for one-component diffusion. The decisive advantage of using the spatial information is due to the fact that the exponential term contains the quantity D only, while the amplitude contains some ratio of D and the amount of substance M together with the dimensionality d. Considering *both* terms in the fitting routine allows to *separate* M and D (as well as d, if required) and is therefore compulsory when considering multi-component diffusion. Moreover, the fitting procedure offers the possibility for an additional iterative estimate of the diameter of the bleaching beam $2w_0$. The only parameters that have to be known are the duration of the bleaching process and the time lag between bleaching and the measurement of the first image to adjust the experimental time scale. However, they are both adjustable in the experiment or can at least be obtained from instrumental settings.

It is required to establish the best estimate of w_0, I_0, pairs of D_i and M_i, and, if desired, d_i. In order to reduce calculation time and to avoid as much as possible any arbitrariness in data fitting, one has to proceed in two steps. In the first step, the *baseline* and the *diameter of the bleaching beam* are determined, with little emphasis on the actual distribution of diffusion coefficients. In the second step, the exact (discrete or continuous) *distribution of diffusion coefficients* is treated, based on the parameters obtained in Step 1. The bleaching process itself is modeled in a stepwise manner (typically 10−100 discrete steps), allowing for diffusive broadening of the concentration profile between successive bleaching steps.

Step 1. In the first step, w_0, I_0, and 3−6 D_i;M_i pairs (as well as d_i, if desired) are taken as adjustable parameters. An iteration method is applied to obtain the parameter set giving the best agreement between experimental data and simulated ones according to eq (3.10). Note that in some cases, w_0 may be composed of several (2−3) $w_{0,j}$ with fractions a_j according to eq (3.10a) which is then used in place of eq (3.10) for the simulation.

Possibly occurring variations of the mean background intensity I_0 can be corrected either by using individual $I_{0,t}$ for each profile, or by incorporating a steady baseline shift as $I_0(t) = I_0(0) + const \cdot t$. The latter approach seems justified to account for bleaching during the scanning process. In this case, the baseline correction has to be complemented with a rescaling of each profile by a factor $I_0(0)/I_0(t)$. The background correction works in highly reliable manner because all $I(r,t)$ are mutually coupled by representing the same (multi-component) FRAP process.

Step 2. From the parameters determined in the first step, w_0 and I_0 may now be assumed as fixed values or functions. The *D*-distribution is then recalculated by starting from *D*-values equally spaced on a logarithmic scale (e.g., ten per decade) and covering the whole range of interest. These values are kept fixed while their weighting is adjusted to obtain the best agreement between experimental and simulated concentration profiles in the whole time domain studied. Whenever a fraction M_i turns out to be negative, it is set to zero in order to avoid physically meaningless results, and the iteration is done over again. As a result of this procedure, one obtains an estimate of the distribution of diffusion coefficients. For further refinement, the procedure can be repeated by employing an increased (e.g., by a factor of 5) number of sampling points on the *D*-scale. To accelerate the calculation, the refinement is restricted to those *D*-ranges where the initial distribution shows non-zero contributions.

It should be noted that this procedure always produces a distribution, even when single-component diffusion is studied. The minimum width depends on the choice of a damping factor for nonlinear parameter estimation as described in detail in the appendix of ref [173], which has to be adjusted to the s/n ratio of the data. Typical widths correspond to ±(10–20)% of the diffusion coefficient.

As an alternative, fitting procedures based on the so-called maximum entropy method [189] can be employed in Step 2. Since it is possible that a good fit can be obtained by different distributions, the one maximizing the value of the Shannon–Jaynes entropy function [190, 191] is selected. This means that from the variety of distributions which satisfy the criteria for a good fit (e.g., $\chi^2 \approx 1$), the one with the minimum number of peaks and the maximum width for each peak is considered optimal. Therewith, the result of the analysis is consistent with the information content of the data set, and a structured distribution is only obtained if warranted by the data.

The procedure involving these two steps yields the distribution of diffusion coefficients without any need for calibration measurements (other than that of the length scale of the microscope) in reasonable computation time (about 1 h on a Pentium III 3 GHz PC when parameters are chosen as exemplified above). Its two major advantages are: significant *diffusion occurring during the bleaching process* is consistently accounted for, and *varying background intensities*, which might occur as a consequence of bleaching during scanning or as a result of varying irradiation intensities, are also appropriately considered.

The computational procedures for this purpose are part of the MATLAB software for automated FRAP analysis already mentioned in Chapter 3.2.1. Since the fitting parameters to be determined are coupled in a complex way, and since their influence on the achieved fitting-progress is distributed in a highly nonlinear manner, some improvements were implemented into the classical Gauss–Newton nonlinear fitting algorithm [192]. They are explained in detail in the mathematical appendix of ref [173]. Regarding the possibilities for maximum entropy based parameter estimation, several ways to implement corresponding algorithms have been described in literature (e.g., cf. [189]).

3.2.2.3 Materials and methods

Samples

Red fluorescently labeled polystyrene microspheres of type “580/605” with nominal diameters of 24 and 100 nm were purchased as aqueous suspensions with concentrations of 2 wt.-%, respectively, from Molecular Probes (Eugene). A check of their particle sizes was performed by dynamic light scattering (DLS), ultracentrifugation (UA), and atomic force microscopy (AFM) in Chapter 3.1.3, as well as by FRAP analyses in Chapter 3.2.1.

Furthermore, UV–vis and fluorescence spectroscopy were utilized to characterize the spectral properties of the spheres. Irrespective of their size, both types of spheres exhibit similar excitation and emission spectra ($\lambda_{\text{max}}^{\text{ex}}$ = 580 nm, $\lambda_{\text{max}}^{\text{em}}$ = 605 nm). Moreover, spectral analyses confirmed that equal masses of the different spheres (corresponding to equal volumes of the parent suspensions) yield equal fluorescence intensity, which is the value to be quantified in FRAP analyses. Hence, *D*-distributions from these samples are obtained as weight-averaged fractions.

As final samples, portions with wt.-ratios of 10:90, 30:70, 50:50, 70:30, and 90:10 of the two differently sized spheres were prepared simply by mixing analogous volumes of the stock solutions, with each mixture being prepared twice. Finally, one of the two samples of each composition was additionally mixed with an aqueous solution of 60 $\text{g}\cdot\text{L}^{-1}$ polyacrylamide (PAAm, prepared by free-radical polymerization in similar manner as described in 3.1.2.1; M_W = 200 000 $\text{g}\cdot\text{mol}^{-1}$, M_W/M_N = 2.11) in a ratio of 50:50 to obtain semidilute polymer solutions with a polymer concentration of 30 $\text{g}\cdot\text{L}^{-1}$ and enclosed microsphere-fractions of together 1 wt.-%. For comparison, the samples with no added PAAm were diluted with deionized water in a ratio of 50:50 in order to show a similar s/n ratio. Due to the selective deceleration of the particle diffusion by the polymer matrix, an efficient separation of the different *D*-values compared to the corresponding basic values in aqueous suspension was achieved and therewith, discrete *D*-distributions covering different *D*-ranges could be prepared.

Estimation of *D*-distributions

FRAP

Samples for FRAP experiments were prepared by placing a droplet of each solution on a microscopy slide, putting a cover glass on top, and sealing the system with nail polish. Subsequently, point-bleaching experiments were performed in the same manner as reported in Section 3.2.1.4. After bleaching, a series of typically 20 images was recorded to document the recovery process with a sampling rate of about 5 fps at a spatial resolution of 256 × 256 pixels in the case of the aqueous microsphere-suspensions as well as about 1 fps at a spatial resolution of 512 × 512 pixels in the case of the slower diffusing microsphere-mixtures in semidilute PAAm matrixes. All experiments were conducted at $T = (25 \pm 0.1)$ °C.

Data extraction and fitting

The analysis of the recorded images was again automatically performed by the MATLAB software mentioned above. All fitting results and interesting intermediate data (such as the averaged intensity profiles) were written to hard disk.

3.2.2.4 Results and discussion

To evaluate the data analysis, suspensions containing two labeled species with different mobilities and thus being characterized by a bimodal distribution of diffusion coefficients were investigated. Appropriate samples were prepared by mixing aqueous suspensions of fluorescently labeled polystyrene microspheres with different sizes (nominal diameters 24 and 100 nm) in various compositions. Note that for the smaller spheres, dynamic light scattering and ultracentrifugation gave a hydrodynamic radius around 14–17 nm, while the particle radius determined by AFM was 12 nm. For the larger spheres, the hydrodynamic radius was identical to the one determined by AFM (~50 nm; cf. Table 3.5, p 95).

A second set of bimodal samples was prepared where the aqueous phase contained 30 $g{\cdot}L^{-1}$ of polyacrylamide (PAAm). The semidilute polymer solution reduces the diffusion coefficients of the spheres significantly with the impact on the larger particles being more pronounced. (The correlation length of the PAAm solution is of the same order of magnitude as the radius of the spheres; q.v., Table 4.8 in Chapter 4.2.4.1. This means that the medium cannot be regarded as a continuum with fixed macroscopic viscosity, unlike pure water. The ratio of the diffusion coefficients of large and small spheres in semidilute PAAm solution is therefore different from their ratio in pure water.)

FRAP experiments performed on the samples were analyzed by the method presented in this chapter. The dimensionality d was either used as a fixed parameter, $d = 2$, or d was included as additional free parameter in the fitting procedure. For comparison, also the single-Gaussian fit treated in Chapter 3.2.1 was applied. Results are summarized in Table 3.7 and depicted in Figure 3.21. The quality of the fit with fixed d is illustrated in Figure 3.22 exemplarily for the system composed of a 70:30 mixture of the 100 and 24 nm spheres in simple aqueous (Figure 3.22a) as well as polymer-containing medium (Figure 3.22b).

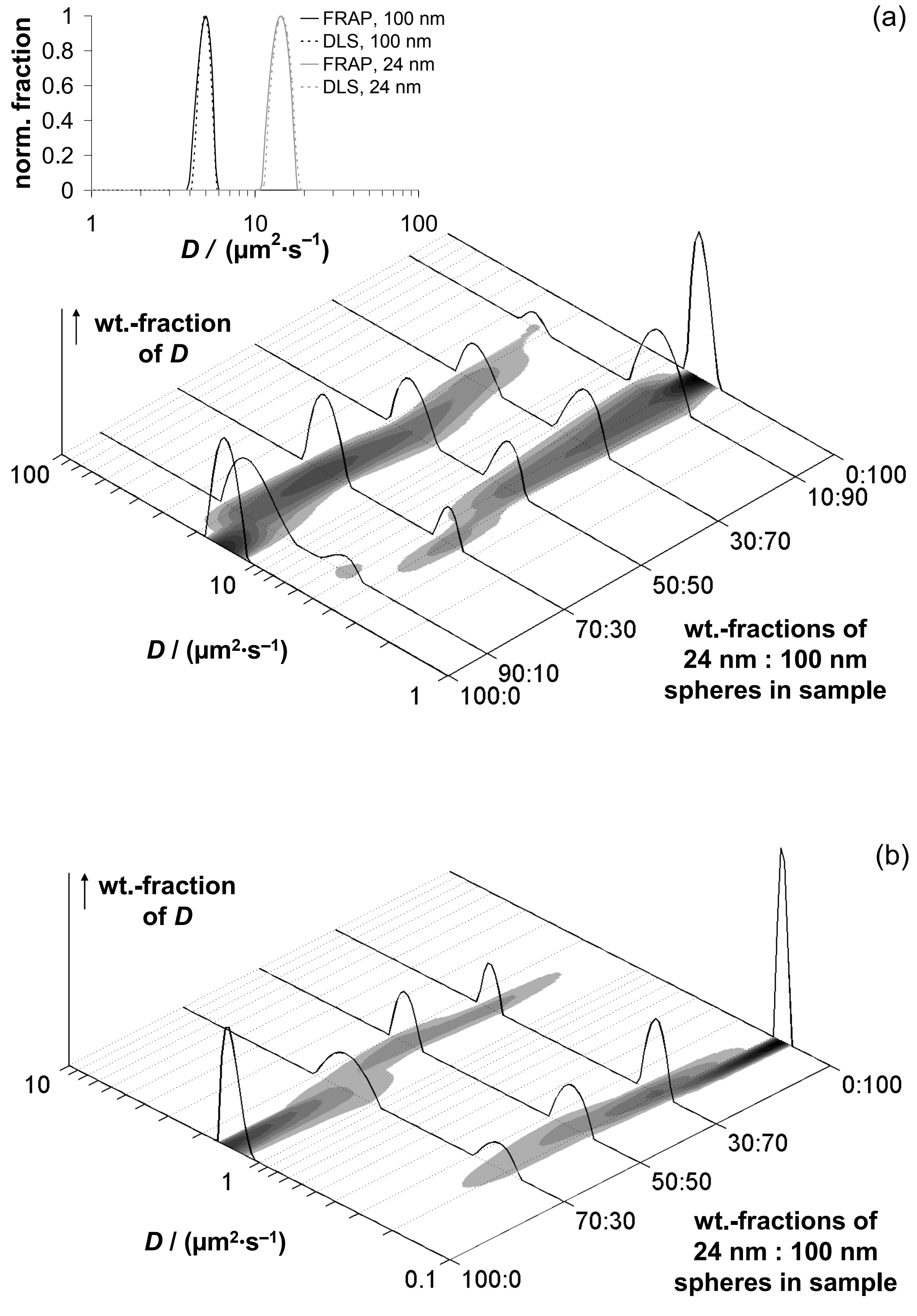

Figure 3.21 D-distributions estimated on mixtures of differently sized polystyrene microspheres in (a) aqueous suspension and (b) 30 g·L^{-1} semidilute PAAm matrix. – The shading below the signals visualizes their intensity in an alternative form. The inset in (a) illustrates the D-peaks of the single species in aqueous suspensions obtained from FRAP in nice agreement with analogously determined data deduced from DLS correlation curves.

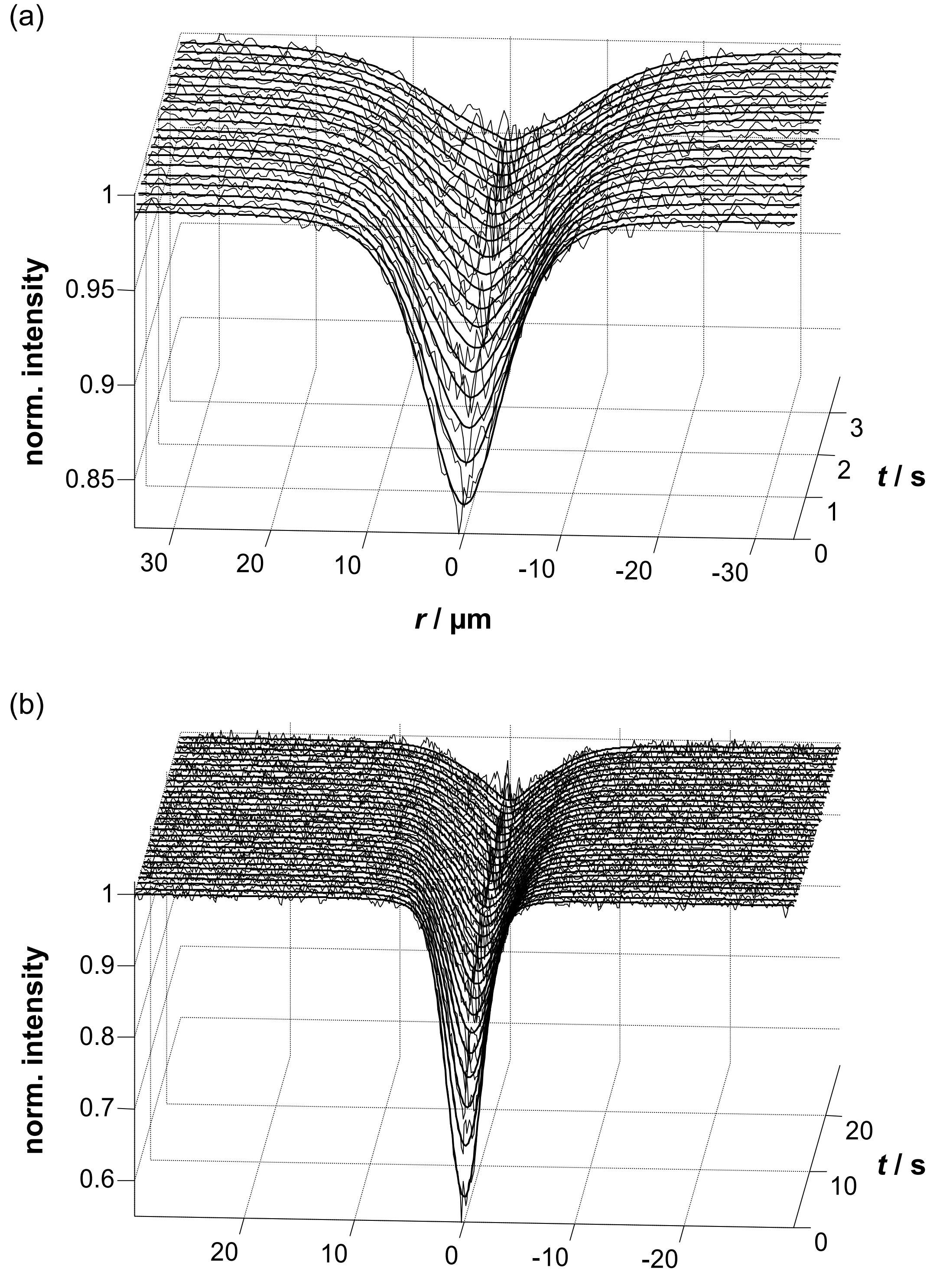

Figure 3.22 Illustration of the fit of eq (3.10) (smooth lines) to experimental data sets (noisy lines) obtained from 70:30 mixtures of 100 and 24 nm microspheres in (a) aqueous suspension and (b) 30 g·L^{-1} semidilute PAAm matrix.

Table 3.7 Results of FRAP measurements on mixtures of differently sized polystyrene microspheres (a) in simple aqueous suspension and (b) in the presence of a 30 g·L^{-1} PAAm matrix. – Compiled are the (apparent) D-values as determined by a single-Gaussian fit according to Chapter 3.2.1 (D_{single}), as well as the individual D-values obtained by analyzing the mixtures by the method described in this chapter (D_{multi} and corresponding percentages) either using a dimensionality fixed to $d = 2$ or including d as additional free fitting parameter.

(a)

Composition of sample		**One-component analysis**	**Multi-component analysis with fixed *d*=2**		**Multi-component analysis with adjustable *d***		
Type of spheres diameter	**Fraction** wt.-%	D_{single} $\mu m^2 \cdot s^{-1}$	D_{multi} $\mu m^2 \cdot s^{-1}$	**Fraction** wt.-%	D_{multi} $\mu m^2 \cdot s^{-1}$	**Fraction** wt.-%	d
24 nm	0	4.8	4.9	100	4.0	100	2.00
100 nm	100						
24 nm	10	4.7	16.7	8.5	5.1[a)]	100[a)]	2.00[a)]
100 nm	90		5.1	91.5			
24 nm	30	6.0	17.8	36.6	15.2	20.3	1.94
100 nm	70		5.1	63.4	6.3	79.7	1.88
24 nm	50	7.3	15.5	57.0	15.5	53.8	2.00
100 nm	50		5.0	43.0	5.2	46.2	2.00
24 nm	70	10.4	17.3	77.1	18.3	66.8	1.97
100 nm	30		4.0	22.9	4.8	33.2	1.96
24 nm	90	13.9	16.6	85.5	17.2	84.7	2.00
100 nm	10		5.6	14.5	5.1	15.3	2.10
24 nm	100	14.8	14.2	100	16.3	100	1.99
100 nm	0						

[a] For this particular system, no separation of the two individual components could be observed.

Table 3.7 *Continued.*

(b)

Composition of sample		One-component analysis	Multi-component analysis with fixed d=2		Multi-component analysis with adjustable d		
Type of spheres diameter	**Fraction** wt.-%	D_{single} $\mu m^2 \cdot s^{-1}$	D_{multi} $\mu m^2 \cdot s^{-1}$	**Fraction** wt.-%	D_{multi} $\mu m^2 \cdot s^{-1}$	**Fraction** wt.-%	d
24 nm 100 nm	0 100	0.19	0.21	100	0.25	100	2.00
24 nm 100 nm	30 70	0.18	1.54 0.21	31.1 68.9	1.14 0.16	29.3 70.7	1.90 2.09
24 nm 100 nm	50 50	0.24	1.29 0.20	48.6 51.4	1.55 0.22	51.8 48.2	2.06 1.94
24 nm 100 nm	70 30	0.36	1.36 0.20	71.6 28.4	1.35 0.20	71.0 29.0	2.00 2.00
24 nm 100 nm	100 0	1.11	1.42	100	1.13	100	2.13

At first, the D-values observed in water (Table 3.7a) are considered. They were calculated by taking the intensity-weighted averages of the corresponding (single) peaks in Figure 3.21a. For the pure species (top and bottom entries), there is good agreement between the results obtained by the methods based upon single and multiple diffusion processes (with a variation below ±10%), and the correct dimensionality was found when d was taken as an adjustable parameter. This is an important finding as it demonstrates that the evaluation allowing for a distribution of diffusion coefficients does *not produce artefacts* when there is actually just one single D. The hydrodynamic radii calculated from the D-values obtained on the aqueous suspensions ($D_{24\text{ nm}} = (15.1 \pm 1.1)\ \mu m^2 \cdot s^{-1}$ and $D_{100\text{ nm}} = (4.6 \pm 0.5)\ \mu m^2 \cdot s^{-1}$) utilizing the Stokes–Einstein equation (2.43) with $T = 25\ °C$ and the viscosity of the surrounding medium $\eta = 0.89$ mPa·s, are

$$r_{24\text{ nm}} = (16.2 \pm 1.2)\text{ nm} \qquad \text{and} \qquad r_{100\text{ nm}} = (53.7 \pm 5.8)\text{ nm}$$

in excellent agreement with the data resulting from dynamic light scattering and ultracentrifugation (cf. Table 3.5, p 95).

Considering the *mixtures* of differently sized microspheres, Figure 3.21a and Table 3.7a show that the evaluation based on multiple diffusion processes and fixed *d* recovers the *D*-values of the constituent components with high precision. This is true for the whole range of mixing ratios studied, even when one component is present in great excess. Additionally, the corresponding percentages of the two species as estimated by integration of the peaks in Figure 3.21a agree reasonably well with their expectations. When *d* was included as a free fitting parameter, most of the results were of similar quality, and the dimensionalities obtained were very close to the expected value of 2. This agreement is particularly noteworthy because the *D*-values of the two components differ only by a factor of about 3.5. It demonstrates that a high resolution of diffusion coefficients can be achieved. There was only one exception: The 90:10 mixture (second entry in Table 3.7a) was not resolved when the method with adjustable *d* was applied. This finding points to the limits of the evaluation procedure and suggests that the method with fixed *d* is preferred when the system contains one of the diffusing species in great excess.

For the polymeric system (Table 3.7b), the diffusion coefficients of the two components are further apart, and the agreement between expected and experimentally determined percentages is significantly better. The results obtained on these model systems show that the method of data evaluation considered in this chapter allows for the quantification of multiple discrete diffusion processes in calibration-free manner with high precision, provided the diffusion coefficients differ by a factor of 3 or more.

When, as an alternative procedure, the maximum entropy method was applied, it was not possible to resolve the two components of the aqueous suspensions, but broad distributions were obtained instead, whose average values were close to the ones achieved by the method based on a single diffusion coefficient. However, a distribution with two separated peaks was achieved for the corresponding measurements on polymer-containing samples, where the diffusion coefficients of the constituent components differed by a factor of approximately 6. The data obtained were close to the distributions listed in Table 3.7b. It can thus be concluded that the maximum entropy method yields separated *D*-values for different components only when their mobilities differ by more than a factor of about 5.

3.2.2.5 Conclusions and summary

FRAP experiments performed on a CLSM yield spatially resolved recovery data containing a multitude of information on a μm length scale. The evaluation of these data has to be adopted to whether the diffusing species is a substance exhibiting one *single* diffusion coefficient or whether it is characterized by a (discrete or continuous) *distribution* of diffusion coefficients. In the first case, the treatment described in Chapter 3.2.1 is appropriate, revealing the diffusion coefficient and the dimensionality of the diffusion process. However, systematic deviations or inconsistencies are observed when polydisperse samples are analyzed in that way. In such cases, plots of w^2 vs. t are *curved* and may even show sections having a *negative* slope. Moreover, unreasonable values are obtained for the dimensionality, because a consistent t_0-correction of the time axis is not possible. All such observations indicate that the system under study cannot be treated as having one single diffusion coefficient.

Therefore, an evaluation procedure based on a *superposition of many diffusion processes* was devised. One is thus able to estimate the *distribution of diffusion coefficients* from one FRAP experiment in calibration-free manner. Experiments on mixtures of fluorescent microspheres modeling a discrete bimodal D-distribution show that reliable results are obtained and that the percentages of the constituent components are recovered to within approximately ±10% when the diffusion coefficients of the individual components differ by a factor of 3. The accuracy is markedly improved when the diffusion coefficients are further apart. The procedure also allows for taking into account effects that in some cases impair FRAP experiments, e.g., a shift in background intensity as it might result from bleaching during scanning.

In principle, the method can be applied to more than two components, provided their diffusion coefficients are sufficiently apart. This would require an appropriately adapted sampling sequence, which can only be selected after some prior knowledge of the expected mobilities. It is therefore generally necessary to perform the experiment twice, where the second run uses an improved sampling sequence based on a rough estimate of the distribution obtained in the first run. If there are many diffusing components with different mobilities, e.g., such as in many natural and synthetic polymers, nanoparticles, and various types of aggregated materials, the exact shape of the derived distribution may be affected by experimental parameters, noise, etc. However, relevant mean values can be calculated reproducibly.

4 Structure and tracer dynamics in polyacrylamide hydrogels

4.1 Hydrogel formation by photocrosslinking of dimethylmaleimide-functionalized polyacrylamide

4.1.1 Introduction

Having performed the preliminary work presented in Chapter 3, one is able to face the main objectives of the present work, that is,

(i) to investigate the *gelation procedure* and the *network structures* in hydrogel systems obtained when photoactive precursor chains are successively crosslinked via a photochemical gelation pathway

and

(ii) to study the *dynamics* of fluorescently labeled *probes* that are enclosed in such systems.

The following chapters focus on these analyses. First, a fundamental examination of the *successive formation of PAAm networks* by means of *photochemical [2+2]-dimerization of pendant dimethylmaleimide (DMMI) moieties* is presented. For this purpose, the DMMI dimerization reaction in aqueous solution is studied on low molecular weight *model compounds*, and the *kinetics* of the gelation process when PAAm hydrogels are formed by means of DMMI sidegroup dimerization is investigated, particularly focusing on the possibilities to *monitor and control the progress of the reaction*. Secondly, *rheological* measurements and *multiple-quantum NMR* experiments provide information on the *network structures* from a macroscopic and a microscopic point of view, respectively. The present chapter thus covers the left part of the comprehensive schedule sketched in Chapter 1 as highlighted in Figure 4.1. A publication of these contents can be found in ref [193].

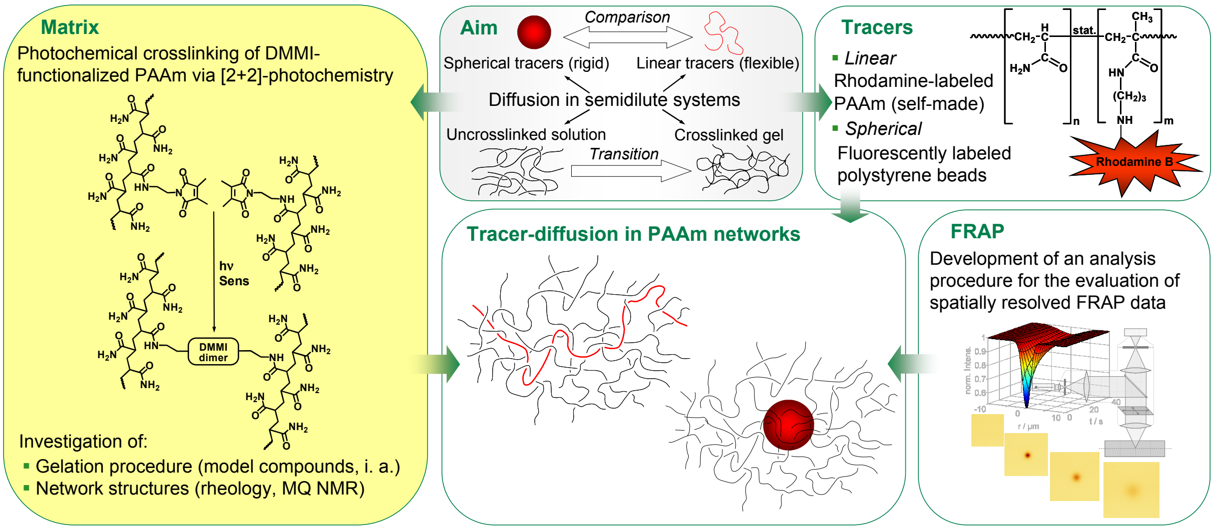

Figure 4.1 Classification of Chapter 4.1 in the context of the present work.

4.1.2 Theoretical background and strategy

As stated in Chapter 2.3.5.3, suitable groups which undergo photodimerization and can therefore be used to photocrosslink accordingly functionalized polymers comprise cinnamate (and related) moieties [105–108, 128–135, 150, 151], coumarins [109–112, 136, 137], and maleic acid derivatives like dimethylmaleimide (DMMI) [113–117, 138–148]. One of the major drawbacks of cinnamates, besides advantageous features such as controlled reversibility of the dimerization [132], is the photochemically induced *cis/trans* isomerization resulting in a noticeable decrease of the quantum yield of photocrosslinking [138]. A second shortcoming is their susceptibility to radical reactions, which precludes them from being used in radical copolymerizations. By contrast, coumarins and DMMIs do not show these disadvantages, since their photoreactive olefinic bonds are protected from radical polymerization by shielding vicinal methyl groups while, additionally, *cis/trans* isomerizations are precluded by inclusion into a ring-structure. Hence, functionalization of polymers with such moieties is possible by various pathways including radical copolymerization with adequate comonomers while, furthermore, the “waste of photons” to undesired side reactions is largely prevented.

For the present work, the DMMI functionality was chosen to be employed because of its higher polarity and water solubility, and because of favorable spectroscopic and electronic properties (see below) in comparison to coumarins.

As also pointed out in Chapter 2.3.5.2, photochemical [2+2]-cycloaddition reactions can basically start from both the excited singlet (S_1) and triplet (T_1) state of one of the two molecules eventually forming the dimer. In the first case, the reaction occurs in a concerted action and yields cyclodimers in the stereospecific *cis* form, whereas the reaction from the T_1 state proceeds in a stepwise manner, and dimeric products thus obtained are a mixture of *cis* and (favored) *trans* isomers.

As the energy of the excited singlet state of DMMI is considerably higher than that of the triplet state, direct excitation of DMMI requires short-wave UV light which might as well cause unwanted degradation of the polymer chains. It is therefore advantageous to proceed from the T_1 state, which can be reached by energy transfer from an excited, suitably chosen *sensitizer* as described by Hammond et al. [118, 122–125]; cf. Chapter 2.3.5.2. Proper sensitizer molecules for this purpose are aromatic ketones since they generally show a combination of small energy gaps between the S_1 and T_1 states as well as strong spin–orbit coupling, thus leading to high quantum yields of intersystem crossing. In addition, their $n\pi^*$ or $\pi\pi^*$ triplet states provide sufficiently high energy levels and lifetimes [126] to enable effective energy transfer to a substrate.

The majority of aromatic ketones possess $n\pi^*$ triplet states. These molecules can undergo various types of side reactions such as hydrogen abstractions or Paterno–Büchi additions [119, 194, 195]. Hence, molecules with $\pi\pi^*$ triplet states are preferred as sensitizers, because unwanted reactions can be largely excluded. There have been several studies showing that the T_1 state of *thioxanthones* in polar media corresponds to a $\pi\pi^*$ transition [196, 197]. Thioxanthones have thus been widely used for photosensitization and -initiation purposes [138, 142, 198, 199]. The energy of their T_1 state is relatively high [119, 122, 200] and only marginally less than that of S_1. Intersystem crossing occurs with high quantum yield [200–202], and they show adequately long triplet lifetimes [196]. For the present work, the sodium salt of thioxanthone disulfonate was employed. It is noteworthy that its sulfonate groups only act in terms of increasing the water solubility without affecting the spectral properties significantly [196, 203].

To illustrate the photophysical properties of the DMMI/TXS system in a quantitative fashion, Table 4.1 compiles some of its characteristic values. The data clearly emphasize the *effective separation* of the excitation wavelengths and energies of the different chromophores, thus enabling a selective excitation of the DMMI substrate only by means of (triplet) energy transfer and, hence, allowing for mild irradiation conditions and for independent adjustment of the concentrations of the light absorbing and the reacting species.

Table 4.1 Important photophysical properties of the chromophores used in this chapter.

λ_{max}(fl.-ex.): wavelength for maximum fluorescence excitation
λ_{max}(fl.-em.): wavelength of maximum fluorescence emission
E_S: energy level of the first excited singlet state
E_T: energy level of the first excited triplet state
τ_S: average lifetime of the first excited singlet state
τ_T: average lifetime of the first excited triplet state
ϕ_{isc}: quantum yield of intersystem crossing

If not otherwise stated, values are reported for aqueous media.

Property	**Thioxanthone disulfonate (TXS)**		**Dimethylmaleimide (DMMI)**	
	Value	References and remarks	Value	References and remarks
λ_{max}(fluo.-ex.) / nm	381	[196]	229	λ_{max} from UV–vis spectrum HE-DMMI
λ_{max}(fluo.-em.) / nm	437	[196]		
E_S / (kJ·mol^{-1})	293	Derived from 0–0-transition in fluorescence spectra	~520	Simply approximated from λ_{max} in UV–vis spectrum of HE-DMMI
E_T / (kJ·mol^{-1})	(274)	Value for parent thioxanthone in nonpolar media [119, 122]	(255)	Value for related dimethylmaleic anhydride [118]
	(267)	Value for parent thioxanthone in acetonitrile [200]		
τ_S / ns	6.8	[196]		
τ_T / μs	109	[196]		
ϕ_{isc}	~1	Value for thioxanthone [201]; may appear reduced in polar media [200, 202]		

4.1.3 Experimental

4.1.3.1 Materials

***N*-(2-Hydroxyethyl)-dimethylmaleimide (HE-DMMI).** HE-DMMI was synthesized in similar manner as described in ref [138] by heating a solution of 75 mmol 2-aminoethanol (Aldrich) and 75 mmol dimethylmaleic anhydride (Aldrich) in 200 mL toluene (Aldrich) for 2 h at 120 °C on a water trap. After removing the solvent, the crude product was purified by solid-state distillation at 110 °C / 0.05 mbar with a cooling water temperature of about 70 °C to give HE-DMMI as a whitish solid in quantitative yield that was characterized by ^{1}H and ^{13}C NMR spectroscopy:

^{1}H NMR (400 MHz, $CDCl_3$): δ = 1.97 (s, 6H, $2CH_3$), 2.78 (br, 1H, OH), 3.61–3.81 (m, 4H, HO–$(C\underline{H}_2)_2$–DMMI) ppm.

^{13}C NMR (100 MHz, $CDCl_3$): δ = 8.7 (CH_3), 40.8 (HO–CH_2–$\underline{C}H_2$–DMMI), 61.2 (HO–$\underline{C}H_2$–CH_2–DMMI), 137.4 (C=C), 172.6 (C=O) ppm.

***N*-(*N’*-Acetyl-2-aminoethyl)-dimethylmaleimide.** A solution of 8 mmol *N*-acetyl-2-diaminoethane (Lancaster, purified by solid-state distillation at 70 °C / 0.1 mbar with a cooling water temperature of about 50 °C) and 8 mmol dimethylmaleic anhydride (Aldrich) in 50 mL toluene (Aldrich) was heated for 3 h at 120 °C on a water trap. After removing the solvent, the crude product was purified by recrystallization from hexane/ethyl acetate (1:1) to give *N*-(*N*’-acetyl-2-aminoethyl)-dimethylmaleimide as a whitish solid in quantitative yield that was characterized by ^{1}H and ^{13}C NMR spectroscopy:

^{1}H NMR (400 MHz, DMSO-d_6): δ = 1.72 (s, 3H, $\underline{H}_3$C–CONH), 1.89 (s, 6H, H_3C–C=C–CH_3), 3.15 (dt, ^3J = 6.1 Hz, 2H, CONH–$C\underline{H}_2$–CH_2–DMMI), 3.41 (t, ^3J = 6.0 Hz, 2H, CONH–CH_2–$C\underline{H}_2$–DMMI), 7.92 (t, ^3J = 5.8 Hz, 1H, CONH) ppm.

^{13}C NMR (100 MHz, DMSO-d_6): δ = 8.5 (C=C–$\underline{C}H_3$), 22.5 ($\underline{C}H_3$–CONH), 36.9 (CONH–$\underline{C}H_2$–CH_2–DMMI), 37.3 (CONH–CH_2–$\underline{C}H_2$–DMMI), 136.6 (C=C), 169.4 (CH_3–$\underline{C}$ONH), 171.7 (ring C=O) ppm.

Sodium thioxanthone-2,7-disulfonate (TXS). TXS as introduced by Gupta et al. [204] was chosen as water-soluble triplet sensitizer. Its properties have been studied by Kronfeld and Timpe [196], whose approach for synthesis and characterization was followed here. The product was obtained as a mixture with Na_2SO_4 containing about 4 wt.-% TXS (sodium salt).

***N*-(*N'*-Acryloyl-2-aminoethyl)-dimethylmaleimide (DMMIAAm).** Synthesis of DMMI-functionalized acrylamide (DMMIAAm) [143] was performed essentially according to [145]: one amine group of 2-diaminoethane (Fluka) was blocked with Boc (Fluka), the other one then reacted with dimethylmaleic anhydride (Aldrich), and, after removing the protecting group, the amine group reacted with acryloyl chloride (Merck). The following purification steps for the intermediate compounds and the final product were applied:

BocNH–$(CH_2)_2$–NH_2 was purified by vacuum distillation at 58 °C / 0.1 mbar, BocNH–$(CH_2)_2$–DMMI was recrystallized from water/ethanol (1:1), H_2N–$(CH_2)_2$–DMMI was intensively washed with methylene chloride, and DMMIAAm was purified by recrystallization from hexane/ethyl acetate (1:1).

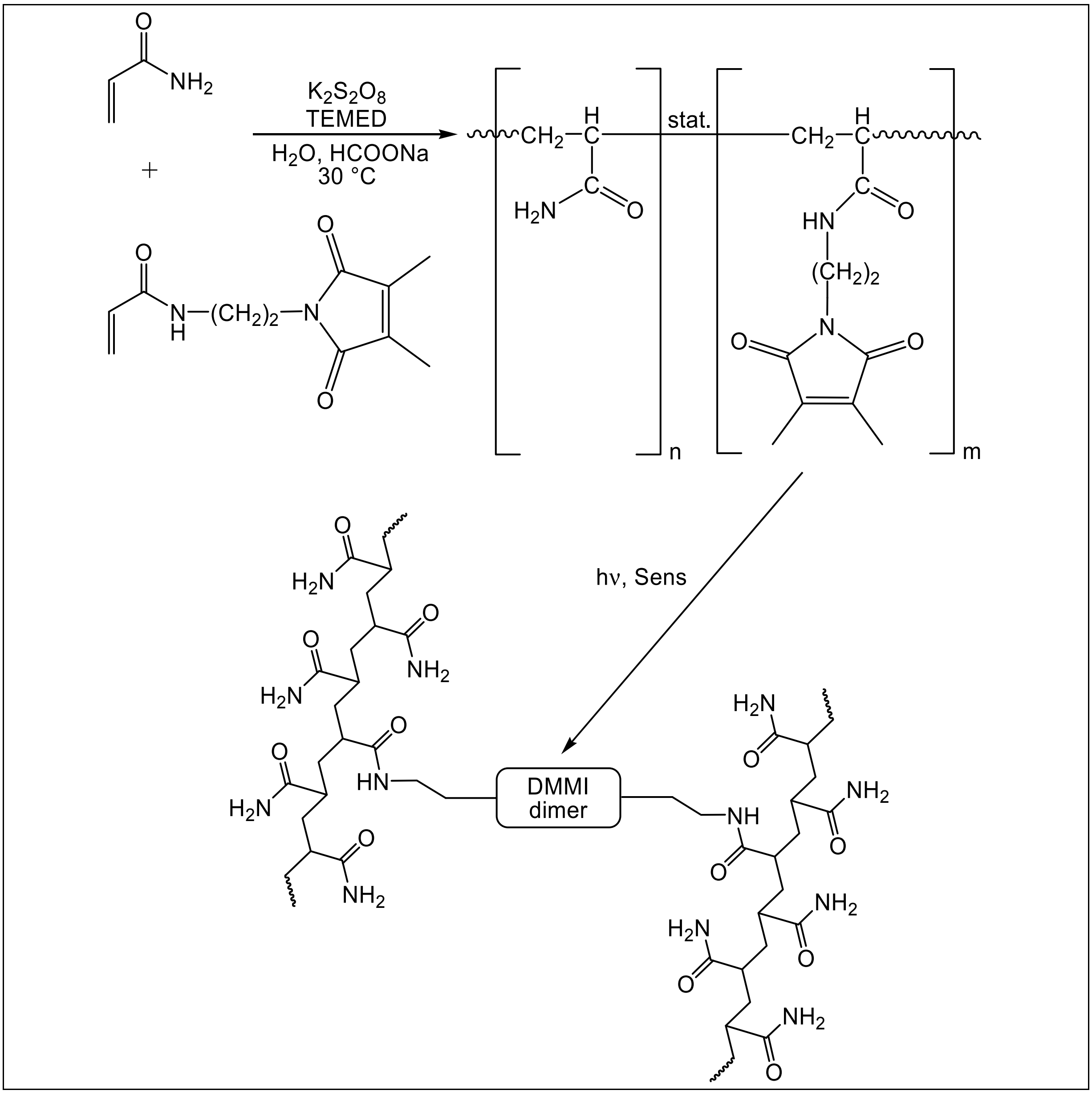

Figure 4.2 Scheme of the copolymerization of acrylamide (AAm) with *N*-(*N'*-acryloyl-2-aminoethyl)-dimethylmaleimide (DMMIAAm) and illustration of the sensitized photocrosslinking of the copolymers.

Poly(AAm-*co*-DMMIAAm). Four high molecular weight samples of P(AAm-*co*-DMMIAAm), here abbreviated as PAAm–DMMI, with varying amounts of DMMI moieties ranging from 0.7 to 2 mol-% were prepared by free-radical copolymerization as depicted in Figure 4.2 in the following manner adopted from [162]:

800 mL of an aqueous solution containing a total of 368 mmol of the monomers AAm (Merck) and DMMIAAm in the ratios summarized in Table 4.2a as well as 11.5 mmol of sodium formate (Fluka) as a chain transfer agent [161, 162] was flushed with nitrogen for about 10 min at 30 °C. The polymerization was initiated by addition of 0.1 mol-% (relating to the total amount of monomers) of potassium peroxodisulfate (Aldrich) and 0.25 mol-% of *N,N,N',N'*-tetramethylethylenediamine (TEMED, Fluka) in the form of small amounts of appropriately concentrated aqueous solutions. Several mechanisms of decomposition of the initiator–accelerator system are discussed in the literature [163, 164]. While the reaction was running at 30 °C under nitrogen atmosphere, aliquots were withdrawn from the mixture and dropped into an excess of methanol in order to check for precipitation. This was done every minute in the beginning and at longer intervals later. When a perceptible precipitation was noticed, the reaction was interrupted by precipitation into a tenfold excess of methanol containing about 2 wt.-% of concentrated hydrochloric acid. Conversions achieved by this procedure were about 5% in all cases treated in this chapter. The corresponding reaction times are listed in Table 4.2a. The crude product was isolated by filtration, washed with methanol, redissolved in water, and dialyzed against water for about ten days. Finally, the purified polymer was isolated by freeze drying. The obtained copolymers were characterized by ^{1}H NMR spectroscopy:

^{1}H NMR (400 MHz, D_2O): δ = 0.80–2.60 (br, xH, all backbone protons + DMMI methyl protons), 3.00–3.70 (br, 4H, CONH–$(C\underline{H}_2)_2$–DMMI) ppm.

The compositions of the copolymers were estimated from the integrals of the corresponding NMR signals. Setting the integral of the broad signal at 3.00–3.70 ppm to 4, the mole ratio of AAm and DMMIAAm groups in the copolymer is obtained from the integral x of the broad high field NMR signal (0.8–2.6 ppm) in the following manner: x was first reduced by 9 (3 backbone protons plus 6 methyl protons in each DMMIAAm residue) and afterwards divided by 3 (3 protons per AAm residue). The resulting number is the ratio AAm/DMMIAAm in the copolymer.

Table 4.2b summarizes the results for the four prepared samples discussed in this work. Also compiled in Table 4.2b are the molecular weights obtained via SEC and measurements of intrinsic viscosity. The fact that they decrease with increasing DMMIAAm fraction indicates that DMMIAAm might act as a controlling agent here (q.v., [144]). However, note that the overlap concentrations calculated from the intrinsic viscosities via eq (2.3) are in the range of 5 $g \cdot L^{-1}$ for all samples prepared, wherefore all polymer solutions treated in this chapter are semidilute.

Table 4.2 (a) Compositions of reaction mixtures for copolymerizations of AAm with DMMIAAm, as well as (b) characteristic data of the obtained low-conversion products.

(a)

Name of sample	**mol-%$_{\mathrm{AAm}}$**	**mol-%$_{\mathrm{DMMIAAm}}$**	**Reaction time**[a)] min
PAAm-DMMI1.0	99.0	1.0	35
PAAm-DMMI1.5	98.5	1.5	60
PAAm-DMMI2.0	98.0	2.0	50
PAAm-DMMI2.5	97.5	2.5	75

[a] Reaction times were adjusted to give conversions of about 5% in each case.

(b)

Name of sample	**Integral *x* in ^{1}H NMR** rel. number of protons	**DMMIAAm fraction in the copolymer** mol-%
PAAm-DMMI1.0	428.71	0.71
PAAm-DMMI1.5	275.78	1.11
PAAm-DMMI2.0	201.75	1.53
PAAm-DMMI2.5	158.97	1.96

(b) – *Continued.*

Name of sample	M_{N}[b)] g·mol^{-1}	M_{W}[b)] g·mol^{-1}	$M_{\mathrm{W}}/M_{\mathrm{N}}$	[η] mL·g^{-1}	M_{η}[b)] g·mol^{-1}
PAAm-DMMI1.0	361 500	920 000	2.55	245.175	640 000
PAAm-DMMI1.5	301 000	775 500	2.58	198.390	480 000
PAAm-DMMI2.0	241 500	574 500	2.38	192.190	460 000
PAAm-DMMI2.5	207 500	531 000	2.56	162.726	370 000

[b] Number and weight average molecular weights (M_{N} and M_{W}) were obtained as apparent pullulan equivalent values by SEC. Viscosity average molecular weights (M_{η}) were calculated from the intrinsic viscosities [η] in polymer solutions in 0.5 mol·L^{-1} aqueous NaCl at 25 °C with the aid of Mark–Houwink–Sakurada parameters as reported by McCarthy et al. [42c].

4.1.3.2 Characterization

UV–vis absorption spectra were obtained on a Jasco V-550 spectrometer.

High-resolution ^{1}H and ^{13}C NMR spectra were recorded on a Bruker Avance 400 digital FT spectrometer at 400 MHz and 100 MHz, respectively. Chemical shifts are reported in ppm relative to internal tetramethylsilane (δ = 0.00 ppm) for organic solvents and relative to internal H_2O (δ = 4.79 ppm [165]) when D_2O was used as solvent. Abbreviations: s = singlet, d = doublet, t = triplet, q = quartet, m = multiplet, br = broad.

Mass spectra were recorded on a Hewlett–Packard HP5989 MS engine with 70 eV electronic ionization.

SEC measurements were performed commercially by Polymer Standards Service GmbH (PSS Mainz, Germany) utilizing PSS Suprema columns with an eluent composed of 0.1 mol·L^{-1} NaCl / 0.1 vol.-% TFAc. Calibration was performed with pullulan standards. Hence, molecular weights are obtained as apparent pullulan equivalent values.

Measurements of solution-viscometry were made on polymer solutions with concentrations of 0.5, 1, 1.5, and 2 g·L^{-1} at 25 °C using an Ubbelohde-viscometer with a capillary diameter of 0.36 mm. The solvent employed was an aqueous solution of 0.5 mol·L^{-1} NaCl in each case. Intrinsic viscosities were estimated with the aid of Huggins plots. For calculation of the viscosity average molecular weight, Mark–Houwink–Sakurada parameters reported by McCarthy et al. [42c] were used.

4.1.3.3 Irradiation conditions

The light source employed for most of the photochemical dimerization and crosslinking reactions was a 100 W xenon short arc lamp (Osram XBO) providing a broad and relatively unstructured spectrum in the range of 200–500 nm. By using two different optical filters, suitable wavelength-ranges were selected: a broad band-pass filter of type BG25 (Reichmann Feinoptik GmbH, Brokdorf, Germany) enabled the efficient excitation of the thioxanthone sensitizer while simultaneously blocking UV light with $\lambda < 310$ nm, while a narrow-band interference filter of type 380FS10-50 (LOT Oriel, Darmstadt, Germany) was chosen for selective excitation at (383 ± 5.6) nm when high intensity was not necessary or appropriate. Figure 4.3 shows the UV–vis absorption spectra of HE-DMMI and of TXS in water together with the transmittance curves of the two filters. Irrespective of which filter is employed, there is overlap only with the long wave absorption band of TXS. This choice of conditions ensures that the DMMI moieties cannot be excited directly, but only via energy transfer from the TXS sensitizer.

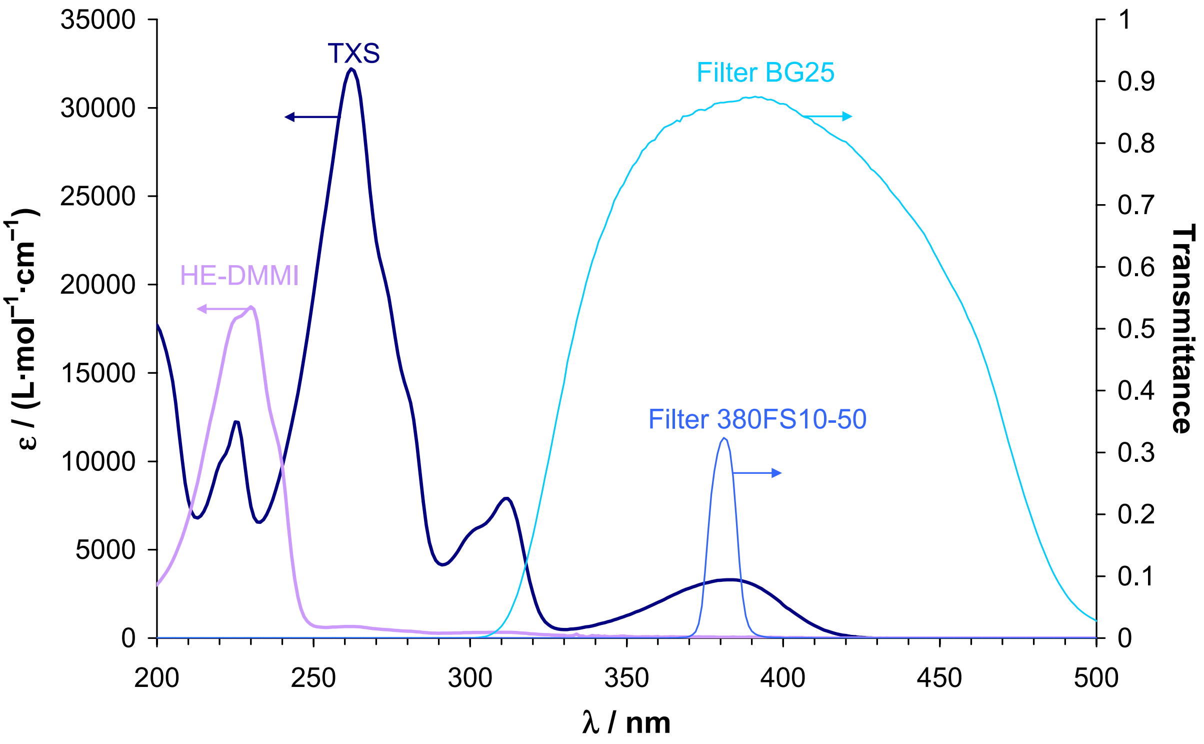

Figure 4.3 UV–vis spectra of *N*-(2-hydroxyethyl)-dimethylmaleimide (HE-DMMI) and sodium thioxanthone disulfonate (TXS) in water, as well as transmittances of the optical filters used for mechanistic and kinetic investigations of the PAAm–DMMI crosslinking.

4.1.3.4 Model reactions

50 mL of an aqueous solution containing 8 mmol·L^{-1} of HE-DMMI and 0.08 mmol·L^{-1} of TXS were irradiated through the band pass filter BG25 in a 100 mL round-bottomed flask for about 45 h as depicted in Figure 4.4a. Thereby, the formation of a small amount of a white precipitate was observed. At several intervals during irradiation, aliquots were withdrawn via syringe and analyzed by UV–vis spectroscopy using quartz cuvettes with a layer thickness of 100 µm (Hellma). When no further conversion was detected (after 45 h), the irradiation was stopped. The precipitate was isolated by filtration to yield about 5 mg of a white solid, while approximately 95 mg of a second whitish solid were obtained by vacuum evaporation of the solvent from the filtrate. (Note that part of this solid is Na_2SO_4 contained in the sensitizer.) Both products were characterized without further purification by ^{1}H and ^{13}C NMR spectroscopy in D_2O (originally dissolved product) and DMSO-*d*$_6$ (precipitate), as well as mass spectrometry.

(a) Precipitated product (cf. Figure 4.6a)

^{1}H NMR (400 MHz, DMSO-*d*$_6$): δ = 1.09 (s, 12H, 4CH_3), 3.51–3.62 (m, 8H, 2(HO–$(C\underline{H}_2)_2$–N)), 4.93 (t, ^3J = 5.2 Hz, 2H, 2OH) ppm.

^{13}C NMR (100 MHz, DMSO-*d*$_6$): δ = 12.1 (CH_3), 41.1 (CH_2–N), 48.7 (cyclobutane-C), 56.8 (CH_2–OH), 177.7 (C=O) ppm.

m/z (EI) = 338 ([M]$^+$, 23).

(b) Dissolved product (cf. Figure 4.6b)

^{1}H NMR (400 MHz, D_2O): δ = 1.19 (d, ^3J = 7.4 Hz, 3H, upper CH_3 in right ring in Fig. 4.6b), 1.34 (s, 3H, CH_3), 1.50 (s, 3H, CH_3), 3.12 (q, ^3J = 6.8 Hz, 1H, methine H in right ring in Fig. 4.6b), 3.54–3.63 (m, 4H, HO–$(C\underline{H}_2)_2$–N in right ring in Fig. 4.6b), 3.69–3.75 (m, 4H, HO–$(C\underline{H}_2)_2$–N in left ring in Fig. 4.6b), 6.05 (d, ^2J = 0.7 Hz, 1H, olefinic), 6.43 (d, ^2J = 0.7 Hz, 1H, olefinic) ppm.

^{13}C NMR (100 MHz, D_2O): δ = 11.1 (upper CH_3 in right ring in Fig. 4.6b), 14.9 (lower CH_3 in right ring in Fig. 4.6b), 17.5 (CH_3 in left ring in Fig. 4.6b), 40.9 (CH_2–N), 50.1 (left C of ring linkage in Fig. 4.6b), 50.9 (right C of ring linkage in Fig. 4.6b), 58.0 (OH–CH_2), 124.7 (C=$\underline{C}H_2$), 139.2 ($\underline{C}$=CH_2), 170.8 (upper C=O in left ring in Fig. 4.6b), 179.7 (lower C=O in right ring in Fig. 4.6b), 181.5 (upper C=O in right ring in Fig. 4.6b), 182.0 (lower C=O in left ring in Fig. 4.6b) ppm.

m/z (EI) = 338 ([M]$^+$, 7).

A similar experiment was performed in the presence of 8 mmol·L^{-1} acetamide serving as a model compound for PAAm. Also, dimerizations of *N*-(2-aminoethyl)-dimethylmaleimide and of *N*-(*N'*-acetyl-2-aminoethyl)-dimethylmaleimide were carried out using similar conditions.

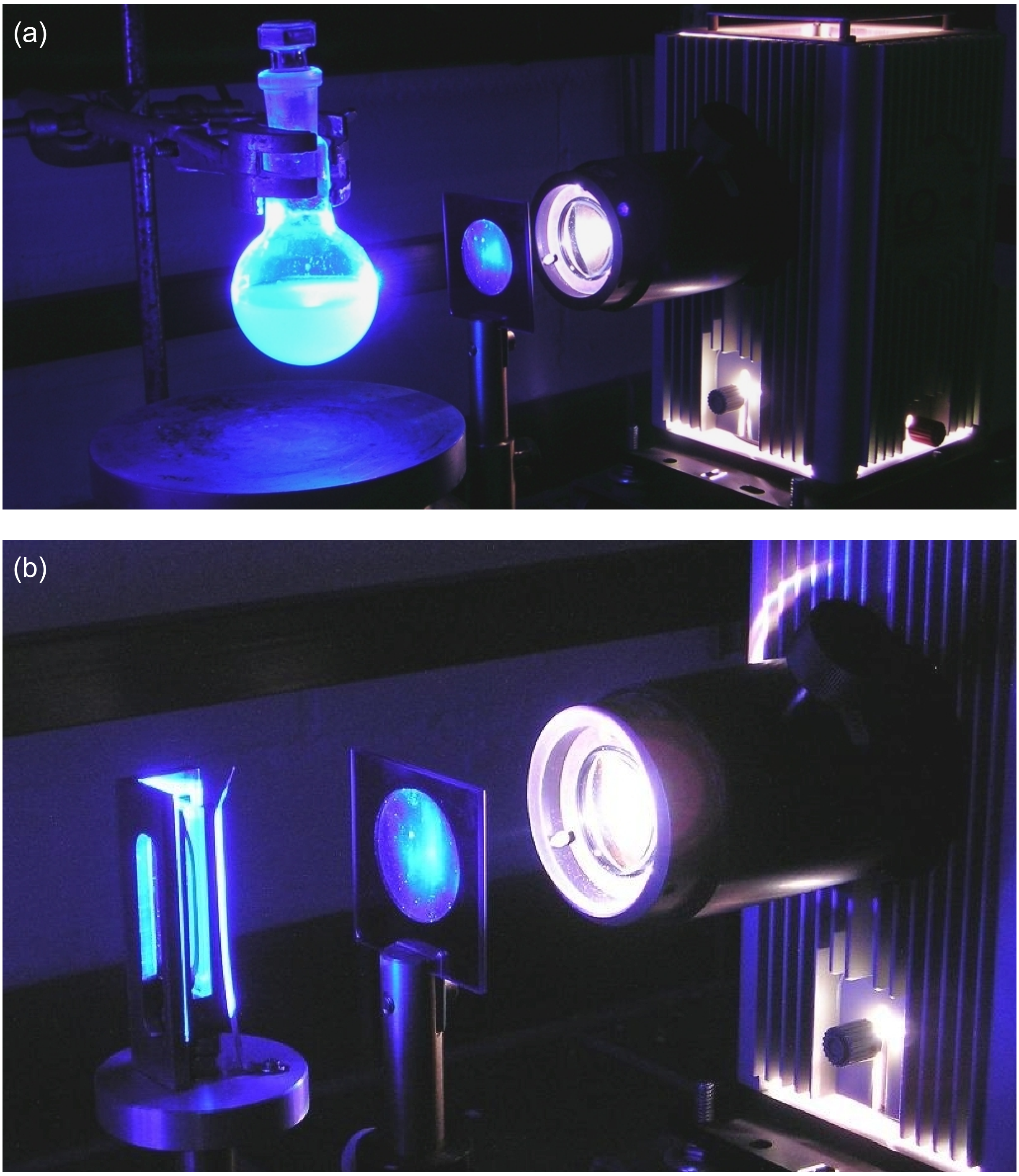

Figure 4.4 (a) Setup for the investigation of the DMMI dimerization in aqueous solution. – Components from left to right: reaction vessel with 50 mL of an aqueous solution of a proper low molecular weight model species (below: magnetic stirrer), optical filter for wavelength selection (here: BG25), UV source (here: xenon short arc lamp).
(b) Setup for kinetic studies on the crosslinking of DMMI-functionalized PAAm in aqueous semidilute solution. – Components from left to right: quartz cuvette with 100 µm layer of the test solution, optical filter for wavelength selection (here: BG25), UV source (here: xenon short arc lamp). All parts of the setup are fixed on an optical bench to realize comparable illumination conditions in each experiment. $T = (25 \pm 0.1)$ °C

4.1.3.5 Photo-induced crosslinking

To study the kinetics of the crosslinking reaction, aqueous solutions containing 50 g·L^{-1} of PAAm-DMMI1.5 and a variable amount of sensitizer were irradiated in quartz cuvettes of thickness 100 µm as depicted in Figure 4.4b. The amount of TXS was adjusted to be 1−100% relating to the concentration of DMMI chromophores. UV–vis spectra were recorded at suitable intervals. For the irradiation experiments, a setup mounted on an optical bench was used to ensure high reproducibility of the arrangement and spacing of light source, filter(s), and specimen. The temperature was kept at $T = (25 \pm 0.1)$ °C, and light intensity was checked frequently during the test series by measurement with a photodiode. Two series of measurements were conducted using either of the two optical filters specified above.

In another test series, the influence of light intensity on the reaction kinetics was analyzed. Attenuation of intensity was achieved by using cascades of the filter 380FS10-50 plus a varying number of additional BG25 filters (which practically act as neutral filters around 383 nm). Relative intensities of 100%, (83.0 ± 0.8)%, (69.5 ± 1.3)%, and (58.2 ± 1.5)% could be adjusted in the wavelength-range of (383 ± 5.6) nm, with 100% corresponding to about 0.1 mW·cm^{-2}. The concentration of PAAm-DMMI1.5 was 50 g·L^{-1} and an equimolar amount of TXS relating to that of DMMI moieties was used in this case. As characteristic values, the half-lives of DMMI conversion were determined from the UV–vis spectra as described in 4.1.4.2, and their dependencies on light dose and concentration of sensitizer were examined.

4.1.3.6 Rheology under UV exposure

Oscillatory measurements of the elastic modulus G' as a function of proceeding crosslinking were performed on a Physica MCR500 plate–plate rheometer (plate diameter 8 mm) equipped with a measurement cell of type P-PTD-UV featuring a UV-transparent lower plate, under which a light guide was positioned. Hence, irradiation of the sample was possible during a running measurement, and the rise of the elastic modulus with progressive DMMI dimerization could be determined. As UV source, an EXFO Novacure 2100 mercury arc lamp was employed, producing a high irradiation intensity of about 15 mW·cm^{-2} at the sample position. Specimens were aqueous semidilute solutions of PAAm-DMMI2.0 with concentrations of 20, 40, 60, and 80 g·L^{-1}. The amount of TXS was 1 mmol·L^{-1} in each case. Measurements were performed at 25 °C at a frequency of 4 Hz and shear amplitude of 0.5%, which was small enough to ensure linear viscoelastic behavior. The layer thickness (plate–plate distance) was 100 µm. The following protocol was used to establish a reproducible sample history:

1. Annealing at 25 °C for 30 s
2. Shearing at constant rate for 2 s (to break inner structures, i.a.)
3. Annealing without deformation for 300 s (to allow for structural recovery, i.a.)
4. Oscillation without UV exposure for 30 s
5. Oscillation under UV irradiation for 300 s
6. Oscillation without UV exposure for 30 s

To quantify the conversion of DMMI with time at these intense illumination conditions, samples of the 60 g·L^{-1} solution were placed in 100 µm quartz cuvettes and irradiated on the same setup for 0, 20, 55, 110, and 240 s. DMMI conversion was estimated by analyzing the corresponding UV–vis spectra as described further below (see Chapter 4.1.4.2).

4.1.3.7 Proton multiple-quantum NMR

^{1}H MQ NMR measurements were performed on a Bruker minispec mp20 with $B_0 = 0.5$ T at 25 °C. The adjustment procedures and pulse sequences applied are specified in refs [59], [62], and [64]. For this study, 90° pulses were set to 1.7 µs and 64 scans were recorded on each sample. Specimens were fully crosslinked samples of PAAm-DMMI1.0 at concentrations of 20, 40, 60, and 80 g·L^{-1} in D_2O in 10 mm OD NMR tubes. The filling height was limited to 7 mm to ensure sufficient field homogeneity over the whole sample when placed in the center of the rf coil. The samples had been crosslinked by irradiating them for 32 h in front of a 6 W laboratory UV lamp of type NU-6K1 (Konrad Benda Laborgeräte und Ultraviolettstrahler, Wiesloch, Germany) providing spatially homogeneous illumination with a spectral range of (365 ± 20) nm. Irradiation intensity was about 0.5 mW·cm^{-2}. The long irradiation time was necessary to achieve complete reaction, since the samples contained only 10 µmol·L^{-1} of TXS to ensure a transmittance > 90% at 383 nm, thus avoiding the build-up of a gradient of crosslink density across the tube. Complete conversion of the crosslinking process was verified by UV–vis measurements on aliquots of the test solutions that were placed in 100 µm cuvettes and irradiated parallel to the NMR tubes.

4.1.4 Results and discussion

4.1.4.1 Photo-induced dimerization of DMMI in aqueous solution

The photo-induced dimerization of DMMI in an aqueous medium was studied using *N*-(2-hydroxyethyl)-dimethylmaleimide (HE-DMMI) as a simple water-soluble model compound. Thioxanthone disulfonate (TXS) was employed as a photosensitizer. The concentration of HE-DMMI was chosen to match the one typically present in polymeric systems, e.g., in a 50 $g{\cdot}L^{-1}$ semidilute solution of a PAAm–DMMI having a degree of functionalization of about 1 mol-%. The progress of the reaction was followed by UV–vis spectroscopy. Spectra depicted in Figure 4.5 show that the absorption band of the monomeric HE-DMMI around 230 nm decreases significantly with irradiation time, while another band appears at 205 nm which must be due to the dimeric product. All spectra intercept in *isosbestic points* at 209, 246, and 261 nm. This means that the spectra measured during the experiment are *linear combinations* of the spectra of the pure monomeric and dimeric compounds, and that the *extent of conversion* can be deduced from them.

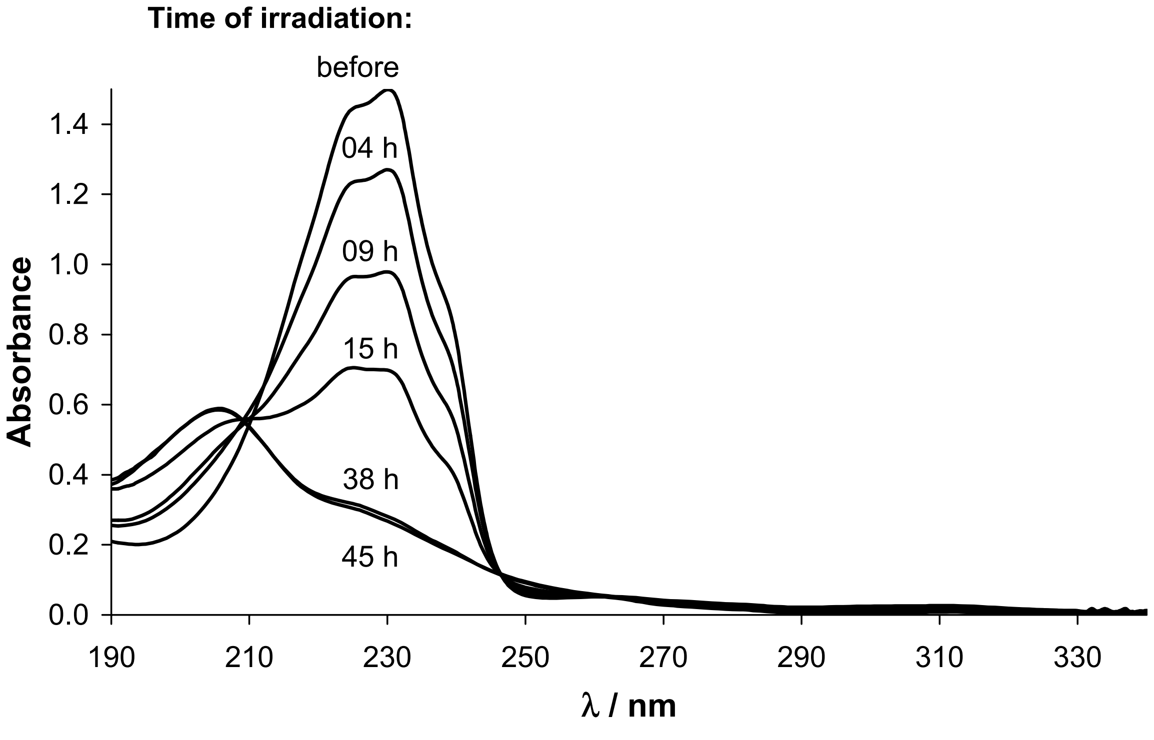

Figure 4.5 UV–vis spectra taken at different reaction times to monitor the progress of the DMMI dimerization in an aqueous solution of 8 $mmol{\cdot}L^{-1}$ HE-DMMI sensitized by 0.08 $mmol{\cdot}L^{-1}$ TXS.

Former studies on this reaction in organic media performed by Schenck et al. [109] and Zweifel et al. [138] revealed that the dimeric product is the *symmetric* cyclobutane derivative in *trans* form, suggesting that a triplet intermediate occurs according to the Hammond mechanism. This mechanism has also been discussed for comparable maleimide dimerizations [142, 203] as well as for dimerizations of dimethylmaleic anhydride [205].

In the current dimerization experiment in an aqueous system, two products could be distinguished. One minor compound appeared as a white precipitate during the reaction, while the other major one was isolated from the solution. NMR analyses of these two compounds (results given in 4.1.3.4) clearly show that they are different. The structures derived from the NMR spectra correspond to *isomeric forms of a HE-DMMI dimer*, which are depicted in Figure 4.6. The *symmetric* cyclobutane derivative (Figure 4.6a), which is the sole product when the photodimerization is carried out in organic solvents, is only formed as a byproduct in aqueous solution, while the major product is the *asymmetric* dimer shown in Figure 4.6b. Formation of the latter compound requires the *shift of a hydrogen atom* at an intermediate reaction stage. Its structure is clearly proven by the signals at 3.12 ppm (methine hydrogen) and at 6.05 and 6.43 ppm (olefinic hydrogens) in proton NMR as well as by the signals at 124.7 and 139.2 ppm (olefinic carbons) in ^{13}C NMR. No indication for residual educt was found in either of the NMR spectra, indicating that the dimerization reaction is complete after sufficient irradiation time.

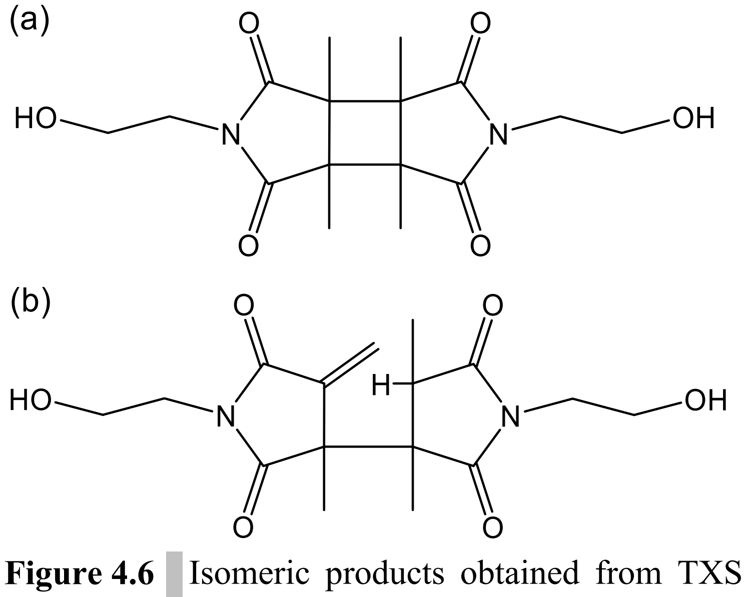

Figure 4.6 Isomeric products obtained from TXS-sensitized photodimerization of HE-DMMI in aqueous medium. – (a) Precipitate; (b) dissolved product.

A rerun of the reaction in D_2O as solvent showed no isotopic effect on the results. This proves that the H-shift occurs within the intermediate dimer complex. According to the Hammond model, this kind of process can be allocated to the T_1 excited dimer that has a wide geometry and is therefore prone to undergo side reactions before returning to the ground state S_0. In several other photochemical homo and hetero cycloadditions [206–208], similar behavior was observed and explained on the basis of H-shifts in an intermediate triplet excimer.

Employing different model compounds such as *N*-(2-aminoethyl)-dimethylmaleimide and *N*-(*N'*-acetyl-2-aminoethyl)-dimethylmaleimide in the photodimerization process in an aqueous medium gave results similar to those obtained with HE-DMMI. There was no precipitate appearing, but the NMR spectra of the products isolated from solution showed that they were mixtures of the corresponding asymmetric and symmetric dimers with the asymmetric compound appearing in large excess. These observations show that the formation of the asymmetric dimer is favored when the photodimerization proceeds in aqueous solution, while only nonpolar media seem to favor the formation of the symmetric cyclobutane derivative. In either case, however, there is a 100% formation of dimers. This means that the photoreaction can be used to crosslink accordingly functionalized polymers, although the chemical structures of the crosslinks generated are different.

To ensure that the dimerization of the DMMI moieties is the only reaction occurring in the polymer system upon irradiation, the model reaction was repeated in the presence of acetamide, regarded to represent PAAm functionalities. There have been some reports suggesting that amide groups can undergo Paterno–Büchi-analogous reactions [209] or photocleavage followed by subsequent interconnection processes. However, experiments in the scope of this work did not show any evidence for such side reactions. While the two isomeric dimers were detected in comparable ratio as in the last experiment, the NMR signals of acetamide were found unchanged in the mixture. Additionally, mass spectra showed no peaks that could be addressed to heteroaddition products (e.g., no peak at $m/z = 228$ that might be interpreted as the M^+-peak of an HE-DMMI–$AcNH_2$ adduct). Hence, unwanted side reactions do *not* occur to an extent exceeding the analytical sensitivity. There was also no evidence for *further* reactions of the DMMI dimers, even though most of them carry olefinic bonds.

4.1.4.2 Photo-induced crosslinking of P(AAm-*co*-DMMIAAm)

UV–vis analysis

The UV–vis spectroscopic analysis of the progress of crosslinking can be nicely exemplified on a semidilute solution of the sample PAAm-DMMI1.5 ($c = 50$ g·L^{-1}) containing 10 mol-% TXS, relating to the concentration of DMMI moieties. Figure 4.7 shows the UV–vis spectra recorded after several periods of irradiation. There is a shoulder around 230 nm that decreases with irradiation time and that can be assigned to the DMMI moieties. It is superimposed on a strong background resulting from PAAm. Also recognized, albeit weak, are the absorption bands of TXS at 270, 310, and 380 nm, whereby the latter band is used for the initiation of the photoreaction. By subtraction of separately recorded spectra of pure sensitizer and PAAm solutions that where scaled to coincide with the composite spectrum in the regions of 382 nm (sensitizer) and 201 nm (PAAm), the signal of the DMMI sidegroups and their dimers could be extracted as depicted in the inset of Figure 4.7. Obviously, there is a strong similarity to the spectra obtained for the reaction of the low molecular weight model compounds shown in Figure 4.5: the signal of the original DMMI moieties at 229 nm decreases, while the band at 205 nm due to the dimeric products is enhanced. Again, all spectra intercept within an isosbestic point at 209 nm and are therefore *linear combinations* of the spectra of the *pure reactants* and their *dimeric products*, corresponding to $t = 0$ and $t = \infty$, respectively. The conversion of the reaction $y(t)$ can be obtained by

$$y(t) = \frac{A(t) - A(0)}{A(\infty) - A(0)} \tag{4.1}$$

where $A(t)$ denotes the absorbance at time t, with $A(0)$ and $A(\infty)$ being the initial and final values. In principle, eq (4.1) holds for every wavelength, but $\lambda = 229$ nm (maximum of DMMI absorbance) is used expediently because the absorbance change is strongest at this wavelength.

To check for the accuracy and reproducibility of this spectroscopic procedure, two experiments were performed in parallel on the dimerization of the model compound HE-DMMI (8 mmol·L^{-1} in aqueous solution containing 1 mmol·L^{-1} TXS), where one solution contained only reactant and sensitizer, while the other one was supplemented with 50 g·L^{-1} PAAm in addition.

The strong background absorbance of PAAm did *not* impair the analysis perceptibly, and identical conversion data were obtained within ±1% (details not shown).

As a further check, spectra were recorded on aqueous solutions of 20, 40, 60, and 80 g·L^{-1} of the polymer sample PAAm-DMMI2.0 and 1 mmol·L^{-1} TXS in 100 μm cuvettes. Spectra were also recorded on the fully crosslinked samples after extensive irradiation. Figure 4.8 shows the absorbances of the DMMI moieties at $\lambda = 229$ nm that were separated from the composite spectra in the manner described above, as a function of the initial concentration of pendant DMMI groups. The results indicate excellent *proportionality* even at high concentrations, where the amount of DMMI is leading to differential absorbances exceeding 2 (for the unreacted solution) and the background absorbance due to polymer is strong. The two lines are well represented by

$$A(0) = 14800\ \mathrm{L{\cdot}mol^{-1}{\cdot}cm^{-1}} \cdot c_{\mathrm{DMMI}}$$
$$A(\infty) = 3460\ \mathrm{L{\cdot}mol^{-1}{\cdot}cm^{-1}} \cdot c_{\mathrm{DMMI}}$$

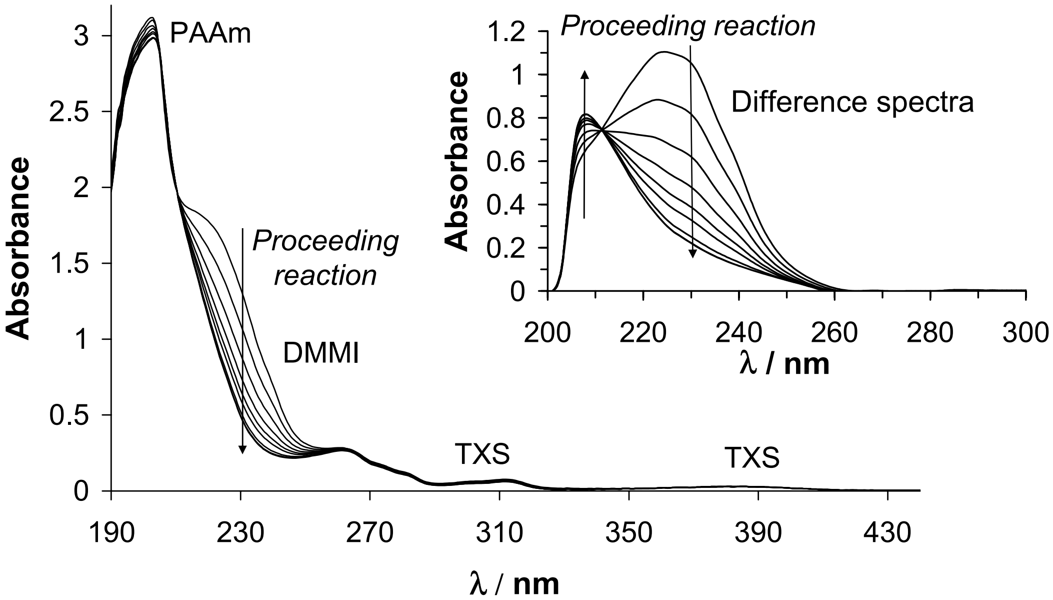

Figure 4.7 UV–vis spectra recorded during crosslinking of a system of 50 g·L^{-1} PAAm-DMMI1.5 in aqueous solution containing 10% TXS, related to the amount of DMMI moieties, at irradiation times of 0, 10, 20, 30, 40, 50, 70, 90, and 150 min. – The inset shows the corresponding difference spectra obtained after subtraction of separately recorded and suitably scaled spectra of pure PAAm and TXS.

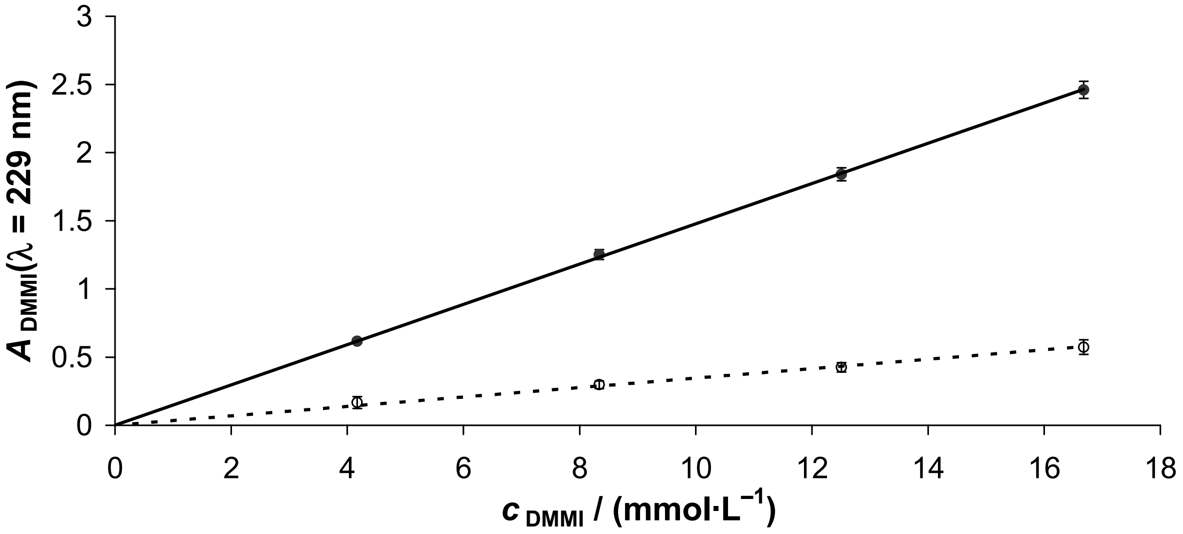

Figure 4.8 Background-corrected absorbances at λ = 229 nm of aqueous PAAm-DMMI2.0 solutions at concentrations of 20, 40, 60, and 80 g·L^{-1} before (full circles, full line) and after complete crosslinking (open circles, dotted line) in 100 µm quartz cuvettes.

Influence of the amount of sensitizer and light dose on gelation kinetics

DMMI conversion $y(t)$ was determined as a function of irradiation time for solutions containing the same amount of polymer (50 g·L^{-1} PAAm-DMMI1.5) and variable quantities of sensitizer, ranging from 1 to 100% relating to the concentration of DMMI moieties. For one series, the incident light was made rather monochromatic (λ = 383 nm) by using the interference filter, while for a second series the broad band-pass filter was applied (λ > 310 nm) and the intensity was higher. From each course of conversion versus time, the half-life τ was determined. Figure 4.9a shows a plot of $1/\tau$ versus the relative concentration of sensitizer. The data points for each series of measurements fall approximately on a straight line passing through the origin. This indicates that the *rate of reaction is proportional to the concentration of sensitizer* within experimental uncertainty. Perceptible deviations only occur at the highest TXS concentrations. The slopes of the two lines depicted are in a ratio of 1:10. The overlap integrals between the absorption band of TXS having its maximum at 382 nm and the transmittance curves of the filters (cf. Figure 4.3) are estimated to be in a ratio of 1:12, which is in reasonably close agreement. Hence, the *rate of reaction is also roughly proportional to the intensity of light* which can be absorbed by the sensitizer.

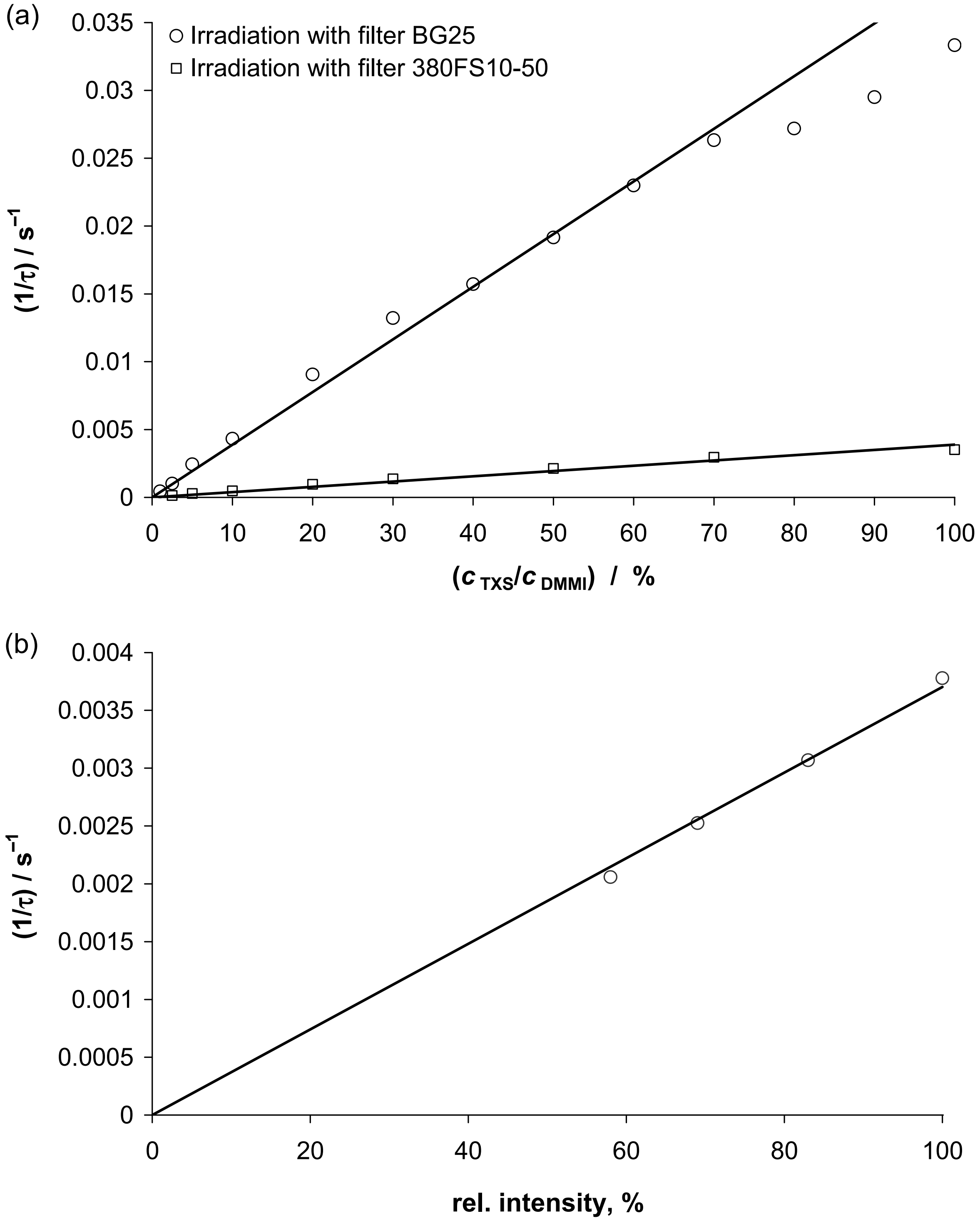

Figure 4.9 Influence of (a) the concentration of sensitizer and (b) irradiation intensity on the half-life of DMMI dimerization in a 50 g·L^{-1} solution of PAAm-DMMI1.5 in water. – Linear fits in (a) are represented by

$(1/\tau)_{\mathrm{BG25}} = 3.9 \times 10^{-4}\ \mathrm{s}^{-1} \cdot (c_{\mathrm{TXS}}/c_{\mathrm{DMMI}})$ / %
$(1/\tau)_{\mathrm{380FS10\text{-}50}} = 3.9 \times 10^{-5}\ \mathrm{s}^{-1} \cdot (c_{\mathrm{TXS}}/c_{\mathrm{DMMI}})$ / %

In (b), the molar concentration of TXS was identical to that of DMMI groups. The linear fit is represented by $(1/\tau) = 3.7 \times 10^{-5}\ \mathrm{s}^{-1} \cdot I_{\mathrm{rel}}$ / %.

To check the second point in a more systematic way, Figure 4.9b shows reciprocal half-lives versus relative light intensities for one selected composition (50 $g \cdot L^{-1}$ PAAm-DMMI1.5, 100% TXS). The attenuation of intensity was achieved by using filter cascades. Although the number of data points is limited, it becomes obvious that $1/\tau$ is proportional to intensity.

These results demonstrate clearly that the crosslinking reaction can be well controlled by adjusting the *concentration of sensitizer* and the *intensity of irradiation*. The rate of DMMI conversion is proportional to either of these two parameters. This means that the quantity of dimers (crosslinks) formed is directly related to the light dose absorbed by TXS molecules. Within the parameter space covered by the experiments in this section, the transfer of energy from the excited sensitizer to the DMMI moieties, resulting in the formation of dimers, is occurring with constant efficiency.

Because of this simple dependency it is possible to reduce the concentration of sensitizer and increase the duration and/or intensity of irradiation in return in order to achieve identical conversion. This is particularly necessary when the layer thickness becomes large. The concentration of sensitizer then has to be adjusted to ensure sufficient transmittance through the sample layer to avoid formation of a gradient (e.g., in the NMR experiments; cf. Chapter 4.1.3.7).[1)]

Two additional observations need to be mentioned: none of the large number of UV–vis spectra that were collected in the context of the present work showed any evidence for photobleaching of TXS. The corresponding absorption bands remained equally strong even when very high illumination intensities were utilized (e.g., in rheology under UV exposure, cf. next subchapter). Also, there was no evidence for oxygen-quenching within the systems studied. Kinetic experiments conducted on nitrogen-flushed samples and on samples under air gave identical results. These facts demonstrate that the TXS-sensitized photoreaction in aqueous medium is rather robust.

---

[1] In the same respect, one also has to take care about homogeneous illumination in the *x*- and *y*-direction, e.g., by employing proper light sources or optical setups.

4.1.4.3 Rheological characterization of the gelation process

The oscillatory shear modulus was measured during the photochemically induced gelation process on samples containing PAAm-DMMI2.0 at concentrations of 20, 40, 60, and 80 g·L^{-1}, as well as 1 mmol·L^{-1} of TXS. Note that the UV irradiation in these runs was considerably more intense than in the other experiments (cf. Chapter 4.1.3.6). The equilibrium (zero frequency) shear modulus G is related to the effective network density of a gel ν_{eff} by eq (2.30), which reads as

$$G = \varphi \nu_{\text{eff}} RT \tag{4.2}$$

where φ is a structure factor that can be equated to 0.5 in the case of tetrafunctional crosslinks in swollen networks. ν_{eff} is the molar number of network strands per volume, which is twice the molar number of crosslinks per volume. The quantity actually measured was the storage modulus G'(4 Hz), and also the corresponding loss modulus G''(4 Hz). If $G' \gg G''$, the storage modulus is close to the equilibrium modulus and can be used to estimate ν_{eff}.

Figure 4.10 shows the temporal course of G' for a 60 g·L^{-1} semidilute sample of PAAm-DMMI2.0 during irradiation. Initially, a polymer solution is present, and the finite storage modulus reflects the temporary entanglement network. Shortly after the onset of irradiation, G' rises steeply and finally approaches a plateau value. (G'' is remaining below 50 Pa throughout the experiment.) This course is due to the formation of the permanent network structure via dimerization of the DMMI moieties. To compare the conversion of DMMI moieties with the rise of G', the chemical conversion in samples irradiated under exactly identical conditions for some selected irradiation periods was determined by UV–vis spectroscopy and plotted in the same graph. The development of both quantities occurs in a *strictly parallel manner*. Hence, *the formation of elastically effective crosslinks is proportional to the DMMI conversion*.

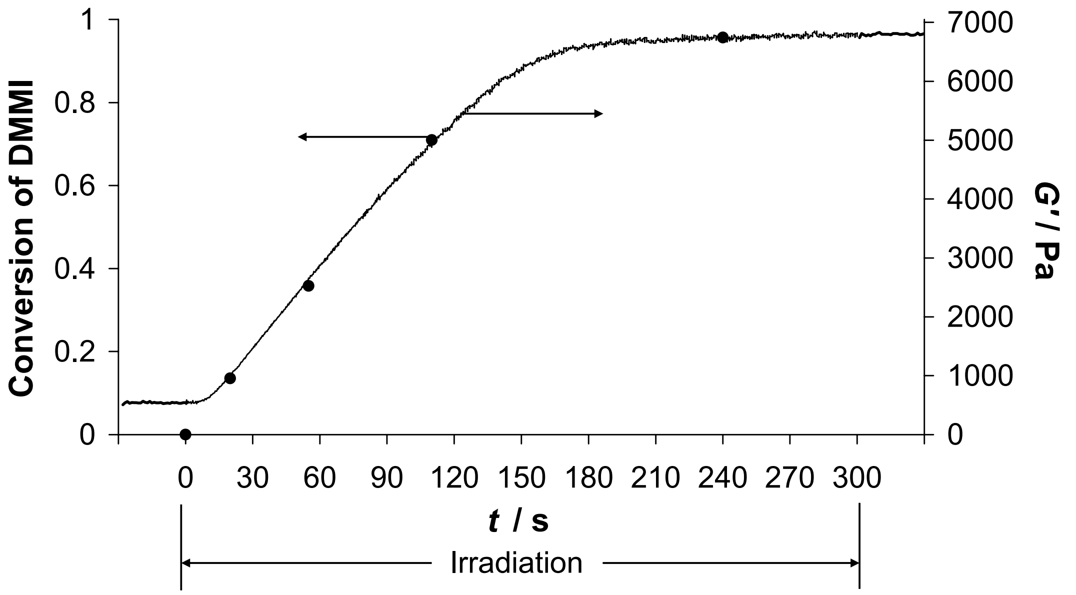

Figure 4.10 Temporal course of *G*' measured by rheology under UV exposure (continuous line) and conversion of pendant DMMI groups estimated by UV–vis spectroscopy (full circles) for an aqueous 60 g·L^{-1} semidilute sample of PAAm-DMMI2.0 with 1 mmol·L^{-1} TXS.

The plateau values of *G*' for the whole series of experiments are listed in Table 4.3 together with other characteristic data. From *G*', the effective network density ν_{eff} was determined, while the molar concentration of DMMI moieties equals the theoretical network density ν_{th}. The ratio of the two, $\nu_{\mathrm{eff}}/\nu_{\mathrm{th}}$, is thus a measure of crosslinking efficiency. The results in Table 4.3 show that the efficiency is around 16% at low polymer concentration, presumably because most dimerizations are formed intramolecularly, but rises distinctly with rising concentration up to more than 60% for the 80 g·L^{-1} system. The crosslinking efficiency achieved with this photochemical procedure is thus by far greater than that observed when PAAm gels are made by crosslinking copolymerization [7].

Table 4.3 Plateau values of *G*'(4 Hz) in the fully crosslinked state of semidilute PAAm-DMMI2.0 hydrogels and crosslinking efficiencies derived thereof.

$c_{\mathrm{PAAm\text{-}DMMI2.0}}$ g·L^{-1}	$c_{\mathrm{DMMI}} = \nu_{\mathrm{th}}$ mmol·L^{-1}	*G*' Pa	ν_{eff} mmol·L^{-1}	**Efficiency of crosslinking;** $\nu_{\mathrm{eff}}/\nu_{\mathrm{th}}$ %
20	4.17	815	0.66	15.8
40	8.34	2092	1.69	20.2
60	12.51	6730	5.43	43.4
80	16.68	12835	10.36	62.1

4.1.4.4 Characterization of the network structures by MQ NMR

In isotropically mobile polymer solutions, orientation-dependent interactions are completely averaged to zero and cannot be detected. However, as described in Chapter 2.1.2.5, the NMR response of network systems is partially solidlike: since chain segment fluctuations are not completely isotropic due to the constraints imposed by crosslinks, the weak residual orientation-dependent interaction leads to coherent dipolar dephasing. Therefore, the detection of residual proton–proton dipolar couplings constitutes a sensitive means to monitor gelation processes [62] and to characterize the microstructure of polymer networks [63] in a quantitative fashion, so that MQ NMR is complementary to rheological or scattering methods.

Analysis of the MQ NMR data: Component separation

As pointed out in Chapter 2.1.2.5, a MQ NMR experiment yields a double-quantum intensity $I_{\mathrm{DQ}}(\tau_{\mathrm{DQ}})$ and a reference intensity $I_{\mathrm{ref}}(\tau_{\mathrm{DQ}})$. These can be determined from an average over the initial 100 μs of the featureless FID after a 90° pulse that follows the actual MQ pulse sequence. The sum of DQ and reference intensities, $I_{\Sigma\mathrm{MQ}} = I_{\mathrm{DQ}}(\tau_{\mathrm{DQ}}) + I_{\mathrm{ref}}(\tau_{\mathrm{DQ}})$, is then normalized to $I_{\Sigma\mathrm{MQ}}(\tau_{\mathrm{DQ}}=0) = 1$, before a contribution termed *C-fraction* can be separated by fitting the long-time tail of the decaying function to a single exponential with initial amplitude f_{C} and relaxation time τ_{C}. The C-fraction corresponds to very *mobile components* such as *solvent and sol* that have the longest relaxation time. It is not of major interest here and was subtracted from $I_{\Sigma\mathrm{MQ}}$.

A second contribution (B) that is polymeric in nature but elastically inactive and can be associated with *dangling chains, loops, and related structures* has to be subtracted as well, for instance in a way described earlier (e.g., [65]). The reliable fitting of this second contribution, which also decays approximately exponentially, was in the current case challenged by the fact that the corresponding relaxation time τ_{B} is very close to the relaxation time of the $I_{\Sigma\mathrm{MQ}}(\tau_{\mathrm{DQ}})$ intensity of the *pure network component* (A) under the given conditions, even though this component is not network-like and does not contribute to the DQ intensity build-up. This is because the ultimately isotropic segmental motions of this component occur on a time scale that is similar to that of the network chains, as opposed to the faster and isotropically mobile part C.

In this case, an alternative approach had to be taken that makes use of the fact that the final DQ intensity of the network part has to evolve to the same level as the corrected reference intensity, which means $I_{\mathrm{DQ}}/I_{\Sigma\mathrm{MQ,corr}} \equiv I_{\mathrm{nDQ}} = 0.5$ as $\tau_{\mathrm{DQ}} \rightarrow \infty$ [59, 65, 67]. This condition was met by multiplying the C-corrected sum intensity $I_{\Sigma\mathrm{MQ}}(\tau_{\mathrm{DQ}})$ by a constant factor $(1 - f_{\mathrm{B}})$ chosen such that the so-called normalized DQ build-up curve $I_{\mathrm{nDQ}}(\tau_{\mathrm{DQ}})$ approaches the theoretically expected value of 0.5 in its long-time limit. The contribution of *effective network chains* (A) to the total signal intensity is then simply given by $f_{\mathrm{A}} = 1 - f_{\mathrm{B}} - f_{\mathrm{C}}$. It should be noted that several experiments conducted at 80 °C yielded the same results for the different fractions within experimental accuracy. However, the relaxation times τ_{A} and τ_{B} were then different so that the B-component could be extracted by direct tail fitting.

Table 4.4 shows a listing of the fractions of the three components A, B, and C, as well as their apparent relaxation times at 25 °C. τ_{C}-values are in the range of several hundred ms, while the common $\tau_{\mathrm{A}} = \tau_{\mathrm{B}}$ is around 10 ms. Besides a roughly constant portion of about 20% sol and solvent in all samples, f_{A} is distinctly increasing with rising polymer concentration on the expense of f_{B}. This is another indication of the fact that the higher the polymer concentration, the more is the formation of *elastically effective* crosslinks favored over the formation of intramolecular linkages leading to loops etc. f_{A} is thus considered a measure of crosslinking efficiency and complements and confirms nicely the results obtained by rheology (Table 4.3). Note that rheological and MQ NMR measurements were performed on PAAm samples which differ in DMMI content by a factor of about 2. This shows that the amount of dimerizable moieties within the precursor chains has only a minor effect on the relative amount of elastically effective junctions formed while the influence of polymer concentration is much more significant.

Table 4.4 Results of MQ NMR experiments on semidilute samples of PAAm-DMMI1.0 in the fully crosslinked state (solvent: D_2O). f_A, f_B, and f_C are the fractions of network chains, dangling chains etc., and sol, respectively, τ_A, τ_B, and τ_C are the corresponding relaxation times, and D_{res} is the residual dipolar coupling parameter. All data correspond to $T = 25$ °C.

$c_{\text{PAAm-DMMI1.0}}$ g·L^{-1}	f_A %	f_B %	f_C %	$\tau_{A,B}$ ms	τ_C ms	D_{res} Hz
20	11.5	56.5	32.0	14.2	1369.9	85.1
40	32.4	48.6	19.0	11.1	404.9	109.6
60	40.4	40.4	19.2	10.4	423.7	128.9
80	44.0	31.8	24.2	8.9	251.9	127.2

Analysis of the network fraction

Figure 4.11 shows the DQ build-up curves of the network component in the gel samples studied, obtained after appropriate normalization as just described. The build-up of I_{nDQ} with τ_{DQ} depends on the residual dipolar coupling constant D_{res} in the following way:

$$I_{nDQ}(D_{res}) = \tfrac{1}{2}\left(1 - \exp\left\{-\tfrac{2}{5} D_{res}^2 \tau_{DQ}^2\right\}\right) \tag{4.3}$$

D_{res} in turn is, as mentioned in Chapter 2.1.2.5, inversely related to the *apparent chain length between restrictions* [61, 63, 64]. In general, a distribution of chain lengths and, hence, a distribution of coupling constants needs to be considered. For the evaluation of the present data, a gamma distribution was assumed as discussed in detail in ref [59]. It is ideally expected in a system with fixed chain length between crosslinks and a Gaussian distribution of end-to-end distances.

$$P(|D_{res}|) = \frac{2}{\sqrt{\pi}} \sqrt{\frac{27|D_{res}|}{8D_{res}^3}} \exp\left(\frac{-3|D_{res}|}{2\bar{D}_{res}}\right) \tag{4.4}$$

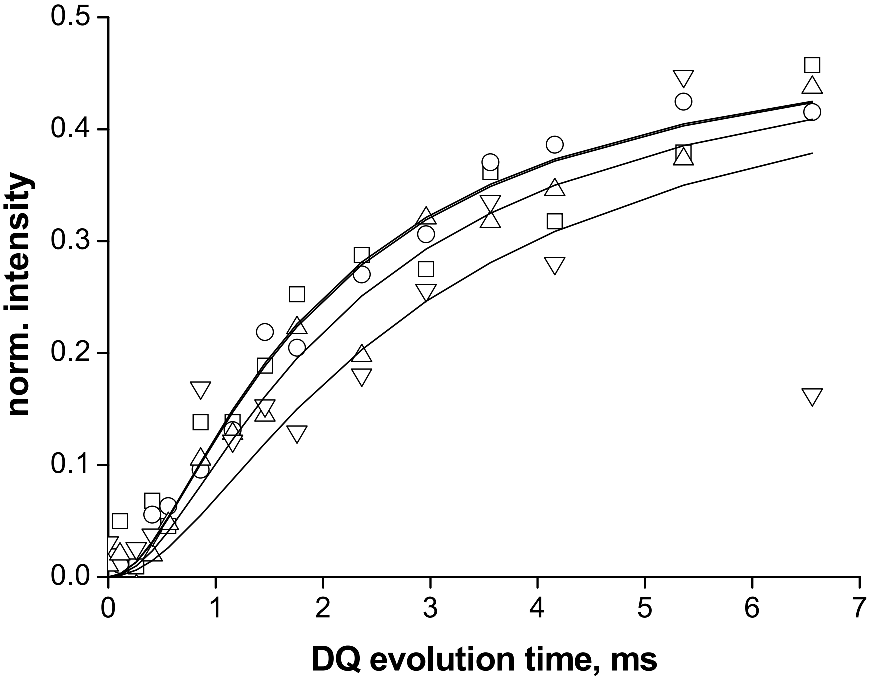

Figure 4.11 Normalized DQ build-up curves obtained from MQ NMR characterization of semidilute PAAm-DMMI1.0 samples in their fully crosslinked states at concentrations of 20 (▽), 40 (△), 60 (○), and 80 $g{\cdot}L^{-1}$ (□) in D_2O, respectively.

The experimental $I_{nDQ}(\tau_{DQ})$ data were then fitted in the region of $I_{nDQ} < 0.45$ by numerically integrating over the entire range of $D_{res} = 0\ldots\infty$ to give a mean value of a relatively broad distribution (the width of a gamma distribution depends on its average, whereby no additional fitting parameter is introduced). Results of these fits are shown in Figure 4.11 as full lines, and the average coupling constants are included in Table 4.4.

The coupling constants and the courses of $I_{nDQ}(\tau_{DQ})$, respectively, are quite *similar for all PAAm–DMMI gels in this series*, despite of different concentrations and crosslinking efficiencies. This indicates that the *mean lengths of active network chains are similar*, and a consideration of the crosslinking mechanism can explain this finding: a linkage between two polymer chains is *only formed upon dimerization of two DMMI sidegroups* and, therefore, the chain length between crosslinks (and its distribution) is essentially predetermined by the given random spacing of DMMI moieties along the initial polymer chains. Indeed, this argument holds only when conversion is complete.

The experimental findings also imply that dimerizations which are not generating elastically active network chains are not leading to chain extension to any appreciable extent. This is a surprising and important observation in view of the marked variation of the A-fraction determined by MQ NMR or the crosslinking efficiency, respectively, with polymer concentration. The necessity to assume a broad distribution of coupling constants according to eq (4.4) to attain reasonable fitting of the build-up curves is in accord with previous observations on swollen networks [67]. While distributions due to variations in the chain length between crosslinks as well as the distribution expected on the basis of a Gaussian distribution of end-to-end distances are screened by the cooperativity of the chain motions ("packing") in unswollen elastomers, such effects, as well as topologically induced swelling heterogeneities, reappear in swollen networks [59, 67, 210].

4.1.5 Conclusions and summary

Photochemical crosslinking of DMMI-functionalized PAAm provides an efficient way to synthesize hydrogels in a *selective* and *controlled* manner. The reaction is conveniently performed in the presence of thioxanthone disulfonate as a triplet sensitizer. It could be shown that the photodimerization of DMMI moieties in aqueous solution yields predominantly *asymmetric* products instead of the initially expected cyclobutane derivatives known from the reaction in organic solvents. However, the dimerization occurs *without perceptible side reactions* and can be readily controlled by the *intensity* and *duration* of UV irradiation and the *concentration of sensitizer*. It is therefore very well suited to crosslink a polymer solution at will if the initial polymer is equipped with such functional groups. On the other hand, one should be able to enclose photochemically *un*functional tracer materials *without interconnecting* them to the matrix.

The gelation process can be interrupted at any stage by discontinuing the UV irradiation to study the system as it changes from a semidilute polymer solution to a chemically crosslinked gel. Thereby, the conversion of DMMI moieties into dimers is *easily quantified by UV–vis spectroscopy*. Since not all such chemical linkages are elastically effective, methods to determine the crosslinking efficiency were applied.

On a macroscopic scale, the rheological measurement of the shear modulus is a measure of the density of effective network chains. The results clearly indicate that the *formation of active network strands occurs in proportion with DMMI conversion*. Comparison with the amount of dimerized DMMI units shows that the crosslinking efficiency is around 16% when a solution containing 20 $g{\cdot}L^{-1}$ of functionalized polymer is crosslinked, and rises to more than 60% at a concentration of 80 $g{\cdot}L^{-1}$. These efficiencies are surprisingly high in view of the fairly small concentrations and markedly exceed the values typically attained when gelation occurred by crosslinking copolymerization of monomer and crosslinker.

The macroscopic determination of crosslinking efficiency is supported by MQ NMR experiments yielding information on the fraction of monomer units present in elastically effective network chains. Quantification of these, becoming possible because of the residual dipolar coupling between such units, gave values comparable to the ones obtained by rheology. Furthermore, the MQ NMR measurements indicate that the *average length of active network chains* is just *slightly dependent on crosslinking efficiency or concentration*, a fact that can be traced back to the importance of the spacing of functional groups along the initial polymer chains. Hence, the results of spectroscopic analysis, rheology, and MQ NMR experiments produce a consistent picture of PAAm network formation through the sensitized photodimerization of pendant DMMI groups.

4.2 Diffusion of linear macromolecules and spherical particles in semidilute PAAm solutions and networks

4.2.1 Introduction

Besides the investigation of the *formation* and the *structure* of PAAm hydrogels, the second central aim of the present work was to study the *diffusion of tracers* inside such systems. By analyzing the influence of a successive sol–gel transition and of a rising density of matrix-crosslinking, an additional new aspect is introduced that may be looked upon in view of the different theoretical models treated in Chapter 2.2.5.2. Although there are quite a few papers in the literature that consider the mobility of tracers enclosed in networks, the study of the *same* system in the *sol* and the *gel* state and, moreover, *during the transition* has not been performed before.

The present work thus intended to realize such a situation by investigating the diffusion of *linear polyacrylamide chains* and comparably sized *spherical polystyrene beads* in PAAm matrixes which can be progressively crosslinked (cf. Chapter 1). To allow for this, extensive preliminary work had to be performed, which has been discussed in the preceding three main chapters. Now, these subprojects converge to their common aim, and the following chapter presents the *systematic investigation on probe mobility in PAAm networks*. A schematic visualization of this final part in the context of the entire work is displayed in Figure 4.12. Note the at the press time of the present thesis, a manuscript about these contents had just been submitted for publication [211].

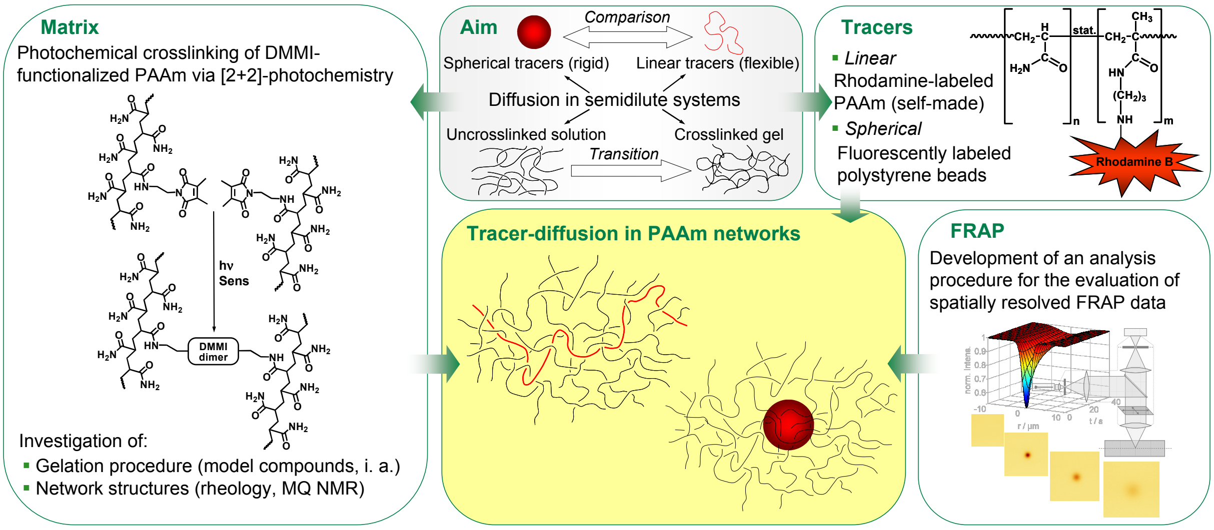

Figure 4.12 Classification of Chapter 4.2 in the context of the present work.

4.2.2 Preliminary consideration of the system studied

It has been stated in the preceding section that polyacrylamide carrying pendant dimethylmaleimide moieties (P(AAm-*co*-DMMIAAm) or briefly PAAm–DMMI) is a proper system to be crosslinked by means of photochemical sidegroup dimerization and thus to achieve *stepwise gelation* by *stepwise irradiation*. By and large, it was found that

(i) Crosslinking of PAAm–DMMI proceeds with high efficiency and allows for the controlled formation of PAAm hydrogels.

(ii) The progress of the photoreaction can be easily observed by UV–vis spectroscopy.

(iii) Even though a fundamental investigation showed that DMMI dimers formed in aqueous media are in fact a mixture of two structures, there seems to be no evidence for further perceptible side reactions — especially no other type of chain interconnection besides the controlled DMMI dimerization.

The latter aspect should thus allow one to embed photochemically unreactive tracers into PAAm–DMMI matrixes *without binding to the matrix material* and then to study their diffusive motion while gradually crosslinking the surrounding network. The use of FRAP for this purpose expediently allows for the use of the *same basis material* (here: PAAm) for the labeled tracers and the crosslinkable matrix.

As proper fluorescent dye to act as label for the linear tracers, rhodamine B (or, analogously, a corresponding dye for the spheres; cf. Chapter 3.1.3.2) was chosen. This chromophore is on the one hand sufficiently water-soluble and exhibits high absorbances and quantum yields of fluorescence when irradiated around its absorption maximum ($\lambda = 558$ nm), e.g., by the 543 nm line of a HeNe laser. Particularly, it is readily bleached by irradiation with the 488 and 514 nm lines of a strong Ar laser in FRAP experiments. On the other hand, UV irradiation around $\lambda = 382$ nm does *not* lead to perceptible excitation since the absorbances of rhodamine B in this wavelength-range are negligible. This ensures sufficient stability of the labels when photocrosslinking of the PAAm–DMMI matrix is performed. In turn, they do not act as internal filter for this process when being used in sufficiently low concentrations.

In combination, the system composed of a PAAm matrix with pendant DMMI moieties on the one hand as well as rhodamine-(analogous)-labeled tracers on the other hand thus allows for the effective separation of the two photochemical processes involved in the current study: While TXS-sensitized matrix-crosslinking can be achieved without affecting the tracers when irradiation proceeds around λ = 382 nm, a quantification of tracer mobility by FRAP can be performed without affecting the reactive DMMI moieties or the TXS sensitizer when wavelengths employed for this purpose lie beyond 450 nm. Figure 4.13 illustrates this aspect by comparing the absorption spectra of the chromophores with the corresponding range of irradiation wavelengths and the laser lines employed for this work. Some relevant photophysical data are also compiled in Table 4.5, thus underlining the interplay of the different photoactive compounds from a quantitative point of view.

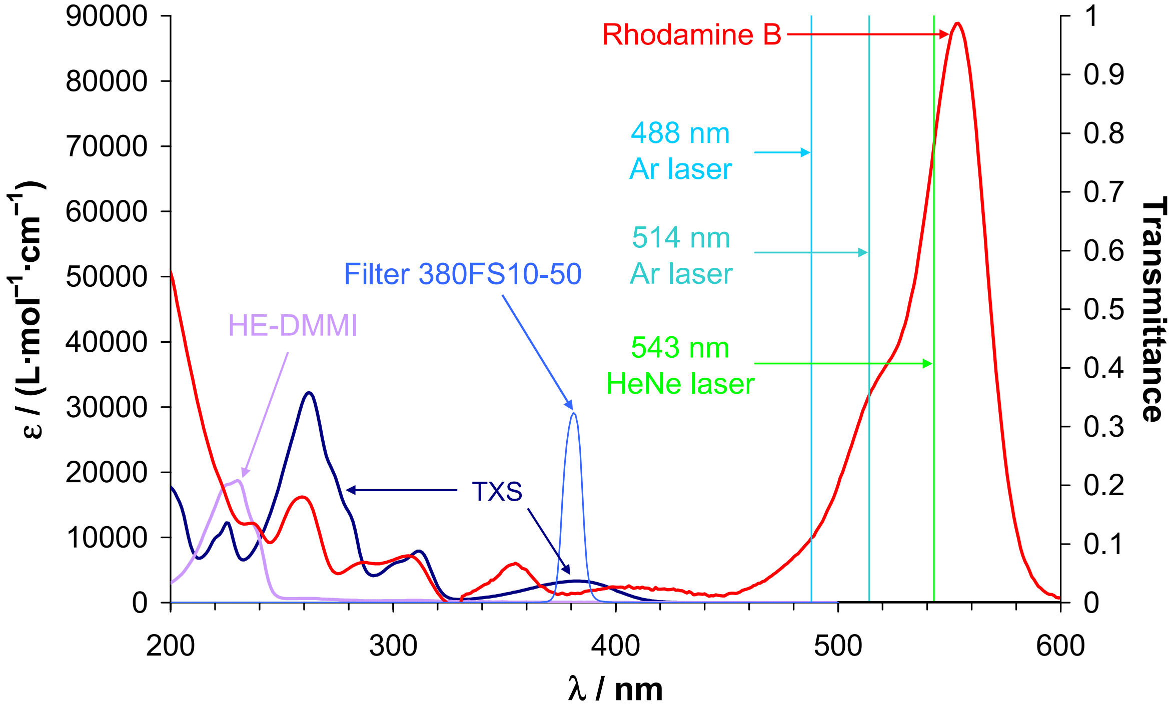

Figure 4.13 Spectroscopic specification of the system studied in this chapter. – Left axis: UV–vis absorption coefficients of rhodamine B, thioxanthone disulfonate (TXS), and the DMMI chromophore as measured for the model compound *N*-(2-hydroxyethyl)-dimethylmaleimide (HE-DMMI) in aqueous solution, respectively. Right axis: Transmittance of the interference filter 380FS10-50 used for wavelength selection to achieve TXS-sensitized photochemical DMMI dimerization. Also illustrated are the laser lines employed for FRAP measurements.

Table 4.5 Important photophysical properties of the chromophores used in this chapter.

λ_{max}(fl.-ex.): wavelength for maximum fluorescence excitation
λ_{max}(fl.-em.): wavelength of maximum fluorescence emission
E_S: energy level of the first excited singlet state
E_T: energy level of the first excited triplet state
τ_S: average lifetime of the first excited singlet state
τ_T: average lifetime of the first excited triplet state
ϕ_{isc}: quantum yield of intersystem crossing

If not otherwise stated, values are reported for aqueous media.

Property	**Rhodamine B**		**Thioxanthone disulfonate (TXS)**		**Dimethylmaleimide (DMMI)**	
	Value	References and remarks	Value	References and remarks	Value	References and remarks
λ_{max}(fl.-ex.), nm	558	cf. Chapter 3.1.2.2	381	[196]	229	λ_{max} from UV–vis spectrum of HE-DMMI
λ_{max}(fl.-em.), nm	583	cf. Chapter 3.1.2.2	437	[196]		
E_S, kJ·mol^{-1}	210	Derived from 0–0-transition in fluoresc. spectra	293	Derived from 0–0-transition in fluorescence spectra	~520	Simply approximated from λ_{max} in UV–vis spectrum of HE-DMMI
E_T, kJ·mol^{-1}	180	Non-aqueous but polar medium [121]	(274)	Value for parent thioxanthone in nonpolar media [119, 122]	(255)	Value for related dimethyl-maleic anhydride [118]
			(267)	Value for parent thioxanthone in acetonitrile [200]		
τ_S / ns	1.6	cf. Chapter 3.1.2.2	6.8	[196]		
τ_T / µs	250	Non-aqueous but polar medium [121]	109	[196]		
ϕ_{isc}	0.005	Non-aqueous but polar medium [121]	~1	Value for thioxanthone [201]; may appear reduced in polar media [200, 202]		

4.2.3 Experimental

4.2.3.1 Materials

Poly(AAm-*co*-DMMIAAm) (matrix material)

Polyacrylamide randomly functionalized with dimethylmaleimide moieties was synthesized and intensely characterized as described in Chapter 4.1. For the present study, the sample PAAm-DMMI2.0 containing 1.53 mol-% of functionalized monomer units was employed. Several of its characteristic data are again compiled in the first line of Table 4.6.

Fluorescently labeled polyacrylamide (linear tracers)

Rhodamine-labeled polyacrylamides used as linear tracers were prepared and characterized as described in Chapter 3.1.2. For the present investigation, four different molar masses were employed. The relevant properties of these materials are also compiled in Table 4.6. Further characteristics, in particular the spectroscopic properties, can be found in Chapter 3.1.2 and Table 4.5.

The molar masses of the linear tracers were chosen such that the range from inferior to equivalent and larger than that of the matrix polymer was covered. However, note again that the molar masses quoted in Table 4.6 were determined by SEC calibrated with pullulan standards. Hence, the absolute values might be somewhat different. The polydispersity of the samples is rather large and increases with rising chain length. Translational diffusion coefficients thus exhibit a corresponding distribution. Although the procedure for FRAP analysis presented in Chapter 3.2.2 is well suited to deal with such distributions and to determine reliable mean values, molar mass dependencies should be discussed with particular care.

Polystyrene microspheres (spherical tracers)

Fluorescently labeled polystyrene microspheres with nominal diameters of 24 and 40 nm were purchased from Molecular Probes, Eugene, (red-fluorescent carboxylate-modified FluoSpheres, 580/605) as aqueous suspensions with concentrations of 2 and 5 wt.-% solids, respectively. They were extensively characterized by UV–vis spectroscopy, fluorescence spectroscopy, dynamic light scattering, ultracentrifugal analyses, and atomic force microscopy in Chapter 3.1.3. For the following investigations, the characterizations of their sizes were supplemented by FRAP measurements. Table 4.7 lists a collection of the corresponding values. As already figured out in Chapter 3.1.3, both types of spheres are somewhat bigger than stated by the manufacturer. For the spheres having the larger nominal diameter, there is an appreciable variation between the results obtained by different methods, whose origin could not be clarified. Since the FRAP method was used to determine the diffusion coefficient in different environments, the spheres are hereinafter referred to by their hydrodynamic radii determined by FRAP in dilute suspension (17 and 36 nm).

Table 4.6 (a) Purposes and (b) properties of the functionalized polyacrylamides employed in the present chapter. M_{N}: number average molecular weight, M_{W}: weight average molecular weight, r_{H}: hydrodynamic radius in dilute aqueous solution, c^*: overlap concentration.

(a)

Name of sample	Origin	Purpose	Functionalization
PAAm-DMMI2.0	Chapter 4.1	Matrix	1.53 mol-% DMMI
PAAm-C0.1-2	Chapter 3.1.2	Tracer	0.11 mol-% rhodamine B
PAAm-C0.1-3	Chapter 3.1.2	Tracer	0.09 mol-% rhodamine B
PAAm-C0.1-4	Chapter 3.1.2	Tracer	0.13 mol-% rhodamine B
PAAm-C0.1-5	Chapter 3.1.2	Tracer	0.09 mol-% rhodamine B

(b)

Name of sample	M_{N} a) g·mol^{-1}	M_{W} a) g·mol^{-1}	$M_{\mathrm{W}}/M_{\mathrm{N}}$	r_{H} nm	c^* b) g·L^{-1}	c^* c) g·L^{-1}
PAAm-DMMI2.0	241 500	574 500	2.4	21.4 ± 3.4 d)	2.7	5.2
PAAm-C0.1-2	423 000	1 280 000	3.0	52.1 ± 1.7 e)	0.4	4.0
PAAm-C0.1-3	232 000	590 000	2.5	25.3 ± 3.8 e)	1.7	5.9
PAAm-C0.1-4	134 000	348 500	2.6	16.2 ± 0.6 e)	3.8	8.6
PAAm-C0.1-5	88 350	201 000	2.3	11.9 ± 0.9 e)	5.5	13.3

[a] Obtained as pullulan equivalent values by size exclusion chromatography; cf. Chapter 3.1.2.2 and 4.1.3.1.

[b] Calculated from eq (2.2), assuming $R_{\mathrm{G}} \approx 2.05\, r_{\mathrm{H}}$ [212].

[c] Calculated from eq (2.3), employing [η]-values from solution-viscometry in 0.5 mol·L^{-1} aqueous NaCl at $T = 25$ °C as listed in Table 3.3 and 4.2.

[d] Estimated by dynamic light scattering on fairly dilute aqueous solutions well below c^* ($T = 25$ °C), employing a similar experimental procedure as described for the spherical tracers in Chapter 3.1.3.1.

[e] Estimated by FRAP on aqueous solutions of the pure tracers ($c = 5$ g·L^{-1}; $T = 25$ °C) as described in Chapter 4.2.3.2.

Table 4.7 (Hydrodynamic) radii of the microspheres employed for the present investigation as estimated by dynamic light scattering (DLS), ultracentrifugal analyses (UA), atomic force microscopy (AFM), and fluorescence recovery after photobleaching (FRAP). – Margins of error denoted for the AFM data reflect the standard deviations of the particle size distributions observed by this technique; cf. Figure 3.10, p 95.

Method	r(17 nm microspheres) nm	r(36 nm microspheres) nm
DLS	16.7	51.5
UA	14.0	21.0
AFM	12.2 ± 3.8	21.5 ± 2.5
FRAP	16.6 a)	35.8 a)

[a] Evaluated by the simple single-component model described in Chapter 3.2.1.

4.2.3.2 Experimental techniques

UV–vis spectroscopy

UV–vis spectra for the present chapter were measured on a Jasco V-550 spectrometer in the range of 190–700 nm. For a basic characterization of the labeled species (cf. Chapter 3.1), test solutions of appropriate concentration were investigated in 1 cm quartz cuvettes (Hellma). Results obtained in this manner were just needed for a proper adjustment of concentrations and irradiation conditions for the photo-induced crosslinking experiments. The determination of the *conversion of photoreactive DMMI groups* by UV–vis spectroscopy was performed on sample cuvettes with layer thicknesses of 100 μm (Hellma) as described in Chapter 4.1.4 and discussed in further detail below.

FRAP

FRAP experiments were performed on a Leica TCS SP2 confocal laser scanning microscope using a 10× DRY objective with an NA-value of 0.3. When the scanning mode was applied, the fluorophores were excited with the 543 nm line of a HeNe laser at 50% of its maximum power (0.22 mW at the object level). Bleaching was accomplished by irradiation of the fluorophores with the 543 nm line of the HeNe laser and the 514 and 488 nm lines of an Ar laser, each with full power (i.e., 0.22, 7.0, and 6.2 mW at the object level, respectively). Further settings were: Beam expander = 3, resolution = 256 × 256 pixels, zoom = 20 (which led to an image size of about 80 × 80 μm^2), and line scanning speed = 1000 Hz in the bidirectional scanning mode, when analyzing fast diffusion processes (e.g., when characterizing the pure tracers in the absence of polymer matrix). By contrast, slower processes, as the ones being observable within polymer matrixes, were analyzed with resolution = 512 × 512 pixels, zoom = 32 (which led to an image size of about 50 × 50 μm^2), and line scanning speed = 800 Hz in unidirectional manner.

All samples for FRAP experiments were placed in the same quartz cuvettes having a layer thickness of 100 μm which were also used for UV–vis spectroscopy (q.v., Figure 4.14). The confocal plane was set to be approximately in the middle of the specimen. Before bleaching, a stack of ten images was scanned to record the prebleach situation. For bleaching a point into the confocal plane, a chosen spot was irradiated for 3 s with the laser settings mentioned above. After bleaching, a series of typically 20 images was recorded to document the recovery process with a sampling rate of about 5 fps in the case of fast diffusion processes or about 0.1–1 fps in the case of slower diffusing probes. The time information was recorded automatically by the Leica confocal software into an information file. All experiments were conducted at a temperature of (25 ± 0.1) °C.

Images recorded after bleaching were analyzed by the procedure reported in Chapter 3.2. Corresponding calculations were automatically performed by the MATLAB software developed for this purpose.

4.2.3.3 Preparation of samples for systematic investigations

Samples containing linear tracers

Samples for the experimental series described below were simply prepared by dissolution of appropriate amounts of matrix and tracer material as well as thioxanthone disulfonate (TXS) as photosensitizer in water. Matrix concentrations were 20, 40, 60, and 80 $g \cdot L^{-1}$, which all lie above the overlap threshold c^* (cf. Table 4.6). Fluorescently labeled linear tracers were included in amounts of 5 $g \cdot L^{-1}$. This concentration does or does not exceed the corresponding c^* depending on whether one regards $c^{*b)}$ or $c^{*c)}$ from Table 4.6. Hence, it is not clear whether or not the labeled chains overlap with each other; however, they do certainly overlap with the matrix polymer.

Volumes prepared were 1 mL in each case. Homogenization of the semidilute solutions was achieved by allowing them to stand for several days. As indicated above, droplets of each solution were finally placed in quartz cuvettes with a layer thickness of 100 µm (Hellma). Note that the concentrations of DMMI moieties in the samples thus prepared lay between 4 and 16 $mmol \cdot L^{-1}$. The concentration of TXS was 1 $mmol \cdot L^{-1}$ in each case.

Samples containing spherical tracers

When microspheres were to be enclosed in photocrosslinkable matrixes, this was achieved by dissolving amounts of 20–80 $g \cdot L^{-1}$ of the matrix polymer PAAm-DMMI2.0 directly in parent suspensions containing 0.5 wt.-% of spheres together with 1 $mmol \cdot L^{-1}$ of TXS and 0.01 $mol \cdot L^{-1}$ of NaOH. (The addition of base should ensure sufficient deprotonation of the spheres' surficial carboxylic groups. Some experiments involving linear tracers were carried out in acidic, neutral, and basic medium. The results obtained were absolutely independent of pH. This proves that a consistent comparison between measurements on spherical and linear tracers is permitted, despite different pH-values.) Volumes prepared were again 1 mL, and sample homogenization was achieved by equilibration over a period of several days. Samples were then again placed in quartz cuvettes with a layer thickness of 100 µm.

4.2.3.4 Schedule for systematic investigations; experimental protocol

Systematic investigations of tracer mobility as a function of progressive matrix-crosslinking were performed in the following manner: One generally starts from a semidilute solution composed of matrix and tracer that has been prepared as described in 4.2.3.3. After measuring the diffusion coefficient in FRAP experiments in the manner described in 4.2.3.2, the sample was irradiated with UV light for some time in order to achieve a partial conversion of DMMI dimerization. The light source employed was a 6 W laboratory UV lamp of type NU-6K1 (Konrad Benda Laborgeräte u. Ultraviolettstrahler, Wiesloch, Germany) providing spatially homogeneous irradiation with a relatively broad spectrum in the range of (365 ± 20) nm. Further spectral selection was achieved by introducing a narrow-band interference filter of type 380FS10-50 (LOT Oriel, Darmstadt, Germany) which confines the irradiation range to (383 ± 5.6) nm (cf. Figure 4.13).

Samples placed in 100 µm cuvettes were irradiated at a distance of 35 mm, corresponding to an intensity of about 15 µW·cm^{-2}. For clarification, Figure 4.14 shows a photograph of a typical setup as just described. At regular intervals, UV exposure was interrupted and samples were analyzed by UV–vis spectroscopy and FRAP to quantify the actual conversion of DMMI (corresponding to the degree of crosslinking) and the tracer mobility, respectively. This procedure was repeated until the sample was fully crosslinked.

For practical handling, it was convenient to always work with sets of six samples of the same matrix concentration, each one of them containing one out of the four linear or two spherical tracers, respectively. All samples of one set were irradiated simultaneously and analyzed at the same intervals. The individual conversions of DMMI in each set were then averaged to obtain a mean value for each matrix concentration.

The photoinduced crosslinking of the matrix polymer has been studied in detail in Chapter 4.1. It has been figured out there that the crosslinking reaction can be well controlled by adjusting the amount of sensitizer and the intensity of irradiation, whereby the rate of DMMI conversion is proportional to either of these two quantities. Due to this simple dependency, it was possible to reduce the concentration of TXS down to a comparatively low value of 1 mmol·L^{-1}, ensuring sufficient transmittance of UV light (> 90%) through the sample layer (100 µm) and thus avoiding formation of a gradient in z-direction. Homogeneous gelation in x- and y-direction was realized by usage of a UV lamp that provides spatially homogeneous irradiation (see above).

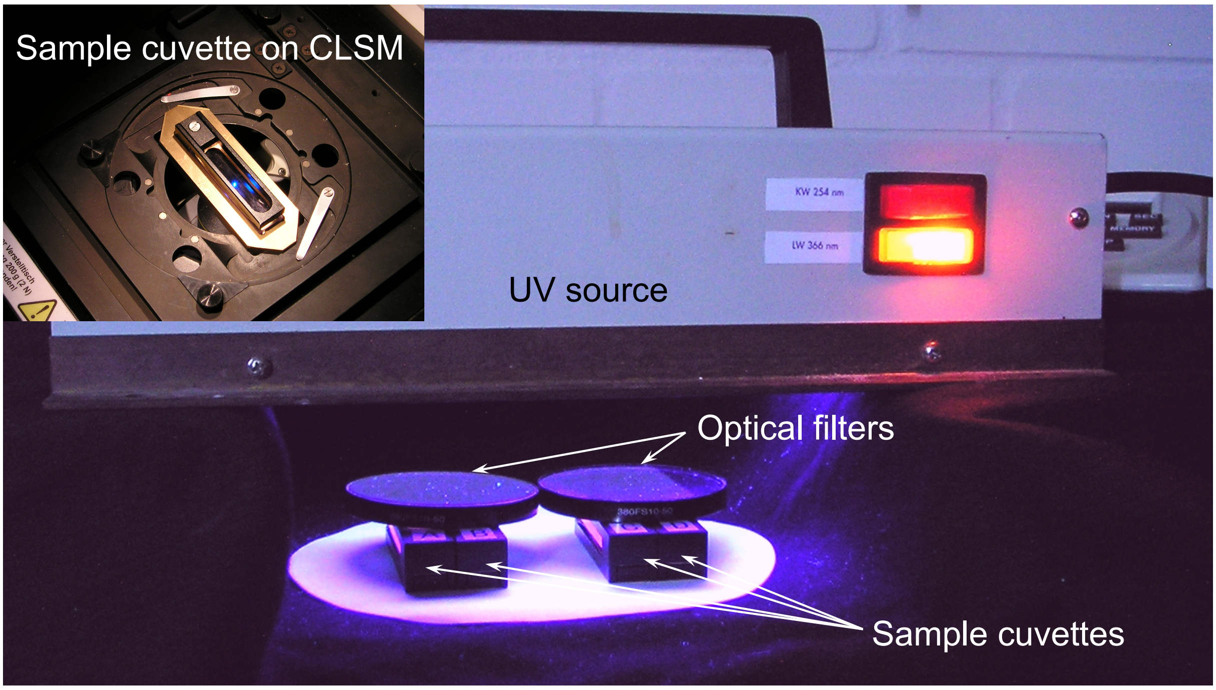

Figure 4.14 Typical setup as described in 4.2.3.4. – The inset shows how the sample cuvettes, which originally are designed for use in UV–vis spectrometers, are placed on a CLSM, thus allowing to employ the same sample for UV–vis spectroscopic quantification of the degree of crosslinking as well as FRAP, respectively.

A proper way to determine the DMMI conversion by quantifying the change of UV absorbance at 229 nm is also described in detail in Chapter 4.1. The absorption band of the DMMI moieties is superimposed on a background predominantly resulting from the PAAm backbone, but also from the TXS sensitizer and to a minor extent from the rhodamine labels of the tracers. These spectral contributions were subtracted before calculating the conversion.

When spherical tracers were employed, the strong UV absorbance of the polystyrene beads prevents this kind of analysis. Therefore, reference samples were prepared having the same composition but not containing microspheres. These were irradiated simultaneously with the actual samples. The UV analysis was then performed on the reference samples. The presence of the microspheres also led to an attenuation of the 383 nm light used to initiate the crosslinking reaction. This effect was taken into account by correcting the conversion data determined on the reference samples by a factor of 0.66, which is the ratio of sample transmittance in the range of (383 ± 5.6) nm with and without microspheres. Moreover, only data obtained at conversions below 0.6 were considered.

In samples containing linear tracers, the concentration of rhodamine B labels was so small (0.07 $\mathrm{mmol \cdot L^{-1}}$) that they did not cause any perceptible absorbance around 383 nm, so that no correction was necessary.

From the data of DMMI conversion with time, the corresponding elastically effective network densities were calculated based on the report in Chapter 4.1: Effective network densities were obtained from modulus measurements, and it was shown that the rise of modulus with time occurs in proportion with DMMI dimerization. Expediently, the material utilized in Chapter 4.1 was identical to the matrix polymer used for the present investigation, and also most experimental conditions were the same.

Translational diffusion coefficients of the tracer species were measured by FRAP as described in Section 4.2.3.2. Experiments were analyzed by the method presented in Chapter 3.2 particularly with regard to the quantification of distributions of diffusion coefficients in order to obtain reliable mean values. This was necessary because the linear tracers had relatively broad distributions of molecular weights as shown in Table 4.6.

4.2.4 Results and discussion

4.2.4.1 Influence of matrix-crosslinking on the diffusion coefficients of linear and spherical tracers

From the FRAP analyses, the distributions of diffusion coefficients were obtained. Some typical examples are shown in Figure 4.15 in order to discuss the characteristic features and the changes that occur when the matrix polymer becomes progressively crosslinked.

When linear tracers were employed (Figure 4.15a), a large mobile fraction with diffusion coefficients distributed over the range of D = 0.1–10 $\mu m^2 \cdot s^{-1}$ was detected besides a small portion (1–30%, depending on the particular composition of the sample) of rather immobile material. This shape of the distribution curves remained *essentially unchanged* over the entire transition from a semidilute solution to the fully crosslinked gel. The portion of the immobile material increased somewhat with rising molar mass of the tracers and rising matrix concentration. However, in no case did it vary systematically with the extent of crosslinking of the matrix. This observation indicates that there was *no chemical binding* of the tracers to the matrix (due to unwanted side reactions) during photocrosslinking. It can be assumed that the small immobile portion is due to branched rather than linear tracer molecules, which may be formed in the synthesis by chain transfer in free-radical copolymerization (cf. Chapter 3.1.2). Since for the current investigation only the behavior of linear tracer molecules shall be focused, the immobile fraction will be disregarded from now on.

Considering only the mobile fraction, the distribution of the diffusion coefficients of the linear tracers and their mean values exhibit *no* or just *small* changes upon crosslinking of the matrix: When matrix concentrations and/or tracer molecular weights are low, there is just some scatter around a mean value and some variation of the width of the distribution, as seen in Figure 4.15a. On the other hand, corresponding measurements on samples with higher matrix concentration and/or tracer molecular weights showed a slight decrease of the average diffusion coefficient upon proceeding gelation.

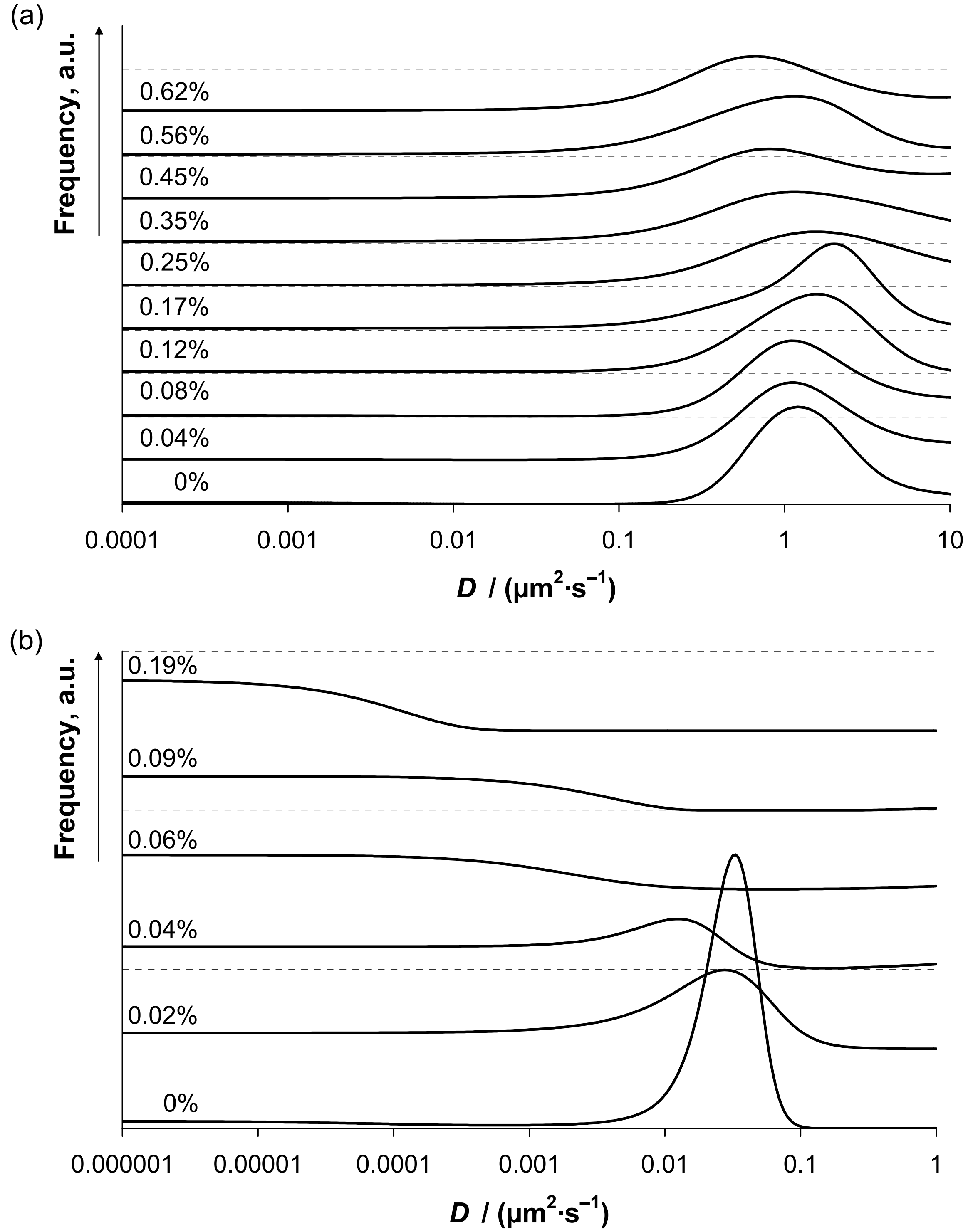

Figure 4.15 Examples of distributions of the translational diffusion coefficients of (a) 5 g·L^{-1} flexible linear PAAm-C0.1-4 (r_H = 16 nm) and (b) 0.5 wt.-% rigid spheres (r_H = 17 nm) enclosed in 60 g·L^{-1} PAAm-DMMI2.0 matrixes at increasing degree of crosslinking, denoted in terms of the concentration of elastically effective strands divided by the total concentration of monomer units (percentage quotation). – Curves were obtained by applying the maximum entropy method for FRAP analyses (cf. Chapter 3.2.2.2) and are shifted vertically for better clarity.

Experiments on samples containing spherical tracers showed a fundamentally different behavior (Figure 4.15b): Prior to crosslinking, *D*-distributions were solely composed of a well-defined sharp peak in the mobile region, appearing at markedly lower values of *D* than the corresponding broader ones observed on samples containing linear tracers. Moreover, the dependence of the diffusion coefficient on the concentration of the uncrosslinked matrix was notably stronger for spherical tracers than for linear tracers (see below). With beginning gelation, the amount of mobile spheres is diminished, and more and more tracer particles become immobilized, until at a certain threshold of crosslinking there is an abrupt change and *all tracers get trapped*. As long as mobile tracers could be detected, their mobility seemed to decrease slightly with increasing degree of crosslinking. There was just one exception to this general feature: In the sample consisting of a 20 $g \cdot L^{-1}$ PAAm matrix (lowest concentration studied), the 17 nm spheres remained equally mobile over the entire crosslinking procedure.

In Figure 4.16, the results of various sets of experiments are compared in a systematic way by plotting the mean diffusion coefficients over the degree of crosslinking. Figure 4.16a shows the diffusion coefficients of all the different tracers when embedded in a matrix of concentration 40 $g \cdot L^{-1}$. For the linear tracers having the lower molar masses (uppermost curves), *D* does not change at all when the matrix is chemically crosslinked, while for the linear tracers with higher molar masses there seems to be a slight but perceptible decrease of *D* when the crosslinking reaction goes to completion. In any case, the molar mass of the tracer molecules has a bigger impact on their diffusion coefficients than the fact that the matrix is or is not crosslinked. On the other hand, the spherical tracers (filled symbols) are only mobile up to a certain extent of crosslinking, which is smaller for the larger spheres.

Figure 4.16b illustrates the effect of matrix concentration. The mean diffusion coefficients of the 17 nm spheres (filled symbols) and of the linear tracer PAAm-C0.1-4 (open symbols) are shown in matrixes having concentrations of 20, 40, 60, and 80 $g \cdot L^{-1}$. The linear tracer was chosen such that its hydrodynamic radius matches that of the hard spheres (cf. Table 4.6 and 4.7). For all matrix concentrations, the diffusion coefficient of the linear tracers remains essentially constant upon gelation. Similar behavior was found for the spheres only in the 20 $g \cdot L^{-1}$ system, while at higher matrix concentrations the mobility of the spheres drops to virtually zero at some characteristic degree of crosslinking, which is the lower the higher the matrix concentration is.

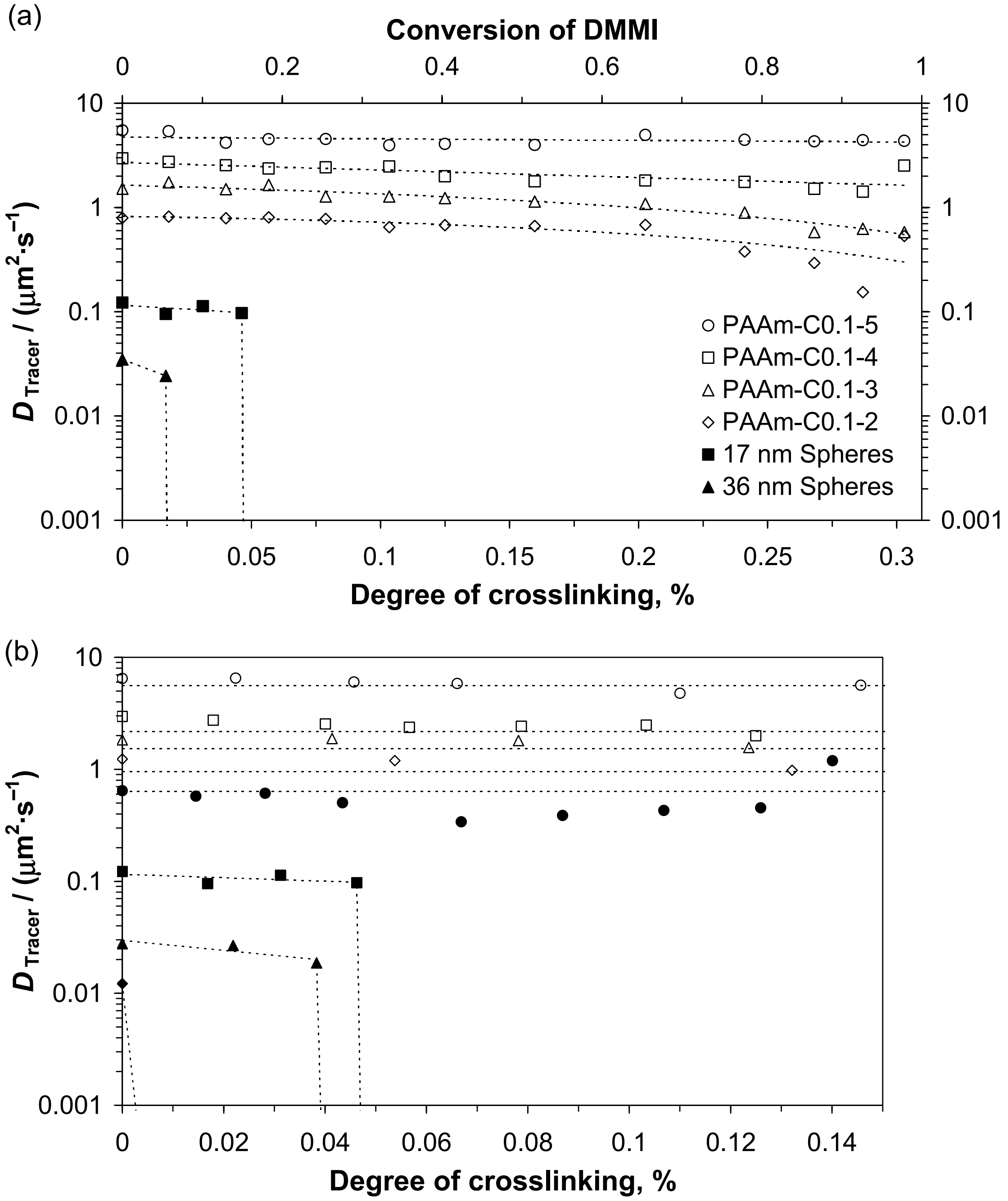

Figure 4.16 Average values of the distributed translational diffusion coefficients of linear polyacrylamides and spherical polystyrene particles during proceeding crosslinking of a surrounding PAAm matrix. – (a) System composed of 40 g·L^{-1} PAAm-DMMI2.0 containing differently sized linear (open symbols) and spherical (filled symbols) tracers. (b) Comparison of linear PAAm-C0.1-4 (open symbols) and 17 nm spheres (filled symbols) in PAAm-DMMI2.0 matrixes with concentrations of 20 (circles), 40 (squares), 60 (triangles), and 80 g·L^{-1} (diamonds). In both (a) and (b), values of DMMI conversion (upper axis in (a)) were estimated by UV–vis spectroscopy as described in 4.2.3.4 and then converted into crosslinking densities (lower axes, number of elastically effective network chains per total number of monomer units) on the basis of the findings reported in Chapter 4.1.

Table 4.8 Average mesh sizes in aqueous semidilute solutions (ξ_{solution}) and chemically crosslinked hydrogels (ξ_{X}) of PAAm-DMMI2.0. Also listed are the values at the level of crosslinking where the mobilities of enclosed 17 nm and 36 nm spheres drop to $D \to 0$, respectively.

c_{Matrix} $\text{g}\cdot\text{L}^{-1}$	ξ_{solution} [a)] nm	ξ_{X} [b)] nm	$\xi_{\text{17 nm spheres immobile}}$ [b)] nm	$\xi_{\text{36 nm spheres immobile}}$ [b)] nm
20	16.0	17.2	no immobilization	33.0
40	9.5	12.5	25.2	32.8
60	7.0	8.5	27.7	48.8
80	5.7	6.9	24.8	44.3

[a] Calculated from eq (2.5), utilizing $c^{*\,\text{c)}}$ and r_{H} from Table 4.6.

[b] Calculated from eq (4.5) on basis of the rheology results reported in Chapter 4.1.4.3.

In order to discuss these findings, it is necessary to consider the relevant length scales of the systems studied. In semidilute solutions, the *correlation length* ξ is a measure of distance up to which a polymer chain is essentially unaffected by other chains. It can be roughly estimated by eq (2.5) (cf. Chapter 2.1.1.2, p 12):

$$\xi_{\text{solution}} \approx R_{\text{G}} \left(c^* / c \right)^{\gamma} \approx 2.05 \cdot r_{\text{H}} \left(c^* / c \right)^{\gamma} \qquad (2.5)$$

with R_{G} being the radius of gyration, r_{H} the hydrodynamic radius, and $\gamma = 0.75$ as well as $R_{\text{G}} \approx 2.05\, r_{\text{H}}$ [212] in good solvents.[1] The ξ-values calculated with eq (2.5) using the hydrodynamic radius of the matrix chains are listed in the first column of Table 4.8.[2] In most cases, they are smaller than the hydrodynamic radii of the linear or spherical tracers.

Another length scale which becomes relevant after crosslinking is the *mean distance between crosslinks*. This quantity, denoted ξ_{X}, could be obtained from the molar concentration of elastically effective junctions, which was in turn deduced from modulus measurements (Chapter 4.1.4.3), according to

$$\xi_{\text{X}} = \sqrt[3]{\frac{1}{c_{\text{junctions}}\, N_{\text{A}}}} \qquad (4.5)$$

---

[1] Generally, aqueous PAAm solutions near room temperature are considered as being in good solvent. χ-parameters reported lie in the range of 0.44–0.495 [43], while the Mark–Houwink–Sakurada exponent is between 0.7 and 0.8 [42].

[2] Note that they are in good agreement with dynamic correlation lengths measured by dynamic light scattering on a similar system (data not shown).

The corresponding data listed in the second column of Table 4.8 are those for the fully crosslinked gels. The fact that the network density grows in direct proportion with DMMI conversion can be used to determine the mean distance between crosslinks at intermediate stages.

It can be seen from Table 4.8 that the ξ_{solution} and ξ_{X} data are strikingly similar. The difference between the semidilute solution and the fully crosslinked gel is therefore not a change of the characteristic length scale, but solely the fact that the *interchain interaction* is *temporary and fluctuating* (in solution) or *permanent* (in a gel). This difference seems to be rather irrelevant for the mobility of the linear tracers, presumably because of their high internal flexibility and dynamics.

The rigid *spherical* particles, on the other hand, are markedly affected by permanent crosslinks: they get trapped when the crosslink density exceeds a certain threshold. The mean distances between crosslinks at the experimentally observed thresholds were calculated for the two sizes of spheres studied and are also listed in Table 4.8, Column 3 and 4. These critical distances between crosslinks seem to be fairly independent of matrix concentration (there is quite some variation), but are correlated with the size of the spheres, as one would expect on grounds of a very simplistic picture. An exception to this behavior was merely found for the system composed of 20 $\mathrm{g \cdot L^{-1}}$ PAAm2.0 with 17 nm spheres (cf. Figure 4.16b), where the mesh size in the gel state seems to be sufficiently large to allow for diffusion of the spheres.

4.2.4.2 Concentration and molecular weight dependence of the tracer-diffusion coefficients in semidilute solutions

In Figure 4.17, all diffusion coefficients determined in uncrosslinked matrixes are plotted as a function of matrix concentration in order to compare the experimental results with theoretical predictions. Also included are the data in dilute (matrix-free) solution.

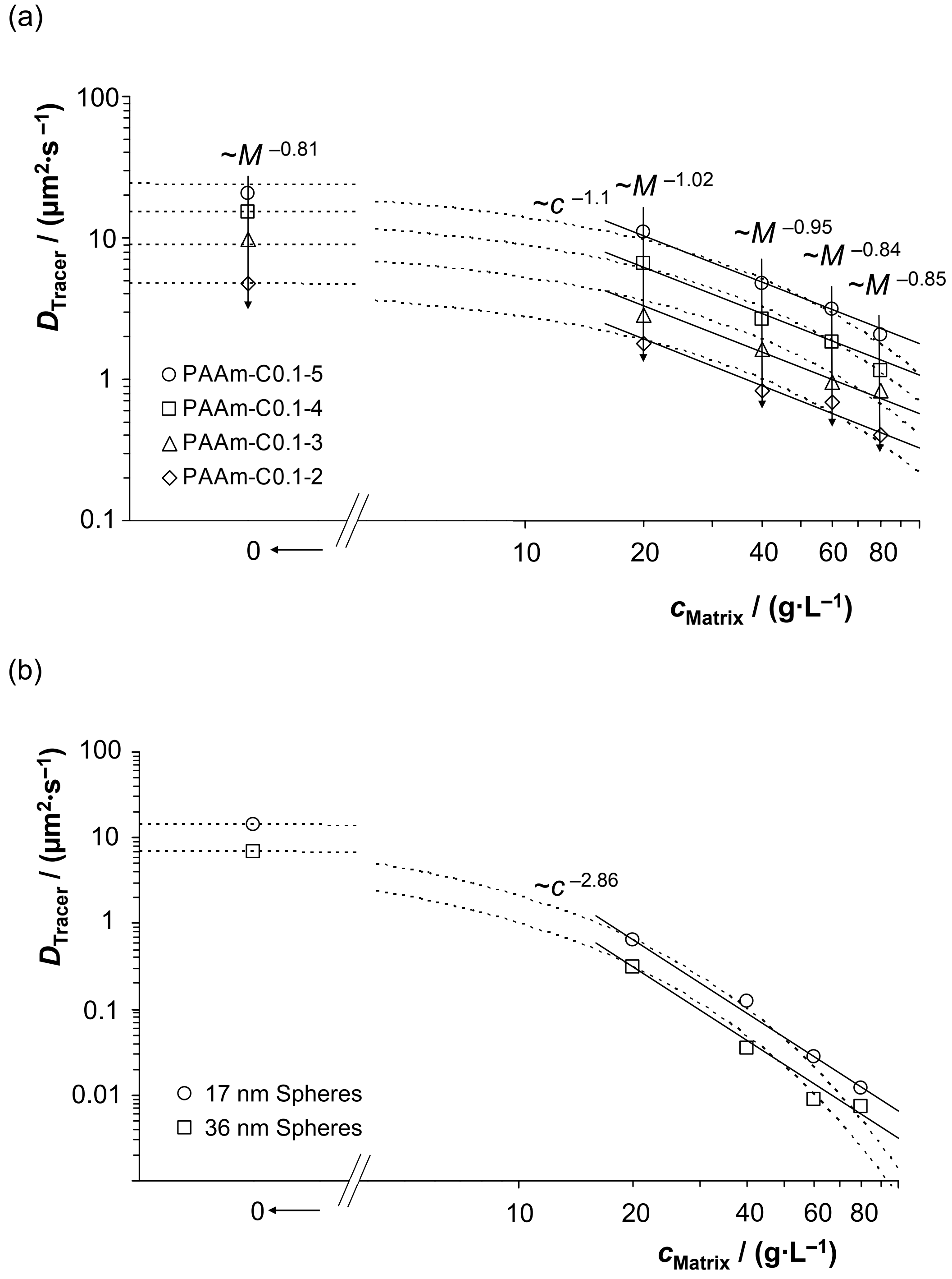

Figure 4.17 Quantitative analyses of the diffusive mobilities D of differently sized linear (a) and spherical (b) tracers as a function of the concentration of a surrounding PAAm matrix. – In both (a) and (b), D-values were measured prior to matrix-crosslinking. Besides the semidilute regime, both plots also contain the values of the pure tracers in the absence of a surrounding matrix. Relations between D and c are analyzed by the application of power laws in the semidilute domain (full lines) as well as Phillies' universal scaling equation in the form of eq (2.71) over the entire range of matrix concentration (dotted lines) in both cases. (a) also contains an indication of the corresponding power law dependences of D on M_{W} (arrows).

Since the main emphasis of the present investigation was on studying the effect of crosslinking, the data obtained on uncrosslinked samples are rather limited and do not allow for an in-depth inspection of concentration or molar mass dependencies. However, some major features can be discussed with appropriate care.

In Figure 4.17a, the course of the diffusion coefficients of the linear tracers over matrix concentration is compared with Phillies' formula, eq (2.71) (dotted lines). For the fit curves, the same values of $\alpha = 0.1$ and $\nu = 0.8$ are presumed. When the four curves were fitted individually, the parameters show a broad scatter ($0.04 \leq \alpha \leq 0.25$ instead of the common value 0.1, and $0.54 \leq \nu \leq 0.97$ instead of the common value 0.8), but no systematic variation with molar mass of the tracers. The combined fit therefore seems to be more appropriate. The fit curves show reasonable agreement with the experimental data, although the curvature in the semidilute regime seems to be too strong.

The full straight lines shown in Figure 4.17a represent the scaling behavior in the semidilute regime. They are drawn with a common slope of –1.10 as a result of a combined fit, while individual fits had slopes between 0.94 and 1.18. This value is definitely higher than 0.5 as predicted for an unentangled semidilute solution in a good solvent (eq 2.62). On the other hand, it is just the predicted value for a θ-solvent, but this solution state is not anticipated for aqueous PAAm solutions. As an alternative, one may argue that the value around 1 lies *between* the predicted values for unentangled (0.5) and entangled (1.75) solutions in a good solvent, and that the solutions investigated exhibit a *gradual change between the two regimes* in the concentration range inspected because of the broad molar mass distribution of the PAAm employed.

Also indicated in Figure 4.17a are the exponents obtained when molar mass dependencies were analyzed. In the semidilute regime they are in the range 0.84–1.02. This is in close agreement with scaling predictions for the unentangled semidilute state; cf. eq (2.60). Note, however, that the corresponding exponent found in dilute solution is 0.81 instead of the expected 0.6. Besides the fact that only very few data points were available, it should be kept in mind that the molar mass distributions of the linear tracers (and also that of the matrix polymer) were relatively broad, and that the weight averages used were determined by SEC employing a pullulan calibration, which may have led to additional errors.

Figure 4.17b contains the data for the spherical tracers as well as the corresponding fit curves. The dotted lines were obtained by application of Phillies' approach with $\alpha = 0.4$ and $\nu = 0.7$. Again, they seem to be curved too strongly in the semidilute range. The full lines, on the other hand, assume a power law behavior with an exponent around –2.86, indicating a much stronger concentration dependence for the spheres than for the flexible linear tracers. In terms of Phillies' approach, this fact is captured by the parameter α which changes from 0.1 for linear tracers to 0.4 for spheres, while the parameter ν is hardly affected. Since only two sizes of spheres were studied, the size dependence cannot be considered.

4.2.5 Conclusions

The investigation of the diffusion of mesoscopic probes in semidilute uncrosslinked and crosslinked polymer systems has revealed the following major observations:

(i) In semidilute polymer solutions, the diffusion coefficient of hard spheres is *markedly smaller* than that of flexible linear macromolecules having a similar coil size in terms of hydrodynamic radius.

(ii) Also the *concentration dependence* of the diffusion coefficient in solution is much *stronger* for spheres than for flexible linear chains.

(iii) Crosslinking of the semidilute matrix has only a *minor influence* on the diffusion of *linear* tracers or no effect at all, while *spherical* tracers get *completely immobilized* when the degree of crosslinking exceeds a certain threshold, provided that the sphere size is perceptibly larger than the mesh size of the network.

In view of these observations, one has to conclude that the rate-determining mechanism of diffusion processes is fundamentally different for the two kinds of probes. The mobility of hard spheres is solely controlled by the structure and dynamics of the surrounding *matrix*, while for linear macromolecules, the internal flexibility and dynamics of the *probes* have a major, decisive influence.

This statement is well accepted for concentrated solutions or polymer melts, where the motions of linear chains occur via the reptation mechanism. The present work, however, covers the semidilute regime with polymer concentrations being only 4–16 times higher than the overlap concentration, which is commonly assumed just to be the *onset* of entanglement effects.

The exponents found for the molar mass dependence of the diffusion coefficient and for its concentration dependence, despite the uncertainty due to broad distributions, also seem to indicate that the systems studied are below the entanglement concentration. Nevertheless, the observation that the diffusion coefficient of linear chains is practically the same in uncrosslinked and crosslinked matrixes, where the hydrodynamic radius of the probe molecules is substantially larger than the mesh size, points to the fact that the translational mobility of the chains is governed by their intramolecular mobility. In order to enable the molecules to move through the permanent meshes, a mechanism somehow similar to reptation needs to be envisaged.

The hydrodynamic scaling model predicts that the translational mobilities of flexible coils and of hard spheres having a comparable size are similar. The results presented in this chapter clearly exclude such behavior in the concentration range studied, although the equation proposed provides a reasonable fit to the individual data sets.

5 Recapitulation, closing remarks, and outlook

In the beginning of this thesis, it has been pointed out that the general aim of the current project was to investigate the formation, the structure, and the properties of polyacrylamide hydrogels. For this purpose, the following two main targets were focused:

(i) Hydrogel formation by photocrosslinking of DMMI-functionalized linear PAAm precursors

(ii) FRAP studies on the dynamics of labeled flexible and rigid probes that are enclosed in the networks from (i)

To investigate these aspects, a comprehensive exploration originating from preliminary projects on the synthesis and characterization of labeled tracers as well as the development of a proper experimental procedure was performed which finally led to the processing of the two above-mentioned main tasks.

In summary, one can state that all of these different parts of the work could be completed successfully: First of all, the synthesis of fluorescently labeled linear PAAm turned out to work well and yielded a versatile type of functionalized water-soluble polymer material covering a wide range of molecular weights. Subsequent studies on the development of a procedure for the analysis of spatially resolved FRAP experiments led to an extremely practical and consistent method. Moreover, photocrosslinking of DMMI-functionalized PAAm turned out to be a convenient approach for the well-defined and highly controlled formation of homogeneous network structures in aqueous media.

Eventually, these three projects converged to the systematic investigation of the mobility of probes in polymer networks that were either (weakly) entangled or chemically crosslinked to varying degrees. The system employed for these investigations turned out to be well thought-out, and there was no evidence for unwanted side effects such as binding of the tracers to the matrix or significant photobleaching of the different chromophores being present in the samples during UV irradiation.

Nevertheless, the latter investigation was impaired by the relatively high polydispersities of the linear polymers employed, which consequently also exhibited broad distributions of diffusion coefficients and, moreover, were accompanied by totally immobile fractions. To account for this, two strategies were mapped out: On the one hand, the syntheses of the linear matrix and tracer materials (Chapter 3.1 and 4.1) were performed in the presence of a chain transfer agent to allow for molecular weight control. On the other hand, FRAP experiments were analyzed by a procedure that is able to deal with multi-component diffusion.

However, as there were still some impairments remaining, the polydispersity-problems should be considered as a motivation for further improvement of the work. In particular, one could think about the following projects:

1. Labeled tracers and their dynamics in networks

To obtain narrowly distributed labeled polymers in aqueous media, one could either try to *fractionate* the PAAm material from the present work or, otherwise, to employ *alternative materials* such as polymethylmethacrylamide (PMAAm), which is not as prone to undergo chain transfer reactions during free-radical polymerization as PAAm. Alternatively, one could also switch to *organic* media, which would offer the possibility to employ the great variety of narrowly distributed well-defined polystyrene standards being readily available. Of course, such a general change of the system would involve a corresponding change of the matrix material too, thus requiring a fundamental exploration of the possibilities to carry out photocrosslinking reactions in organic media. (Naturally, this would also apply to the labeling of the tracers.)

In addition to the narrowing of the molecular weight distributions of the linear tracers, it would be desirable to extend the studies on the diffusion of *spherical* tracers in polymer matrixes to a broader range of particle sizes. Unfortunately, labeled polystyrene beads as employed for the present work are hardly available in the interesting range below 100 nm. An alternative could thus be to use labeled *dextrans*, which are purchasable over a wide range of sizes between 1 and 100 nm.

Finally, another interesting project would be to study the dynamics of probes that fall between the two extremes of flexible linear chains on the one hand and rigid particles on the other hand and thus to employ materials such as star-shaped macromolecules or (semi)rigid linear chains like polyelectrolytes.

Moreover, further studies could aim at the incorporation of *functional* materials such as biomacromolecules or drugs with regard to practical applications of polymer hydrogels in fields like bioseparation or enzyme immobilization.

2. FRAP

In principle, there is no urgent demand to improve the method for FRAP analysis developed here, as it turned out to be versatile and well-working. However, a further project could aim at the modification of the procedures presented in Chapter 3.2.2 in order to apply the method to the analysis of *anisotropic* diffusion processes within the confocal ($x;y$)-plane. Basically, this should merely require the extension of the algorithm to a 4-dimensional fit of direction-dependent Gaussians to the temporal and 2-dimensional spatial course of fluorescence intensity quantified by each FRAP image. The principal axes of the medium would thereby be obtained from the direction-dependent width of the Gaussian profiles when point-bleaching experiments were performed.

Eventually, this could allow for the investigation of probe dynamics in chemical networks during mechanical deformation, or, likewise, exposure to electric or magnetic fields. Regarding the latter aspect, the work would then head for possible applications of hydrogels in the field of electrophoresis.

3. Photocrosslinking

Similar to the preceding point, there is no fundamental need to modify or improve the photocrosslinking procedures of DMMI-functionalized PAAm, as the reaction basically proceeds in highly efficient and controlled manner, yielding networks that exhibit homogeneous topologies. However, with regard to the possible applications of hydrogels as “smart materials” in fields like pharmaceutical research or biophysics, another challenging aim would be to explore the possibilities for *reversible* photocrosslinking of PAAm networks in aqueous media, which could be achieved by employing particular pendant moieties such as cinnamates or acridizinium groups with the PAAm basis material. It has been reported that these functionalities are able to dimerize upon irradiation with wavelengths above 300 nm, whereas exposure to wavelengths below 260 nm re-cleaves the dimers [132, 213]. Ultimately, this feature could thus allow for the design of photoswitchable hydrogels to be used for purposes like the controlled release of enclosed (functional) materials in systems that can be exposed to UV light.

In summary, one may recognize that there are several possibilities for improvement and follow-up projects for the present work. It seems thus worth mentioning as a closing remark for this thesis that at the time of its publication, some of them were already in progress in the group of Prof. Oppermann at Clausthal University of Technology.

6 References

[1] Thomas, W. M. *Acrylamide Polymers*; in: Bikales, N. M., editor. *Encyclopedia of Polymer Science and Technology*, Vol. 1; Wiley: New York, 1964.

[2] Montgomery, W. H. *Polyacrylamide*; in: Davidson R. L.; Sitting M., editors. *Water-Soluble Resins*, 2nd ed.; Van Nostrand Reinhold: New York, 1968.

[3] Bikales, N. M. *Water-Soluble Polymers*; in: Bikales N. M., editor. *Polymer Science and Technology*, Vol. 2; Plenum Press: New York, 1973.

[4] Molyneux, P. *Water-Soluble Synthetic Polymers: Properties and Behavior*; CRC Press: Boca Raton, FL, 1984.

[5] White, M. L. *J. Phys. Chem.* **1960**, *64*, 1563.

[6] Mallam, S.; Horkay, F.; Hecht, A. M.; Geissler, E. *Macromolecules* **1989**, *22*, 3356.

[7] Lindemann, B.; Schröder, U. P.; Oppermann, W. *Macromolecules* **1997**, *30*, 4073.

[8] Kizilay, M. Y.; Okay, O. *Macromolecules* **2003**, *36*, 6856.

[9] Ichimura, K.; Watanabe, S. *J. Polym. Sci. Polym. Chem. Ed.* **1982**, *20*, 1419.

[10] Ichimura, K. *J. Polym. Sci. Polym. Chem. Ed.* **1984**, *22*, 2817.

[11] Shindo, Y.; Katagiri, N.; Ebisuno, T.; Hasegawa, T.; Mitsuda, M. *Angew. Makromol. Chem.* **1996**, *240*, 231.

[12] Cockburn, E. S.; Davidson, R. S.; Pratt, J. E. *J. Photochem. Photobiol. A* **1996**, *94*, 83.

[13] Schinner, R.; Wolff, T.; Kuckling, D. *Ber. Bunsenges. Phys. Chem.* **1998**, *102*, 1710.

[14] Graessley, W. W. *Adv. Polym. Sci.* **1974**, *16*, 1.

[15] Tirrel, M. *Rubber Chem. Techn.* **1984**, *57*, 523.

[16] Pearson, D. S. *Rubber Chem. Techn.* **1987**, *60*, 439.

[17] Skolnick, J.; Kolinski, A. *Adv. Chem. Phys.* **1989**, *78*, 223.

[18] Lodge, T. P.; Rotstein, N. A.; Prager, S. *Adv. Chem. Phys.* **1990**, *79*, 1.

[19] Watanabe, H. *Prog. Polym. Sci.* **1999**, *24*, 1253.

[20] McLeish, T. C. B. *Adv. Phys.* **2002**, *51*, 1379.

[21] De Gennes, P. G. *J. Chem. Phys*. **1971**, *55*, 572.

[22] De Gennes, P. G. *Macromolecules* **1976**, *9*, 587 and 594.

[23] De Gennes, P. G. *Scaling Concepts in Polymer Physics*; Cornell University Press: Ithaca and London, 1979.

[24] Edwards, S. F. *J. Phys. A* **1975**, *8*, 1670.

[25] Doi, M.; Edwards, S. F. *J. Chem. Soc. Faraday Trans. II* **1978**, *74*, 1789, 1802, and 1818.

[26] Doi, M.; Edwards, S. F. *The Theory of Polymer Dynamics*; Clarendon Press: Oxford, 1986.

[27] Phillies, G. D. J.; Ullmann, G. S.; Ullmann, K.; Lin, T. H. *J. Chem. Phys.* **1985**, *82*, 5242.

[28] Phillies, G. D. J. *Macromolecules* **1986**, *19*, 2367.

[29] Phillies, G. D. J. *Macromolecules* **1987**, *20*, 558.

[30] Phillies, G. D. J. *Macromolecules* **1988**, *21*, 3101.

[31] Phillies, G. D. J. *J. Phys. Chem.* **1989**, *93*, 5029.

[32] Phillies, G. D. J. *Macromolecule*s **1990**, *23*, 2742.

[33] Phillies, G. D. J. *J. Phys. Chem.* **1992**, *96*, 10061.

[34] Phillies, G. D. J.; Quinlan, C. A. *Macromolecules* **1995**, *28*, 160.

[35] Phillies, G. D. J. arXiv:cond-mat/0403109, 2004.

[36] Cowie, J. M. G. *Chemie und Physik der synthetischen Polymeren*; Vieweg: Braunschweig/Wiesbaden, 1997.

[37] Flory, P. J. *J. Chem. Phys*. **1942**, *10*, 51.

[38] Flory, P. J. *Principles of Polymer Chemistry*; Cornell University Press: Ithaca and London, 1953.

[39] Hildebrand, J. H.; Scott, R. L. *The Solubility of Nonelectrolytes*, 3rd ed.; Van Nostrand Reinhold: New York, 1959.

[40] Brandrup, J.; Immergut, E. H.; Grulke, E. A., editors. *Polymer Handbook*, 4th ed.; Wiley: New York, 1999.

[41] a) Bohdanecký, M.; Petrus, V.; Sedlácek, B. *Makromol. Chem*. **1983**, *184*, 2061; b) Izyumnikov, A. L.; Mineyev, L. V.; Maslennikov, V. A.; Sidorina, L. S.; Samsonova, O. S.; Abkin, A. D. *Polym. Sci. USSR* **1988**, *30*, 1062; c) Schwartz, T.; Sabbadin, J.; Francois, J. *Polymer* **1981**, *22*, 609.

[42] a) Scholtan, W. *Makromol. Chem*. **1954**, *14*, 169; b) Klein, W. M.; Conrad M. *Makromol. Chem.* **1978**, *179*, 1635; c) McCarthy, K. J.; Burkhardt, C. W.; Parazak, D. P. *J. Appl. Polym. Sci.* **1987**, *33*, 1699.

[43] a) Silberberg, A.; Eliassaf, J.; Katchalksy, A. *J. Polym. Sci.* **1959**, *23*, 259; b) Misra, G. S.; Bhattacharya, S. N. *Eur. Polym. J.* **1979**, *15*, 125; c) Day, J. C.; Robb, I. D. *Polymer* **1981**, *22*, 1530.

[44] Ying, Q.; Chu, B. *Macromolecules* **1987**, *20*, 362.

[45] Des Cloizeaux, J.; Jannink, G. *Polymers in solution. Their modelling and structure*; Clarendon Press: Oxford, 1990.

[46] Elias, H. G. *Makromoleküle; Band 2: Physikalische Strukturen und Eigenschaften*, 6th ed.; Wiley-VCH: Weinheim, 2001.

[47] Rubinstein, M.; Colby, R. H. *Polymer Physics*; Oxford University Press: New York, 1999.

[48] De Gennes, P. G. *J. Phys. (Paris) Lett.* **1976**, *37*, *L-1*, 61.

[49] Peniche-Covacs, C.; Dev, S.; Gordon, M.; Judd, M.; Kajiwara, K. *Polymer Networks*; Chompff, A.; Newman, S., editors; Plenum Press: New York, 1971.

[50] Chambon, F.; Winter, H. H. *Polym. Bull.* **1985**, *13*, 499.

[51] Kuhn, W. *Kolloid-Z.* **1934**, *68*, 2.

[52] Kuhn, W. *Kolloid-Z.* **1936**, *76*, 258.

[53] Wall, F. T. *J. Chem. Phys.* **1942**, *10*, 485.

[54] Treloar, L. R. G. *Trans. Farad. Soc.* **1943**, *39*, 241.

[55] Hermans, J. J. *Trans. Farad. Soc.* **1947**, *43*, 591.

[56] Flory, P. J. *J. Chem. Phys.* **1949**, *17*, 303.

[57] James, H.; Guth, E. *J. Chem. Phys.* **1947**, *15*, 669.

[58] Kuhn, W.; Grün, F. *Kolloid-Z.* **1942**, *101*, 248.

[59] Saalwächter, K. *Prog. NMR Spectrosc.* **2007**, *51*, 1.

[60] Saalwächter, K. *Heteronuclear Recoupling Methods in Solid-State NMR*; PhD Thesis, Johannes Gutenberg University of Mainz, 2000.

[61] Cohen-Addad, J. P. *J. Chem. Phys.* **1973**, *60*, 2440; Gotlib, Y. Y.; Lifshitz, M. I.; Shevelev, V. A.; Lishanskij, I. S.; Balanina, I. V. *Vysokomol. Soed.* **1976**, *A18*, 2299.

[62] Saalwächter, K.; Gottlieb, M.; Liu, R.; Oppermann, W. *Macromolecules* **2007**, *40*, 1555.

[63] Saalwächter, K.; Herrero, B.; López-Manchado, M. A. *Macromolecules* **2005**, *38*, 9650.

[64] Saalwächter, K.; Ziegler, P.; Spyckerelle, O.; Haidar, B.; Vidal, A.; Sommer, J. U. *J. Chem. Phys.* **2003**, *119*, 3468.

[65] Saalwächter, K.; Klüppel, M.; Luo, H.; Schneider, H. *Appl. Magn. Reson.* **2004**, *27*, 401.

[66] Baum, J.; Pines, A. *J. Am. Chem. Soc.* **1986**, *108*, 7447.

[67] Saalwächter, K.; Kleinschmidt, F.; Sommer, J. U. *Macromolecules* **2004**, *37*, 8556.

[68] Fick, A. *Poggendorffs Ann. Phys.* **1855**, *94*, 59.

[69] Einstein, A. *Z. Elektrochem*. **1908**, *14*, 235.

[70] Crank, J. *The Mathematics of Diffusion*; Clarendon Press: Oxford, 1975.

[71] Smoluchowski, M. *Ann. Phys.* **1906**, *21*, 756.

[72] Rouse, P. E. *J. Chem. Phys.* **1953**, *21*, 1272.

[73] Zimm, B. H. *J. Chem. Phys.* **1956**, *24*, 269.

[74] Yamada, T.; Yoshizaki, T.; Yamakawa, H. *Macromolecules* **1992**, *25*, 377.

[75] Arai, T.; Abe, F.; Yoshizaki, T.; Einaga, Y.; Yamakawa, H. *Macromolecules* **1995**, *28*, 3609.

[76] Kirkwood, J. G.; Riseman, J. *J. Chem. Phys*. **1948**, *16*, 565.

[77] Wang, F. W.; Zimm, B. H. *J. Polym. Sci.: Polym. Phys. Ed.* **1974**, *12*, 1619.

[78] Hess, W. *Macromolecules* **1986**, *19*, 1395.

[79] Hess, W. *Macromolecules* **1987**, *20*, 2587.

[80] Brochard, F.; De Gennes, P. J. *Macromolecules* **1977**, *10*, 1157.

[81] Schaefer, D. W.; Joanny, J. F.; Pincus, P. *Macromolecules* **1980**, *13*, 1280.

[82] Graessley, W. W. *Adv. Polym. Sci.* **1982**, *47*, 67.

[83] Doi, M. *J. Polym. Sci.: Polym. Phys. Ed.* **1983**, *21*, 667.

[84] Franck, J. *Trans. Farad. Soc.* **1926**, *21*, 536.

[85] Condon, E. *Phys. Rev.* **1926**, *28*, 1182.

[86] Condon, E. *Phys. Rev.* **1928**, *32*, 858.

[87] Atkins, P. W. *Physikalische Chemie*, 2nd ed.; Wiley-VCH: Weinheim, 1996.

[88] Jablonski, A. *Z. Phys.* **1934**, *94*, 38.

[89] Kasha, M. *Disc. Faraday Soc.* **1950**, *9*, 14.

[90] Stokes, G. G. *Phil. Trans. R. Soc. (London)* **1852**, *142*, 463.

[91] Lakowicz, J. R. *Principles of Fluorescence Spectroscopy*, 2nd ed.; Kluwer Academic/Plenum Publishers: New York, 1999

[92] Förster, T. *Ann. Phys. (Berlin)* **1948**, *2*, 55.

[93] Klessinger, M.; Michl, J. *Lichtabsorption und Photochemie organischer Moleküle*; Wiley-VCH: Weinheim, 1989.

[94] Lindquist, L. *Arkiv för Kemi* **1969**, *16*, 79.

[95] Kasche, V.; Lindquist, L. *J. Phys. Chem.* **1964**, *68*, 817.

[96] Usui, Y.; Itoh, K.; Koizumi, M. *Bull. Chem. Soc. Jpn.* **1965**, *38*, 1015.

[97] Song, L.; Hennink, E. J.; Young, I. T.; Tanke, H. J. *Biophys. J.* **1995**, *68*, 2588.

[98] Song, L.; Varma, C. A. G. O.; Verhoeven, J. W.; Tanke, H. J. *Biophys. J.* **1996**, 70, 2959.

[99] Gollnick, K.; Franken, T.; Fouda, M. F. R.; Paur, H. R.; Held, S. *J. Photochem. Photobiol. B: Biol.* **1992**, *12*, 57.

[100] Krüger, U.; Memming, M. *Ber. Bunsenges. Phys. Chem.* **1974**, *78*, 670.

[101] Krüger, U.; Memming, M. *Ber. Bunsenges. Phys. Chem.* **1974**, *78*, 679.

[102] Wilkinson, F.; Helman, W. P.; Ross, B. A. *J. Phys. Chem. Ref. Data* **1993**, *22*, 113.

[103] Eggeling, C.; Widengreen, J.; Rigler, R.; Seidel, C. A. M. *Anal. Chem.* **1998**, *70*, 2651.

[104] Dittrich, P. S.; Schwille, P. *Appl. Phys. B* **2001**, *73*, 829.

[105] Farnum, D. G.; Mostashari, A. J. *Org. Photochem. Synth.* **1971**, *1*, 103.

[106] Cohen, M. D.; Schmidt, J. M. G. *J. Chem. Soc.* **1964**, 1996.

[107] Rennert, J.; Ruggiero, E. M.; Rapp, J. *Photochem. Photobiol.* **1967**, *6*, 29.

[108] Rennert, J. *Photogr. Sci. Eng.* **1971**, *15*, 60.

[109] Schenck, G. O.; Von Wilucki, I.; Krauch, C. H. *Chem. Ber.* **1962**, *95*, 1409.

[110] Krauch, C. H.; Farid, S.; Schenck, G. O. *Chem. Ber.* **1966**, *99*, 625.

[111] Hammond, G. S.; Stout, C. A.; Lamola, A. A. *J. Am. Chem. Soc.* **1964**, *86*, 3103.

[112] Kuznetsova, N. A.; Kaliya, O. L *Russ. Chem. Rev.* **1992**, *61*, 683.

[113] Schenck, G. O.; Hartmann, W.; Mannsfeld, S. P.; Metzner, W.; Krauch, C. H. *Chem. Ber.* **1962**, *95*, 1642.

[114] De Schryver, F. C.; Bhardwai, I.; Put, J. *Angew. Chem.* **1969**, *81*, 224.

[115] De Schryver, F. C.; Feast, W. J.; Smets, G. *J. Polym. Sci A-1* **1970**, *8*, 1939.

[116] De Schryver, F. C.; Boens, N.; Smets, G. *J. Polym. Sci. A-1* **1972**, *10*, 1687.

[117] Put, J.; De Schryver, F. C. *J. Am. Chem. Soc.* **1973**, *95*, 137.

[118] Steinmetz, R. *Fortschr. Chem. Forsch.* **1967**, *7*, 445.

[119] Becker, H. G. O.; Böttcher, H.; Dietz, F.; Rehorek, D.; Roewer, G.; Schiller, K.; Timpe, H. J. *Einführung in die Photochemie*; Deutscher Verlag der Wissenschaften: Berlin, 1991.

[120] Fleming, I. *Grenzorbitale und Reaktionen organischer Verbindungen*; Wiley-VCH: Weinheim, 1990.

[121] Wöhrle, D.; Tausch, M. W.; Stohrer, W. D. *Photochemie*; Wiley-VCH: Weinheim, 1998.

[122] Herkstroeter, W. G.; Lamola, A. A.; Hammond, G. S. *J. Am. Chem. Soc.* **1964**, *86*, 4537.

[123] Hammond, G. S.; Turro, N. J.; Leermakers, P. A. *J. Phys. Chem.* **1962**, *66*, 1144.

[124] Wilkinson, F. *J. Phys. Chem.* **1962**, *66*, 2569.

[125] Scharf, H. D. *Fortschr. Chem. Forsch.* **1969**, *11*, 216.

[126] Murov, S. L. *Handbook of Photochemistry*; Marcel Dekker, Inc: New York, 1973.

[127] Schenck, G. O.; Steinmetz, R. *Bull. Soc. Chim. Belg.* **1962**, *71*, 78.

[128] Tsuda, M. *J. Chem. Soc. Jpn.* **1969**, *42*, 905.

[129] Oikawa, S.; Tsuda, M.; Ueno, N.; Sugita, K. *Chem. Phys. Lett.* **1980**, *74*, 379.

[130] Tsuda, M. *J. Polym. Sci. A* **1964**, *2*, 2907.

[131] Egerton, P. L.; Pitts, E.; Reiser, A. *Macromolecules* **1981**, *14*, 95.

[132] Nakayama, Y.; Matsuda, T. *J. Polym. Sci. A* **1992**, *30*, 2451.

[133] Minsk, L. M.; Smith, I. G.; Wright, J. F. *J. Appl. Polym. Sci.* **1959**, *2*, 302.

[134] Robertson, E. M.; Van Deusen, W. P.; Minsk, L. M. *J. Appl. Polym. Sci.* **1959**, *2*, 308.

[135] Coqueret, X. *Macromol. Chem. Phys.* **1999**, *200*, 1567.

[136] Chujo, Y.; Sada, K.; Saegusa, T. *Macromolecules* **1990**, *23*, 2693.

[137] Ngai, T.; Wu, C. *Macromolecules* **2003**, *36*, 848.

[138] Zweifel, H. *Photogr. Sci. Eng.* **1983**, *27*, 114.

[139] Berger, J.; Zweifel, H. *Angew. Makromol. Chem.* **1983**, *115*, 163.

[140] Finter, J.; Widmer, E.; Zweifel, H. *Angew. Makrolom. Chem.* **1984**, *128*, 71.

[141] Finter, J.; Haniotis, Z.; Lohse, F.; Meier, K.; Zweifel, H. *Angew. Makromol. Chem.* **1985**, *133*, 147.

[142] Decker, C.; Bianchi, C. *Polym. Int.* **2003**, *52*, 722.

[143] Ling, L.; Habicher, W. D.; Kuckling, D.; Adler, H. J. P. *Des. Monom. Polym.* **1999**, *2*, 351.

[144] Kuckling, D.; Adler, H. J. P.; Ling, L.; Habicher, W. D.; Arndt, K. F. *Polym. Bull.* **2000**, *44*, 268.

[145] Duan Vo, C.; Kuckling, D.; Adler, H. J. P.; Schönhoff, M. *Colloid Polym. Sci.* **2002**, *280*, 400.

[146] Kuckling, D.; Duan Vo, C.; Wohlrab, S. E. *Langmuir* **2002**, *18*, 4263.

[147] Kuckling, D.; Duan Vo, C.; Adler, H. J. P.; Völkel, A.; Cölfen, H. *Macromolecules* **2006**, *39*, 1585.

[148] Roth, M.; Muller, B. *Polym. Paint Col. J.* **1988**, *178*, 209.

[149] Williams, J. L. R.; Farid, S. Y.; Doty, J. C.; Daly, R. C.; Specht, D. P.; Searle, R.; Borden, D. G.; Chang, H. J.; Martic, P. A. *Pure & Appl. Chem.* **1977**, *49*, 523.

[150] Williams, J. L. R. *Fortschr. Chem. Forsch.* **1969**, *13*, 227.

[151] Webb, R. H. *Rep. Prog. Phys.* **1996**, *59*, 427.

[152] Peters, R.; Peters, J.; Tews, K. H.; Bähr, W. *Biochim. Biophys. Acta* **1974**, *367*, 282.

[153] Axelrod, D.; Koppel, D. E.; Schlessinger, J.; Elson, E.; Webb, W. W. *Biophys. J.* **1976**, *16*, 1055.

[154] Meyvis, T. K. L.; De Smedt, S. C.; Van Oostveldt, P.; Demeester, J. *Pharm. Res.* **1999**, *16*, 1153.

[155] Sukhishvili, S. A.; Chen, Y.; Müller, J. D.; Gratton, E.; Schweizer, K. S.; Granick, S. *Macromolecules* **2002**, *35*, 1776.

[156] Zettl, H.; Häfner, W.; Böker, A.; Schmalz, H.; Lanzendörfer, M.; Müller, A. H. E.; Krausch, G. *Macromolecules* **2004**, *37*, 1917.

[157] Liu, R.; Gao, X.; Adams, J.; Oppermann, W. *Macromolecules* **2005**, *38*, 8845.

[158] Haugland, R. P. *Handbook of Fluorescent Probes and Research Products*, 9th ed.; Molecular Probes Inc.: Eugene, OR, 2002.

[159] Seiffert, S. *Diffusion linearer Polyacrylamidketten in konzentrierten Systemen*; Diploma Thesis, Clausthal University of Technology, 2004.

[160] Seiffert, S.; Oppermann, W. *Macromol. Chem. Phys.* **2007**, *208*, 1744.

[161] Pabon, M.; Selb, J.; Candau, F.; Gilbert, R. G. *Polymer* **1999**, *40*, 3101.

[162] Fevola, M. J.; Hester, R. D.; McCormick, C. L. *J. Polym. Sci.: Part A* **2003**, *41*, 560.

[163] Tanaka, T. *Sci. Amer.* **1981**, *244*, 124.

[164] Gupta, M. K.; Bansil, R. *Am. Chem. Soc. Pol. Prepr.* **1981**, *22*, 375.

[165] Gottlieb, H. E.; Kotlyar, V.; Nudelman, A. *J. Org. Chem.* **1997**, *62*, 7512.

[166] Kélen, T.; Tüdös, F. *J. Macromol. Sci.-Chem.* **1975**, *A9(1)*, 1.

[167] Gribbon, P.; Hardingham, T. *Biophys. J.* **1998**, *75*, 1032.

[168] Liu, R.; Oppermann, W. *Macromolecules* **2006**, *39*, 4159.

[169] Collins, J. S.; Goldsmith, T. H. *J. Histochem. Cytochem.* **1981**, *29*, 411.

[170] Cantow, H. J. *Makromol. Chem.* **1964**, *70*, 130.

[171] Scholtan, W.; Lange, H. *Kolloid-Z. u. Z. Polymere* **1972**, *250*, 782.

[172] Seiffert, S.; Oppermann, W. *J. Microsc.* **2005**, *220*, 20.

[173] Hauser, G. I.; Seiffert, S.; Oppermann, W. *J. Microsc.* **2008**, accepted.

[174] Seiffert, S. *G.I.T. Imaging&Microscopy* **2007**, *4/2007*, 49.

[175] Salmon, E. D.; Saxton, W. M.; Leslie, R. J.; Karow, M. L.; McIntosh, J. R. *J. Cell Biol.* **1984**, *99*, 2157.

[176] Kubitscheck, U.; Wedekind, P.; Peters, R. *Biophys. J.* **1994**, *67*, 948.

[177] Cheng, Y.; Prud'homme, R. K.; Thomas, J. L. *Macromolecules* **2002**, *35*, 8111.

[178] Ross, J. L.; Fygenson, D. K. *Biophys. J.* **2003**, *84*, 3959.

[179] Soumpasis, D. M. *Biophys. J.* **1983**, *41*, 95.

[180] Lopez, A. L.; Dupou, A.; Altibelli, A.; Trotard, J.; Tocanne, J. *Biophys. J.* **1988**, *53*, 963.

[181] Gordon, G. W.; Chazotte, B.; Wang, X. F.; Herman, B. *Biophys. J.* **1995**, *68*, 766.

[182] Braeckmans, K.; Peters, L.; Sanders, N. N.; De Smedt, S. C.; Demeester, J. *Biophys. J.* **2003**, *85*, 2240.

[183] Kubitscheck, U.; Wedekind, P.; Peters, R. *J. Microsc.* **1998**, *192*, 126.

[184] Yguerabide, J.; Schmidt, J. A.; Yguerabide, E. E. *Biophys. J.* **1982**, *40*, 69.

[185] Van Zoelen, E. J. J.; Tertoolen, L. G. J.; De Laat, S. W. *Biophys. J.* **1983**, *42*, 103.

[186] Greenberg, M. L.; Axelrod, D. *J. Membr. Biol.* **1993**, *131*, 115.

[187] Periasamy, N.; Verkman, A. S. *Biophys. J.* **1998**, *75*, 557.

[188] Blonk, J. C. G.; Don, A.; Van Aalst, H.; Birmingham, J. J. *J. Microsc.* **1993**, *169*, 363.

[189] Skilling, J.; Bryan, R. K. *Mon. Not. R. astr. Soc.* **1984**, *211*, 111.

[190] Shannon, C. *Bell System Tech. J.* **1948**, *27*, 379 and 623.

[191] Jaynes, E. T. *Phys. Rev.* **1957**, *106*, 620 and *108*, 171.

[192] Johnson, M. L.; Faunt, L. M. *Meth. Enzymol.* **1992**, *210*, 1.

[193] Seiffert, S.; Oppermann, W.; Saalwächter, K. *Polymer* **2007**, *48*, 5599.

[194] Engel, P. S.; Monroe, B. M. *Adv. Photochem.* **1972**, *8*, 245.

[195] Lathioor, E. C.; Leigh, W. J. *Photochem. Photobiol.* **2006**, *82*, 291.

[196] Kronfeld, K. P.; Timpe, H. J. *J. prakt. Chem.* **1988**, *330*, 571.

[197] Ferreira, G. C.; Schmitt, C. C.; Neumann, M. G. *J. Braz. Chem. Soc.* **2006**, *17*, 905.

[198] Green, W. A.; Timms, A. W. *Photoinitiating Systems*; in: Fouassier, J. P.; Rabek, I., editors. *Radiation Curing in Polymer Science and Technology*, Vol. 2; Elsevier: UK, 1993.

[199] Fouassier, J. P. *Photoinitiation, Photopolymerization, and Photocuring*; Hanser Gardner: Cincinnati, 1995.

[200] Allonas, X.; Ley, C.; Bibaut, C.; Jacques, P.; Fouassier, J. P. *Chem. Phys. Lett.* **2000**, *322*, 483.

[201] Lewis, F. D.; Saunders, W. H. *J. Am. Chem. Soc.* **1968**, *90*, 7033.

[202] Krystkowiak, E.; Maciejewski, A.; Kubicki, J. *ChemPhysChem* **2006**, *7*, 597.

[203] Meier, K.; Zweifel, H. *J. Photochem.* **1986**, *35*, 353.

[204] Gupta, A.; Mukhtar, R.; Seltzer, S. *J. Phys. Chem.* **1990**, *84*, 2356.

[205] Bryce-Smith, D.; Bullen, G. J.; Clark, N. H.; Connett, B. E.; Gilbert, A. *J. Chem. Soc. C* **1966**, 167.

[206] Mark, G.; Matthäus, H.; Mark, F.; Leitich, J.; Henneberg, D.; Schomburg, G.; Von Wilucki, I.; Polanski, O. E. *Monatsh. Chem.* **1971**, *102*, 37.

[207] Wexler, A. J.; Hyatt, J. A.; Raynolds, P. W.; Cottrell, C.; Swenton, J. S. *J. Am. Chem. Soc.* **1978**, *100*, 512.

[208] Hanifin, J. W.; Cohen, E. *J. Am. Chem. Soc.* **1969**, *91*, 4494.

[209] Tominaga, T.; Tsutsumi, S. *Tetrahedron Lett.* **1969**, *37*, 3175.

[210] Saalwächter, K.; Sommer, J. U. *Macromol. Rapid. Commun.* **2007**, *28*, 1455.

[211] Seiffert, S.; Oppermann, W. *Macromolecules* **2008**, submitted.

[212] Burchard, W. *Adv. Polym. Sci.* **1999**, *143*, 113.

[213] Kuckling, D.; Ivanova, I. G.; Adler, H. J. P.; Wolff, T. *Polymer* **2002**, *43*, 1813.

Curriculum Vitae

Sebastian Seiffert

Institute of Physical Chemistry
Clausthal University of Technology
Arnold-Sommerfeld-Str. 4
D-38678 Clausthal-Zellerfeld, Germany
Phone: +49(0) 5323 72 3642
Fax: +49(0) 5323 72 2863
Email: sebastian.seiffert@tu-clausthal.de

Born: Feb. 23, 1979, Göttingen, Germany
Nationality: German

Education and Qualifications

12/2007 PhD degree, Clausthal University of Technology

- Predicate: summa cum laude
- PhD thesis with Prof. W. Oppermann, Institute of Physical Chemistry, Clausthal University of Technology: *“Structure and Tracer Dynamics in Polyacrylamide Hydrogels”*

08/2004–12/2007 PhD student in the group of Prof. W. Oppermann, Institute of Physical Chemistry, Clausthal University of Technology

- Subject of research: *Structure and Dynamics in Hydrogels*

07/2004 Diploma in Chemistry, Clausthal University of Technology

- Degree: Dipl.-Chem.; predicate: passed with distinction (mit Auszeichnung bestanden, 1.0)
- Diploma thesis with Prof. W. Oppermann, Institute of Physical Chemistry, Clausthal University of Technology: *“Diffusion of Linear Polyacrylamide Chains in Semidilute Systems” (“Diffusion linearer Polyacrylamidketten in konzentrierten Systemen”)*

02/2002	Nominee for scholarship by the German National Academic Foundation
10/2001	Intermediate Diploma in Chemistry, Clausthal University of Technology; grade: very good (1.0)
10/1999–08/2004	Study of Chemistry at Clausthal University of Technology
09/1998–10/1999	Alternative Civilian Service (Zivildienst) at the Youth Hostel Altenau, Germany
07/1998	Abitur, Robert-Koch-Schule Clausthal-Zellerfeld, Germany; grade: good (2.2)

Positions

Since 08/2004	Scientific assistant with Prof. W. Oppermann, Institute of Physical Chemistry, Clausthal University of Technology
09/2003–07/2004	Assistant at the Institute of Physical Chemistry, Clausthal University of Technology

List of Publications

Peer Reviewed Articles

“Diffusion of Linear Macromolecules and Spherical Particles in Semidilute Polymer Solutions and Polymer Networks.” Submitted to *Macromolecules* **2008** [with W. Oppermann].

“Systematic Evaluation of FRAP Experiments Performed in a Confocal Laser Scanning Microscope – Part II: Multiple Diffusion Processes.” Accepted by *J. Microsc.* **2008** [with G. I. Hauser and W. Oppermann].

“Hydrogel Formation by Photocrosslinking of Dimethylmaleimide Functionalized Polyacrylamide.” *Polymer* **2007**, *48*, 5599–5611 [with W. Oppermann and K. Saalwächter].

“Amine-Functionalized Polyacrylamide for Labeling and Crosslinking Purposes.” *Macromol. Chem. Phys.* **2007**, *208*, 1744–1752 [with W. Oppermann].

“Systematic Evaluation of FRAP Experiments Performed in a Confocal Laser Scanning Microscope.” *J. Microsc.* **2005**, *220*, 20–30 [with W. Oppermann].

Reviews and Articles in Popular Scientific Journals

“Systematic Analysis of FRAP Experiments.” *G.I.T. Imaging&Microscopy* **2007**, *4/2007*, 48–50.

“Konfokale Laserscanningmikroskopie als vielseitiges Werkzeug in der Polymerforschung – Arbeitsweise, Anwendungen und Ansätze einer Life Science Technologie in den Materialwissenschaften.” *TUContact* **2005**, *17*, 68–71 [with A. Langhoff and W. Oppermann].

Talks and Poster Presentations

"Estimation of Diffusion Coefficients by FRAP"; talk at the MRes seminar of the School of Physical Sciences and Engineering, Kings College London, UK, 11/2007.

"Systematic Evaluation of FRAP Experiments as a Function of Time and Space Performed on a Confocal Laser Scanning Microscope"; talk at the "Focus on Microscopy 2007" conference, Valencia, Spain, 04/2007.

"Diffusion of Linear and Spherical Tracers in Semidilute Polymer Solutions and Gels"; poster presentation at the meeting of the German Chemical Society on "Polymers & Coatings 2006", Mainz, Germany, 09/2006.

"Diffusion of Linear Macromolecules and Spherical Particles in Semidilute Polymer Solutions and Polymer Networks"; talk at the Polymer Networks Group conference on "Functional and Biological Gels and Networks", Sheffield, UK, 09/2006.

"Estimation of Diffusion Coefficients by FRAP"; talk at the Photonic Net Forum on "Life Science Microscopy", Göttingen, Germany, 12/2004.

"Dynamics in Polyacrylamide Solutions Studied by FRAP"; talk at the meeting of the European Graduate School on "Microstructural Control in Free-Radical Polymerization", Clausthal-Zellerfeld, Germany, 09/2004.